Mass Spectrometric and Computational Study of Gaseous L-Glutathione Non-Covalent Complexes

By

©Mahsa Sharifi

A dissertation submitted to the School of Graduate Studies in partial fulfillment of the requirement for the degree of Master of Science

Department of Chemistry

Memorial University of Newfoundland

St. John's, Newfoundland and Labrador, Canada

October 2024

ABSTRACT

This study investigates the structures, energetics, and unimolecular reactions of glutathione complexes with various metal cations, including alkali metals, alkaline earth metals, transition metals, and heavy metals. Using sustained off-resonance irradiation collision-induced dissociation (SORI-CID) and infrared multiphoton dissociation (IRMPD) spectroscopy, combined with computational techniques, the research explores the coordination chemistry and dissociation dynamics of these metal-GSH complexes. Additionally, the study examines the dissociation behaviors of protonated amino acid-GSH complexes, correlating these findings with proton affinity data and kinetic parameters.

Chapter 2 explores SORI-CID and IRMPD (or vibrational) spectroscopy results for $[M(GSH)]^+$ complexes (where M is an alkali metal cation), highlighting differences in fragmentation behaviors linked to metal size and charge density. The study reveals that smaller cations like Li^+ and Na^+ lead to extensive fragmentation of glutathione, whereas larger cations like Rb^+ and Cs^+ predominantly result in the loss of glutathione itself. The lowest energy alkali metal-glutathione complexes are tetracoordinated, with the metal binding to the amino nitrogen and three carbonyl oxygens, while O2 interacts with the thiol and forms a hydrogen bond with the amine. The vibrational spectra for these structures are in good agreement with experimental IR spectra.

In Chapter 3, the fragmentation patterns of doubly charged metal glutathione complexes are analyzed. SORI-CID results for metals including Mg^{2+}, Ca^{2+}, and Zn^{2+} reveal fragmentation pathways such as the loss of water, ammonia, and pyroglutamic acid. The IRMPD spectra and computational models offer detailed structural insights, showing that metal coordination affects the binding geometry and stability of these complexes.

Chapter 4 investigates the dissociation dynamics of protonated glutathione complexes with various amino acids using BIRD experiments. Temperature-dependent studies reveal that arginine, with

its high proton affinity, shows the most rapid dissociation, while lysine exhibits slower kinetics. The findings underscore the influence of amino acid side chain properties on dissociation mechanisms and provide a comprehensive understanding of their stability and reactivity.

Overall, this thesis integrates experimental and computational approaches to elucidate the structural and dynamic properties of metal-GSH and amino acid-glutathione complexes, offering valuable insights into their fragmentation patterns, structural configurations, and reactivity under varying conditions.

ACKNOWLEDGMENTS

There are numerous people who have motivated and supported me throughout my graduate studies, and without their help, the research presented in this thesis would not have been accomplished.

First and foremost, I extend my sincere gratitude to my supervisor, Prof. Travis D. Fridgen for their unwavering support, patience, and invaluable guidance throughout my academic journey. I am deeply grateful for the opportunity to present my research at various conferences and for their consistent encouragement.

I would like to give recognition to my supervisory committee, Dr. Christina Bottaro and Dr. Heather Reader, for reviewing my thesis and providing insightful comments on my work. I am also thankful for the wonderful staff in the chemistry department general office for their help and support during my masters' program.

I am particularly thankful for the support of FELIX and CLIO laboratories, as well as for the assistance of Jonathan Martens from FELIX and Estelle Loire from CLIO in conducting the experiments. Finally, I owe a special debt of gratitude to my family. I am profoundly grateful to my wonderful husband, Javad, and my cherished daughter, Eilie, for their unwavering support, patience, and encouragement throughout these years. Their boundless love and understanding have been my greatest source of strength and inspiration. I would also like to thank my immediate family have been a constant source of love, concern, support, and strength all these years.

Table of Contents

LIST OF TABLES

LIST OF FIGURES

Chapter 1 - Introduction and Overview

1.1 Glutathione

The tripeptide, L-γ-glutamyl-L-cysteinyl-glycine, known as glutathione (GSH) (Fig. 1.1), is made up of three amino acids: glutamic acid, cysteine, and glycine, and it is the most abundant non-protein sulfhydryl widely dispensed in eukaryotic cells [1] with cellular concentrations ranging from 0.5–10 mM [2]. GSH, is a critical low molecular weight antioxidant that is synthesized in cells [3]. It is present in its reduced form over 90% of the time. The oxidized form of GSH, glutathione disulfide (GSSG), is also present in microbial cells, tissues, and plasmas [4]. The GSH molecule contains many basic sites, including two carboxyls, one thiol, one amino, and two pairs of carbonyl and amide sites making up the two peptide bonds, all which can coordinate with both hard and soft metal cations to form a stable complex [5, 6]. Hence, the coordination chemistry of GSH acts as a model system for the binding of metal ions of larger peptide and protein molecules and whose study is of significant importance [7].

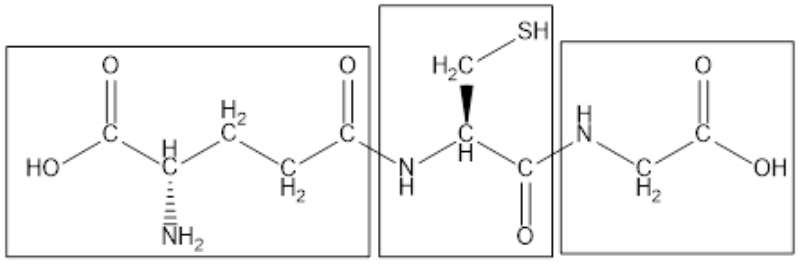

Figure 1.1: The structure of glutathione (GSH, L-γ-glutamyl-L-cysteinyl-glycine).

Although GSH plays various important roles in many physiological processes, the general functions of GSH can be divided into three main categories: serving as an antioxidant, an immunity booster, or a detoxifier in higher eukaryotic organisms [8].

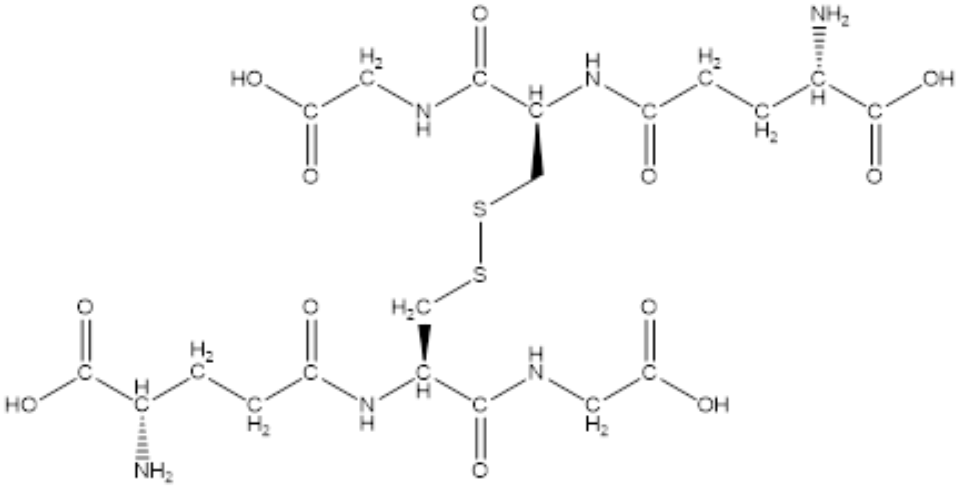

Figure 1.2: The structure of oxidized glutathione.

A variety of processes can result in the oxidation of GSH under conditions of marked toxicity or oxidative stress to form the oxidized form, GSSG [9, 10] (Fig. 1.2). First, based on the relatively high intracellular concentration of GSH and its powerful electron-donating properties, it helps to maintain a reduced cellular environment. As such, it works as an essential antioxidant in living cells to protect DNA, proteins, and other biomolecules against various oxidants, free radicals, and cytotoxic agents [11]. GSH has antioxidant activity throughout the entire body due to its solubility in fat and water [12]. Second, GSH is a key player in the immune system via white blood cell production and is known as an effective anti-viral agent. Finally, GSH coordinates to exogenous electrophiles and diverse xenobiotics accomplishing detoxification of the cell. In fact, an important role of GSH is removing metabolic waste in the liver's detoxification system, as well as in the complexation and elimination of some toxic metals from organisms [13]. Transporting amino acids into cells is

also an important role of GSH [1]. Indeed, GSH is considered the most powerful, versatile, and important self-generating defense molecules [11].

In 1888, GSH was discovered by J. de Rey-Paihade as a substance extracted from yeast by ethanol and was referred to as "philothion." After further assessment of its molecular structure in 1912, it was renamed glutathione [14]. In 1929, Hopkins proposed that cysteine, glutamate, and glycine form the tripeptide glutathione. The structure of glutathione, which is γ-glutamate-cysteine-glycine, was confirmed by Harington and Mead in 1935 through chemical synthesis from N-carbobenzoxycystine, and glycine ethyl ester [15]. GSH can be formed by chemical synthesis, enzymatic catalysis, microbial fermentation, or genetic/metabolic engineering. A GSH can be yielded from enzymatic production and genetic/metabolic pathways [16, 17], but their industrial applications are limited due to the relatively high cost of three precursor amino acids. The synthesis of GSH via chemical methods and microbial fermentation pathways were commercialized in the 1950s and 1980s, respectively. Chemical synthesis results in a racemic mixture of the D- and LGSH, so separation is required to purify the physiologically active L-form from its D-isomer [18].

The biosynthesis of glutathione from its constituent amino acids involves the combination of cysteine with glutamate to produce c-glutamylcysteine. This process is catalyzed by glutamate-cysteine ligase (GCL) and called glutamylcysteine synthetase [3] (Fig. 1.3). In the next step, the enzyme glutathione synthetase catalyzes the addition of glycine to the dipeptide to produce GSH (c-glutamylcysteinylglycine). Both stages of GSH synthesis require coupling to ATP hydrolysis to drive peptide bond formation [1, 19, 20]. Since hydrogen peroxides are released during autooxidation, simple thiols like cysteine function as a cellular toxin, so the autooxidation can be slowed by blocking the cysteine amino group in g-glutamyl-

cysteine formation [21]. So, linking glycine to the γ-glutamyl-cysteine dipeptide by GSH synthetase to form GSH enhances resistance to autooxidation [22]. Additionally, more extended carboxyl sites are provided in this reaction for substrate recognition and active site by many GSH-dependent enzymes [21].

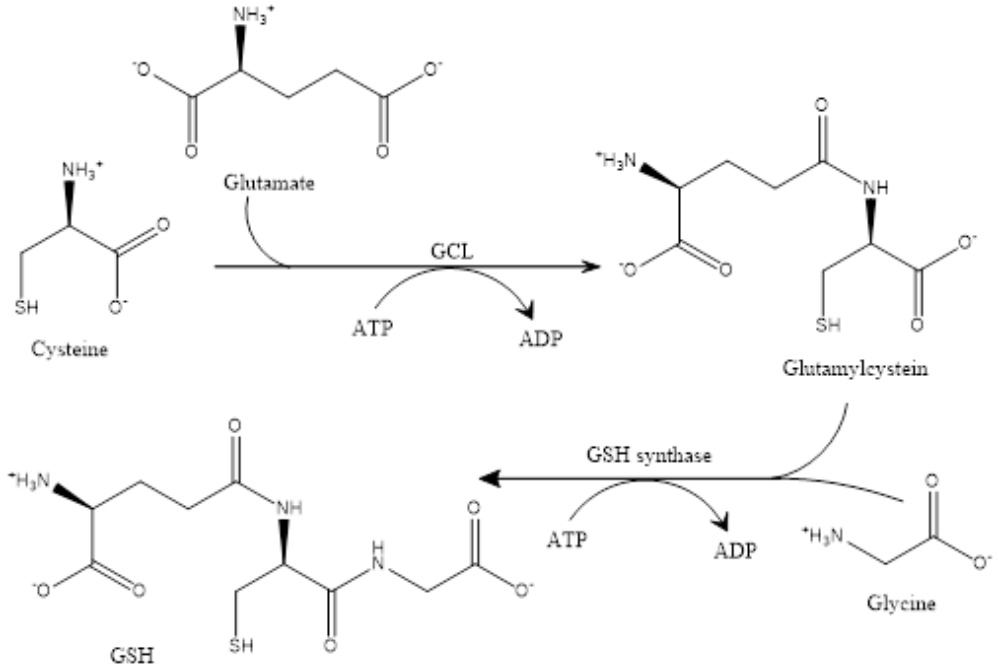

Figure 1.3: Glutathione synthesis. The sequential ATP-dependent formation of amide bonds between cysteine and the γ-carboxyl group of glutamate and then between glycine and cysteine are shown.

It has been demonstrated that several human disease states, including HIV infection, liver cirrhosis, pulmonary diseases, gastrointestinal and pancreatic inflammations, diabetes, neurodegenerative diseases, and aging, have been associated with GSH deficiency [11]. GSH has been widely used in the pharmaceutical industry and can be used in food additives and the cosmetic industry [23]. In the human body, the antioxidant properties of glutathione are well known for their ability to scavenge physiological free radicals [24]. Changes in the GSH has been observed in patients with Alzheimer's disease [25, 26], Parkinson's disease [27, 28],

diabetes mellitus [29, 30], atherosclerosis [31, 32], arthritis [33], epilepsy [34], aging [35], and numerous types of cancer [36].

Overproduction of free radicals in the brain can cause oxidative damage [37]. Millimolar concentrations of GSH in the brain play a pivotal role in protecting cells from oxidative damage [38]. For instance, an alteration in GSH homeostasis can enhance oxidative stress that has been linked to various neurodegenerative diseases, such as Parkinson's disease (PD). With a prevalence of approximately 1% over the age of 65, PD is a progressive neurodegenerative disorder characterized by impaired motor and cognitive functions [39].

Lower GSH concentrations in plasma, whole blood, and gastric mucosa [40] indicate antioxidant defence impairment which has been seen in the elderly [41]. Calvin A. Lang et al. (2000) [42] revealed a link between age-related chronic illnesses in older people to their blood glutathione concentrations. The elderly individuals with lower GSH levels become more susceptible to diseases compared with elderly individuals with normal GSH concentrations [42].

In addition, the higher concentration of GSH in liver cells is congruous with its acting as a major detoxifying organ of the body. Several genetic diseases associated with altered GSH synthesis and metabolism can significantly disrupt liver function and can be conditionally lethal in some instances. In humans, hepatic intracellular GSH levels range from 0.5 to 10 mM, maintained by using the regular dietary intake of precursor sulfur-containing amino acids [43, 44].

Considering the importance of glutathione roles in antioxidant defence, nutrient metabolism, and regulation of cellular events, and also its interaction with other biologically important molecules such as enzyme active sites, metal cations, other proteins, peptides, and

amino acids, this work aims to understand the structures and thermodynamics of metal cation chelation to glutathione in addition to identifying the molecular level details of interactions between these species.

1.2 Metals

Metal ions play vital structural and functional roles in all life. They are essential in biological processes such as osmotic regulation, catalysis, metabolism, and cell signaling and have many functions in biochemistry [45]. Metal ions with high electron affinity can significantly promote several chemical processes, including bond cleavage and formation, electron transfer, and radical reactions [46, 47].

Essential metal ions in human body fluids include alkali metal ions, especially sodium (Na^+) and potassium (K^+) [48]. The most abundant cation in the extracellular fluid is Na^+, and it is a key player in maintaining the right balance of fluids and electrolytes. It plays a part in regulation of blood volume, pressure, osmotic equilibrium, and pH values. On the other hand, K^+ concentration is greater inside human cells. The biological roles of K^+ are similar to those of Na^+, including maintaining fluid and electrolyte balances, acid-base homeostasis, systemic blood pressure control, hormone secretion and action, glucose and insulin metabolism, and neurotransmission [45]. The action potential is a voltage caused by differences between the concentrations of sodium ions and potassium ions in extracellular and intracellular fluids and is critical for body functions such as neurotransmission, muscle contraction, and heart function [49].

Next-most-abundant metal ion in living cells is Mg^{2+}. Protein synthesis, muscle and nerve function, blood glucose control, and blood pressure regulation are biochemical functions that require Mg^{2+} as a cofactor in the human body [50]. Ca^{2+} is the fifth most abundant element

found in the human body with ninety-nine percent of all calcium in the body is present in bones and teeth. The remaining 1% is found in the blood and soft tissue where Ca^{2+} plays a role as a secondary messenger in cell-signalling pathways [51, 52]. They are responsible for vasoconstriction and vasodilation, nerve impulse transmission, muscle contraction, and the secretion of hormones like insulin. In addition, calcium ions act as a cofactor for many enzymes in several coagulation factors. The alkaline earth metal ions, Ca^{2+} and Mg^{2+}, are critical messengers in cell signalling, including neurotransmission. They are also involved in enzyme function [50, 53]. One biological viewpoint is that alkali and alkaline earth metal ions are attached to proteins under physiological conditions [54]. Alkali and alkaline earth metal ions bound to proteins serve several functions of living systems, such as regulating enzyme activity, stabilizing biological membranes, and transporting glaucids and amino acids to proteins through transmembrane channels [55, 56].

Manganese ion (Mn^{2+}) is implicated in the formation of reactive oxygen species and their subsequent reactions with macromolecules such as proteins, lipids, polysaccharides, and nucleic acids resulting in changes to membrane fluidity, loss of enzyme activity, and genomic damage [57]. There is some evidence that shows a link between exposure to manganese and the development of neurologic impairment resembling Parkinsonism [58] or epilepsy [59]. Iron is classified as the most common and abundant transition metal in the human body with two biologically relevant oxidation states, the ferrous form (Fe^{2+}) and the ferric form (Fe^{3+}). The essential roles of iron in many biological processes [60] are oxygen transport, energy production, DNA synthesis, as well as cell growth and replication through iron-dependent proteins. In addition, iron-sulfur (Fe-S) clusters are ubiquitous protein cofactors associated with energy production, DNA synthesis, and DNA replication and repair [61]. Cobalt is

essential to humans, as it is found at the center of vitamin B_{12} [62]. However, higher cobalt concentrations can be induced by the generation of reactive oxygen species and their carcinogenic properties [63]. While intracellular nickel plays an essential role in the functioning of the human body, by increasing hormonal activity and involvement in lipid metabolism, the accumulation of Ni(II) can transform normal human cells into cancer cells [64]. The intracellular GSH concentration is an important factor in increasing cellular resistance to Ni(II) [65]. Copper, an essential trace dietary metal, is present mainly in the liver, muscles, and bones of the human body [66], and it helps with the proper growth, development, and support of bones, connective tissues, and many organs in the body such as the brain and heart. Also, it is necessary for red blood cell formation, iron metabolism, cholesterol and glucose metabolism, and the synthesis and release of life-sustaining proteins and enzymes. In addition, the immune response to fight infections, repair injured tissues, and promote healing can be supported by copper [67]. Although copper has an essential role in many biological processes, it is also important in bioorganisms. Excess copper can cause damage to lipids, nucleic acids, and proteins by enhancing the level of reactive oxygen species (ROS) [64, 68]. Zinc is one of the highest concentration transition metals in the human body and it is the most abundant within the brain. While Zn^{2+} is vital for cellular function, sustained increases in free Zn^{2+} levels lead to a cell death mechanism and mitochondrial dysfunction by Zn^{2+}-induced loss of cellular antioxidant capacity with depleting cellular GSH [69]. As the chemical behaviors of the transition metal ions is changed inside the cell, it can become toxic and disrupt the biological systems [70, 71]. Transition metals such as Fe^{2+}/Fe^{3+}, Zn^{2+}, and Cu^{2+} act as a part of the of proteins and enzymes or enzymes activators, so they are involved in many vital

biological processes including oxygen transport, energy production, neurotransmission, gene expression and regulation, and a synthesis of important type of molecules [60, 72].

One of glutathione's roles is protecting against Cd^{2+} toxicity by forming Cd^{2+}-GSH complexes [73]. Cadmium, a highly toxic metal, leads to selective toxic effects on olfactory neurons, causing loss of the ability to smell [74]. The toxicity of mercury (elemental, inorganic, and organic forms) and its ability to bind covalently to sulfhydryl groups are well known [75]. Studies have been undertaken to demonstrate Hg^{2+} binds strongly to a ligand sulfur donor group [76]. Binding Hg^{2+} with the SH group adversely effects on the activity of proteins and enzymes with free-SH groups [77, 78]. Also, lead, a highly toxic heavy metal, can cause different neurobehavioral syndromes [79]. Glutathione is an SH-containing chelating agent and forms a mercaptide bond with heavy metal ions like Zn^{2+}, Cu^{2+}, Cd^{2+}, and Pb^{2+}, preventing further redox cycling and the generation of free radicals [80, 81]. Indeed, GSH is an essential component for redox balance in the cell.

Over the past decade, there has been extensive investigation on the interactions of Li^{+}, Na^{+}, K^{+}, Cs^{+}, Rb^{+}, Mg^{2+}, Ca^{2+}, Sr^{2+}, and Ba^{2+} with biological molecules, such as amino acids,[82-85] cytidine,[86] nucleic acid bases, etc. [87-94]. These interactions are interesting because of a key role of metal cations in the folding and stability of large DNA and RNA molecules and complex protein structures [95-97]. Some research illustrates the stabilizing effect provided by metal ions to the structure of DNA and RNA when a metal ion interacts with a phosphate group of the nucleic acid chain due to charge neutralization and noncovalent interactions with the phosphate backbone of the nucleic acid [98-100]. Liu et al. (2013) [54], studied the complexes of GSH with alkali (Li^{+}, Na^{+}, K^{+}) and alkaline earth (Be^{2+}, Mg^{2+}, Ca^{2+}) metal cations using the B3LYP/6-31G(d,p) density function method. They showed that the

coordination behaviors of the alkali and alkaline metal ions with GSH are similar. The cations prefer to coordinate with the N atom of NH_2 and the O atom of the carboxylic and the carbonyl groups to form pentacoordinate structures as the lowest energy structure [54]. The bonding between some metal cations such as Li^+, Na^+, K^+, Mg^{2+}, and Ca^{2+} with proteins under physiological conditions, have received the attention of biologists because they are involved in several functions of living systems such as regulating enzymes, stabilizing biological membranes, transporting glaucids, and amino acids to proteins through transmembrane channels [55, 56, 101] .

In the investigation of complexes formed by glutathione (GSH) with metal cations such as Cr^{2+}, Mn^{2+}, Fe^{2+}, Co^{2+}, Ni^{2+}, Cu^{2+}, Zn^{2+}, Cd^{2+}, and Hg^{2+} using density functional theory (DFT), Liu et al. (2014) [102], revealed the effect on the binding energy of the interactions of GSH-metal cations in nine different stable complexes. In general, the binding energies of GSH to metal cations in the same period is in the following order: $Cu^{2+} > Ni^{2+} > Co^{2+} > Fe^{2+} > Cr^{2+} > Zn^{2+} > Mn^{2+}$; although the binding energies decrease down through the groups of the periodic table in order of $Zn^{2+} > Hg^{2+} > Cd^{2+}$. Moreover, sulfur and nitrogen transfer more charge to transition metal cations than O atoms. Additionally, while the bond length ranks in the order of M-S > M-N > M-O as a general trend, it decreases from Cr^{2+} to Hg^{2+}. Furthermore, the values of the Wiberg bond indices (WBIs), which are used to compare bond densities, showed that WBIs of M-S (M denotes metal cations) were larger than M-N and then M-O for Fe^{2+}, Co^{2+}, Ni^{2+}, Cu^{2+}, Zn^{2+}, Cd^{2+} and Hg^{2+} complexes; while for Cr^{2+} complexes, the most of the M-O bond WBIs were higher than those of M-S and M-N [102].

The electron shells in alkali and alkaline earth metal ions are generally classified as hard metal cations. They are spherically symmetrical and cannot be polarized easily. These

cations tend to have electrostatic interactions with their ligands having donor atoms such as oxygen or nitrogen. In contrast, 'soft' cations such as Cd^{2+} and Pb^{2+} have a soft electron cloud that is easily polarized. They form an electrostatic interaction with donor atoms with similar properties, such as sulfur. The affinity of metal ions to thiol groups has been reported in order of $Cd^{2+} > Pb^{2+} > Cu^{+}/Cu^{2+}$ by Połeć-Pawlak et al. (2007) [103], is confirmed by the hard-soft acid-base (HSAB) theory [104]. Transition metal ions typically have intermediate character, although some cations, like Cr^{3+} and Fe^{3+}, show a high oxygen affinity, whereas others, like Mn^{2+}, have a relatively low tendency to form bonds [105, 106].

1.3 Amino acids

Recently, the characterization of non-covalent complexes formed from small molecules and biomacromolecules, such as proteins, polypeptides, and oligonucleotides [107-109], has attracted significant interest considering their potential application in pharmacology. The non-covalent interactions of proteins with other components existing in living cells define their biological function. These non-covalent interactions are investigated to figure out the cellular processes in healthy or disease states [110, 111].

Organic compounds containing both basic ($-NH_2$) and acidic (-COOH) functional groups, along with a generic side chain (R group), are called "amino acids" are the basic units of proteins. A series of amino acids are joined together by peptide bonds to form a polypeptide or protein. More than 500 amino acids have been identified naturally, but only 20 amino acids are encoded by the universal genetic code. Others occur in living organisms but are not found in proteins or are not produced directly by regular cellular processes [112].

In this thesis, GSH complexes with seven amino acids are studied. The amino acids, include the basic amino acids arginine (Arg), lysine (Lys), and histidine (Hys); Arg contains a

guanidine group and is produced from citrulline in all cell types. Its major functions include cell division, wound healing, removing ammonia from the body, and immune function. Lys has an amine side chain and is an essential amino acid which must be obtained from the diet. The main role of Lys is as a building block in protein synthesis. His has a heterocyclic imidazole side chain and is also an essential amino acid with unique roles in proton buffering, metal ion chelation, reactive oxygen and nitrogen species scavenging, erythropoiesis, and the histaminergic system.

Two structurally similar neutral amino acids with polar side chains, asparagine (Asn) and glutamine (Gln), are also studied. Gln is abundant as a free amino acid in plasma and is used in the intercellular synthesis of GSH by conversion to glutamate. Asn and Gln play an essential role in supporting growth, proliferation, and survival of cancerous cells.

Two acidic amino acids, aspartic acid (Asp) and glutamic acid (Glu) were also complexed with GSH in this work. Both have regulatory roles in nutrition, energy metabolism, and oxidative stress (Fig. 1.4) [113].

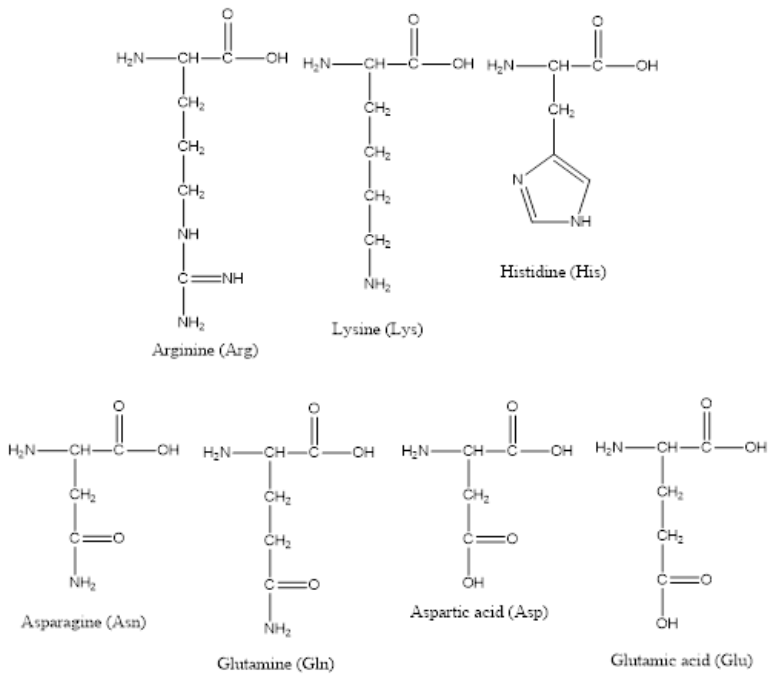

Figure 1.4: The structure of Amino acids Arginine, Lysine, Histidine, Asparagine, Glutamine, Aspartic acid, and Glutamic acid).

Non-covalent interactions between GSH and eight common amino acids found in the human body were investigated by Dai and coworkers in 2008 [114]. In this paper, collision-induced dissociation (CID) in a tandem mass spectrometer is produced by electrospray ionization mass spectrometry (ESI-MS) to examine the binding of GSH-amino acid complexes. Their ESI mass spectra demonstrate that the noncovalent interactions between GSH and amino acids such as Met, Phe, Tyr, Ser, and Ile are of differing strengths. Afterward, the improved calculation formula derived due to the existence of some oligomeric species, was used to obtain the dissociation constants of GSH binding to Glu, His, or Gln. Then the structural information provided from Fourier transform ion cyclotron mass spectra for GSH-amino acids complexes illustrated that amino acids may bind to the thiol (–SH) group of Cys or N-terminal amino group of Glu residue in glutathione by electrostatic attraction force [114].

1.4 Experimental Methods

The aim of this section is to introduce the experimental methods that have been used to study the intrinsic properties _in the absence of solvent_ of ion-molecule complexes in the gas phase. These experimental results were conducted in the laboratory to study the energetics, structures, and reactions of gaseous ions using a Bruker Apex Qe7 Fourier transform ion cyclotron resonance (FTICR) mass spectrometer at Memorial University of Newfoundland (Figure 1.6). There are at least four steps involved in most mass spectrometry experiments such as ionization, trapping, ion activation, and data analysis. The basic principles of instrumentation and techniques will be introduced in this section. The incorporation of ion dissociation methods such as collision induced dissociation (CID), infrared multiphoton dissociation (IRMPD), and blackbody infrared radiative dissociation (BIRD) are facilitated in the low-pressure environment of the FTICR. The mechanism of fragmentation involved in each method will also be discussed below.

1.4.1 Determining the Structures of Biomolecules Using Mass Spectrometric Techniques.

A mass spectrometer has three main parts: the ion source, the analyzer, and the detector. However, the nature of the sample determines the choice of the ion source and the suitable analyzer type. Different types of ionization sources, mass analyzers, and mass analyzer configurations have proven useful to study the physical chemistry of gaseous ions.

1.4.1.1 Ion sources

The first part of every mass spectrometer is the ion source. In the present work, electrospray ionization (ESI) has been used [115]. The first known use of an ESI source coupled with mass spectrometry was in 1968 by Malcolm Dole [116]. ESI is considered to be

a “soft” source of ions in that ions with low internal energy are transferred from solution to the gas phase. As such, ESI has been especially useful for the characterization of biomolecules by mass spectrometry.

In ESI, ions are transferred from the solution to the gas phase under atmospheric pressure. After dissolving the sample in a proper solvent, it is injected into a thin conducting capillary at high voltage causing a strong electric field of around 10^6 V m^{-1} at the capillary exit. A Taylor cone is created from the assemblage of charge near the droplet surface at the capillary tip [117-120]. Charged droplets, containing analyte ions, are emitted from the Taylor cone in the presence of a strong potential applied between the capillary and the inlet of the mass spectrometer. Repulsive coulombic forces stress the droplets as they undergo evaporation of the solvent, causing splitting and the formation of smaller droplets. The desolvated ions are released to the gas phase and enter the mass spectrometer (Figure 1.5).

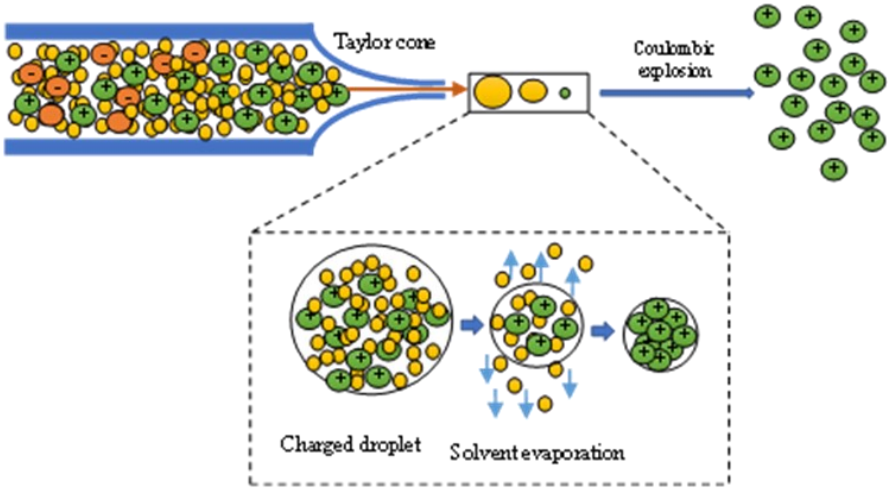

Figure 1.5: Schematic of an electrospray ionization process for a positive ionization mode.

The ion source operates under high pressure, ~mbar, while mass analyzers operate in a high vacuum.

1.4.1.2 Mass analyzers

Ions are characterized based on their mass-to-charge ratio (m/z) in all mass analyzers. There are two main classes of mass analyzers. First is the beam type mass analyzer, for example, the time of flight (TOF). Second are the ion trapping mass analyzers, such as the quadrupole ion trap or Fourier-transform ion cyclotron resonance (FTICR), in which ions can be isolated and stored for relatively long periods to allow further probing manipulations of the ions such as activation processes [115]. The FTICR can be an ultra-high-resolution mass analyzer with great mass accuracy. It can be used to investigate fine isotope structures of proteins with masses up to 100 kDa and is used in wide-ranging applications. A high upper mass limit is one of the advantages of the FTICR mass analyzers, limited only by the radius of the ion trap. Other advantages of the FTICR include the mass resolving power and the larger number of ions trapped compared to other trapping devices [115, 121, 122]. One of the instruments used in this research is shown in Figure 1.6.

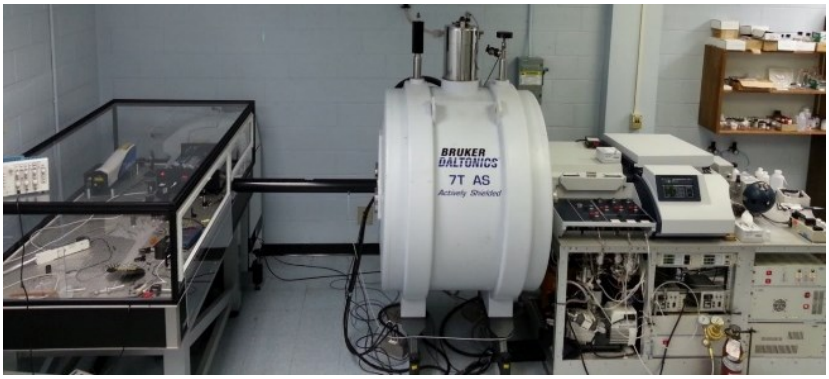

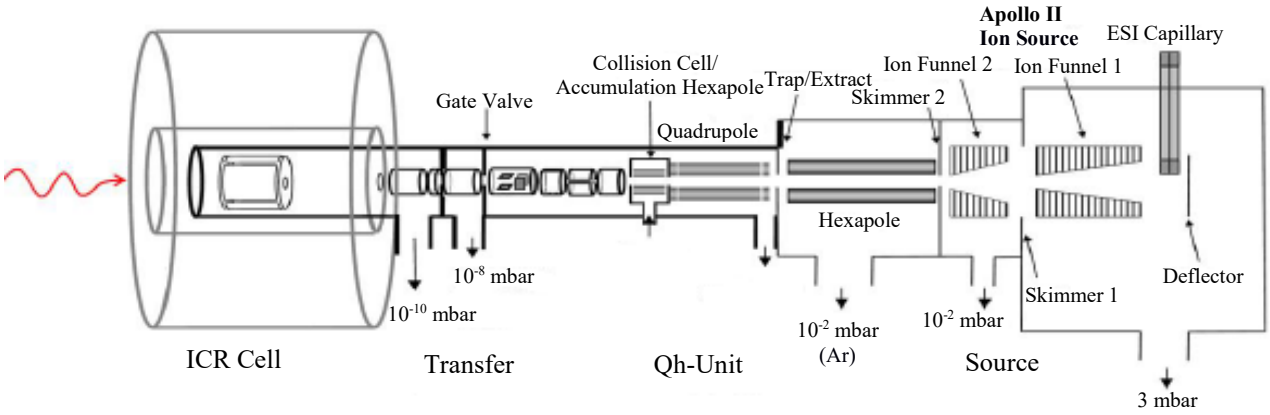

Figure 1.6: Top: The OPO lasers/Bruker Apex Qe 70 FTICR-MS located at Memorial University [89], Bottom: The schematic of the Bruker Apex Qe 7.0 T FTICR-MS used with permission from [90].

Inside the ICR cell, an ion with mass (m) moves in a circular trap of radius (r) in the presence of a uniform magnetic field ($\vec{B}$) acting perpendicular to the velocity of the ion ($\vec{v}$) with charge (q). So, the balanced of the ion's centrifugal force by the Lorentz force (centripetal) is given by:

$$q\vec{v}\vec{B} = \frac{m\vec{v}^2}{r} \tag{1.1}$$

Where q is the charge number, e is the elementary-charge constant. The frequency of orbit of an ion, called cyclotron frequency (w_c), is expressed as:

$$w_c = \frac{\vec{v}}{2\pi r} = \frac{ze\vec{B}}{r} \tag{1.2}$$

and the angular frequency is:

$$w = 2\pi\vec{v}_c = \frac{ze}{m}\vec{B} \tag{1.3}$$

Upon rearranging, the *m/z* is obtained:

$$\frac{m}{z} = \frac{e\vec{B}}{w} \tag{1.4}$$

Hence, the *m/z* is determined by the measured frequency of the ions' rotation in the ICR cell [123].

Ions are trapped in the xy or radial direction in the presence of the magnetic field, and an electric potential is applied to trapping plates at both ends of the ICR cell, leading to trapping ions in the third dimension (right side of Figure 1.7). The left side of Figure 1.7 illustrates confining $\vec{B}$ ions in its circular trajectory of ions and in the xy direction by applying a magnetic field.

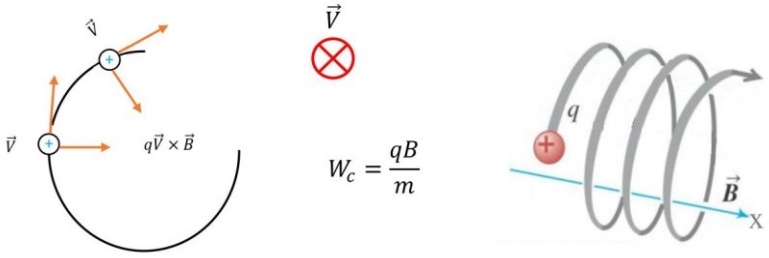

Figure 1.7: A schematic of the side view of a cylindrical geometric FTICR mass analyzer in a strong magnetic field.

There are three pairs of plates in the ICR cell, or analyzer cell, of the FTICR, depicted in Figure 1.8-a. As discussed above, two end cap trapping plates keep the ions constrained axially by applying a small potential voltage. There are two excitation plates to which a radio

frequency (RF) electric field is applied. This RF potential accelerates the trapped ions causing an increase in their radius of orbit and velocity (Figure 1.8-a) while maintaining their characteristic frequency of orbit.

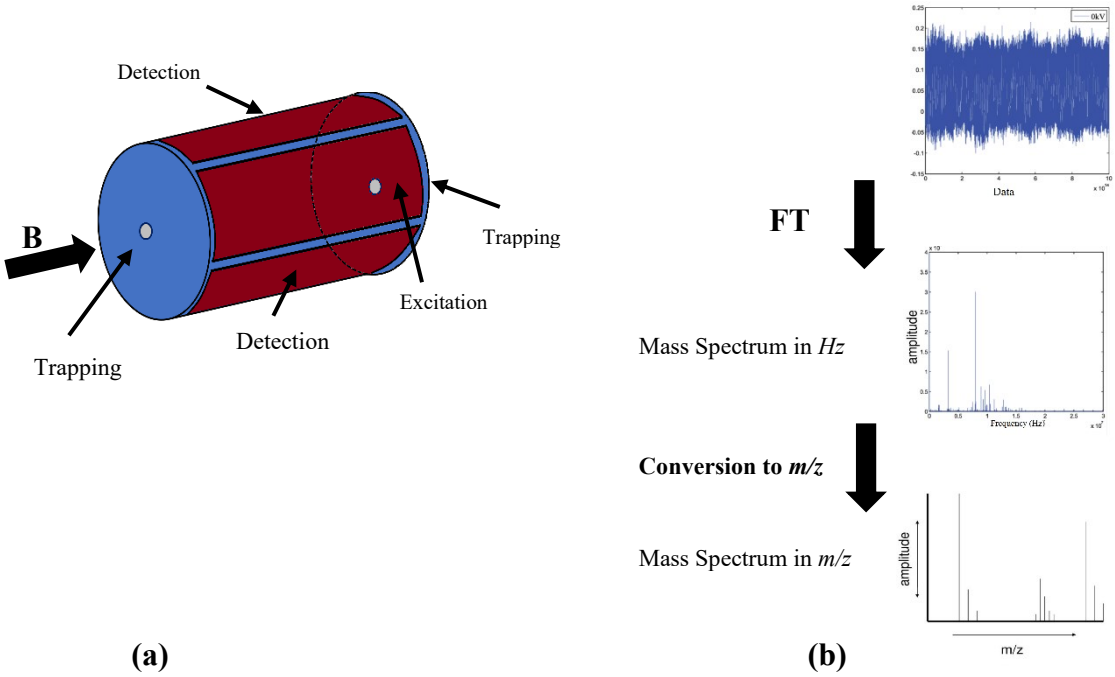

Figure 1.8: a) A schematic of the cross-section view of an FTICR mass analyzer located within a strong magnetic field and b) the procedure of converting the time domain transient of raw data to the frequency domain and then calibrated regarding m/z.

All ions of all masses are excited during a fast sweep of all RF frequencies. This excitation process converts the incoherent orbiting motion of the ion packet to detectable coherent motions of several ion packets each characterized by a particular *m/z*. As a ion packets pass the detection plate, an image current is induced oscillating at the cyclotron frequencies corresponding to the m/z values of the ions present in the trap. When as the ion packet moves away from detection plate toward the opposite plate electrons in the plate are attracted toward the approaching ion packet. The image current of one ion packet is sinusoidal, with an

amplitude representing the number of ions and a frequency equal to that of the ion's cyclotron frequency. The detected signal is a composite of the sinusoidal image currents with different frequencies and amplitudes for many ion packets. A mathematical procedure known as a Fourier transform converts the detected time-domain signal, or transient, into the frequency domain. Eventually, the *m/z* is provided from the frequencies using Equation 1.4 (Figure 1.8-b).

1.4.2 Mass Spectrometric Fragmentation Techniques of Gas-Phase Ions

While mass spectrometry produces useful information such as *m/z*, structural characteristics and thermochemical quantities can also be determined using fragmentation methods. These methods include energetic collisions, absorption of photons from lasers, electron capture, or even absorption of ambient blackbody infrared radiation. Simply stated, these techniques increase the internal energy of an ion above its dissociation threshold, resulting in fragmentation of the ion. The fragmentation patterns provide useful information about their structures.

Tandem mass spectrometry in an ICR involves at least two steps of mass analysis. Generally, in the first step, precursor ions are selected and isolated. In the isolation process, all ions except the ion of interest are excited by applying an rf pulse and ejected from the ICR cell. Fragment ions are created by an activation process such as collision-induced dissociation (CID). CID is an activation process; collisions increase the internal energy leading to dissociation. A mass spectrum containing the masses of all the fragments can then be acquired. If desired, a product ion can be isolated in a subsequent stage and subjected to additional CID, producing another group of product ions. In this thesis, fragmentation techniques such as CID

and infrared multiphoton dissociation (IRMPD) are used to study the properties of non-covalent glutathione complexes and will be described below.

1.4.2.1 Collision-induced dissociation

CID is probably the most widely used activation technique. Ions are accelerated through a potential difference, increasing their translational energy. The ions then collide with a neutral target gas, which converts a portion of their kinetic energy to internal energy. Depending on the instrument, ions undergo one or many collisions, increasing their internal energy above the dissociation threshold of the ion, leading to fragmentation.

The CID technique used in FTICR MS is called sustained off-resonsant irradiation or SORI. SORI-CID starts out similar to how ions are excited during detection. It involves applying an RF voltage across the excitation plates for a period of time, where the RF is very close to the cyclotron frequency of the ions, accelerating the ion's cyclotron motion while a pulse of argon gas fills the ICR cell to a pressure of about 10^{-4} mbar for a short period of time. Each collision transfers a few tenths of an eV of internal energy, so the ion encounters many collisions to increase its internal energy above its dissociation threshold.

1.4.2.1.1 Infrared Multiphoton Dissociation (IRMPD)

IRMPD is a technique used in mass spectrometry to dissociate ions in the gas phase by absorbing low energy photons from a high-intensity infrared laser (commonly a CO_2 laser). In IRMPD, ions are trapped in the quadrupole ion trap or FTICR-MS and absorb many infrared photons from an intense light source. The resonance between the wavelength of a tunable infrared laser and vibrational modes of the ion allows the absorption of multiple photons. This absorption increases the internal energy of the ion and surpasses the dissociation threshold causing dissociation of the ion [124].

The energy of infrared photons typically ranges from 10-40 kJ mol^{-1}, so like SORI-CID, it is a slow activation process, and as such, the lowest-energy dissociation pathways are usually observed [125-127]. Because the photons in the IR region are so low in energy, many photons are required, hence the multiple in IRMPD. IRMPD begins by the absorption of a single photon resonant with a vibrational mode of the ion. The energy of the photon is quickly distributed throughout the ion in a process known as intramolecular vibrational-energy redistribution (IVR), so in the absence of collisions or radiative relaxation, the internal energy of the ion is increased. Following IVR, the electron in the absorbing mode returns to the ground state, so will be free to absorb another photon. After repeating the process of absorption followed by rapid IVR the internal energy of the ion exceeds the dissociation threshold, and fragmentation of the ion occurs [128]. Figure 1.9 depicts the IRMPD process.

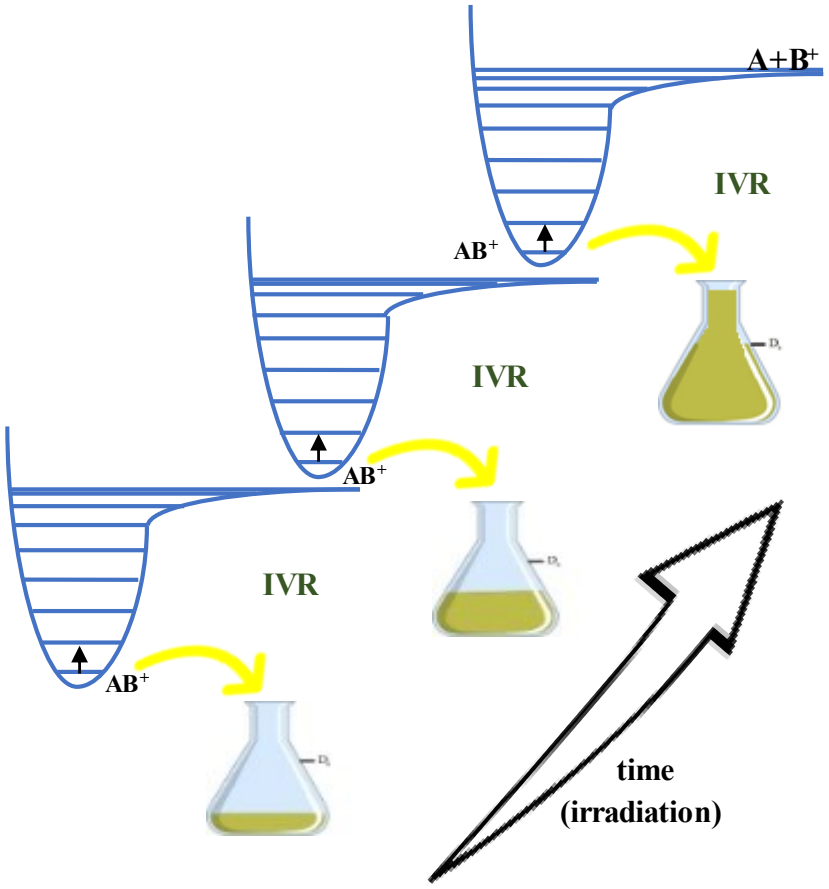

Figure 1.9: Schematic of the mechanism of the IVR process in IRMPD.

If a tunable infrared laser is used, fragmentation efficiency can be recorded as a function of laser wavelength producing an IRMPD spectrum or vibrational spectrum. IRMPD spectroscopy is a vibrational spectroscopy, so one can obtain structural information, like functional group identity. Eexperimental spectra are usually compared to computed gas phase infrared spectra for potential structures, which provides further evidence for proposed ion structures [129].

There are two sources of tunable infrared radiation in two different wavelength regions used in this work. The first is the so-called fingerprint region (900 – 2000 cm^{-1}). This range is covered by free-electron lasers (FELs) at either the Centre Laser Infrarouge d'Orsay (CLIO)

just outside Paris, France, or the Free-Electron Laser for Infrared Experiments (FELIX) in Nijmegen, Netherlands. The second region covers the C-H/N-H/O-H stretching region (2700 – 3800 cm^{-1}) and is covered by an optical parametric oscillator (OPO) in the Laboratory for the Study of Structures, Energetics, and Reaction of Gaseous Ions at Memorial University.

1.4.2.1.2 Blackbody Infrared Radiative Dissociation

Blackbody infrared radiative dissociation (BIRD) is another soft activation technique. BIRD relies on absorbing ambient black-body infrared (IR) radiation by the ion trapped in a low-pressure environment. Weakly-bound ionic complexes have an internal energy distribution such that ions are at or above the dissociation threshold. The absorption of a single photon increases the rate constant for dissociation such that it is observable on the timeframe of the experiment. As a very slow activation method, BIRD requires irradiation times on the scale of seconds or even 100s seconds to observe sufficient dissociation to obtain a kinetic plot. An FTICR is used for these experiments due to the ability to trap ions for this timescale [130, 131].

Equation 1.5 shows the mechanism for BIRD and includes activation, deactivation, and dissociation of the non-covalently bound complex, $AB^{\pm}$:

$$AB^{\pm} \underset{k_{em}}{\overset{k_{abs}}{\leftrightarrows}} AB^{\pm *} \xrightarrow{k_d} A + B^{\pm} \tag{1.5}$$

Where k_{abs}, k_{em} and k_d represent photon absorption, photon emission, and the dissociation rate constants, respectively. The apparent rate constant for unimolecular decomposition, k_{uni}, is defined the steady-state approximation (Equation 1.6).

$$\mathbf{k}_{uni} = \left(\frac{\mathbf{k}_{abs}\mathbf{k}_d}{\mathbf{k}_{em}+\mathbf{k}_d}\right) \tag{1.6}$$

The unimolecular dissociation rate constant, k_{uni}, can be determined from the slope of the logarithmic plot of the precursor ion abundance as a function of time, t. is the time dependence of the ion intensity is shown in Equation 1.7 [132]. Where $I(AB^+)$ is the normalized intensity, t is the time.

$$\mathbf{I(AB^+)} = e^{-k_{uni}t} \tag{1.7}$$

The emission and absorption rate constants are large for large molecules with many vibrational degrees of freedom, and the dissociation rate constant is expected to be smaller due to being the energy being randomized throughout the molecule. At this limit, the rapid exchange (REX) of radiation limit, $k_d \ll k_{em}$, therefore Equation 1.6 can be simplified to Equation 1.8.

$$\mathbf{k}_{uni} = \left(\frac{\mathbf{k}_{abs}\mathbf{k}_d}{\mathbf{k}_{em}}\right) \tag{1.8}$$

It has been shown that thermal equilibrium is reached for these large complexes in the REX limit [130, 133-136], so that the emission and absorption rate constants are equal so that equation 1.8 can be further simplified to 1.9:

$$\mathbf{k}_{uni} = k_d \tag{1.9}$$

At thermal equilibrium in this large molecule limit, threshold dissociation energies, E_0, can be extracted directly from the Arrhenius plot [131].

The Arrhenius activation energies (E_a) used to help determine the threshold for dissociation found from a plot of the logarithm of temperature dependent k_{uni} vs. T^{-1}(equation 1.10).

$$\mathbf{k}_{uni} = Ae^{-\mathbf{E}_a/\mathbf{k}_B\mathbf{T}} \tag{1.10}$$

where A is the pre-exponential factor and k_B is the Boltzmann constant. The entropy of activation ($\Delta S\dagger$) is defined by Equation 1.11,

$$A = \frac{k_B T}{h} e^{(1+\left(\frac{\Delta S_{\ddagger}}{k_B}\right))} \quad (1.11)$$

For systems (less than about 100 degrees of freedom), the rate of dissociation may be significantly higher than the absorption and emission rate constant ($k_d >> k_{em}$), the so-called slow exchange (SEX) limit and thermal equilibrium between these systems and their surroundings may not occur. Under these circumstances, the true dissociation threshold is estimated to be higher than the E_a values, and master equation modelling is required to extract the dissociation threshold from the experimental Arrhenius plots.

1.5 Computational Methods

In this work, the experimental results are compared to structures and thermodynamic properties obtained through electronic structure calculations. These computational methods can provide structures and properties of gaseous non-covalent complexes. For example, computed IR spectra are usually compared with experimental IRMPD spectra. Electronic structure methods generally include a level of theory and a basis set.

1.5.1 Density Functional Theory (DFT) Methods

There are different groups of electronic structure techniques, such as ab initio techniques and DFT methods. In ab initio methods, the Schrödinger equation for many-electron systems is solved by assuming the Born-Oppenheimer approximation which uncouples nuclear motion from electronic motion [137]. This method determines the electronic energy of the ground electronic state in a fixed nuclear configuration by changing nuclear degrees of freedom. The potential energy surface (PES) is defined by obtaining electronic energies as a function of the reaction coordinate. One of the most common ab initio methods is the Hartree-Fock (HF) technique which is a computationally expedient method to solve the

Schrödinger equation for atoms, molecules, and nanostructures. Post-Hartree-Fock methods, such as Møller-Plesset (MP) [138, 139], is a set of methods developed to improve the accuracy of the Hartree–Fock (HF) method. Electron correlation added in post HF methods provide more accurate results. The computational cost and time are limitations in both methods, which incentivized the development of methods dependent on the electron density. Density Functional Theory (DFT) is a method to study the structural and electronic properties of molecules in which functions of electron density are used to calculate properties of the system. In this work, the primary methods used to predict the minimum energy structures of ions of interest are DFT methods.

1.5.1.1 Basis sets

Basis sets are finite sets of functions that have a key role in making molecular orbitals in all of the above calculations. Molecular orbitals are represented as a linear combination of atomic orbitals. Gaussian-type functions (GTF) are the most popular type of atomic orbitals in use [140, 141]. The core and valance shell orbitals are described by one or more basis functions. K-LMG is a common class of basis set expressed by the split-valance basis set and used in this work. The K and LM parts correspond to the number of core Gaussian functions (G) and the valence shell atomic orbitals, respectively. Polarization functions are functions of higher angular momentum quantum numbers that are unoccupied in the atom. They can be added to the basis sets to improve results as they add more flexibility. For example, by adding d or * to the basis set, a d-function is added to the heavy atoms in the selected basis set, or when d,p or ** is added to the selected basis set, it means polarization functions (a p orbital) are also added to light atoms. In addition, + or aug represents the addition of diffuse function to the basis set. Diffuse functions are typically added to the anions and excited states basis sets

to obtain more reliable results [142]. In larger atoms containing many electrons, effective core potentials (ECP), a pseudopotential method, are used where the ECP represents the core electron instead of Gaussian functions.

The first step in the calculations is to guess an initial geometry constructed from chemical intuition Gaussview. Then the geometry optimizations and the frequency calculations are performed. A full geometry optimization is an iterative procedure controlled by geometry convergence criteria, and this process continues until achieving the minimum energy geometry. Then the frequency analysis is carried out by calculating the normal mode according to the forces applied to each nucleus (from the second derivative/gradient of potential energy).

The vibrational frequency, v for each n normal mode, can be determined from the second energy derivatives with respect to the Cartesian nuclear coordinates. The sum of the energy of each normal vibrational mode in a molecule with N atoms acquires the vibrational energy, $E_{vib,}$ which can be calculated by equation 1.12, where h is Planck's constant.

$$E_{vib} = \sum_l \left(\frac{1}{2} h v_i\right) \tag{1.12}$$

After analyzing the normal mode, the frequency of each vibrational normal mode can be determined. The zero-point energy (E_{zp}) is calculated from the energy of each mode, and it is added to the electronic energy (E_{elec}). Consequently, the enthalpy (H) and Gibbs energy (G) of the system are computed using the frequency calculations and their contributions to the enthalpy (H) and entropy (S) of the system. Therefore, the obtained IR spectrum, which is obtained from the frequency analysis on the optimized structure, can be compared with the experimental IRMPD spectrum.

The total internal energy of the molecule (E_{tot}) resulting from the sum of the electronic (E_{elec}), vibrational (E_{vib}), rotational (E_{rot}), translational (E_{trans}), and zero-point (E_{zp}) energies is represented in equation 1.13.

$$E_{tot} = E_{elec} + E_{vib} + E_{rot} + E_{trans} + E_{zp} \quad (1.13)$$

The total internal energy is used to calculate H, and G, by the following thermochemical relations as shown in Equations 1.14 and 1.15.

$$H = E_{tot} + RT \quad (1.14)$$

$$G = E_{tot} + RT - TS_{tot} = H - TS_{tot} \quad (1.15)$$

Where the total entropy (S_{tot}) is calculated from translational (S_{trans}), rotational (S_{rot}), vibrational (S_{vib})and electronic (S_{elec}) motions (Equation 1.16).

$$S_{tot} = S_{trans} + S_{rot} + S_{vib} + S_{elec} \quad (1.16)$$

In this work, all calculations were done using the Gaussian 16 suite of programs [143] to obtain the geometry optimization, enthalpies and Gibbs energies. Dispersion corrections were used to evaluate the short-range and London dispersion interactions between ions to improve the performance of DFT methods. Becke's 3-parameter-Lee-Yang-Parr (B3LYP) is a prevalent modified version of the density function and yields good geometries and thermochemical properties. 6-31+G(d,p) and Def2SVP basis sets have been used in all calculations. In this thesis, all harmonic frequencies were corrected using scaling factors of 0.975 and 0.945 in the fingerprint (1000-1900 cm^{-1}) and C–H/N–H/O–H stretching (2700-3800 cm^{-1}) regions, respectively. Theoretical IR spectra were convoluted using Gaussian functions (10 cm^{-1} fwhm). Electronic energies were refined with single-point calculations using B3LYP/6-311+G(3df,3pd) for all atoms except Rb^{+}, Cs^{+}, Sr^{2+}, Ba^{2+}, Cd^{2+}, Hg^{2+} and Pb^{2+}, for which the Def2TZVP basis set was used. For comparison, geometry optimizations and

frequency were calculated using B3LYP6/6-311G(2d,d,p) for all atoms, and B3LYP/Def2TZVP were used for Rb^+, Cs^+, Sr^{2+}, Ba^{2+}, Cd^{2+}, Hg^{2+} and Pb^{2+} atoms.

1.6 Objectives of Thesis

The main scope of this thesis is to study the intrinsic properties of glutathione adducts (alkali metal, alkaline earth metals, transition metals, some heavy metals, and seven amino acids) in the gas phase using tandem mass spectrometry along with computational chemistry. The motivation behind experiments stems from the important bioactivity and the potential pharmaceutical application of glutathione adducts in biological systems. Following this aim, in Chapter 2, the structures of GSH-alkali metal complexes are investigated using SORI-CID and IRMPD spectroscopy in the 1000 to 1900 cm^{-1} regions.

Due to GSH intracellular abundance, it is a likely target for metal cations, especially those having high affinity to form mercaptide bonds with heavy metals via their thiol groups, providing a primary defense against metal cation toxicity [102]. So, the investigation of the structures, energetics, and reactivities of gas-phase $[M(GSH-H)]^+$ complexes (M=alkaline earth metals, transition metals, and heavy metals) using SORI-CID and IRMPD spectroscopy in the 2700 to 3800 cm^{-1} and the 1000 to 1900 cm^{-1} regions are discussed in Chapter 3.

In addition, Glutathione conjugation facilitates the transfer of amino acids out of the cell by binding its electrophiles sites to amino acids [144]. In Chapter 4, it is shown that BIRD kinetic measurements can be used for complexes in the gas phase. In this research, the gas-phase stabilities of glutathione-amino acids cations were studied by blackbody infrared radiative dissociation (BIRD) to examine its binding energy and stability in the gas phase.

1.7 References

(1) Alberts, B. *Molecular biology of the cell*; Garland science, **2017**.

(2) Blanco, A.; Blanco, G. *Medical biochemistry*; Academic Press, **2017**.
(3) Forman, H.J., H. Zhang, and A. Rinna, Glutathione: overview of its protective roles, measurement, and biosynthesis. Molecular aspects of medicine, **2009**. 30(1-2): p. 1-12.
(4) Forbes, J.; Krishnamurthy, K. Biochemistry, Peptide. **2020**.
(5) Giblin, F.J., Glutathione: a vital lens antioxidant. Journal of Ocular Pharmacology and Therapeutics, **2000**. 16(2): p. 121-135.
(6) Alanazi, A. M.; Mostafa, G. A.; Al-Badr, A. A. Glutathione. Profiles of drug substances, excipients and related methodology **2015**, 40, 43-158.
(7) Matsui, R.; Ferran, B.; Oh, A.; Croteau, D.; Shao, D.; Han, J.; Pimentel, D. R.; Bachschmid, M. M. Redox regulation via glutaredoxin-1 and protein S-glutathionylation. *Antioxidants & Redox Signaling* **2020**, *32* (10), 677-700.
(8) Pastore, A., et al., Analysis of glutathione: implication in redox and detoxification. Clinica chimica acta, **2003**. 333(1): p. 19-39.
(9) Knapen, M.F., et al., Glutathione and glutathione-related enzymes in reproduction: a review. European Journal of Obstetrics & Gynecology and Reproductive Biology, **1999**. 82(2): p. 171-184.
(10) Harfield, J.C., C. Batchelor-McAuley, and R.G. Compton, Electrochemical determination of glutathione: a review. Analyst, **2012**. 137(10): p. 2285-2296.
(11) Wu, G., et al., Glutathione metabolism and its implications for health. The Journal of nutrition, **2004**. 134(3): p. 489-492.
(12) Shankar, R. and P. Kolandaivel, Coordination and binding properties of zwitterionic glutathione with transition metal cations. Inorganica Chimica Acta, **2012**. 387: p. 125-136.
(13) Li, Y.; Wei, G.; Chen, J. Glutathione: a review on biotechnological production. Applied microbiology and biotechnology **2004**, 66 (3), 233-242.
(14) Penninckx, M.J. and M.T. Elskens, Metabolism and functions of glutathione in micro-organisms. Advances in microbial physiology, **1993**. 34: p. 239-301.
(15) Alanazi, A.M., G.A. Mostafa, and A.A. Al-Badr, Glutathione. Profiles of drug substances, excipients and related methodology, **2015**. 40: p. 43-158.
(16) Ohtake, Y., et al., The expression of the γ-glutamylcysteine synthetase gene of Escherichia coli B in Saccharomyces cerevisiae. Agricultural and biological chemistry, **1988**. 52(11): p. 2753-2762.
(17) Mahajan, S. and W.M. Atkins, *The chemistry and biology of inhibitors and pro-drugs targeted to glutathione S-transferases.* Cellular and Molecular Life Sciences CMLS, **2005**. 62(11): p. 1221-1233.
(18) Li, Y., et al., Using Lactococcus lactis for glutathione overproduction. Applied microbiology and biotechnology, **2005**. 67(1): p. 83-90.
(19) Meister, A., Glutathione; Metabolism and function via the γ-glutamyl cycle. Life sciences, 1974. 15(2): p. 177-190.
(20) Dimitrova, M., S. Turmanova, and K. Vassilev, *Complexes of glutathione with heavy metals as catalysts for oxidation.* Reaction Kinetics, Mechanisms and Catalysis, **2009**. 99(1): p. 69-78.

(21) Douglas, K.T., Reactivity of glutathione in model systems for glutathione S-transferases and related enzymes. Glutathione Conjugation, Mechanism and Biological Significance. Academic Press, London, **1988**: p. 1-41.
(22) Sundquist, A.R. and R.C. Fahey, Evolution of antioxidant mechanisms: thiol-dependent peroxidases and thioltransferase among procaryotes. Journal of molecular evolution, **1989**. 29(5): p. 429-435.
(23) Sies, H., Glutathione and its role in cellular functions. Free Radical Biology and Medicine, **1999**. 27(9-10): p. 916-921.
(24) Klatt, P. and S. Lamas, Regulation of protein function by S-glutathiolation in response to oxidative and nitrosative stress. European journal of biochemistry, **2000**. 267(16): p. 4928-4944.
(25) Liu, H., et al., Glutathione metabolism during aging and in Alzheimer disease. Annals of the New York Academy of Sciences, **2004**. 1019(1): p. 346-349.
(26) Pinnen, F., et al., Ibuprofen and glutathione conjugate as a potential therapeutic agent for treating Alzheimer's disease. Archiv der Pharmazie, **2011**. 344(3): p. 139-148.
(27) Lang, A.E., The progression of Parkinson disease: a hypothesis. Neurology, **2007**. 68(12): p. 948-952.
(28) Zeevalk, G.D., R. Razmpour, and L.P. Bernard, Glutathione and Parkinson's disease: is this the elephant in the room? Biomedicine & Pharmacotherapy, **2008**. 62(4): p. 236-249.
(29) Whillier, S., J.E. Raftos, and P.W. Kuchel, Glutathione synthesis by red blood cells in type 2 diabetes mellitus. Redox Report, **2008**. 13(6): p. 277-282.
(30) Nwose, E.U., et al., Changes in the erythrocyte glutathione concentration in the course of diabetes mellitus. Redox Report, **2006**. 11(3): p. 99-104.
(31) Margutti, P., et al., Autoantibodies to the C-terminal subunit of RLIP76 induce oxidative stress and endothelial cell apoptosis in immune-mediated vascular diseases and atherosclerosis. Blood, The Journal of the American Society of Hematology, **2008**. 111(9): p. 4559-4570.
(32) Schutte, R., et al., Blood glutathione and subclinical atherosclerosis in African men: the SABPA Study. American journal of hypertension, **2009**. 22(11): p. 1154-1159.
(33) Pedersen-Lane, J.H., R.B. Zurier, and D.A. Lawrence, Analysis of the thiol status of peripheral blood leukocytes in rheumatoid arthritis patients. Journal of leukocyte biology, **2007**. 81(4): p. 934-941.
(34) Pence, S., et al., Total brain tissue sialic acid levels due to glutathione effect in experimental epilepsy. International Journal of Neuroscience, **2007**. 117(11): p. 1523-1535.
(35) Goncharova, N., et al., Hypothalamic-pituitary-adrenal system and enzymes of the glutathione-dependent antioxidant system during stress and aging. Bulletin of Experimental Biology and Medicine, **2007**. 144(5): p. 730-733.
(36) Wong, D.Y.-K., et al., Glutathione concentration in oral cancer tissues. Cancer letters, **1994**. 81(2): p. 111-116.
(37) Niki, E., et al., Membrane damage due to lipid oxidation. The American journal of clinical nutrition, **1991**. 53(1): p. 201S-205S.

(38) Luo, J.-L., et al., Skeletal muscle glutathione after surgical trauma. Annals of surgery, **1996**. 223(4): p. 420.
(39) Shew, S., et al. A prospective randomized trial of parenteral cysteine supplementation to enhance glutathione synthesis in premature neonates. in 5th International Symposium on Amino Acid/Protein Metabolism in Health and Disease, Perugia, Italy. **1999**.
(40) Lawrence, N.S., J. Davis, and R.G. Compton, Electrochemical detection of thiols in biological media. Talanta, **2001**. 53(5): p. 1089-1094.
(41) Ling, Y.Y., X.F. Yin, and Z.L. Fang, Simultaneous determination of glutathione and reactive oxygen species in individual cells by microchip electrophoresis. Electrophoresis, 2005. 26(24): p. 4759-4766.
(42) Lang, C.A., et al., Blood glutathione decreases in chronic diseases. Journal of Laboratory and Clinical Medicine, 2000. 135(5): p. 402-405.
(43) Hudson, V.M., Rethinking cystic fibrosis pathology: the critical role of abnormal reduced glutathione (GSH) transport caused by CFTR mutation. Free radical biology and medicine, 2001. 30(12): p. 1440-1461.
(44) Townsend, D.M., K.D. Tew, and H. Tapiero, The importance of glutathione in human disease. Biomedicine & pharmacotherapy, 2003. 57(3-4): p. 145-155.
(45) Zheng, X., et al., Detection of metal ions in biological systems: A review. Reviews in Analytical Chemistry, 2020. 39(1): p. 231-246.
(46) Vyas, N. and A.K. Ojha, A study on interaction of Be^{++}, Mg^{++} and Ca^{++} with phenylalanine: Binding energies, metal ion affinities and IR signature of complex stability. Vibrational Spectroscopy, 2011. 56(1): p. 42-50.
(47) Ragsdale, S.W., Metals and their scaffolds to promote difficult enzymatic reactions. Chemical reviews, 2006. 106(8): p. 3317-3337.
(48) Carter, K.P., A.M. Young, and A.E. Palmer, Fluorescent sensors for measuring metal ions in living systems. Chemical reviews, 2014. 114(8): p. 4564-4601.
(49) Ding, Y., et al., Fluorescent and colorimetric ion probes based on conjugated oligopyrroles. Chemical Society Reviews, 2015. 44(5): p. 1101-1112.
(50) Rude, R.K., Magnesium metabolism and deficiency. Endocrinology and metabolism clinics of North America, 1993. 22(2): p. 377-395.
(51) Brini, M., et al., Intracellular calcium homeostasis and signaling, in Metallomics and the Cell. 2013, Springer. p. 119-168.
(52) Brini, M., et al., Calcium in health and disease. Met Ions Life Sci. 2013; 13: 81–137. Epub 2014/01/29. https://doi. org/10.1007/978-94-007-7500-8_4 PMID: 24470090.
(53) Weaver, C., et al., Present knowledge in nutrition. 9th edtion, International Life Science Institute Press, Washington DC, USA, 2006: p. 373-382.
(54) Liu, J., et al., Theoretical study on the interaction of glutathione with group IA (Li^{+}, Na^{+}, K^{+}), IIA (Be^{2+}, Mg^{2+}, Ca^{2+}), and IIIA (Al^{3+}) metal cations. Structural Chemistry, 2013. 24(1): p. 251-261.
(55) Rulíšek, L. and Z. Havlas, Theoretical studies of metal ion selectivity. 1. DFT calculations of interaction energies of amino acid side chains with selected transition

metal ions (Co^{2+}, Ni^{2+}, Cu^{2+}, Zn^{2+}, Cd^{2+}, and Hg^{2+}). Journal of the American Chemical Society, 2000. 122(42): p. 10428-10439.
(56) Marino, T., N. Russo, and M. Toscano, Gas-phase metal ion (Li^{+}, Na^{+}, Cu^{+}) affinities of glycine and alanine. Journal of Inorganic Biochemistry, 2000. 79(1-4): p. 179-185.
(57) Shi, Q., et al., Silicon-mediated alleviation of Mn toxicity in Cucumis sativus in relation to activities of superoxide dismutase and ascorbate peroxidase. Phytochemistry, 2005. 66(13): p. 1551-1559.
(58) Olanow, C.W., Manganese-induced parkinsonism and Parkinson's disease. Annals of the New York Academy of Sciences, 2004. 1012(1): p. 209-223.
(59) Hernandez, E.H., et al., Manganese intoxication: the cause of an inexplicable epileptic syndrome in a 3 year old child. Neurotoxicology, 2003. 24(4-5): p. 633-639.
(60) Aggett, P., Iron. U: Present Knowledge in Nutrition. Erdman JW, Macdonald IA, Zeisel SH. 2012, Washington DC, Wiley-Blackwell.
(61) Winter, W.E., L.A. Bazydlo, and N.S. Harris, The molecular biology of human iron metabolism. Laboratory medicine, 2014. 45(2): p. 92-102.
(62) Galanis, A., A. Karapetsas, and R. Sandaltzopoulos, Metal-induced carcinogenesis, oxidative stress and hypoxia signalling. Mutation research/Genetic toxicology and environmental mutagenesis, 2009. 674(1-2): p. 31-35.
(63) Valko, M., H. Morris, and M. Cronin, Metals, toxicity and oxidative stress. Current medicinal chemistry, 2005. 12(10): p. 1161-1208.
(64) Bal, W. and K.S. Kasprzak, Induction of oxidative DNA damage by carcinogenic metals. Toxicology letters, 2002. 127(1-3): p. 55-62.
(65) Li, W., Y. Zhao, and I.-N. Chou, Mg2+ antagonism on Ni^{2+}-induced changes in microtubule assembly and cellular thiol homeostasis. Toxicology and applied pharmacology, 1996. 136(1): p. 101-111.
(66) Porter, R.S., et al., The Merck manual home health handbook. 2009: Merck Research Laboratories.
(67) Stern, B.R., Essentiality and toxicity in copper health risk assessment: overview, update and regulatory considerations. Journal of Toxicology and Environmental Health, Part A, 2010. 73(2-3): p. 114-127.
(68) Kim, B.-E., T. Nevitt, and D.J. Thiele, Mechanisms for copper acquisition, distribution and regulation. Nature chemical biology, 2008. 4(3): p. 176-185.
(69) Wiseman, D.A., S. Sharma, and S.M. Black, Elevated zinc induces endothelial apoptosis via disruption of glutathione metabolism: role of the ADP translocator. Biometals, 2010. 23(1): p. 19-30.
(70) Belcastro, M., et al., Interaction of cysteine with Cu2+ and group IIb (Zn^{2+}, Cd^{2+}, Hg^{2+}) metal cations: a theoretical study. Journal of mass spectrometry, 2005. 40(3): p. 300-306.
(71) Glusker, J.P., Structural aspects of metal liganding to functional groups in proteins. Advances in protein chemistry, 1991. 42: p. 1-76.
(72) Nielsen, F.H., Ultratrace minerals. Modern Nutrition in Helath and Disease, 1999: p. 284-303.

(73) Singhal, R.K., M.E. Anderson, and A. Meister, Glutathione, a first line of defense against cadmium toxicity. The FASEB Journal, 1987. 1(3): p. 220-223.
(74) Mascagni, P., et al., Olfactory function in workers exposed to moderate airborne cadmium levels. Neurotoxicology, 2003. 24(4-5): p. 717-724.
(75) Goyer, R.A. and T.W. Clarkson, Toxic effects of metals. Casarett and Doull's toxicology: the basic science of poisons, 1996. 5: p. 691-736.
(76) Lund, B.-O., D.M. Miller, and J.S. Woods, Studies on Hg (II)-induced H2O2 formation and oxidative stress in vivo and in vitro in rat kidney mitochondria. Biochemical pharmacology, 1993. 45(10): p. 2017-2024.
(77) Oram, P.D., et al., The formation constants of mercury (II)− glutathione complexes. Chemical research in toxicology, 1996. 9(4): p. 709-712.
(78) Stricks, W. and I. Kolthoff, Reactions between mercuric mercury and cysteine and glutathione. Apparent dissociation constants, heats and entropies of formation of various forms of mercuric mercapto-cysteine and-glutathione. Journal of the American Chemical Society, 1953. 75(22): p. 5673-5681.
(79) Vigliani, E. and G. Baldi, Unusual epidemics of mercury poisoning in a felt hat factory. 1949. La Medicina del Lavoro, 2001. 92(6): p. 391-398.
(80) Cobbett, C. and P. Goldsbrough, Phytochelatins and metallothioneins: roles in heavy metal detoxification and homeostasis. Annual review of plant biology, 2002. 53(1): p. 159-182.
(81) Milne, L., et al., Effects of glutathione and chelating agents on copper-mediated DNA oxidation: pro-oxidant and antioxidant properties of glutathione. Archives of Biochemistry and Biophysics, 1993. 304(1): p. 102-109.
(82) Reddy, A.S. and G.N. Sastry, Cation [M= H^+, Li^+, Na^+, K^+, Ca^{2+}, Mg^{2+}, NH4+, and NMe4+] interactions with the aromatic motifs of naturally occurring amino acids: a theoretical study. The Journal of Physical Chemistry A, 2005. 109(39): p. 8893-8903.
(83) Tehrani, Z.A., A. Fattahi, and A. Pourjavadi, DFT study of the interaction of cytidine and 2′-deoxycytidine with Li^+, Na^+, and K^+: effects of metal cationization on sugar puckering and stability of the N-glycosidic bond. Carbohydrate research, 2009. 344(6): p. 771-778.
(84) Marino, T., N. Russo, and M. Toscano, Interaction of Li^+, Na^+, and K^+ with the proline amino acid. Complexation modes, potential energy profiles, and metal ion affinities. The Journal of Physical Chemistry B, 2003. 107(11): p. 2588-2594.
(85) Remko, M. and B.M. Rode, Effect of metal ions (Li^+, Na^+, K^+, Mg^{2+}, Ca^{2+}, Ni^{2+}, Cu^{2+}, and Zn2+) and water coordination on the structure of glycine and zwitterionic glycine. The Journal of Physical Chemistry A, 2006. 110(5): p. 1960-1967.
(86) Monajjemi, M., R. Ghiasi, and M.S. Sadjadi, Metal-stabilized rare tautomers: N4 metalated cytosine (M= Li^+, Na^+, K^+, Rb^+ and Cs^+), theoretical views. Applied organometallic chemistry, 2003. 17(8): p. 635-640.
(87) Gu, J., J. Wang, and J. Leszczynski, Iso-guanine quintet complexes coordinated by mono valent cations (Na^+, K^+, Rb^+, and Cs^+). Journal of Computational Chemistry, 2007. 28(11): p. 1790-1795.

(88) Gu, J. and J. Leszczynski, Origin of Na+/K+ selectivity of the guanine tetraplexes in water: the theoretical rationale. The Journal of Physical Chemistry A, 2002. 106(3): p. 529-532.
(89) Kabelac, M. and P. Hobza, Na^{+}, Mg^{2+}, and Zn^{2+} binding to all tautomers of adenine, cytosine, and thymine and the eight most stable keto/enol tautomers of guanine: a correlated ab initio quantum chemical study. The Journal of Physical Chemistry B, 2006. 110(29): p. 14515-14523.
(90) Chen, J., et al., A theoretical prediction on the ground-state complexes bound by metal ions to thymine base isomers. Journal of Physical Organic Chemistry, 2012. 25(2): p. 126-131.
(91) Rodgers, M. and P. Armentrout, Noncovalent interactions of nucleic acid bases (uracil, thymine, and adenine) with alkali metal ions. Threshold collision-induced dissociation and theoretical studies. Journal of the American Chemical Society, 2000. 122(35): p. 8548-8558.
(92) Azargun, M. and T.D. Fridgen, Guanine tetrads: an IRMPD spectroscopy, energy resolved SORI-CID, and computational study of M (9-ethylguanine) $^{4+}$(M= Li, Na, K, Rb, Cs) in the gas phase. Physical Chemistry Chemical Physics, 2015. 17(39): p. 25778-25785.
(93) Power, B., et al., Structures of bare and singly hydrated [M (Ura-H)(Ura)]+(M= Mg, Ca, Sr, Ba) complexes in the gas phase by IRMPD spectroscopy in the fingerprint region. International Journal of Mass Spectrometry, 2015. 378: p. 328-335.
(94) Gillis, E.A. and T.D. Fridgen, The hydrated Li+–adenine–thymine complex by IRMPD spectroscopy in the N–H/O–H stretching region. International Journal of Mass Spectrometry, 2010. 297(1-3): p. 2-8.
(95) Biot, C., R. Wintjens, and M. Rooman, Stair motifs at protein− DNA interfaces: nonadditivity of H-bond, stacking, and cation− π interactions. Journal of the American Chemical Society, 2004. 126(20): p. 6220-6221.
(96) McFail-Isom, L., X. Shui, and L. Williams, Biochemistry1998, 37, 17105− 17111. Google Scholar There is no corresponding record for this reference.
(97) De Vos, A.M., M. Ultsch, and A.A. Kossiakoff, Human growth hormone and extracellular domain of its receptor: crystal structure of the complex. Science, 1992. 255(5042): p. 306-312.
(98) Pyle, A.M., Ribozymes: a distinct class of metalloenzymes. Science, 1993. 261(5122): p. 709-714.
(99) Hanna, R. and J.A. Doudna, Metal ions in ribozyme folding and catalysis. Current opinion in chemical biology, 2000. 4(2): p. 166-170.
(100) Nelson, D.L., A.L. Lehninger, and M.M. Cox, Lehninger principles of biochemistry. 2008: Macmillan.
(101) Da Silva, J.F. and R.J.P. Williams, The biological chemistry of the elements: the inorganic chemistry of life. 2001: Oxford University Press.
(102) Liu, J., et al., Probing the coordination properties of glutathione with transition metal ions (Cr 2+, Mn 2+, Fe 2+, Co 2+, Ni 2+, Cu 2+, Zn 2+, Cd 2+, Hg 2+) by density functional theory. Journal of biological physics, 2014. 40(4): p. 313-323.

(103) Połeć-Pawlak, K., R. Ruzik, and E. Lipiec, Investigation of Cd (II), Pb (II) and Cu (I) complexation by glutathione and its component amino acids by ESI-MS and size exclusion chromatography coupled to ICP-MS and ESI-MS. Talanta, 2007. 72(4): p. 1564-1572.
(104) Pearson, R.G., Hard and soft acids and bases. Journal of the American Chemical society, 1963. 85(22): p. 3533-3539.
(105) Stumm, W., J.J. Morgan, and J.I. Drever, Aquatic chemistry. Journal of environmental quality, 1996. 25(5): p. 1162.
(106) Cotton, F., G. Wilkinson, and C. Murillo, Chemistry of the transition elements. Advanced Inorganic Chemistry, 1980. 4: p. 786.
(107) König, S., et al., Detection of ATP-binding to growth factors. Journal of the American Society for Mass Spectrometry, 2008. 19(1): p. 91-95.
(108) Yanes, O., et al., Exploring the "intensity fading" phenomenon in the study of noncovalent interactions by MALDI-TOF mass spectrometry. Journal of the American Society for Mass Spectrometry, 2007. 18(2): p. 359-367.
(109) Baytekin, B., H.T. Baytekin, and C.A. Schalley, Mass spectrometric studies of non-covalent compounds: why supramolecular chemistry in the gas phase? Organic & biomolecular chemistry, 2006. 4(15): p. 2825-2841.
(110) Bovet, C., et al., Estrogen receptor–ligand complexes measured by chip-based nanoelectrospray mass spectrometry: An approach for the screening of endocrine disruptors. Protein science, 2007. 16(5): p. 938-946.
(111) Lin, Z.J., W. Li, and G. Dai, Application of LC–MS for quantitative analysis and metabolite identification of therapeutic oligonucleotides. Journal of pharmaceutical and biomedical analysis, 2007. 44(2): p. 330-341.
(112) Romero, C.M. and M.A. Esteso, Thermodynamic and Transport Properties of Amino Acids in Aqueous Solution. Chemistry and Chemical Engineering for Sustainable Development: Best Practices and Research Directions, 2020: p. 83.
(113) Hortin, G.L., Amino Acids, Peptides, and. Tietz Fundamentals of Clinical Chemistry and Molecular Diagnostics-E-Book, 2014: p. 286.
(114) Dai, Z.-y., et al., Investigation of non-covalent complexes of glutathione with common amino acids by electrospray ionization mass spectrometry. Acta Pharmacologica Sinica, 2008. 29(6): p. 759-771.
(115) Laskin, J. and J.H. Futrell, Collisional activation of peptide ions in FT-ICR mass spectrometry. Mass spectrometry reviews, 2003. 22(3): p. 158-181.
(116) Dole, M., et al., Molecular beams of macroions. The Journal of Chemical Physics, 1968. 49(5): p. 2240-2249.
(117) Nemes, P., I. Marginean, and A. Vertes, Spraying mode effect on droplet formation and ion chemistry in electrosprays. Analytical chemistry, 2007. 79(8): p. 3105-3116.
(118) Yamashita, M. and J.B. Fenn, Electrospray ion source. Another variation on the free-jet theme. The Journal of Physical Chemistry, 1984. 88(20): p. 4451-4459.
(119) Konermann, L., A simple model for the disintegration of highly charged solvent droplets during electrospray ionization. Journal of the American Society for Mass Spectrometry, 2009. 20(3): p. 496-506.

(120) Steen, H. and M. Mann, The ABC's (and XYZ's) of peptide sequencing. Nature reviews Molecular cell biology, 2004. 5(9): p. 699.
(121) Cho, Y., et al., Developments in FT-ICR MS instrumentation, ionization techniques, and data interpretation methods for petroleomics. Mass spectrometry reviews, 2015. 34(2): p. 248-263.
(122) Marshall, A.G., C.L. Hendrickson, and G.S. Jackson, Fourier transform ion cyclotron resonance mass spectrometry: A primer. 1998: Hoboken. p. 1-35.
(123) Fridgen, T.D., Infrared consequence spectroscopy of gaseous protonated and metal ion cationized complexes. Mass spectrometry reviews, 2009. 28(4): p. 586-607.
(124) Jami-Alahmadi, Y., The physical chemistry of gaseous protonated and metal cation-coordinated proline containing complexes studied by tandem mass spectrometry methods. 2017, Memorial University of Newfoundland.
(125) Scigelova, M., et al., Fourier transform mass spectrometry. Molecular & Cellular Proteomics, 2011: p. mcp. O111. 009431.
(126) Carl, D.R., et al., Infrared multiple photon dissociation spectroscopy of cationized methionine: effects of alkali-metal cation size on gas-phase conformation. Physical Chemistry Chemical Physics, 2010. 12(14): p. 3384-3398.
(127) Dunbar, R.C., et al., Dimeric complexes of tryptophan with M2+ metal ions. The Journal of Physical Chemistry A, 2009. 113(5): p. 845-851.
(128) Piatkivskyi, A., et al., Structure and reactivity of the distonic and aromatic radical cations of tryptophan. Journal of the American Society for Mass Spectrometry, 2013. 24(4): p. 513-523.
(129) Grant, E., et al., Is multiphoton dissociation of molecules a statistical thermal process? Physical Review Letters, 1978. 40(2): p. 115.
(130) Lee, S.-S., et al., Chiral Differentiation of D-and L-alanine by Permethylated β-cyclodextrin: IRMPD Spectroscopy and DFT Methods. Physical Chemistry Chemical Physics, 2017. 19(22): p. 14729-14737.
(131) Price, W.D., P.D. Schnier, and E.R. Williams, Tandem mass spectrometry of large biomolecule ions by blackbody infrared radiative dissociation. Analytical Chemistry, 1996. 68(5): p. 859-866.
(132) Dunbar, R.C., et al., Zero-pressure thermal-radiation-induced dissociation of gas-phase cluster ions: comparison of theory and experiment for (H2O) 2Cl-and (H2O) 3Cl. Journal of the American Chemical Society, 1995. 117(51): p. 12819-12825.
(133) Jockusch, R.A. and E.R. Williams, Binding energies of proton-bound dimers of imidazole and n-acetylalanine methyl ester obtained by blackbody infrared radiative dissociation. The Journal of Physical Chemistry A, 1998. 102(24): p. 4543-4550.
(134) Price, W.D., et al., Unimolecular reaction kinetics in the high-pressure limit without collisions. Journal of the American Chemical Society, 1996. 118(43): p. 10640-10644.
(135) Schnier, P.D., et al., Blackbody infrared radiative dissociation of bradykinin and its analogues: Energetics, dynamics, and evidence for salt-bridge structures in the gas phase. Journal of the American Chemical Society, 1996. 118(30): p. 7178-7189.

(136) Price, W.D. and E.R. Williams, Activation of peptide ions by blackbody radiation: factors that lead to dissociation kinetics in the rapid energy exchange limit. The Journal of Physical Chemistry A, 1997. 101(47): p. 8844-8852.
(137) Jockusch, R.A., et al., Effects of charge state on fragmentation pathways, dynamics, and activation energies of ubiquitin ions measured by blackbody infrared radiative dissociation. Analytical chemistry, 1997. 69(6): p. 1119-1126.
(138) Brunk, E. and U. Rothlisberger, Mixed quantum mechanical/molecular mechanical molecular dynamics simulations of biological systems in ground and electronically excited states. Chemical reviews, 2015. 115(12): p. 6217-6263.
(139) Head-Gordon, M., J.A. Pople, and M.J. Frisch, MP2 energy evaluation by direct methods. Chemical Physics Letters, 1988. 153(6): p. 503-506.
(140) Møller, C. and M.S. Plesset, Note on an approximation treatment for many-electron systems. Physical Review, 1934. 46(7): p. 618.
(141) Boys, S.F., Electronic wave functions-I. A general method of calculation for the stationary states of any molecular system. Proc. R. Soc. Lond. A, 1950. 200(1063): p. 542-554.
(142) Jensen, F., Atomic orbital basis sets. Wiley Interdisciplinary Reviews: Computational Molecular Science, 2013. 3(3): p. 273-295.
(143) Davidson, E.R. and D. Feller, Basis set selection for molecular calculations. Chemical Reviews, 1986. 86(4): p. 681-696.
(144) Frisch, M., et al., Gaussian 16. 2016, Gaussian, Inc. Wallingford, CT.
(145) Gad, S.C., Glutathione. 2005.

Chapter 2 - Structures and Unimolecular Chemistry of Alkali Metal Cation Complexes with Glutathione in the Gas Phase

2.1 Preface

A version of this chapter has been published in the International Journal of Mass Spectrometry (2024). I am the primary author of this paper. Along with the co-authors, Estelle Loire, Jonathan Martens, and Travis D. Fridgen. I carried out most of the literature review, experiments, simulations, and results. I prepared the first draft of the manuscript and subsequently revised the manuscript based on the co-authors' feedback. The co-author, Travis Dr. Fridgen, contributed to defining the project, data analysis, helped with computations, as well as reviewing and revising the manuscript. The co-authors, Estelle Loire and Jonathan Martens, contributed provided advice on the discussion of the results and editorial support.

2.2 Abstract

This study investigates the unimolecular reactions of glutathione complexes with alkali metal cations in the gas phase through sustained off-resonance irradiation collision-induced dissociation and examines their structures using a combination of infrared multiphoton dissociation spectroscopy and computational techniques. Under soft CID conditions, glutathione complexes with charge-dense cations such as Li^+, Na^+, and K^+ show significant fragmentation of glutathione, while complexes with heavier cations, Rb^+ and Cs^+, primarily undergo loss of glutathione. This behavior is attributed to the stronger non-covalent binding between smaller metal cations and glutathione, which competes with the dissociation thresholds of covalent interactions within the peptide complex. Using CREST, a tool for determining trial structures which were submitted to density functional theory calculations, a thorough investigation of the conformational space revealed many possible structures,

including pentacoordinated structures for the Na^+ and K^+ complexes, as well as tetra- tri-, bi-, and monocoordinated structures along with zwitterionic structures for all metal cation/GSH complexes. For all alkali metal cation complexes, the thermodynamically most stable structures were found to be tetracoordinated A-type structures where the metal cation is bound to the amine nitrogen and three of the carbonyl oxygens—all except O2, the amide between glycine and cysteine. These computed infrared spectra for these lowest energy complexes were also consistent with the experimental vibrational spectra in the fingerprint region. Based on relative energies and the comparison of computed and experimental infrared spectra in the fingerprint region, the tetracoordinate A-type structures are concluded to be the dominant forms of the $[M(GSH)]^+$ complexes in the gas phase.

2.3 Introduction

Low molecular weight (LMW) biomolecules containing thiol groups (R-SH; where R represents an organic substituent) can be oxidized and regenerated in the cell where they play a crucial role in biochemical and pharmacological reactions [1-3]. Glutathione (GSH) is a ubiquitous LMW tripeptide with the sequence γ-L-glutamyl-L-cysteinyl-glycine and is an essential nonprotein thiol for the transport of amino acids across cell membranes via the γ-glutamyl cycle [4-6]. The level of GSH in human tissues is typically between 0.1 and 10 mM and is most concentrated in the liver (up to 10 mM) but has also been found in the spleen, kidney, erythrocytes, and leukocytes [6].

In previous studies, the biochemical effects of sodium, potassium, and to a lesser extent lithium has been assessed on enzyme regulation [7], membrane stabilization, and transporting amino acids across cell membranes [4-6]. These alkali metal cations accomplish these

processes by complexing with proteins and peptides like GSH under physiological conditions [8-11]. Thus, the coordination chemistry of GSH in binding to alkali metal cations is an important aspect of these fundamental biological processes.

There are ten basic binding sites in GSH: the carbonyl and hydroxyl oxygens of the two carboxylic acid groups, the N and O of the two amides, an amino group, and the thiol group. There are also several acidic protons that can contribute to intramolecular hydrogen bonding. Due to the variety of coordination sites in the reduced glutathione molecule, the coordination chemistry of GSH with metals is complicated and interesting. Two general coordination modes have been studied in the complexes of metal cations with GSH; soft metals prefer to coordinate to the soft base thiol site and auxiliary oxygens of the glycine moiety, whereas the glutamic moiety of GSH is the coordination site for harder metal cations such as those in groups 1 and 2 and the first row transition metal cations [12]. Several factors have been known to affect the stability of GSH/metal cation complexes including the radius and charge of metal ions, the electron configuration, and the coordination number of the metal cation with the ligand [13, 14]. By way of illustration, Lui et al. analyzed the properties of the metal ion that affects the metal-binding selectivity with GSH by evaluating multiple coordination modes of the GSH-M (M=Li^+, Na^+, K^+, Be^+, Mg^+, Ca^+) complexes. These species were explored by DFT methods and modelled using the B3LYP/6-31G(d,p) level of theory and basis set. For example, they revealed that the coordination distance and strength of binding between the metal cation and ligand is related to the ionic radius of the metal cation $Li^+ < Na^+ < K^+$, $Be^{2+} < Mg^{2+} < Ca^{2+}$, and $Al^{3+} < Mg^{2+} < Na^+$ which is attributed to the difference in ionic radius of the metal cations [14].

The present work involves the study of the structures, energetics, and unimolecular reactivities of gas-phase $[M(GSH)]^+$ complexes (M = Li, Na, K, Rb, and Cs) using a combination of sustained off-resonance irradiation-collision-induced dissociation (SORI-CID), infrared multiphoton dissociation (IRMPD) spectroscopy, and computational methods with a view to better understand their structures and binding of the metal to GSH.

2.4 Methods

2.4.1 Experimental

In these studies, ions were generated by electrospray ionization (ESI) using an Apollo II ion source coupled to the FTICR-MS. Solutions containing the relevant species were pumped into the source at 100 μLh^{-1} using a syringe pump. Glutathione (Sigma Aldrich) was used without further purification. All solutions were prepared by adding three drops of 10 mmol L^{-1} alkali metal chloride and two drops of 1% formic acid to 1 ml of 1 mmol L^{-1} GSH in a 50/50 mix of 18 MΩ-cm (Millipore) water and methanol.

All sustained off-resonance irradiation collision induced dissociation (SORI-CID) experiments were done using a Bruker ApexQe 7.0 hybrid Fourier transform ion cyclotron resonance (FTICR) mass spectrometer (MS) in the Laboratory for the Study of Structures, Energetics, and Reactions of Gaseous Ions at Memorial University. The $[M(GSH)]^+$ ion of interest was isolated inside the ICR cell ($P = 10^{-10}$ mbar) and exposing them to Ar inside the ICR cell at higher pressures ($P \approx 10^{-5}$–10^{-6} mbar). At these pressures, in the 250 ms excitation time, there are on the order of 10's to 100's of collisions [15].

Infrared multiphoton dissociation (IRMPD) spectroscopy [16-18] experiments in the fingerprint region were conducted at either the Centre Laser Infrarouge d'Orsay (CLIO) a free

electron laser facility just outside Paris, France, or at the free-electron laser for infrared experiments (FELIX) in Nijmegen, Netherlands. At CLIO [19], a FTICR-MS coupled to the FEL was used to collect the spectra for the $[M(GSH)]^+$, M=Li, Na, K complexes. These ions were isolated in the FTICR and irradiated with FEL radiation for 250 ms at 5 cm^{-1} intervals. The spectra for the M=Rb and Cs complexes were measured at FELIX after being isolated in a modified 3D quadrupole ion trap mass spectrometer (Bruker AmaZon Speed ETD) [20]. These ions were electrosprayed from the solutions described above, which were first diluted 100-fold with acetonitrile. The trapped and isolated ions were irradiated with FEL radiation scanned at 3 cm^{-1} intervals with 2 pulses of tunable infrared radiation [21]. In the C-H/N-H/O-H stretching region (2700 – 4000 cm^{-1}) region IRMPD spectroscopy experiments were performed in the Laboratory for the Study of Structures, Energetics, and Reactions of Gaseous Ions at Memorial University which has been previously described [22]. Briefly, ions were isolated in the FTICR-MS where they were irradiated with the output from an OPO laser operating at 500 mW for 2 s at 2 cm^{-1} intervals.

The reported IRMPD intensities are the negative of the natural logarithm of the product ion intensities divided by the total ion intensity. No corrections for fluctuation in laser intensities were used.

2.4.2 Computational

In this work, all calculations were done with the Gaussian 16 program [23]. Structures were optimized and their infrared spectra were computed using density functional theory (DFT) with the B3LYP-D3 functional (which includes Grimme's empirical dispersion correction) and the 6-31+G(d,p) split valance basis set [23, 24] for all atoms except Rb and Cs where the Def2SVP basis set and effective core potential were used. Further single-point

energy calculations were done using the 6-311+G(3df,3pd) basis on all atoms except Rb and Cs where the Def2TZVP basis sets were used. These single-point electronic energies were corrected with the thermochemistries computed using the B3LYP-D3/6-31+(d,p) calculations. All relative enthalpies and Gibbs free energies reported are 298 K values. The computed IR spectra were scaled using 0.945 and 0.975 in the higher (2700-3800 cm^{-1}) and lower (1000-1900 cm^{-1}) energy regions, respectively [25-27].

A search of the conformational space of the $[M(GSH)]^+$ complexes was done with a combination of chemical intuition and using CREST (Conformer-Rotomer Ensemble Sampling Tool) [28, 29]. The CREST calculations were done using the default GFNN semiempirical level of theory [30], and between 10 and 130 structures for the $[M(GSH)]^+$ complexes were generated which were all submitted to B3LYP-D3/6-31+G(d,p) level of theory as described above. The CREST search for $[K(GSH)]^+$ produced the largest number of conformers and following the density functional calculations 109 unique structures were found. For these optimized structures, K^+ was then replaced with Li^+, Na^+, Rb^+, and Cs^+, and reoptimized. In all, 74, 61, 47, and 50 unique conformers were found for $[Li(GSH)]^+$, $[Na(GSH)]^+$, $[Rb(GSH)]^+$, $[Cs(GSH)]^+$, respectively.

Further computations were conducted at the CBS-QB3 level of theory on the lowest energy complexes of glutathione with Li^+.

2.5 Results and Discussion

2.5.1 SORI-CID of $[M(GSH)]^+$, M = Li, Na, K, Rb, and Cs.

In Figure 2.1 is a comparison of the SORI-CID results for the alkali metal-glutathione complexes. The primary losses are indicated by letters which are described in Table 2.1 and

Scheme 2.1. For all $[M(GSH)]^+$ complexes, the loss of water (fragment b, 18.0 Da) and pyroglutamic acid (fragment e, 129.0 Da) are common fragmentations observed. The loss of pyroglutamic acid has also been observed as a major product for protonated glutathione [31] and protonated glutathione conjugates [32-35], and has been used for the screening of various metabolites by conjugating with glutathione. For $[Rb(GSH)]^+$ and $[Cs(GSH)]^+$ the predominant fragmentation is by loss of neutral glutathione (307.2 Da) leaving the metal cation. Metal cation was not observed as a product for $[K(GSH)]^+$. If metal cation was produced in the CID of $[Li(GSH)]^+$ and $[Na(GSH)]^+$ it would not have been observed in these experiments as their m/z ratios were below low mass cut off for these experiments, but given that K^+ was not observed as a product in the CID of $[K(GSH)]^+$, it would not be expected that the smaller ions would be products in the CID of their complexes with GSH. Other minor primary fragmentation products identified in the CID spectra of $[Li(GSH)]^+$ are loss of NH_3 (fragment a, loss of 17 Da), H_2S (fragment c, loss of 34 Da) and $C_2H_5NO_2$ (glycine, fragment d, loss of 75 Da) at m/z 297.3, 280.2, 239.2, respectively.

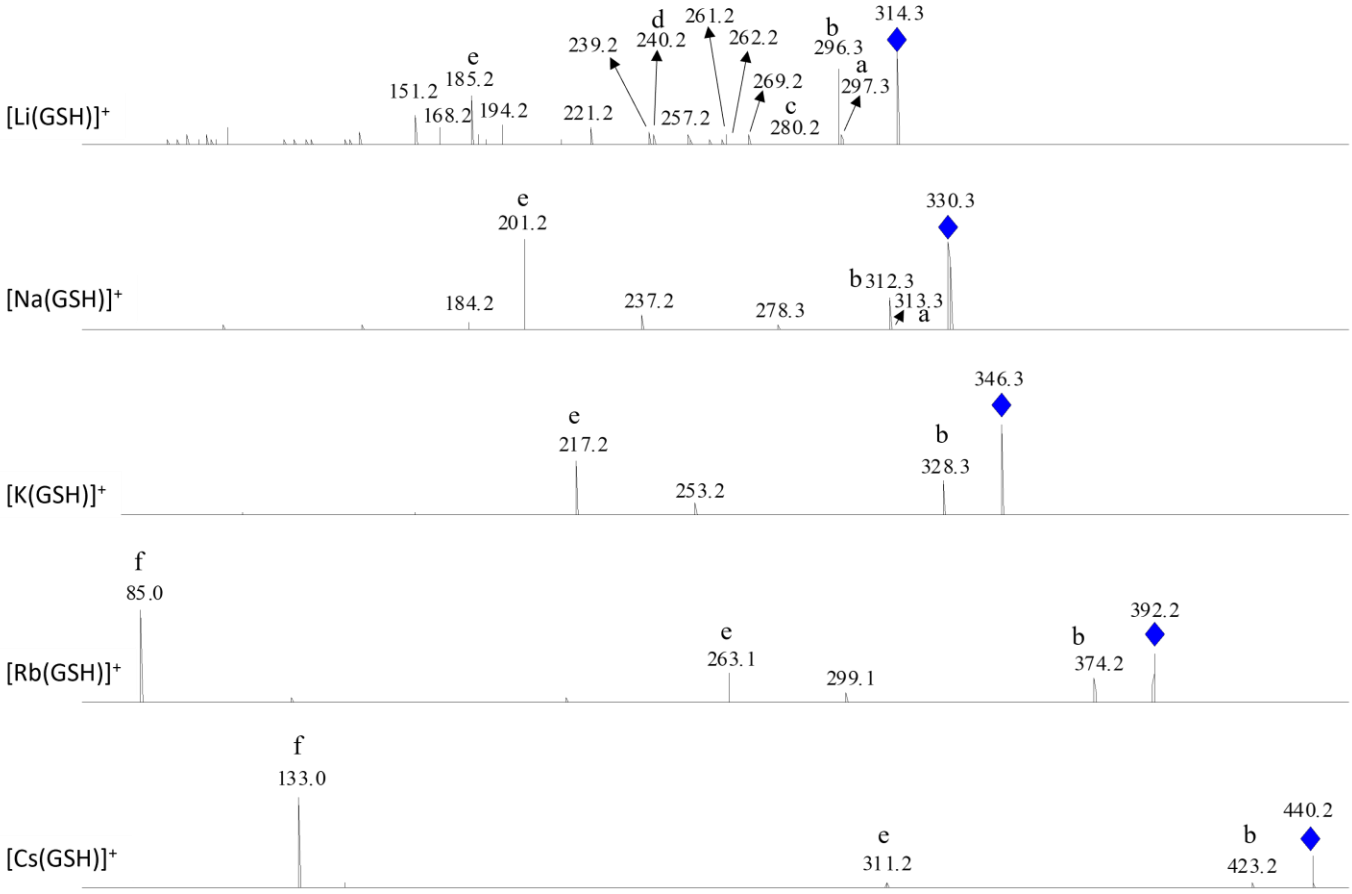

Figure 2.1: SORI/CI D spectra obtained for [M(GSH)]+ where M+, Li+, Na+, K+, Rb+, and CS+.

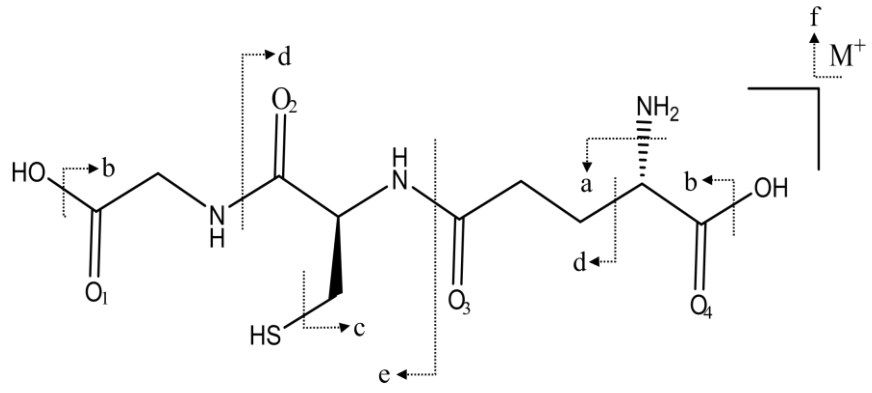

Scheme 2.1: Fragmentation pathways of $[M(GSH)]^+$ complexes where M^+, Li^+, Na^+, K^+, Rb^+, and CS^+.

following SORI-CID

Table 2.1: Fragmentation pathways of $[M(GSH)]^+$ complexes following SORI-CID.

fragment type	neutral loss / Da	fragment identity
a	17.0	NH_3
b	18.0	H_2O
c	34.1	H_2S
d	75.0	glycine
e	129.0	pyroglutamic acid
f	307.0	glutathione

$[Li(GSH)]^+$, $[Na(GSH)]^+$, $[K(GSH)]^+$ and $[Rb(GSH)]^+$ also produce ions at m/z 221.2, 237.3, 253.2, and 299.1, respectively, which are identified as secondary loss of glycine (75.0 Da) from the b fragments as shown in the MS/MS spectra (Figures S2.1-II – S2.4-II). The e fragments from $[Li(GSH)]^+$ and $[Na(GSH)]^+$ are observed to lose NH_3 producing ions at m/z 168.2 and 184.2, respectively. Ions at m/z 175.2 and 191.2 are generated by the loss of cysteine (121.0 Da) from the b fragment in $[Li(GSH)]^+$ and $[Na(GSH)]^+$, respectively. Also, $[Li(GSH)]^+$ and $[Na(GSH)]^+$ lost H_2S from the b fragment to produce ions at m/z 262 .2 and 278.2, respectively, and then the loss of glycine (75.0 Da) is observed at m/z 187.2 and 203.2 respectively (Figures S1-V and S2-V).

Other secondary fragmentations, unique to $[Li(GSH)]^+$, that were identified include m/z 269.2 which is most likely loss of CO (28 Da) from fragment a. The ion at m/z 151.2 is the loss of pyroglutamic acid (fragment e, 129.0 Da) from the c fragment in $[Li(GSH)]^+$.

It is not surprising that the complexes of the more densely charged cations Li^+, Na^+, and K^+ would show more extensive fragmentation of glutathione compared to the heavier cations which show

primarily glutathione loss. This difference is presumably due to the stronger non-covalent binding of the smaller metal cations to glutathione. The stronger electrostatic interactions with the smaller alkali metal cations may also result in weakening of covalent bonds within the peptide.

2.5.2 Vibrational Spectra of Glutathione Complexes with Alkali Metals.

The nomenclature of the structures is as follows. Taking the lowest energy structure for $[Li(GSH)]^+$ GSH-Li-IV-$A_{1,3,4}$-i, as an example, the capital Roman numeral indicates the coordination number of the metal: monocoordinated (I), dicoordinated (II), tri-coordinated (III), and tetracoordinated (IV). This is followed by a letter (A, B or C) indicating the coordination groups as follows. A is used when the metal is coordinated to the N-terminal amino group and at least one of the carboxyl or carbonyl groups of glycine and glutamic acid. B indicates the metal is only bound to carboxyl or carbonyl oxygens and C depicts the complexation of metal to the thiol group and to carboxyl or carbonyl groups. In all cases, the subscripts indicate which carbonyl or hydroxyl oxygens are bound to the metal, (see Scheme 2.1 for the numbering scheme for carbonyl and hydroxyl oxygens). The lowercase Roman numeral is used to distinguish different conformational isomers based on the relative Gibbs energies, from lowest to highest energy. Similar structures with only a different conformation of the thiol group have the same lower case roman numeral and are differentiated in terms of energy by subscripts of either a, b, c, d, but with subscripted SH replacing one of these if there is an S-H---O2 interaction. Finally, the prefix "z" indicates a zwitterionic structure.

In Figure 2.2 the IRMPD spectra for all five-alkali metal cationized GSH complexes are compared to the computed spectra for the lowest energy structures. All lowest energy structures are GSH-M-IV-$A_{1,3,4}$-i_{SH} where the metal cations are bound through ion-dipole interactions with the amine group and the three carbonyl oxygens labeled 1, 3, and 4. These structures also have S-H--O2 interactions as well as a hydrogen bond between O2 and one of the hydrogens of the amine group. The S-H--O2 distance slightly elongates as the metal cation gets larger, 2.455 Å in GSH-Li-IV-A1,3,4-i_{SH} to 2.586 Å in GSH-Cs-IV-$A_{1,3,4}$-i_{SH}. The amine to O2 hydrogen bond decreases from 2.158 Å to 2.114

Å to 2.105 Å in GSH-Li-IV-$A_{1,3,4}$-i_{SH}, GSH-Na-IV-$A_{1,3,4}$-i_{SH}, and GSH-K-IV-$A_{1,3,4}$-i_{SH}, respectively, then remains the same for the heavier metals. As expected, the metal cation to N and O distances increase as the metal cation gets larger. In Figure 2.3, for GSH-Li-IV-$A_{1,3,4}$-i_{SH} Li^+ sits in a cavity and binds in a tetrahedral-like fashion to the four ligands. For Na^+, the metal and three binding oxygens are virtually co-planar with the amine N bound in what might be described as half a trigonal bipyramid. For the K^+, Rb^+, and Cs^+ complexes, the cation sits outside the cavity, above glutathione. In Table 2.2, the positions of prominent features in the experimental vibrational spectra of the $[M(GSH)]^+$ complexes are listed with the assigned modes. The C=O involving the two carboxylic acids and O2, the amide carbonyl that is not bound to the metal cation, are all observed between 1745 and 1779 cm^{-1}.

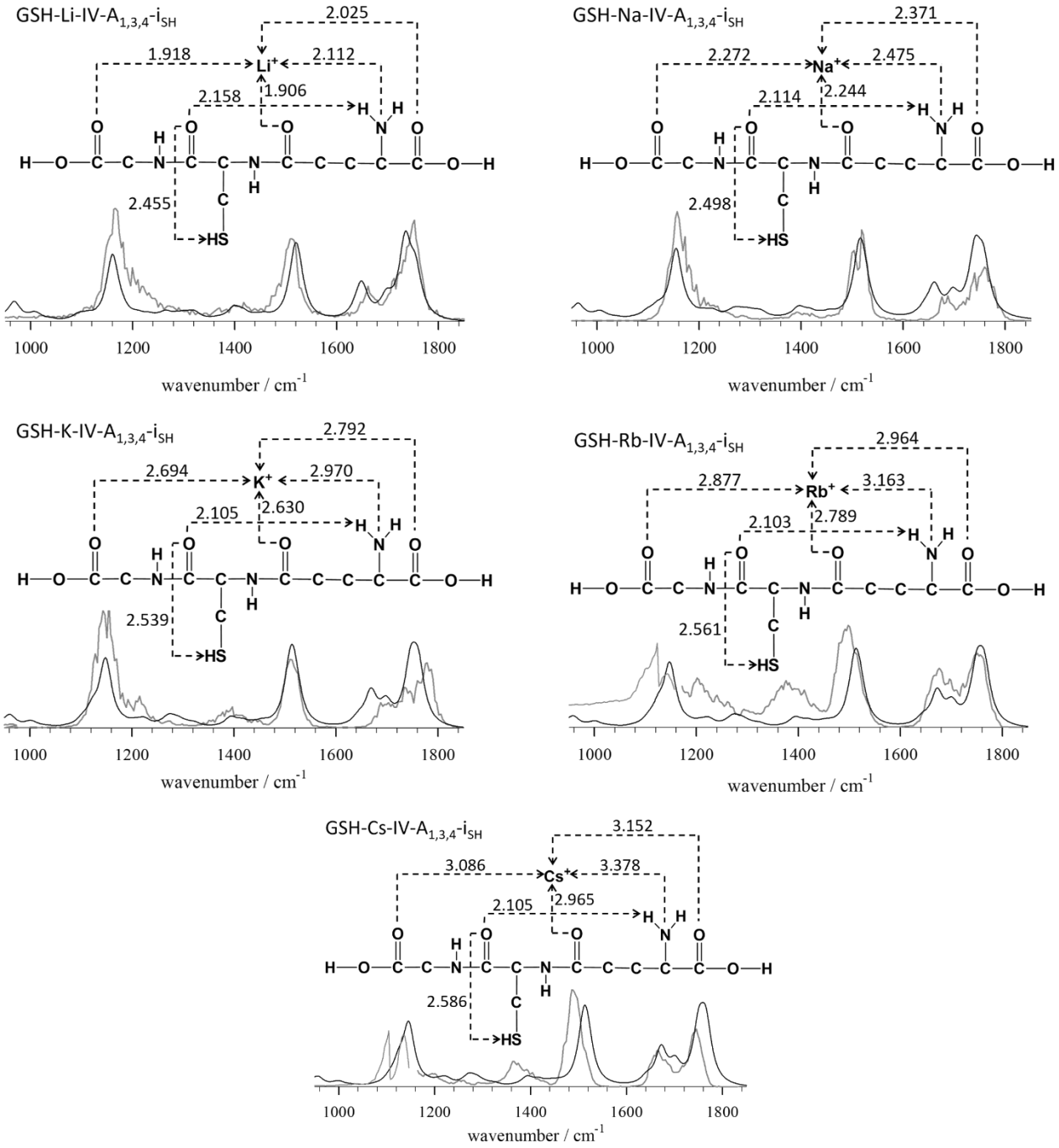

Figure 2.2: Experimental IRMPD spectra (gray traces) and computed infrared spectra (black traces) for $[M(GSH)]^+$ where $M^+ = Li^+$, Na^+, K^+, Rb^+, and CS^+.

Table 2.2: Positions[a] and assignments of the observed vibrational bands for the $[M(GSH)]^+$ complexes.

Mode	$[LiGSH]^+$	$[NaGSH]^+$	$[KGSH]^+$	$[RbGSH]^+$	$[CsGSH]^+$
C=O str (O1, O2, O4)	1753	1759	1779	1760	1745
C=O3 str/ NH_2 bend	1662	1676	1688	1679	1666
amide C-N-H bend	1512	1522/1503	1510	1501	1497
CH/CH_2 scissoring/ CC str	1400	1402	1400	1388	1404
C-OH str/C-O-H bend	1166	1161	1150	1130	1110/1140

a: in cm^{-1}.

The C=O stretch involving O3, the other amide carbonyl, is red shifted to be centred between 1662 and 1688 cm^{-1}; this absorption also contains the NH_2 bending vibration. The two amide C-N-H bending vibrations are observed in each of the spectra centred between 1497 and 1522 cm^{-1}. CH/CH_2 scissoring and C-C stretching involving the carboxylic acids are observed as weaker, but prominent bands centred between 1388 and 1404 cm^{-1}. The C-OH stretch and C-O-H bending modes are observed centred at between 1130 and 1166 cm^{-1}. Between these last two absorptions, broad absorption is observed and is due to tortional modes mainly due to the CH and CH_2 groups.

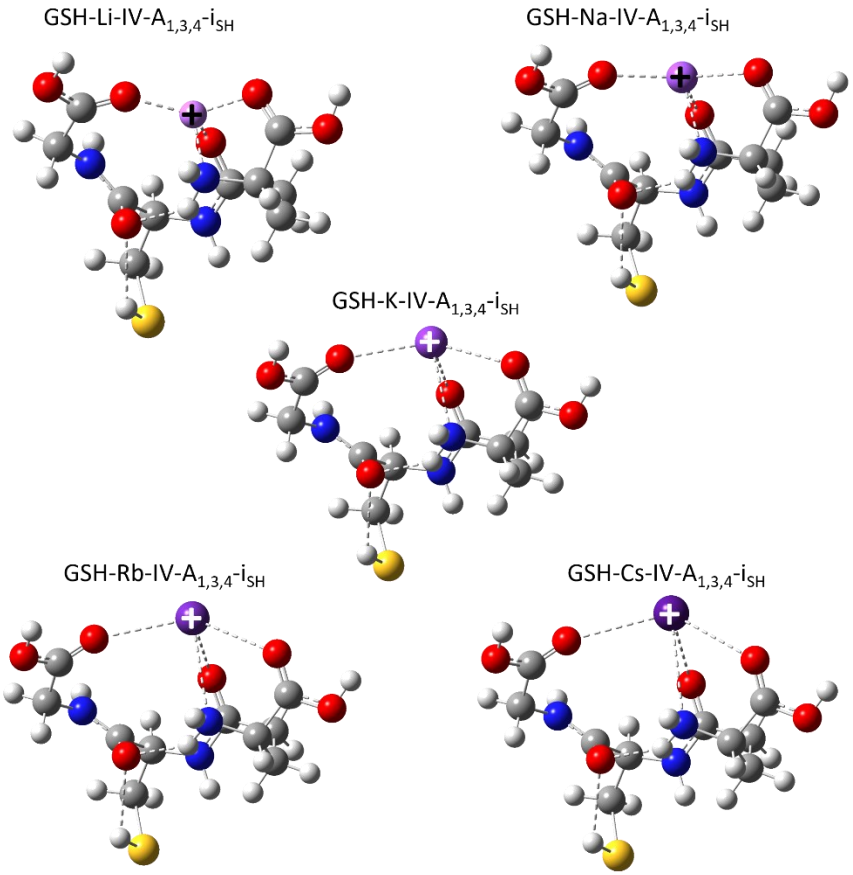

Figure 2.3: Molecular depictions of the lowest energy $[M(GSH)]^+$ complexes.

Spectra were also collected in the higher energy CH/NH/OH region. In all cases, a strong O-H stretch absorption was observed at maxima occurring between 3535 and 3550 cm^{-1} indicative of a carboxylic acid O-H group [36, 37] (see Figure S2.10). For $[Li(GSH)]^+$ and $[Na(GSH)^+]$ there is little else seen in the 2700 – 3700 cm^{-1} region, likely due to the high energy required for dissociation. For $[K(GSH)^+]$, $[Rb(GSH)^+]$, and $[Cs(GSH)^+]$, there are some weak but broad absorptions due to N-H stretching. However, this higher energy region is not as diagnostic of structure for these $[M(GSH)]^+$ complexes since even the highest energy complexes have free carboxylic acid O-H groups and N-H stretching resulting in similar expected spectra.

2.5.3 Higher Energy Structures

2.5.3.1 $[Li(GSH)]^+$

In all, using a mixture of molecular dynamics (CREST) computations and chemical intuition 74 unique $[Li(GSH)]^+$ structures were computed up to more than 200 kJ mol^{-1} higher in energy than the lowest energy structure. While our CREST calculations revealed the GSH-Li-IV-$A_{1,3,4}$-i_c structure, it was chemical intuition that resulted in the lowest energy GSH-Li-IV-$A_{1,3,4}$-i_{SH} by realizing that an SH—O2 interaction resulted in further energy stabilization of the structure. In total there are three other structures similar to the lowest energy structure GSH-Li-IV-$A_{1,3,4}$-i_{SH}. They are GSH-Li-IV-$A_{1,3,4}$-i_b, GSH-Li-IV-$A1_{,3,4}$-i_c, and GSH-Li-IV-$A_{1,3,4}$-i_d that differ in the orientation of the S-H group and are higher in Gibbs energy by 4.4, 4.6, and 7.4 kJ mol^{-1}, respectively, and whose computed IR spectra are indistinguishable in the 1000-2000 cm^{-1} region. Computed energies using B3LYP/6-311+G(3df,3pd) single point electronic energies and CBS-QB3 do not differ significantly from the B3LYPD3/6-31+G(d,p) energies (see Table 3), although at the CBS-QB3, the relative Gibbs energies are 3.6, 3.7, and 4.8 kJ mol^{-1} for the GSH-Li-IV-$A_{1,3,4}$-i_b, GSH-Li-IV-$A_{1,3,4}$-i_c, and GSH-Li-IV-$A_{1,3,4}$-i_d structures, respectively.

The next lowest-energy structure is GSH-Li-IV-$A_{1,3,4}$-ii_{SH}, similar to GSH-Li-IV-$A_{1,3,4}$-i_{SH} and differs in the O3CCC dihedral angle in the glutathione reside. In the lowest energy structure, this dihedral angle is 91.8 degrees while in GSH-Li-IV-$A_{1,3,4}$-ii_{SH} it is -23.1 degrees. The Li^+ to O1 and O4 bond lengths both decrease slightly by about 0.03 Å in GSH-Li-IV-$A_{1,3,4}$-ii_{SH}, and the Li^+ to amine bond increases slightly by about 0.04 Å. The main result of the difference in dihedral angle is that there is no hydrogen bond between the amine group and O2. This results in an increase in enthalpy and Gibbs energy by 21.5 and 16.9 kJ mol^{-1},

respectively, with respect to the lowest energy structure. Spectroscopically this structure is nearly identical to the lowest energy structure in the 1000-2000 cm^{-1} region (Figure S5). The other three GSH-Li-IV-$A_{1,3,4}$-ii structures without the SH--O interaction are higher in energy with similar computed IR spectra.

The lowest energy B type structure is GSH-Li-III-$B_{1,3,4}$-i_{SH}, and is higher in enthalpy and Gibbs energy by 21.4 and 20.5 kJ mol^{-1} respectively. Without a metal to amine interaction, the O4 and O3 to metal interactions are shorter resulting in a significant computed red shift for the carbonyl stretching bands so that the C=O stretch region does not adequately match the IR spectrum. Comparisons of the computed spectra of the other B type structures (Figure S5) and structures with less metal binding interactions ie. II-B and III-A type structures result in higher energy structures and ones whose computed spectra do not compare well with the experimental spectra.

Using B3LYP/6-31G(d,p) Liu et al.[14] computed a lowest energy structure that was a pentacoordinated structure, where the amine and the O1, O2, and O3 were bound to the Li^+ as well as the hydroxyl oxygen of the glutamic acid residue. We did a calculation using B3LYP/6-31G(d,p), like Liu et al., and found that the pentacoordinate structure , GSH-Li-V-$A_{1,2,3,4}$, where the amine and all four carbonyls are bound to Li^+ (rather than the hydroxyl O) is lower in enthalpy and Gibbs energy by 16.1 and 18.1 kJ mol^{-1}, respectively. It makes sense that the GSH-Li-V-$A_{1,2,3,4}$ significantly lower in energy than the GSH-Li-V-$A_{1,2,3,4a}$ structure (where 'a' indicates that the OH oxygen is bound instead of the carbonyl oxygen) because the carbonyl oxygen is more basic than the hydroxide oxygen. However, when the GSH-Li-V-$A_{1,2,3,4}$ and GSH-Li-V-$A_{1,2,3,4a}$ B3LYP/6-31G(d,p) structures were submitted to optimization at the B3LYPD3/6-31+G(d,p) level, they optimized to the tetracoordinate GSH-Li-IV-$A_{1,3,4}$-ii_b and

GSH-Li-IV-$A_{1,3,4a}$-ii_b, respectively. As expected GSH-Li-IV-$A_{1,3,4a}$-ii_b is significantly higher in enthalpy and Gibbs energy (17.1 and 19.1 kJ mol^{-1}, respectively) using B3LYPD3/6-31+G(d,p) than GSH-Li-IV-$A_{1,3,4}$-ii_b and is 45.4 and 40.6 kJ mol^{-1} higher in energy than the lowest energy structure found in this work. The computed IR spectrum for the GSH-Li-IV-$A_{1,3,4a}$-ii_b structure is not consistent with the experimental vibrational spectrum; notably, the free carboxylic acid C=O stretch is predicted to be above 1800 cm^{-1}.

Eight zwitterionic structures were found with tetra-, tri-, and bi- coordination, but were all significantly higher in energy. The lowest energy zwitterionic structure is also a C type structure, zGSH-Li-IV-$C_{1,2,4}$-iii, that is 48.0 and 54.8 kJ mol^{-1} higher in enthalpy and Gibbs energy, respectively, than the lowest energy structure and their computed infrared spectra do not agree with the experimental vibrational spectrum (Table S2.1 and Figure S2.5).

2.5.3.2 $[Na(GSH)]^+$

For $[Na(GSH)]^+$, 61 distinct structures were obtained by employing molecular dynamics simulations and chemical intuition. Our CREST simulations revealed the GSH-Na-IV-$A_{1,3,4}$-i_b structure, and like before, we determined the lowest energy structure, GSH-Na-IV-$A_{1,3,4}$-i_{SH}, by incorporating an SH—O2 stabilizing interaction.

In total, three other structures similar to the lowest-energy structure, GSH-Na-IV-$A_{1,3,4}$-i_{SH}, are identified, namely GSH-Na-IV-$A_{1,3,4}$-i_b, GSH-Na-IV-$A_{1,3,4}$-i_c, and GSH-Na-IV-$A_{1,3,4}$-i_d. These structures vary in the orientation of the S-H group and are higher in Gibbs energy by 4.4, 4.8, and 6.5 kJ mol^{-1}, respectively. There is no noticeable distinction exists between the calculated energy derived from B3LYP/6-311+G(3df,3pd) single point electronic computations and B3LYPD3/6-31+G(d,p) energies (see Table S2). As seen in Figure S6, the

computed IR spectra for these slightly higher-energy complexes are in good agreement with the experimental vibrational spectrum.

The next lowest-energy configuration is GSH-Na-IV-$A_{1,3,4}$-ii_{SH}, which is similar to GSH-Na-IV-$A_{1,3,4}$-i_{SH} but again differs in the O3CCC dihedral angle. The dihedral angle in GSH-Na-IV-$A_{1,3,4}$-ii_{SH} is -18.6 degrees, while it is 104.7 degrees in the lowest energy structure. There are three reasons for the variation in the dihedral angle. First, in GSH-Na-IV-$A_{1,3,4}$-ii_{SH}, the lengths of the Na^+ bonds to O3 and O4 are somewhat shorter by about 0.065 Å and 0.03 Å, respectively. Secondly, the Na^+ bond to amine is slightly longer by about 0.09 Å. The enthalpy and Gibbs energy are observed to increase by 16.8 and 15.6 kJ mol^{-1}, respectively, in comparison to the lowest energy configuration. This structure is spectroscopically similar to the lowest energy structure in the 1000-2000 cm^{-1} range (see Figure S6). Several other higher energy IV-A type structures are also shown in Figure S6, many of them do not agree well with the experimental spectrum.

For $[Na(GSH)]^+$, pentacoordinate type V-A structures were computed and are in fair agreement with the experimental vibrational spectra but are 17.0 kJ mol^{-1} higher in Gibbs energy or more.

The tricoordinated GSH-Na-III-$B_{1,3,4}$-i is the lowest energy B-type structure having a relative Gibbs energy value of 16.1 kJ mol^{-1}. The computed IR spectrum of the lowest energy structure is only roughly consistent with the experimental IRMPD spectrum (Figure S6), but most of these structures do not agree as well with the experimental vibrational spectra. Similarly, when the computed spectra of the other higher energy, B-type structures with higher and lower coordination (such as the IV-B, II-B type structures) there is not nearly as good

agreement with the experimental vibrational spectrum as the lowest energy IV-A type structures (Figure S2.6).

The C-type structure, GSH-Na-IV-$C_{1,3,4}$-i_{SH}, where there is an interaction between the metal cation and the thiol group is the lowest energy C-type structure and is 35.5 kJ mol^{-1}, higher in Gibbs energy than the lowest energy structure. Bicoordinated and monocoordinated structures are even less energetically favourable with higher enthalpy and Gibbs energies (see Table S2.2). The lowest energy zwitterionic structure, zGSH-Na-IV-$C_{1,4,4}$-ii is 44.3 kJ mol^{-1} higher in Gibbs energy. The computed infrared spectra for these structures are not in good agreement with the experimental IRMPD spectrum (Figure S2.6).

As was the case for the Li^+ structures, the computed structures of Liu et al.[14] where the -OH of the carboxylic acid groups are bound to the Na^+, rather than the carbonyl, are higher in energy and the IRMPD spectra do not agree with the computed IR spectra of that isomer (Figure S2.6).

2.5.3.3 $[K(GSH)]^+$

As it was for Li^+ and Na^+, the lowest energy K^+ structure is GSH-K-IV-$A_{1,3,4}$-i_{SH}, where there is an interaction between SH and O2, and there are similar structures without the SH—O2 interaction GSH-K-IV-$A_{1,3,4}$-i_b, GSH-K-IV-$A_{1,3,4}$-i_c, and GSH-K-IV-$A_{1,3,4}$-i_d structures, whose computed IR spectra agree well with the $[K(GSH)]^+$ experimental spectrum and are only 3.3, 4.4, and 5.7 kJ mol^{-1} higher in Gibbs energy, respectively.

Tricoordinate and tetracoordinate, B-type structures dominate the list of $[K(GSH)]^+$ structures with the tricoordinate being of the lower energy structures. For example, GSH-K-III-$B_{1,3,4}$-i_{SH} is only 5.0 kJ mol^{-1} higher in Gibbs energy at the B3LYP/6-31+G(d,p) level or 4.6

kJ mol^{-1} using B3LYP/6-311+G(3df/3pd)//B3LYP/6-31+G(d,p). While this structure is not a terrible match to the experimental spectrum, it is not as good as the tetracoordinate A-type structures discussed above (Figure S2.7). GSH-K-IV-B1,2,3,4-ii is 15.1 kJ mol^{-1} higher in Gibbs energy than the lowest energy structure; it and the other tetracoordinate B-type structures in general are not good matches to the experimental spectrum and/or are computed to be quite high in Gibbs energy.

In general, the bicoordinate structures and the monocoordinated structure are very high in energy. GSH-K-II-$B_{2,4}$-i is actually lower in enthalpy than the lowest energy structure by 2.5 kJ mol-1, but owing to extensive hydrogen bonding is 8.7 kJ mol-1 higher in Gibbs energy. The computed infrared spectra do not agree well with the experimental spectrum (Fig. S2.7).

Four zwitterionic structures were identified, the lowest in energy of which is zGSH-K-III-$B_{1a,2,4}$-xxiv and is 28.2 kJ mol^{-1} higher in Gibbs energy relative to the lowest energy structures found at the B3LYP/6-31G(d,p), but only 13.5 kJ mol-1 lower in enthalpy. The larger relative Gibbs energy is due to strong intramolecular hydrogen bonding. The computed spectrum for this or any of the zwitterionic structures are not in good agreement with the computed IRMPD spectrum (Figure S2.7).

Using B3LYP/6-31(d,p) Liu et al[152] determined the GSH-K-V-$A_{1,2,3,4a}$-i structure (see Figure S2.7) to be the lowest in energy $[K(GSH)]^+$. We were able to optimize two pentacoordinated structures, GSH-K-V-$A_{1,2,3,4}$-i and GSH-K-V-$A_{1,2,3,4a}$-i with the amine and all four carbonyl structures coordinated to the metal cation and which were 12.5 and 36.5 kJ mol^{-1} higher in Gibbs energy than the lowest energy GSH-K-IV-$A_{1,3,4}$-i_{SH}. Besides finding 23

structures lower in energy than the lowest energy pentacoordinated structure, the latter are not good matches to the experimental spectrum.

2.5.3.4 [Rb(GSH)]+

The lowest energy structure for $[Rb(GSH)]^+$ was found to be GSH-Rb-IV-$A_{1,3,4}$-i_{SH} and like for the other metals, there are similar structures with different orientations of the thiol moiety which are slightly higher energy, and all are adequate matches for the experimental spectrum.

The lowest enthalpy structure, GSH-Rb-II-$B_{2,4}$-i_a, has two of the carbonyls interacting with Rb^+ and three intramolecular hydrogen bonds: one between the Glu OH and the glycine carbonyl, one between the Glu/Cys amide NH and the Glu amine, and a final one between the Gly/Cys amide NH and the Glu/Cys amide carbonyl. Because of these hydrogen bonds, this structure is entropically less favoured than the lowest energy structure resulting in a relative Gibbs energy of 4.2 kJ mol^{-1}. As seen in Figure S8 there is very poor agreement between the computed infrared spectrum for GSH-Rb-II-$B_{2,4}$-i and the experimental vibrational spectrum. Some other bicoordinate structures, such as GSH-Rb-II-$B_{1,3}$-iv_{SH}, have spectra that are not terrible matches to the experimental spectrum, but are too high in energy to be expected to contribute to the ion population.

There are several tri- and tetracoordinate structures under about 26 kJ mol^{-1} in Gibbs energy, followed by several more bi- and tri- coordinate structures up to about 55 kJ mol^{-1} in Gibbs energy. Most of the computed infrared spectra do not agree well with the experimental spectra, but there are a few tetra- and tricoordinate B-type structures (such as GSH-Rb-IV-$B_{1,2,3,4}$-i_{SH}, GSH-Rb-IV-$B_{1,2,3,4}$-ii_c, and GSH-Rb-III-$B_{1,3,4}$-iii) that are also in good agreement,

but are more than 10 kJ mol^{-1} higher in Gibbs energy and not likely contributors to the IRMPD spectrum.

No pentacoordinate structures were found to be minima, likely because the charge density on the metal cation is not high enough, as in Na^+ and K^+, to make strong enough interactions to coordinate the five main basic sites of GSH.

Three zwitterionic structures were identified, the lowest energy one, zGSH-Rb-III-$B_{1,2,4}$-ix, being 25.2 kJ mol^{-1} higher in energy and who's computed IR spectrum is not in good agreement with the experimental spectrum (Figure S2.8).

2.5.3.5 $[Cs(GSH)]^+$

The lowest energy structure found at the B3LYP/6-31+G(d,p) and B3LYP/6-311+G(3df,3pd) (Def2SVP or Def2TZVP for Cs) was the tetracoordinated GSH-Cs-IV-$A_{1,3,4}$-i_{SH} structure, as discussed above, is consistent with the experimental spectrum. GSH-Cs-IV-$A_{1,3,4}$-i_b, GSH-Cs-IV-$A_{1,3,4}$-i_c, and GSH-Cs-IV-$A_{1,3,4}$-i_d are similar structures with a different orientation of the thiol group and are only 2.6, 4.4, and 5.9 kJ mol^{-1} higher in Gibbs energy, and their computed infrared spectra are in agreement with the experimental vibrational spectrum.

There are several structures that are computed to be lower in enthalpy than GSH-Cs-IV-$A_{1,3,4}$-i_{SH} at the B3LYP/6-31+(d,p) level of theory, but they are still higher in Gibbs energies, although some of them only slightly (Table S2.5 and Figure S2.9). The computed relative enthalpies and Gibbs energies increase by between 4 and 6 kJ mol^{-1}. The two which are the lowest in energy are bi-coordinated B-type structures GSH-CS-II-$B_{2,4}$-i_a and GSH-CS-II-$B_{2,4}$-i_b. These structures are stabilized by several intramolecular hydrogen bonds which are

also responsible for their unfavourable entropy and higher relative Gibbs energy. The computed IR spectra for these two structures do not agree with the experimental vibrational spectrum. Compared with the other metals, there are many bi coordinated structures computed to be within about 20 kJ mol^{-1} of Gibbs energy than the lowest energy structure, but none of their computed IR spectra match the experimental one except GSH-Cs-II-$B_{1,3}$-vii, but it's Gibbs energy is 22.4 kJ mol^{-1} higher than the lowest energy structure. Similarly, none of computed IR spectra for the tricoordinated structures are in good agreement with the experimental vibrational spectrum.

Finally, for $[Cs(GSH)]^+$, only one zwitterionic structure was found, with zGSH-Cs-II-$B_{1,4}$-xviii being 39.8 kJ mol^{-1} higher Gibbs energy than the lowest energy structure at the B3LYP/6-31G(d,p) level of theory. The computed spectrum for the zwitterionic structure did not agree well with the experimental IRMPD spectrum (Figure S2.9 and Table S2.5).

2.6 Conclusions

The present research focuses on investigating the unimolecular reactions of glutathione complexes with alkali metal cations in the gas phase through SORI-CID, as well as their structures through a combination of infrared multiphoton dissociation spectroscopy and computational techniques. Under soft CID conditions, glutathione complexes with charge-dense cations such as Li^+, Na^+, and K^+ exhibit significant fragmentation of glutathione compared to complexes with the heavier cations, Rb^+ and Cs^+ which predominantly undergo loss of glutathione. The reason for this difference is the stronger non-covalent binding between smaller metal cations and glutathione, which rival the dissociation thresholds of covalent interactions within the peptide complex.

For all the alkali metal cation complexes, the thermodynamically most stable complex at both the B3LYP/6-31+G(d,p) and B3LYP/6-311+G(3dp,3df)//B3LYP/6-31+G(d,p) levels were tetracoordinated A-type structures, where the metal cation is bound to the amino nitrogen as well as three of the carbonyl oxygens—all carbonyl oxygens except O2, the amide between glycine and cystine. O2 was not free, however, it interacted with the thiol and via a hydrogen bond with the amine group of glutamic acid. The computed infrared spectra for these complexes were consistent with the experimental vibrational spectra. Several similar structures, low in relative energy to the lowest energy structure were also consistent with the experimental spectra, but only differed in the orientation of the S-H bond.

With the aforementioned level of theory, combined with CREST, a tool to determine trial structures, a thorough investigation of the conformational space was done. This work revealed many possible higher energy structures including pentavalent structures for the Na^+ and K^+ complexes, as well as tri-, bi-, and monocoordinated complexes along with zwitterionic complexes. However, based on relative energies as well as a comparison between their computed infrared spectra and the experimental spectrum in the fingerprint region, the tetracoordinate A-type structures can be concluded to be the dominant structures in the gas phase.

Acknowledgements

We are grateful for the excellent support from the FELIX and CLIO technical staff. We thank the Nederlandse Organisatie voor Wetenschappelijk Onderzoek (NWO) for support of the FELIX Laboratory. This research was enabled in part by support provided by (ACENET, Compute Ontario, and the BC DRI Group) and the Digital Research Alliance of Canada.

Finally, T.D.F. recognizes the financial contributions from NSERC, the Canadian Foundation for Innovation, and the Memorial University of Newfoundland.

2.7 References

(1) Alanazi, A., G. Mostafa, and A. Al-Badr, Glutathione, in Profiles of Drug Substances, Excipients and Related Methodology. **2015**. p. 43–158.
(2) Forman, H.J., H. Zhang, and A. Rinna, Glutathione: overview of its protective roles, measurement, and biosynthesis. Molecular aspects of medicine, **2009**. 30(1-2): p. 1-12.
(3) Li, Y., G. Wei, and J. Chen, Glutathione: a review on biotechnological production. Applied microbiology and biotechnology, **2004**. 66(3): p. 233-242.
(4) Valencia, E., A. Marin, and G. Hardy, Glutathione - Nutritional and Pharmacological Viewpoints: Part II. Nutrition (Burbank, Los Angeles County, Calif.), **2001**. 17(6): p. 485-6.
(5) Zhang, H., H.J. Forman, and J. Choi, γ-Glutamyl transpeptidase in glutathione biosynthesis. Methods in enzymology, **2005**. 401(1): p. 468-483.
(6) Meister, A. and M.E. Anderson, Glutathione. Annual review of biochemistry, **1983**. 52(1): p. 711-760.
(7) Page, M.J. and E. Di Cera, Role of Na^+ and K^+ in enzyme function. Physiological reviews, **2006**. 86(4): p. 1049-1092.
(8) Rulíšek, L. and Z. Havlas, Theoretical studies of metal ion selectivity. 1. DFT calculations of interaction energies of amino acid side chains with selected transition metal ions (Co^{2+}, Ni^{2+}, Cu^{2+}, Zn^{2+}, Cd^{2+}, and Hg^{2+}). Journal of the American Chemical Society, **2000**. 122(42): p. 10428-10439.
(9) Da Silva, J.F. and R.J.P. Williams, The biological chemistry of the elements: the inorganic chemistry of life. **2001**: Oxford University Press.
(10) Marino, T., N. Russo, and M. Toscano, Gas-phase metal ion (Li^+, Na^+, Cu^+) affinities of glycine and alanine. Journal of inorganic biochemistry, **2000**. 79(1-4): p. 179-185.
(11) Shui, X., et al., The B-DNA dodecamer at high resolution reveals a spine of water on sodium. Biochemistry, **1998**. 37(23): p. 8341-8355.
(12) Krezel, A. and W. Bal, Coordination chemistry of glutathione. Acta Biochimica Polonica, **1999**. 46(3): p. 567-580.
(13) Liu, J., et al., Probing the coordination properties of glutathione with transition metal ions (Cr^{2+}, Mn^{2+}, Fe^{2+}, Co^{2+}, Ni^{2+}, Cu^{2+}, Zn^{2+}, Cd^{2+}, Hg^{2+}) by density functional theory. Journal of biological physics, **2014**. 40(1): p. 313-323.
(14) Liu, J., et al., Theoretical study on the interaction of glutathione with group IA (Li^+, Na^+, K^+), IIA (Be^{2+}, Mg^{2+}, Ca^{2+}), and IIIA (Al^{3+}) metal cations. Structural Chemistry, **2013**. 24(1): p. 251-261.
(15) Chen, Y., et al., Glycine in a basket: protonated complexes of 1, 1, n, n-tetramethyl [n](2, 11) teropyrenophane (n= 7, 8, 9) with glycine in the gas-phase. Physical Chemistry Chemical Physics, **2023**. 25(24): p. 16597-16612.
(16) Polfer, N.C. and J. Oomens, Vibrational spectroscopy of bare and solvated ionic complexes of biological relevance. Mass spectrometry reviews, **2009**. 28(3): p. 468-494.

(17) Fridgen, T.D., Infrared consequence spectroscopy of gaseous protonated and metal ion cationized complexes. Mass spectrometry reviews, **2009**. 28(4): p. 586-607.
(18) Eyler, J.R., Infrared multiple photon dissociation spectroscopy of ions in Penning traps. Mass spectrometry reviews, **2009**. 28(3): p. 448-467.
(19) Bakker, J.M., et al., Gas-phase structure of a π-allyl− palladium complex: efficient infrared spectroscopy in a 7 T Fourier transform mass spectrometer. The Journal of Physical Chemistry A, **2007**. 111(51): p. 13415-13424.
(20) Martens, J., et al., Infrared ion spectroscopy in a modified quadrupole ion trap mass spectrometer at the FELIX free electron laser laboratory. Review of Scientific Instruments, **2016**. 87(10).
(21) Nieuwjaer, N., et al., IRMPD Spectroscopy and Quantum Chemistry Calculations on Metal-Ligand Cluster Ions.
(22) Azargun, M. and T.D. Fridgen, Guanine tetrads: an IRMPD spectroscopy, energy resolved SORI-CID, and computational study of M(9-ethylguanine)$^{4+}$ (M = Li, Na, K, Rb, Cs) in the gas phase. Physical Chemistry Chemical Physics, **2015**. 17(39): p. 25778-25785.
(23) Frisch, M.J., et al., Gaussian 16 Rev. C.01. **2016**: Wallingford, CT.
(24) Ehrlich, S., et al., System-dependent dispersion coefficients for the DFT-D3 treatment of adsorption processes on ionic surfaces. ChemPhysChem, **2011**. 12(17): p. 3414-3420.
(25) Cheng, R., et al., An IRMPD spectroscopic and computational study of protonated guanine-containing mismatched base pairs in the gas phase. Physical Chemistry Chemical Physics, **2020**. 22(5): p. 2999-3007.
(26) Menard, K.J., J. Martens, and T.D. Fridgen, A vibrational spectroscopic and computational study of the structures of protonated imidacloprid and its fragmentation products in the gas phase. Physical Chemistry Chemical Physics, **2021**. 23(5): p. 3377-3388.
(27) Fedorova, I.V. and L.P. Safonova, Proton transfer between sulfonic acids and various propylamines by density functional theory calculations. Journal of Molecular Modeling, **2023**. 29(8): p. 230.
(28) Pracht, P., et al., CREST—A program for the exploration of low-energy molecular chemical space. The Journal of Chemical Physics, **2024**. 160(11).
(29) Grimme, S., Exploration of chemical compound, conformer, and reaction space with meta-dynamics simulations based on tight-binding quantum chemical calculations. Journal of chemical theory and computation, **2019**. 15(5): p. 2847-2862.
(30) Bannwarth, C., S. Ehlert, and S. Grimme, GFN2-xTB—An accurate and broadly parametrized self-consistent tight-binding quantum chemical method with multipole electrostatics and density-dependent dispersion contributions. Journal of chemical theory and computation, **2019**. 15(3): p. 1652-1671.
(31) Gregori, B., et al., Vibrational signatures of S-nitrosoglutathione as gaseous, protonated species. The Journal of Physical Chemistry B, **2014**. 118(43): p. 12371-12382.
(32) Dieckhaus, C.M., et al., Negative ion tandem mass spectrometry for the detection of glutathione conjugates. Chemical research in toxicology, **2005**. 18(4): p. 630-638.
(33) Castro-Perez, J., et al., A high-throughput liquid chromatography/tandem mass spectrometry method for screening glutathione conjugates using exact mass neutral loss acquisition. Rapid Communications in Mass Spectrometry: An International Journal Devoted to the Rapid Dissemination of Up-to-the-Minute Research in Mass Spectrometry, **2005**. 19(6): p. 798-804.

(34) Baillie, T.A. and M.R. Davis, Mass spectrometry in the analysis of glutathione conjugates. Biological mass spectrometry, **1993**. 22(6): p. 319-325.
(35) Xie, C., D. Zhong, and X. Chen, A fragmentation-based method for the differentiation of glutathione conjugates by high-resolution mass spectrometry with electrospray ionization. Analytica Chimica Acta, **2013**. 788(1): p. 89-98.
(36) Atkins, C.G., et al., Structure of $[Pb(Gly-H)]^+$ and the Monosolvated Water and Methanol Solvated Species by Infrared Multiple-Photon Dissociation Spectroscopy, Energy-Resolved Collision-Induced Dissociation, and Electronic Structure Calculations. The Journal of Physical Chemistry B, **2009**. 113(43): p. 14457-14464.
(37) Atkins, C.G., et al., Infrared Multiple Photon Dissociation Spectra of Proton- and Sodium Ion-Bound Glycine Dimers in the N−H and O−H Stretching Region. The Journal of Physical Chemistry A, **2008**. 112(41): p. 10220-10225.

Chapter 3 - Structures and Unimolecular Chemistry of Doubly Charged Metal Cation Complexes With Glutathione

3.1 Abstract

In this study the structures, energetics, and unimolecular reactivity of glutathione complexes with various doubly charged metal cations were investigated, including alkaline earth metals, transition metals, and heavy metals. Employing SORI-CID and IRMPD spectroscopy, combined with computational methods, the research explores the coordination chemistry of these metal-GSH complexes. Results indicate that the dissociation pathways and binding energies vary significantly among different metal cations. The study identifies common fragmentation patterns, such as the loss of water, ammonia, and pyroglutamic acid, and reveals distinct dissociation behaviors for certain metals. This study compares IRMPD spectra of protonated glutathione complexes with alkaline earth metals (Mg^{2+}, Ca^{2+}, Sr^{2+}, Ba^{2+}) to computed spectra of their lowest energy conformations. The metal cations coordinate to the amine group and four carbonyl oxygens, with additional S-H--O2 interactions and a hydrogen bond. Experimental spectra in the 1000-1800 cm^{-1} region show characteristic bands that align with computed spectra. The structures that best match the experimental vibrational spectra are those identified as the lowest Gibbs energy structures using CREST at the GFNN semi-empirical level of theory. The study identifies both pentacoordinated and hexacoordinated structures, revealing variations in metal-ligand interactions and providing insights into the structural dynamics of these complexes. This comprehensive approach bridges experimental observations with theoretical models, offering valuable insights into the complex chemistry of metal-GSH interactions.

3.2 Introduction

Glutathione, composed of glutamic acid, cysteine, and glycine, is a potent antioxidant crucial for shielding cells from oxidative stress, defending against free radicals and reactive oxygen species. GSH levels can vary due to factors like age, diet, and disease; contributing to conditions such as cancer, neurodegenerative diseases, and cardiovascular issues [1-3]. In recent decades, pharmaceutical literature has emphasized metal-ligand protein coordination, with GSH offering ten potential binding sites for metal ions, including carboxylic acid, amino, and sulfhydryl groups. Furthermore, metal cations, known for their unique properties, have significant roles in biochemistry due to their small size, positive charge, and versatile coordination capabilities [4-12].

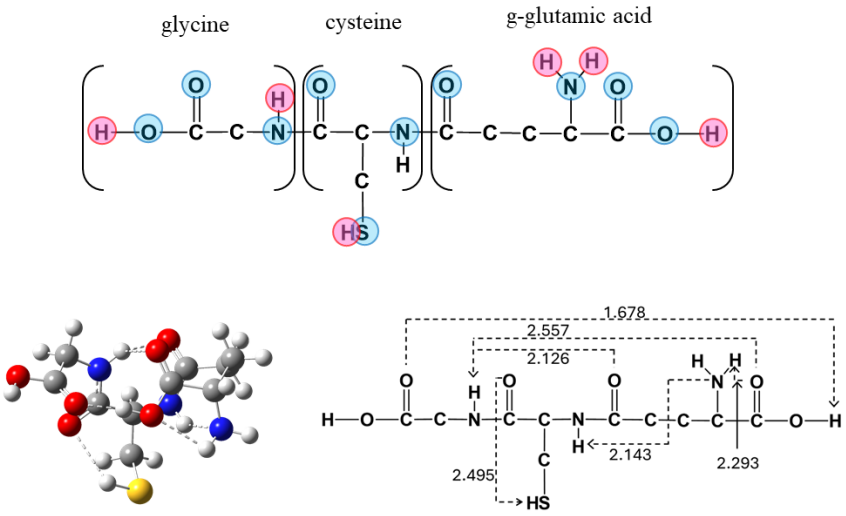

Figure 3.1: Optimized Structure of L-Glutathione with Potential Binding Sites and Hydrogen Bonding Interactions.

Figure 3.1 illustrates the optimized structure of L-glutathione, determined using B3LYP-D3/6-31+G(d,p) computational methods, showcasing its potential binding sites (blue circles in Figure 3.1) and hydrogen bonding interactions (pink circles in Figure 3.1). This visualization underscores the importance of glutathione in both antioxidant defense and metal

ion coordination in biological systems. GSH is an immediate defence within cells by detoxifying and binding metals upon entry [13, 14]. This antioxidant plays a vital role in safeguarding cells against oxidative damage. The formation of metal-glutathione complexes can have varying effects on cells, either beneficial or harmful, contingent on the specific metal and complex involved [15].

Heavy metal ions pose significant toxicity risks, as they compete with biologically essential metals for binding sites and interact with biologically active groups. These interactions often target enzymes and proteins rich in sulfhydryl moieties (-SH), such as GSH, helping organisms mitigate the adverse effects of heavy metals [5, 8, 16]. GSH's interactions with heavy cations (Cr [6, 17-22], As [23-26], Cd [6, 27, 28], Sb [29], Hg [6, 30, 31], Pb [32], Bi [33, 34]) have been extensively studied. Liu et al. [35] investigated GSH complexes with various metal cations including Li^+, Na^+, K^+, Be^{2+}, Mg^{2+}, Ca^{2+}, and Al^{3+}. Using DFT, they studied binding energies and geometries of these complexes. Results revealed stronger interactions with lower atomic number and higher charge ($Be^{2+} > Mg^{2+} > Ca^{2+} > Li^+ > Na^+ > K^+$). Similarly, Shankar et al. [36] investigated GSH interacting with Cd^{2+}, Hg^{2+}, and Zn^{2+} in the gas and aqueous phases using B3LYP/LANL2DZ and MP2/LANL2DZ theories. The study found there are strong interactions between Zn^{2+} and glutathione. Also, as the ionic radius of the metal ions increase, the amount of charge transferred from electronegative atoms to metal ions decreases. Consequently, as the radius of the metal ions increases, the metal-ligand coordination bond lengths also become longer, which correlates with the positive charge on the metal ions. Liu et al. [37] utilizing DFT, also investigated complexes between glutathione and various transition metal cations (Cr^{2+}, Mn^{2+}, Fe^{2+}, Co^{2+}, Ni^{2+}, Cu^{2+}, Zn^{2+}, Cd^{2+}, Hg^{2+}) in the gas phase. The study identified nine stable complexes and examined factors influencing

binding energy. The binding energies follow the order $Cu^{2+} > Ni^{2+} > Co^{2+} > Fe^{2+} > Cr^{2+} > Zn^{2+} > Mn^{2+}$ for metals in the same period and $Zn^{2+} > Hg^{2+} > Cd^{2+}$ within the same group. Notably, charge transfer from S or N atoms to transition metal cations is more significant than from O atoms.

In characterization and measurement of biologically occurring compounds within the GSH metabolome, structural and analytical mass spectrometry has played a pivotal role [38, 39]. Burford's study used electrospray ionization mass spectrometry (ESI-MS) to identify and characterize metal-GSH complexes, revealing potential impacts on metal toxicity and bioavailability in living systems [7]. Electrospray mass spectrometry studied metal ion complexes with bioligands, including GSH, exploring both weak and stable complexes with various coordinating interactions [35]. Banu et al. [40] investigated metal-GSH complexes in the gas phase, focusing on Co^{2+}, Ni^{2+}, Cu^{2+}, and Zn^{2+}. Their study, using collision-induced dissociation (CID) experiments, revealed distinct dissociation patterns. Co^{2+}, Ni^{2+}, and Zn^{2+} complexes shared similar pathways, indicating cysteine sidechain binding while preserving the ligand structure. Cu^{2+} complexes, however, exhibited unique dissociations, involving Cu^{2+} reduction to Cu^{+} and subsequent elimination of cysteine residue fragments.

Overall, some research highlights the importance of understanding the coordination of metals in biological systems, as it can have significant implications for their toxicity and transport in the environment. The present work addresses a gap in previous research on GSH-metal diction complexes by comparing the different types of cation coordination in GSH. Specifically, this study investigates the structures, energetics, and unimolecular reactivity of GSH complexes with the alkaline earth metal cations, as well as some transition and heavy metal dications, the investigation utilizes a combination of sustained off-resonance irradiation-

collision-induced dissociation, infrared multiphoton dissociation spectroscopy, and computational methods.

3.3 Methods

3.3.1 Experimental

ESI was performed using an Apollo II ion source connected to a Bruker ApexQe 7.0 hybrid FTICR-MS to generate the ions. A syringe pump was used to inject solutions containing the target species into the ion source. Notably, the experiment was conducted without further purification of glutathione 99% (Sigma Aldrich). In all solutions, three drops of 10 mmol/L doubly charged metal chloride and two drops of 1% formic acid were added to 1 mL of 1 mmol/L GSH, which was prepared in a 50/50 mixture of 18 MΩ-cm (Millipore) water and methanol.

SORI-CID was performed using FTICR-MS. In the ICR cell ($P = 10^{-10}$ mbar), an ion of interest, $M(GSH-H)^+$ (where M represents Mg^{2+}, Ca^{2+}, Sr^{2+}, Ba^{2+}, Mn^{2+}, Fe^{2+}, Co^{2+}, Ni^{2+}, Cu^{2+}, Zn^{2+}, Cd^{2+}, Hg^{2+}, or Pb^{2+}), was isolated and then exposed to argon at elevated pressures ($P \approx 10^{-5}$–10^{-6} mbar). During the 250 ms excitation period, several dozen to several hundred collisions occurred at these pressures.

IRMPD-MS experiments in the fingerprint region were conducted at the Centre Laser Infrarouge d'Orsay (CLIO) near Paris, France, using a free electron laser facility coupled to FTICR-MS. In these experiments, ions ($M(GSH-H)^+$, where M includes Mg^{2+}, Ca^{2+}, Sr^{2+}, Ba^{2+}), were isolated in the FTICR, diluted 100-fold with methanol, and electrosprayed. The ions were irradiated with FEL radiation at 5 cm^{-1} intervals for 250 ms, scanning at 3 cm^{-1} intervals using two pulses of tunable infrared radiation.

The reported IRMPD intensity values are the negative of the natural logarithm of the product ion intensities which is divided by the total ion intensity. No corrections for fluctuation in laser intensities were used.

3.4 Computational

All calculations in this study were performed for $M(GSH-H)^+$, (M= Mg^{2+}, Ca^{2+}, Sr^{2+}, Ba^{2+}) complexes using the Gaussian 16 program [41]. A density functional theory (DFT) approach was used to optimize the structures and calculate their infrared spectra utilizing the B3LYP-D3 functional (including Grimme's empirical dispersion correction) and the 6-31+G(d,p) split valance basis set [42-44] for all atoms except Sr^{2+}, Ba^{2+} where the Def2SVP basis set and effective core potential were used. Also, the conformational space of the $M(GSH-H)^+$ complexes was explored using CREST [45] at the GFNN semi-empirical level of theory [46]. The structures generated by CREST were then evaluated using the B3LYP-D3/6-31+G(d,p) level of theory as previously described.

It has been noted that all relative enthalpies and Gibbs free energies are reported in 298 K. In the (1000-1800 cm^{-1}), the computed IR spectra were scaled by 0.975 [47, 48].

3.5 Results and Discussion

3.5.1 SORI/CID of $M(GSH-H)^+$, M = Mg^{2+}, Ca^{2+}, Sr^{2+}, Ba^{2+}, Mn^{2+}, Fe^{2+}, Co^{2+}, Ni^{2+}, Cu^{2+}, Zn^{2+}, Cd^{2+}, Hg^{2+} and Pb^{2+}.

Figure 3.2 compares the SORI-CID results for the complexes of doubly charged metals with glutathione. The primary losses resulting from the dissociation of these complexes are indicated by letters, which are further described in Scheme 3.1 and Table 3.1.

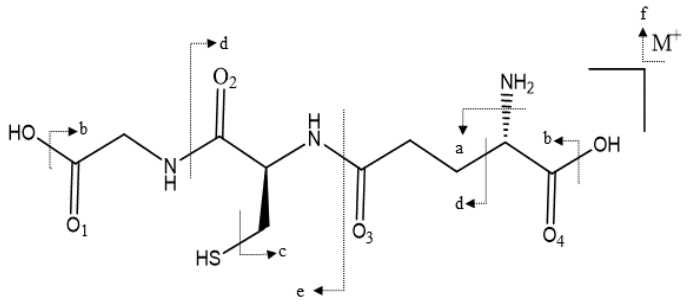

Scheme 3.1. Fragmentation pathways of $M(GSH-H)^+$ where M = Mg^{2+}, Ca^{2+}, Sr^{2+}, Ba^{2+}, Mn^{2+}, Fe^{2+}, Co^{2+}, Ni^{2+}, Cu^{2+}, Zn^{2+}, Cd^{2+}, Hg^{2+} and Pb^{2+} where following CID.

Table 3.1: Fragmentation pathways of doubly charged metal glutathione complexes following CID. P represents the $M(GSH-H)^+$ ion of the GSH complexes.

Fragment type	Positive m/z	Fragment Name
a	P-17.0	Loss of NH_3
b	P-18.0	Loss of H_2O
c	P-34.1	Loss of H_2S
d	P-75.0	Loss of Glycine or $C_2NO_2H_5$
e	P-129.0	Loss of Pyroglutamic acid
f	P-307.0	Loss of Glutathione

Upon SORI activation, the common primary fragmentation pathways involved the loss of water (fragment b, 18.0 Da) in most $M(GSH-H)^+$ complexes with doubly charged metals (excluding Ni^{2+}, Cu^{2+}, and Hg^{2+}). However, $Ni(GSH-H)^+$ and $Cu(GSH-H)^+$ SORI mass spectra showed the loss of NH_3 (fragment a, loss of 17.0 Da). Additionally, all metals except Mn, Zn, and Hg experienced the loss of pyroglutamic acid (fragment e, 129.0 Da). The loss of H_2S (fragment c, with a mass loss of 34.0 Da) resulted in the formation of ions at m/z 312.1 and 330.2 for $Ca(GSH-H)^+$ and $Ni(GSH-H)^+$, respectively. The ion at m/z 237.2 was generated by the loss of glycine (75.0 Da) from the b fragment in $Mg(GSH-H)^+$, or vice versa. The main

fragmentation observed in Co, Ni, Zn, and Cd complexes was the loss of $C_2H_5NO_2$ (glycine, fragment d, loss of 75.0 Da). However, in the case of $Cu(GSH-H)^+$ and $Pb(GSH-H)^+$, glycine was found to be lost as a minor primary fragmentation pathway (Figure 3.2).

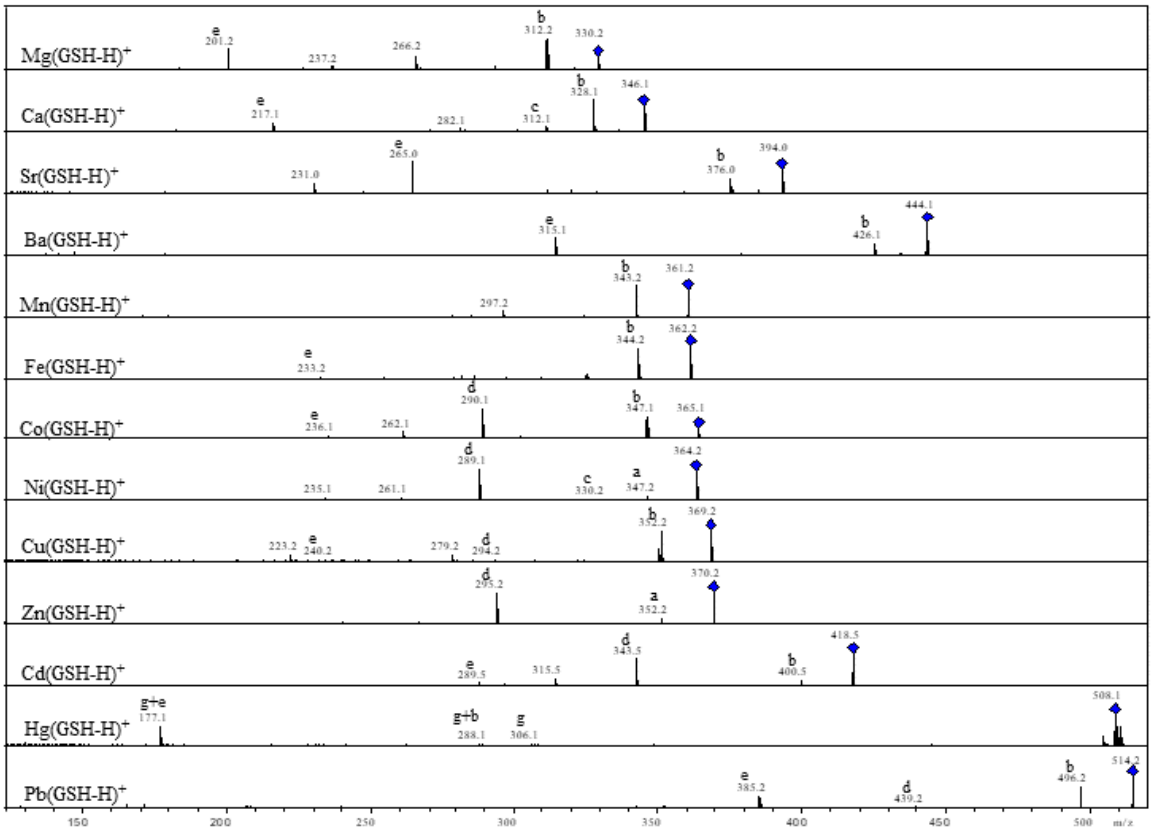

Figure 3.2: SORI/CID spectra obtained for $M(GSH-H)^+$ where M = Mg^{2+}, Ca^{2+}, Sr^{2+}, Ba^{2+}, Mn^{2+}, Fe^{2+}, Co^{2+}, Ni^{2+}, Cu^{2+}, Zn^{2+}, Cd^{2+}, Hg^{2+} and Pb^{2+}.

In the case of $Hg(GSH-H)^+$, ions at m/z 306.1, 288.1, and 177.1 were produced, which correspond to the loss of Hg^+, Hg^++b, and Hg^++e, respectively. However, The $Pb(GSH-H)^+$ undergoes fragmentation through the elimination of neutral glutathione (307.0 Da), resulting in the separation of the metal cation. Figure 3.2 and Figures S3.1-S3.9 illustrate the fragmentation pathways.

3.5.2 Computed structures and vibrational spectra of glutathione complexes with doubly charged metals.

The naming conventions for structures, such as the lowest energy configuration for $Mg(GSH-H)^+$, O_1-GSH-Mg-V-$A_{1,1a,3,4}$-i_{SH}, are as follows. The uppercase Roman numeral denotes the metal's coordination number: monocoordinated (I), dicoordinated (II), tri-coordinated (III), tetracoordinated (IV), pentacoordinated (V), and hexacoordinated (VI). This is succeeded by a letter (A, B, or C) indicating the coordination groups: A when the metal coordinates with the N-terminal amino group and at least one carboxyl or carbonyl group of glycine and glutamic acid, B when the metal is exclusively bound to carboxyl or carbonyl oxygens, and C when the metal complex involves the thiol group along with carboxyl or carbonyl groups. The subscripts specify which carbonyl or hydroxyl oxygens are bound to the metal, following the numbering scheme in Scheme 3.1. The lowercase Roman numerals are used to distinguish conformational isomers based on their relative Gibbs energies, arranged from lowest to highest. Structures that differ only in the conformation of the thiol group are assigned the same lowercase Roman numeral. They are distinguished by energy using subscripts a, b, c, d, except when an S-H---O2 interaction is present, in which case the subscripted SH replaces one of these letters. Finally, the prefix "Z" signifies a zwitterionic structure, while the prefix "O", indicates the protonated locations of H in protonated GSH.

3.5.2.1 $M(GSH-H)^+$ where M = Mg^{2+}, Ca^{2+}, Sr^{2+} and Ba^{2+}.

In Figure 3.3 the IRMPD spectra of protonated glutathione complexes with alkaline earth metals (Mg^{2+}, Ca^{2+}, Sr^{2+}, and Ba^{2+}) are compared with the theoretically computed spectra of their lowest energy conformations. In these lowest energy structures, glutathione (GSH) is deprotonated at the carboxylic acid group of glycine and the metal cations are coordinated to the amine group and the four carbonyl oxygens (labeled 1, 1a, 3, and 4) through ion-dipole interactions. These structures also exhibit S-H--O2 interactions and a hydrogen bond between O2 and a hydrogen atom from the amine group. Notably, the SH--O2 distance slightly increases from 2.636 Å in $Mg(GSH-H)^+$ to 2.691 Å in $Ba(GSH-H)^+$. Similarly, the hydrogen bond distance between the amine and O2 decreases from 2.114 Å to 1.925 Å across the series

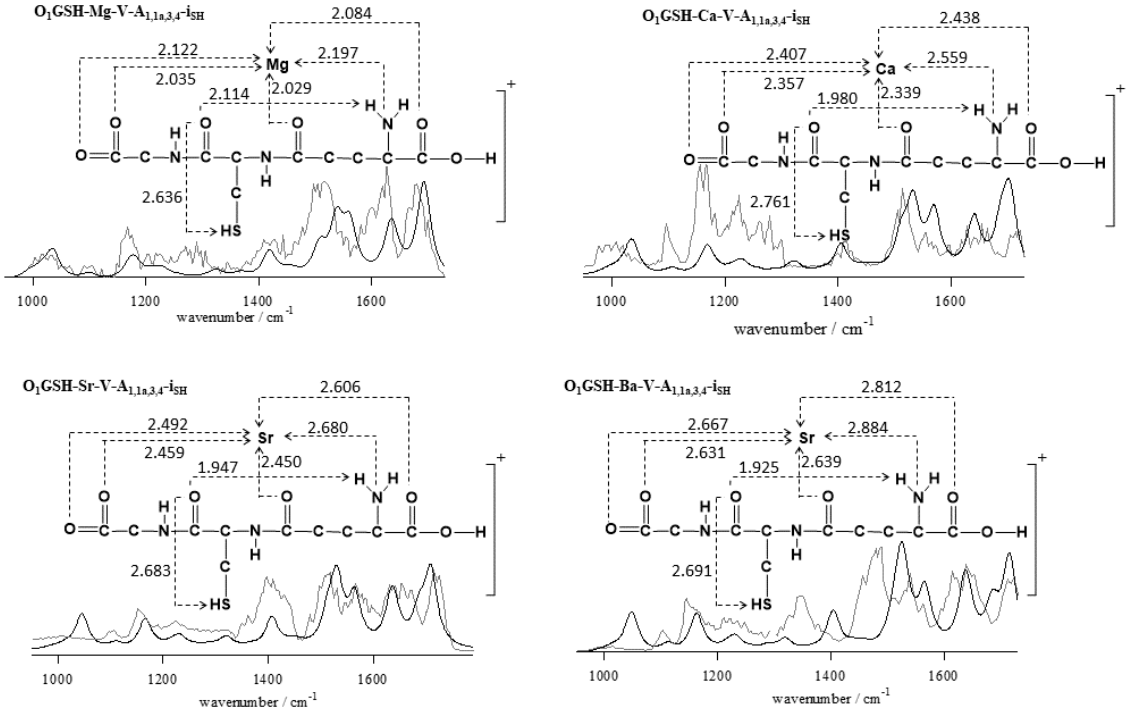

Figure 3.3: Experimental IRMPD spectra (gray traces) and computed infrared spectra (black traces) for $M(GSH-H)^+$ where M = $Mg^{2+,}$ Ca^{2+}, Sr^{2+}, and Ba^2.

of complexes. As expected, the distances between the metal cations and N/O atoms increase with the size of the metal cation.

Based on the good agreement between the experimental IRMPD spectra of $Mg(GSH-H)^+$ and $Sr(GSH-H)^+$ and the spectra of the lowest energy structures, the experimental bands in the fingerprint region can be assigned, as shown in Figure 3.2. From 1700 cm^{-1} to 1770 cm^{-1}, all spectra for alkaline earth metals exhibit absorptions indicative of $C=O_2$, and $C=O_4$, stretching. Specifically, a peak at 1736 cm^{-1} in $Mg(GSH-H)^+$ corresponds to the C=O stretching of a free carbonyl group and $C=O_4$. Common features across all spectra include a prominent band around 1546 cm^{-1} and 1455 cm^{-1}, potentially associated with CNH bending and C–COO stretching, along with a well-defined shoulder at approximately 1683 cm^{-1}, possibly assigned to NH_2 scissoring motions. Furthermore, intense bands ranging from 1600 cm^{-1} to 1680 cm^{-1} are attributed to $C=O_3$ stretching. Additionally, distinctive characteristics below 1300 cm^{-1} are observed, representing modes such as COH bending and CH_2 rocking.

Figure 3.4 compares the structures of glutathione complexes involving group 1 and group 2 cations with the lowest energy configurations. Group 1 cations, which are singly charged metals, were discussed in the previous chapter. In contrast, group 2 cations are doubly charged and form complexes with deprotonated glutathione. In the lowest energy configuration, glutathione is deprotonated at the carboxylic acid group of glycine, the most acidic group within glutathione [2]. Lithium is used as an example of alkali metals, and magnesium represents alkaline earth metals. The Li complex is tetracoordinated, whereas the Mg complex is pentacoordinated. In their lowest energy structures, the metal cations coordinate with the amine group and the four carbonyl oxygens through ion-dipole

interactions. Both structures exhibit S-H--O2 interactions and a hydrogen bond between O2 and a hydrogen atom from the amine group.

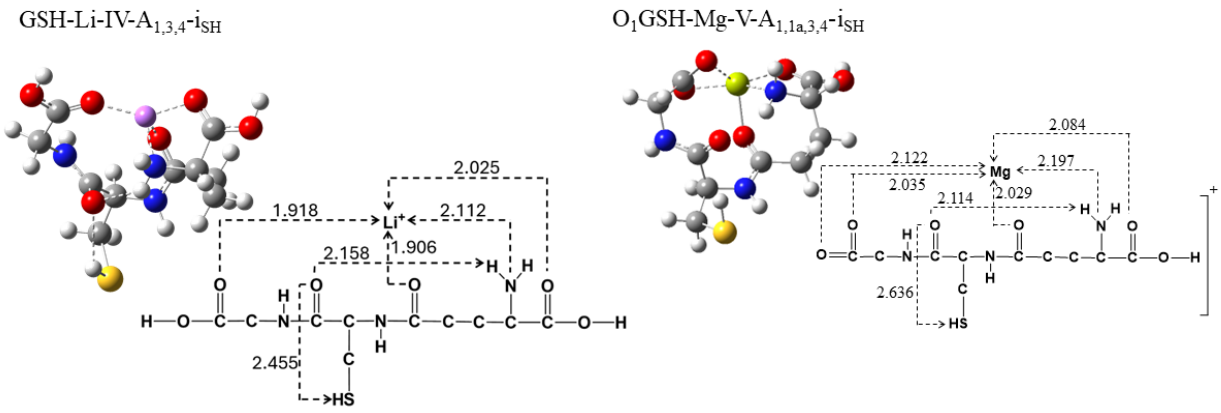

Figure 3.4: Comparison of Glutathione Complex Structures with Group 1 (Li) and Group 2 (Mg) Cations in Their Lowest Energy Configurations.

The lowest energy configuration for $M(GSH-H)^+$ ($M=Mg^{2+}$, Ca^{2+}, Sr^{2+}, and Ba^{2+}) is the pentacoordinated O_1-GSH-M-V-$A_{1,1a,3,4}$-i, as determined at the B3LYP-D3/6-31+G(d,p) level of theory. The lowest energy structures indicate that glutathione is deprotonated at the carboxyl group of the C-terminal glycine, consistent with it being the most acidic functional group of GSH.

The next lowest energy structure for all alkaline earth metals found at the B3LYP/6-31+G(d,p) and B3LYP/6-311+G(3df,3pd) (Def2SVP or Def2TZVP for Sr and Ba) were shown in Figure 3.5. However, $Mg(GSH-H)^+$ and $Ba(GSH-H)^+$ are pentacoordinated, while $Ca(GSH-H)^+$ and $Sr(GSH-H)^+$ are hexacoordinated. O2 interacts more strongly with the metal in Ca and Sr structures. The A-type structure, O_1GSH-Mg-V-$A_{1,1a,3,4}$-ii_{SH}, is 12.5 kJ mol^{-1}, higher in Gibbs energy than the lowest energy structure and in good agreement with the experimental IRMPD spectrum. The computed IR spectrum of the O_1-GSH-Ca-VI-$A_{1,1a,2,3,4}$-i_{SH} complex is

only 11.4 kJ mol^{-1} higher in Gibbs energy and matches the experimental spectrum well above 1450 cm^{-1}, including the C=O stretch region, but not below 1450 cm^{-1}. The hexacoordinated

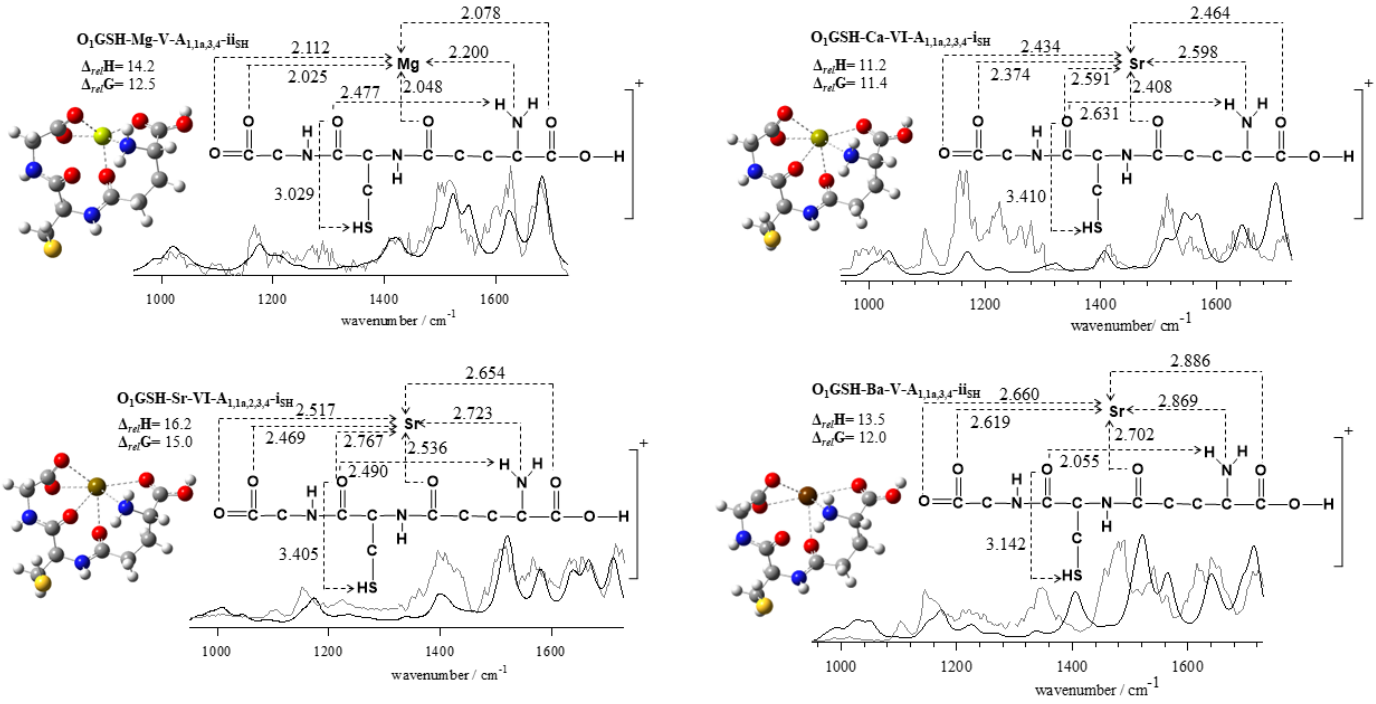

Figure 3.5: Experimental IRMPD spectra (gray traces) and computed infrared spectra (black traces) for M(GSH-H)$^+$ where M = Mg^{2+}, Ca^{2+}, Sr^{2+}, and Ba^2.

O_1-GSH-Sr-VI-$A_{1,1a,2,3,4}$-i_{SH} complex and its computed IR spectrum align well with the experimental IRMPD spectrum, but its Gibbs energy is 15.0 kJ mol^{-1} higher than the lowest energy structure. The IR spectrum of the pentacoordinated structure with 12.0 kJ mol^{-1} higher in Gibbs energy than the lowest energy, O_1-GSH-Ba-V-$A_{1,1a,3,4}$-ii_{SH}, also matches well with the experimental spectrum above 1650 cm^{-1}, though the agreement is less satisfactory in the fingerprint region below 1650 cm^{-1} (Figure 3.5).

3.6 Conclusions

In conclusion, the SORI/CID analysis of $M(GSH-H)^+$ complexes provided insights into their primary fragmentation pathways, revealing common trends and distinct behaviours among different metal ions. While most complexes exhibited the loss of water as a primary fragmentation product, variations such as the loss of NH_3, pyroglutamic acid, glycine, and H_2S were observed depending on the metal ion involved. Additionally, the fragmentation patterns of $Cu(GSH-H)^+$ and $Pb(GSH-H)^+$ differed from the general trends, indicating unique dissociation mechanisms for these complexes.

Furthermore, computational studies elucidated the structures and vibrational spectra of glutathione complexes with doubly charged metals. The lowest energy configurations of these complexes were identified, showcasing variations in coordination numbers and binding patterns based on the metal ion. The comparison between experimental IRMPD spectra and computed spectra provided valuable insights into the coordination geometries and vibrational modes of these complexes. While overall agreement was observed between experimental and theoretical spectra, discrepancies were noted in certain regions, suggesting areas for further investigation and refinement in computational models.

Overall, the combined experimental and computational approaches presented in this study deepen our understanding of the structural and chemical properties of $M(GSH-H)^+$ complexes, laying the groundwork for future research in metal-ligand interactions and their implications in biological systems.

3.7 References

(1) Mahajan, S.; Atkins, W. M. The chemistry and biology of inhibitors and pro-drugs targeted to glutathione S-transferases. Cellular and Molecular Life Sciences CMLS **2005**, 62 (11), 1221-1233. DOI: 10.1007/s00018-005-4524-6.

(2) Kosower, N. S.; Kosower, E. M. The Glutathione Status of Cells11This article is dedicated to the memory of Dr Chaim Sheba, who provided, with warmth and wisdom, the original stimulus for our studies on the importance of glutathione. In International Review of Cytology, Bourne, G. H., Danielli, J. F., Jeon, K. W. Eds.; Vol. 54; Academic Press, 1978; pp 109-160.
(3) Sigel, H. Metal Ions in Biological Systems, Volume 9: Amino acids and Derivatives as Ambivalent Ligands. Journal of The Electrochemical Society **1980**, 127 (5), 215C. DOI: 10.1149/1.2129856.
(4) Belcastro, M.; Marino, T.; Russo, N.; Toscano, M. The role of glutathione in cadmium ion detoxification: coordination modes and binding properties–a density functional study. Journal of Inorganic Biochemistry **2009**, 103 (1), 50-57.
(5) Belcastro, M.; Marino, T.; Russo, N.; Toscano, M. Interaction of cysteine with Cu^{2+} and group IIb (Zn^{2+}, Cd^{2+}, Hg^{2+}) metal cations: a theoretical study. Journal of mass spectrometry **2005**, 40 (3), 300-306.
(6) Fuhr, B. J.; Rabenstein, D. L. Nuclear magnetic resonance studies of the solution chemistry of metal complexes. IX. Binding of cadmium, zinc, lead, and mercury by glutathione. Journal of the American Chemical Society **1973**, 95 (21), 6944-6950.
(7) Burford, N.; Eelman, M. D.; Groom, K. Identification of complexes containing glutathione with As (III), Sb (III), Cd (II), Hg (II), Tl (I), Pb (II) or Bi (III) by electrospray ionization mass spectrometry. Journal of Inorganic Biochemistry **2005**, 99 (10), 1992-1997.
(8) Baloun, J.; Adam, V.; Trnkova, L.; Beklova, M.; Svobodova, Z.; Zeman, L.; Kizek, R. Complexes of glutathione with heavy metal ions as a new biochemical marker of aquatic environment pollution. Environmental Toxicology and Chemistry: An International Journal **2010**, 29 (3), 497-500.
(9) Dimitrova, M.; Turmanova, S.; Vassilev, K. Complexes of glutathione with heavy metals as catalysts for oxidation. Reaction Kinetics, Mechanisms and Catalysis **2009**, 99 (1), 69-78.
(10) Da Silva, J. F.; Williams, R. J. P. The biological chemistry of the elements: the inorganic chemistry of life; Oxford University Press, 2001.
(11) Bertini, I.; Sigel, A. Handbook on metalloproteins; CRC Press, 2001.
(12) Christianson, D. W.; Cox, J. D. Catalysis by metal-activated hydroxide in zinc and manganese metalloenzymes. Annual review of biochemistry **1999**, 68 (1), 33-57.
(13) Singhal, R. K.; Anderson, M. E.; Meister, A. Glutathione, a first line of defense against cadmium toxicity. The FASEB Journal **1987**, 1 (3), 220-223.
(14) Ochi, T.; Otsuka, F.; Takahashi, K.; Ohsawa, M. Glutathione and metallothioneins as cellular defense against cadmium toxicity in cultured Chinese hamster cells. Chemico-biological interactions **1988**, 65 (1), 1-14.
(15) Hsu-Kim, H. Stability of metal− glutathione complexes during oxidation by hydrogen peroxide and Cu (II)-catalysis. Environmental science & technology **2007**, 41 (7), 2338-2342.
(16) Glusker, J. P. Structural aspects of metal liganding to functional groups in proteins. Advances in protein chemistry **1991**, 42, 1-76.
(17) Connett, P.; Wetterhahn, K. In vitro reaction of the carcinogen chromate with cellular thiols and carboxylic acids. Journal of the American Chemical Society **1985**, 107 (14), 4282-4288.
(18) O'Brien, P.; Pratt, J.; Swanson, F. J.; Thornton, P.; Wang, G. The isolation and characterization of a chromium (V) containing complex from the reaction of glutathione with chromate. Inorganica chimica acta **1990**, 169 (2), 265-269.

(19) Gaggelli, E.; Berti, F.; Gaggelli, N.; Maccotta, A.; Valensin, G. A Homodinuclear CrV− CrV Complex Forms from the Chromate− Glutathione Reaction in Water. Journal of the American Chemical Society **2001**, 123 (36), 8858-8859.
(20) Levina, A.; Zhang, L.; Lay, P. A. Structure and Reactivity of a Chromium (V) Glutathione Complex1. Inorganic chemistry **2003**, 42 (3), 767-784.
(21) Levina, A.; Lay, P. A. Solution structures of chromium (VI) complexes with glutathione and model thiols. Inorganic chemistry **2004**, 43 (1), 324-335.
(22) Codd, R.; Dillon, C. T.; Levina, A.; Lay, P. A. Studies on the genotoxicity of chromium: from the test tube to the cell. Coordination Chemistry Reviews **2001**, 216, 537-582.
(23) Scott, N.; Hatlelid, K. M.; MacKenzie, N. E.; Carter, D. E. Reactions of arsenic (III) and arsenic (V) species with glutathione. Chemical research in toxicology **1993**, 6 (1), 102-106.
(24) Gailer, J.; Lindner, W. On-column formation of arsenic–glutathione species detected by size-exclusion chromatography in conjunction with arsenic-specific detectors. Journal of Chromatography B: Biomedical Sciences and Applications **1998**, 716 (1-2), 83-93.
(25) Raab, A.; Meharg, A. A.; Jaspars, M.; Genney, D. R.; Feldmann, J. Arsenic–glutathione complexes—their stability in solution and during separation by different HPLC modes. Journal of Analytical Atomic Spectrometry **2004**, 19 (1), 183-190.
(26) Rey, N. A.; Howarth, O. W.; Pereira-Maia, E. C. Equilibrium characterization of the As (III)–cysteine and the As (III)–glutathione systems in aqueous solution. Journal of Inorganic Biochemistry **2004**, 98 (6), 1151-1159.
(27) Rabenstein, D. L.; Fairhurst, M. T. Nuclear magnetic resonance studies of the solution chemistry of metal complexes. XI. Binding of methylmercury by sulfhydryl-containing amino acids and by glutathione. Journal of the American Chemical Society **1975**, 97 (8), 2086-2092.
(28) Cruz-Vásquez, B. H.; Díaz-Cruz, J. M.; Ariño, C.; Esteban, M.; Tauler, R. Study of Cd 2+ complexation by the glutathione fragments Cys–Gly (CG) and γ-Glu–Cys (γ-EC) by differential pulse polarography. Analyst **2002**, 127 (3), 401-406.
(29) Sun, H.; Yan, S. C.; Cheng, W. S. Interaction of antimony tartrate with the tripeptide glutathione: Implication for its mode of action. European Journal of Biochemistry **2000**, 267 (17), 5450-5457.
(30) Taylor, N. J.; Wong, Y. S.; Chieh, P. C.; Carty, A. J. Syntheses, X-ray crystal structure, and vibrational spectra of L-cysteinato (methyl) mercury (II) monohydrate. Journal of the Chemical Society, Dalton Transactions **1975**, (5), 438-442.
(31) Rabenstein, D. L.; Reid, R. S. Nuclear magnetic resonance studies of the solution chemistry of metal complexes. 20. Ligand-exchange kinetics of methylmercury (II)-thiol complexes. Inorganic Chemistry **1984**, 23 (9), 1246-1250.
(32) Cruz, B. H.; Díaz-Cruz, J. M.; Díaz-Cruz, M. S.; Ariño, C.; Esteban, M.; Tauler, R. Differential pulse polarographic study of the Pb (II) complexation by glutathione. Journal of Electroanalytical Chemistry **2001**, 516 (1-2), 110-118.
(33) Sadler, P. J.; Sun, H.; Li, H. Bismuth (III) Complexes of the Tripeptide Glutathione (γ-L-Glu–L-Cys–Gly). Chemistry–A European Journal **1996**, 2 (6), 701-708.
(34) Burford, N.; Eelman, M. D.; Mahony, D. E.; Morash, M. Definitive identification of cysteine and glutathione complexes of bismuth by mass spectrometry: assessing the biochemical fate of bismuth pharmaceutical agents. Chemical communications **2003**, (1), 146-147.

(35) Liu, J.; Xia, X.; Li, Y.; Wang, H.; Li, Z. Theoretical study on the interaction of glutathione with group IA (Li^+, Na^+, K^+), IIA (Be^{2+}, Mg^{2+}, Ca^{2+}), and IIIA (Al^{3+}) metal cations. Structural Chemistry **2013**, 24. DOI: 10.1007/s11224-012-0031-1.
(36) Shankar, R.; Kolandaivel, P. Coordination and binding properties of zwitterionic glutathione with transition metal cations. Inorganica Chimica Acta **2012**, 387, 125-136.
(37) Liu, J.; Liu, H.; Li, Y.; Wang, H. Probing the coordination properties of glutathione with transition metal ions (Cr^{2+}, Mn^{2+}, Fe^{2+}, Co^{2+}, Ni^{2+}, Cu^{2+}, Zn^{2+}, Cd^{2+}, Hg^{2+}) by density functional theory. Journal of biological physics **2014**, 40 (4), 313-323.
(38) Tang, W.; Stearns, R. A.; Bandiera, S. M.; Zhang, Y.; Raab, C.; Braun, M. P.; Dean, D. C.; Pang, J.; Leung, K. H.; Doss, G. A. Studies on cytochrome P-450-mediated bioactivation of diclofenac in rats and in human hepatocytes: identification of glutathione conjugated metabolites. Drug Metabolism and Disposition **1999**, 27 (3), 365-372.
(39) Scholz, K.; Dekant, W.; Völkel, W.; Pähler, A. Rapid detection and identification of N-acetyl-L-cysteine thioethers using constant neutral loss and theoretical multiple reaction monitoring combined with enhanced product-ion scans on a linear ion trap mass spectrometer. Journal of the American Society for Mass Spectrometry **2005**, 16 (12), 1976-1984.
(40) Banu, L.; Blagojevic, V.; Bohme, D. K. Dissociations of gas-phase complexes of deprotonated glutathione with Co^{2+}, Ni^{2+}, Cu^{2+} and Zn^{2+}: The importance of metal ion reduction. International Journal of Mass Spectrometry **2013**, 345, 142-152.
(41) Frisch, M.; Trucks, G.; Schlegel, H.; Scuseria, G.; Robb, M.; Cheeseman, J.; Scalmani, G.; Barone, V.; Petersson, G.; Nakatsuji, H. Gaussian 16. Gaussian, Inc. Wallingford, CT: 2016.
(42) Trucks, G.; Schlegel, H.; Scuseria, G.; Robb, M.; Cheeseman, J.; Scalmani, G.; Barone, V.; Mennucci, B.; Petersson, G.; Nakatsuji, H. Gaussian 09. Revision A **2009**, 2.
(43) Frisch, M.; Trucks, G.; Schlegel, H.; Scuseria, G.; Robb, M.; Cheeseman, J.; Montgomery Jr, J.; Vreven, T.; Kudin, K.; Burant, J. Gaussian, Inc., Wallingford, CT, 2004; C. Lee, W. Yang, RG Parr. Phys. Rev. B **1988**, 37, 785.
(44) Ehrlich, S.; Moellmann, J.; Reckien, W.; Bredow, T.; Grimme, S. System-Dependent Dispersion Coefficients for the DFT-D3 Treatment of Adsorption Processes on Ionic Surfaces. ChemPhysChem **2011**, 12 (17), 3414-3420.
(45) Grimme, S. Exploration of chemical compound, conformer, and reaction space with meta-dynamics simulations based on tight-binding quantum chemical calculations. Journal of chemical theory and computation **2019**, 15 (5), 2847-2862.
(46) Bannwarth, C.; Ehlert, S.; Grimme, S. GFN2-xTB—An accurate and broadly parametrized self-consistent tight-binding quantum chemical method with multipole electrostatics and density-dependent dispersion contributions. Journal of chemical theory and computation **2019**, 15 (3), 1652-1671.
(47) Cheng, R.; Loire, E.; Martens, J.; Fridgen, T. D. An IRMPD spectroscopic and computational study of protonated guanine-containing mismatched base pairs in the gas phase. Physical Chemistry Chemical Physics **2020**, 22 (5), 2999-3007.
(48) Menard, K. J.; Martens, J.; Fridgen, T. D. A vibrational spectroscopic and computational study of the structures of protonated imidacloprid and its fragmentation products in the gas phase. Physical Chemistry Chemical Physics **2021**, 23 (5), 3377-3388.
(49) Meister, A.; Anderson, M. E. Glutathione. Annual review of biochemistry **1983**, 52 (1), 711-760.

Chapter 4 - Analysis of Non-Covalent Interactions Between Glutathione and Seven Amino Acids: Exploring Binding Energy and Stability in the Gas Phase

4.1 Abstract

This study uses the BIRD technique across various temperatures to explore the dissociation dynamics of protonated amino acid-GSH complexes. We investigated the dissociation behaviors of $[Arg(GSH+H)]^+$, $[Lys(GSH+H)]^+$, $[His(GSH+H)]^+$, $[Asn(GSH+H)]^+$, $[Gln(GSH+H)]^+$, $[Asp(GSH+H)]^+$, and $[Glu(GSH+H)]^+$, and correlated these findings with proton affinity data and kinetic parameters. Arginine, with the highest proton affinity, primarily dissociated to produce protonated arginine, unlike other complexes which more frequently resulted in the production of protonated GSH. Kinetic analyses, derived from Arrhenius plots, revealed that dissociation rates increase with temperature, with $[Asp(GSH+H)]^+$ showing the fastest dissociation ($k = 0.339\ s^{-1}$ at 74°C), and $[Lys(GSH+H)]^+$ demonstrating the slowest rate ($k = 0.004\ s^{-1}$ at 74°C). Activation energies and pre-exponential coefficients varied significantly among complexes, with slower dissociating species displaying higher activation energies and pre-exponential factors. Entropy changes ($\Delta S\dagger$) upon dissociation were also diverse, with most complexes exhibiting either neutral to loose transition states, while $[Asp(GSH+H)]^+$ and $[Glu(GSH+H)]^+$ showed more ordered transition states. These findings offer insights into the influence of proton affinity, temperature, and structural features on the dissociation kinetics of protonated amino acid complexes.

4.2 Introduction

Proteins, recognized as vital constituents of life, are complex molecules essential for the operation of living organisms. They are primarily comprised of carbon, hydrogen, oxygen,

nitrogen, and often sulfur. These macromolecules are constructed by linking amino acids (AA)s together, with 20 standard proteinogenic amino acids composing their structure [1]. Amino acids possess a shared structure characterized by an acid or carboxyl group (─COOH) and a basic or amine group (most often ─NH2) [2]. Amino acids are typically classified as polar and non-polar and further characterized as basic, acidic, or neutral based on their side chain attributes.

Peptides play essential roles in both plant and animal systems, consisting of chains of amino acids interconnected by peptide bonds [6]. The function of peptides hinges on factors like the number, sequence, arrangement, and biological activity of the constituent amino acids [6]. Glutathione is one of the fundamental and essential small biomolecules, found in millimolar concentrations within the cells of all organisms. It plays a multitude of vital physiological roles, including acting as a significant guardian within cells by serving as a pivotal antioxidant, antitoxin, and cofactor. The Meister cycle involves γ-glutamyl transpeptidase, which aids in the covalent binding of glutathione to transport extracellular amino acids into cells. Given its importance, we have investigated the non-covalent interactions between glutathione and seven different amino acids in an in vitro equilibrium system, focusing on the formation of protonated complexes in the gas phase [2, 7, 8]. In previous chapters, we investigated the non-covalent interactions between glutathione and various alkali metals, alkaline earth metals, as well as some transition and heavy metals. In this chapter, I focus on the non-covalent interactions between glutathione and seven different amino acids. arginine (Arg) which contains a guanidine group, lysine (Lys) with an additional amine functional group, and histidine (His) with heterocyclic imidazole side chain, are polar and acidic, capable of accepting protons and resulting in a positive charge under physiological

pH conditions. asparagine (Asn) and glutamine (Gln) studied in this work, are examples of polar neutral amino acids. Structurally, they share similarities due to the presence of amide groups in their side chains. Glutamine, a plentiful free amino acid in plasma, is utilized in intracellular GSH synthesis by transforming into glutamate [3, 4]. Both Asn and Gln are vital for promoting the growth, proliferation, and survival of certain cancer cells. aspartic acid (Asp) and glutamic acid (Glu) are categorized as acidic amino acids due to the presence of an extra carboxyl group. These amino acids play important regulatory roles in areas such as nutrition, energy metabolism, and responses to oxidative stress [5].

To study the non-covalent interactions between GSH and amino acids, we employed the BIRD technique, which originated in the mid-1990s as zero-pressure thermal-radiation induced dissociation (ZTRID) [9-11]. BIRD has proven effective in determining the binding energies of weakly-bound ionic complexes trapped in a Fourier transform ion cyclotron resonance mass spectrometer [12, 13]. This technique is particularly useful for studying the binding energies of noncovalent gas-phase complexes, providing valuable insights into their behavior in solution[18]. Unlike some methods, BIRD is cost-effective and easy to implement, requiring no laser alignment or ion axialization, and employs broadband blackbody radiation from the vacuum chamber storing the ions [14-19].

Through the application of BIRD, our study aims to provide a deeper understanding of the non-covalent interactions between glutathione and common amino acids, contributing to the broader knowledge of cellular function and potential pharmacological applications

It is a well-known fact that a protein's biological purpose is frequently linked to its non-covalent interactions with other components present in a living cell. Examining these

associations could be advantageous in revealing the mysteries of cellular function during both health and disease states [20, 21]. It is imperative that we investigate the non-covalent interactions between small molecules and biomacromolecules. This interest arises from the potential applications of these interactions in the field of pharmacology [22, 23]. Glutathione is regarded as one of the fundamental and essential small biomolecules. It exists in millimolar concentrations within the cells of all organisms and plays a multitude of vital physiological roles [24, 25]. Glutathione plays a critical role in safeguarding cells through a triple protective function, serving as an indispensable antioxidant, antitoxin, and cofactor. Glutathione also acts as a significant guardian within cells, providing a triple shield by serving as a pivotal antioxidant, antitoxin, and cofactor. The Meister cycle involves γ-glutamyl transpeptidase, which aids in the covalent binding of glutathione to transport extracellular amino acids into cells [26]. In human blood, the concentrations of glutathione typically fall within the range of 1 to 3 mmol L^{-1}, while for typical amino acids, the concentrations are in the range of 10^{-2} to 10^{-6} mol L^{-1} [27]. This observation suggests that the formation of non-covalent complexes between glutathione and amino acids is feasible under these specific conditions, given the differences in their concentration ranges in human blood. Through the involvement of γ-glutamyl transpeptidase, glutathione can actively facilitate the transport of extracellular amino acids into cells via covalent binding within the framework of the Meister cycle. Recently, Schmidt and colleagues conducted a quantitative evaluation of the binding of phenylarsenic species to glutathione, isotocin, and thioredoxin using ESI–MS [28]. Their research has rekindled our interest in delving into the non-covalent interactions between glutathione and other small molecules.

However, there is still a lack of comprehensive research on the non-covalent binding of glutathione to common amino acids. Due to the limited research on the non-covalent binding of glutathione to common amino acids, our study utilized the BIRD technique to investigate the interaction between glutathione and common amino acids in an in vitro equilibrium system.

4.3 Methods

In this work, the $[Aa(GSH+H)]^+$ complexes were prepared as a solution containing 1 ml of 1 mM Glutathione (Sigma Aldrich), 1 ml of 1 mM Aa (Aa = His, Arg, Lys, Gln, Asn, Glu, and Asp) and two drops of 1% formic acid was made in a 50/50 mix of 18 MΩ-cm (Millipore) water and methanol. All experiments were carried out utilizing a Bruker ApexQe 7.0 hybrid FTICR mass spectrometer in the Laboratory for the study of the energetics, structures, and reactions of gaseous ions at Memorial University [29]. The ICR cell was heated using a heating jacket wrapped around the flight tube, which extended from the ICR cell to the gate valve [16]. BIRD studies required the isolation of a single complex within the ICR cell over a period of time, allowing for the continuous monitoring of dissociation processes. This enabled the monitoring of variations in the presence or quantity of precursor and fragment ions at a specific temperature as a function of time. In this method, molecules were isolated within the ICR cell under a background pressure of 10^{-10} mbar and specific temperature, and the intensities of precursor and product ions were recorded after a varying period. Depending on the specific complex, the electrosprayed ions of $[Aa(GSH+H)]^+$ were allowed to accumulate in the ion source for varying durations, ranging from 1.0 to 30 seconds. Subsequently, these ions underwent mass selection using a quadrupole mass filter and were then further accumulated in a hexapole collision cell for periods ranging from 1.0 to 2.0 seconds After

which they were guided to the ICR cell where they are stored and allowed to react for varying times and analyzed.

The analysis of the BIRD data involved the determination of unimolecular dissociation rate constants (k) by fitting the observed intensities of precursor ions at various times to the following equation:

$$[I]_t = [I]_0 e^{-kt} \quad (1)$$

In Equation 1, $[I]_0$ represents the initial precursor ion intensity, and it is set to 1 as part of the normalization process. $[I]_t$ represents the normalized intensity of the quadruplex at reaction time, t. Additionally, k is the first order rate constant for dissociation of the precursor ion. The determination of the rate constant for a specific dissociation pathway involves assessing the relative product yields. Subsequently, a plot of BIRD rate constants versus the reciprocal temperature, T, was used to determine the Arrhenius pre-exponential factor (A_{obs}) and activation energy (E_a) according to the Arrhenius equation:

$$\ln k = \ln A_{obs} - \frac{E_a}{k_B T} \quad (2)$$

$$\Delta S^{\dagger} = \left(\ln(A_{obs}) - \ln\left(\frac{k_B T}{h}\right) - 1\right) \times R \quad (3)$$

where R and h are the gas constant and the Planck constant, respectively.

4.4 Results and discussion

Figure 4.1 demonstrates BIRD dissociation acquired for $[Arg(GSH+H)]^+$, $[Lys(GSH+H)]^+$, $[His(GSH+H)]^+$, $[Asn(GSH+H)]^+$, $[Gln(GSH+H)]^+$, $[Asp(GSH+H)]^+$, and $[Glu(GSH+H)]^+$, respectively.

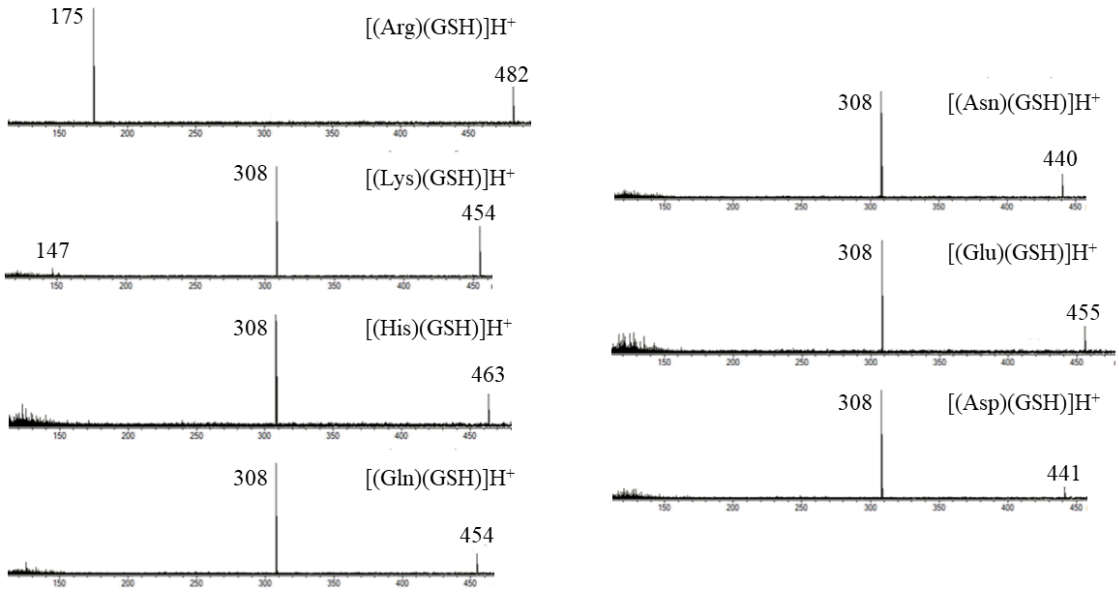

Figure 4.1: BIRD Analysis of Dissociation of Protonated Glutathione and Seven Amino Acids.

The BIRD analysis reveals that in the dissociation of $[Arg(GSH+H)]^+$ the only fragment observed is protonated arginine at 175 *m/z*. In contrast, $[Lys(GSH+H)]^+$ dissociates into both protonated GSH and protonated lysine at 308 *m/z* and 147 *m/z*. For $[His(GSH+H)]^+$, $[Asn(GSH+H)]^+$, $[Gln(GSH+H)]^+$, $[Asp(GSH+H)]^+$, and $[Glu(GSH+H)]^+$ dissociation results in only the protonated glutathione at 308 *m/z* as the observed fragment (see Figure 4.1).

To compare this result with existing literature, Uddin et al. [31] benchmarked the thermochemical properties of common α-amino acids, including proton affinity and gas-phase basicity for both protonated and deprotonated forms, using B3LYP/6-31+G(d,p) and CBS-QB3 methods. Gronert et al. [32] calculated the proton affinities of 20 common amino acids at

the G3MP2 level, utilizing structures from extensive conformational searches. In this work, proton affinities were computed using the structures of the neutral and protonated amino acids with the lowest Gibbs energy at 298 K. For the values in parentheses, the lowest 298 K enthalpy structures were used. Table 4.1 compares these computational results with experimental proton affinity and gas-phase basicity values obtained from the NIST website [33] .

Table 4.1: Computed and Experimental Proton Affinities and Gas Basicities for Various Amino Acids and Glutathione.

	B3LYP/6-31+G(d,p)		G3MP2		CBS-QB3		Exp [34]
	Uddin [32]	This work	Gronert [33]	This work	Uddin [32]	This work	
Arg	1053	1059[1025]	1046	1047[1014]	1044[1009]	1045[1011]	1051[1007]
Lys	1000	1018 [971]	1000	1002 [956]	997 [960]	1001 [955]	996 [951]
His	985	988 [955]	979	979 [947]	977 [945]	977 [944]	988 [950]
Gln	977		973		973		938
Asn	944		936		936		928
Glu	953		948		948		913
Asp	924		916		916		909
GSH		981 [957]		978 [947]		975 [951]	

In Table 4.1, arginine demonstrates the highest proton affinity and gas basicities, significantly contributing to the dissociation of protonated amino acids, while in other complexes, protonated GSH tends to be the primary product. The arginine side chain's strong basicity results from the stabilization of its positive charge through resonance. Histidine's side chain, with its two nitrogens, has a relatively moderate affinity for an additional proton (H^+). Lysine's overall basic nature is due to its possession of two amine groups, particularly the second isolated amine group.

The kinetic parameters were derived from the Arrhenius plots. Figures 4.2 and S4.1-8 represent the kinetic plots obtained for $[Aa(GSH+H)]^+$, (Aa = Arg, Lys, His, Gln, Asn, Glu,

Asp) at different temperatures ranging from 20-74°C. And they are listed in Table 4.2. The rate constants denoted in the figures were determined from the slope of a linear least squares fit applied to the kinetic data at each temperature. Note that the BIRD rate constants for all complexes are within the rapid exchange limit in the 10-3 s^{-1} regime [34, 35].

Figure 4.2 displays a representative set of BIRD data for $[Arg(GSH+H)]^+$ collected at various temperatures ranging from 54 to 74 °C, illustrating the exponential decay from which k(T) values are derived. As expected, the dissociation rate accelerates at higher temperatures, as evidenced by the increase in the rate constant. For example, at 74°C, the rate constant is 0.1911 s^{-1}, compared to 0.0031 s^{-1} at 54°C.

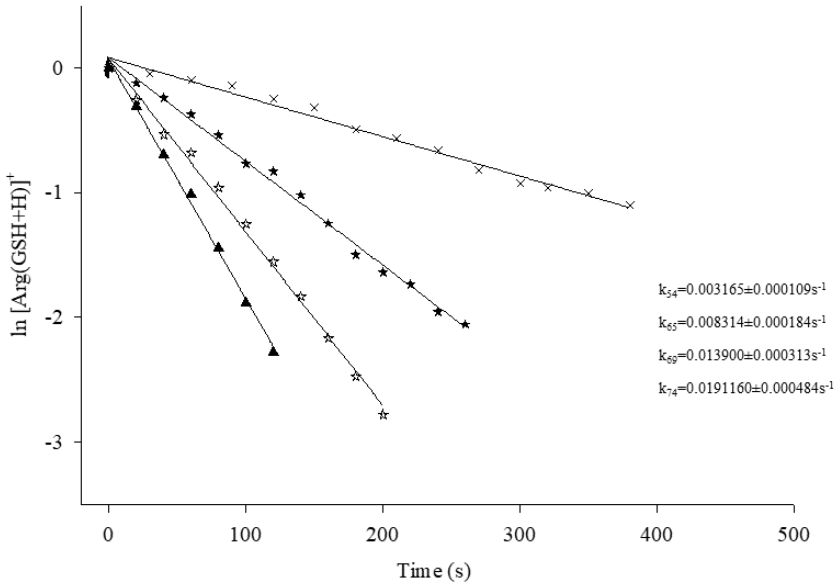

Figure 4.2: BIRD Data for Dissociation of $[Arg(GSH+H)]^+$ Across Different Temperatures.

Table 4.2: The rate constant for Various Amino Acids and Glutathione at different temperatures.

T (°C) / Species	20	26	35	44	54	65	69	74
$[Arg(GSH+H)]^+$					0.0032	0.0083	0.0139	0.0191
$[Lys(GSH+H)]^+$					0.0004	0.0012	0.0021	0.0040
$[His(GSH+H)]^+$				0.0007	0.0027	0.0138	0.0177	0.0206
$[Asn(GSH+H)]^+$	0.0019	0.0041	0.0109	0.0223	0.0580	0.0968	0.1414	0.2037
$[Gln(GSH+H)]^+$			0.0006	0.0017	0.0066	0.0190	0.0275	0.0441
$[Asp(GSH+H)]^+$	0.0067	0.0114	0.0302	0.0560	0.1342	0.2148	0.2762	0.3390
$[Glu(GSH+H)]^+$	0.0020	0.0043	0.0124	0.0244	0.0639	0.0873	0.1678	0.2284

The BIRD rate constants for the dissociation of $[Lys(GSH+H)]^+$ at various temperatures are displayed in Figure S4.1. When compared to the $[Arg(GSH+H)]^+$ results, the dissociation process for $[Lys(GSH+H)]^+$ proceeds at a slower pace and takes more time to reach completion as seen in Table 4.2 and Figure S4.1. This is reflected in the longer dissociation times and the smaller values of k at the same temperatures, confirming the differences in dissociation kinetics for this species. This may indicate that $[Lys(GSH+H)]^+$ is a more strongly bound complex, which requires more energy for dissociation, resulting in the observed longer dissociation times and smaller k values at the same temperatures (see Table 4.2 and Fig S4.1). Figure S4.2 presents the findings for $[His(GSH+H)]^+$, revealing dissociation with a lower rate constant that begins at 44°C. This observation confirms a higher dissociation rate with increasing temperature. Notably, at T=74°C, the dissociation rate constant is as low as k=0.02054 s^{-1}, indicating the accelerated dissociation kinetics at higher temperatures for this particular species. For $[Asn(GSH+H)]^+$, compared to the previous complex, we can note that dissociation observed at a lower temperature (20°C) shown in Table 4.2 and Figure S4.3. Furthermore, the

dissociation rate constant "k" is larger at the same temperatures, with a value of k = 0.2037 s^{-1} at T = 74°C, signifying a faster dissociation rate for $[Asn(GSH+H)]^+$ in comparison to the previous cases. In Figure S4.4 and Table 4.2, which focus on $[Gln(GSH+H)]^+$, we can observe that the dissociation process commences at T=35°C. As the temperature increases, the dissociation process occurs more rapidly, as indicated by higher rate constants, suggesting an accelerated dissociation process. In Figure S4.5 and Table 4.2, our BIRD study focused on $[Asp(GSH+H)]^+$. Remarkably, the dissociation process for this complex was initiated at a relatively low temperature of 20°C. At T=74°C, we observed the highest value for the dissociation rate constant, measuring at 0.339 s^{-1}. This "k" value stands out as the highest among all the complexes examined at the same temperature, indicating a notably rapid dissociation for [Asp(GSH+H)]+ compared to the others. In Figure S4.6 and Table 4.2, our study investigated the dissociation of $[Glu(GSH+H)]^+$. Similar to the previously discussed complex, the dissociation process for $[Glu(GSH+H)]^+$ commenced at T=20°C. Notably, as the temperature increased, the dissociation rate consistently increased across all seven temperature points examined. To compare the BIRD constants effectively, we can focus on the "k" value measured at T=74°C, which was determined for all complexes. In descending order, the "k" values rank as follows: $[Asp(GSH+H)]^+$, $[Glu(GSH+H)]^+$, $[Asn(GSH+H)]^+$, $[Gln(GSH+H)]^+$, $[His(GSH+H)]^+$, $[Arg(GSH+H)]^+$, and $[Lys(GSH+H)]^+$.

We determined Arrhenius activation energies by examining the temperature-dependent dissociation rate constants, as shown in Figure 4.3. These Arrhenius data were accurately fitted using linear regressions, resulting in high coefficients of determination (R^2) ranging from 0.94 to 0.99. Figure 4.3 presented the base-10 logarithm of the pre-exponential factors log A_{obs} and activation entropies $\Delta S^{\dagger}$. Consistently, the activation energy (E0) and Log Aobs for the

complex with a slower dissociation rate was higher compared to its faster dissociating counterpart, aligning with the outcomes derived from the BIRD constants.

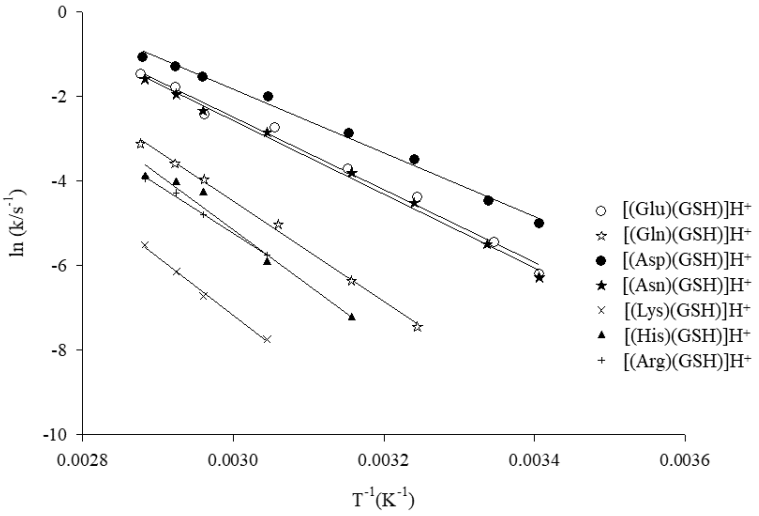

Species	E_0(KJ mol^{-1})
[(Asp)(GSH)]H$^+$	62.6±2.11
[(Glu)(GSH)]H$^+$	71.4±3.02
[(Gln)(GSH)]H$^+$	98.4±2.81
[(Asn)(GSH)]H$^+$	72.2±2.04
[(Lys)(GSH)]H$^+$	114.3±6.10
[(His)(GSH)]H$^+$	109.5±1.08
[(Arg)(GSH)]H$^+$	94.4±5.49

Figure 4.3: Arrhenius Plot for Temperature-Dependent Dissociation Rate Constants of [Arg(GSH+H)]+ and Other Complexes.

$\Delta S^{\dagger}$signifies the difference in entropy between the reactant and the transition state. The positive value of $\Delta S^{\dagger}$ signifies a transition state less ordered than the reactants, characterizing it as "loose" and providing insights into the reaction's nature. A negative $\Delta S^{\dagger}$ indicates a more ordered, "tight" transition state compared to the reactants, typically associated with rearrangement reactions, while "loose" transition states, correlated with bond cleavage reactions, display a positive $\Delta S^{\dagger}$. In the present cases, [His(GSH+H)]$^+$, [Lys(GSH+H)]$^+$, and [Gln(GSH+H)]$^+$ are expected to be neutral to loose, with transition state entropies of 32.4, 30.1, and 4.8 J mol^{-1} K^{-1}. And large negative activation entropies of [Asp(GSH+H)]$^+$, [Glu(GSH+H)]$^+$, [Asn(GSH+H)]$^+$, and [Arg(GSH+H)]$^+$ may suggest that the dissociation reactions occur with a tight transition state without a significant barrier (-80.6, -59.8, -57.8,

and -13.47 J mol^{-1} K^{-1}), compared to the -80.6, -59.8, -57.8, and -13.47 J mol^{-1} K^{-1} entropy of $[Asp(GSH+H)]^+$, $[Glu(GSH+H)]^+$, $[Asn(GSH+H)]^+$, and $[Arg(GSH+H)]^+$.

Upon dissociation, the higher entropy values (32.4, 30.1, and 4.8 J mol^{-1} K^{-1}) of components $[His(GSH+H)]^+$, $[Lys(GSH+H)]^+$, and $[Gln(GSH+H)]^+$ compared to the -80.6, -59.8, -57.8, and -13.47 J mol^{-1} K^{-1} entropy of $[Asp(GSH+H)]^+$, $[Glu(GSH+H)]^+$, $[Asn(GSH+H)]^+$, and $[Arg(GSH+H)]^+$ result in a more entropically favorable.

4.5 Conclusion

This study presents a examination of the dissociation kinetics of protonated amino acid-GSH complexes using BIRD methodology, revealing significant variations in dissociation rates and mechanisms influenced by temperature and amino acid proton affinity. Arginine, characterized by its high proton affinity, demonstrates the most substantial role in dissociation dynamics, while lysine exhibits slower dissociation rates with its dual amine groups. The kinetic data indicate that dissociation rates generally increase with temperature, underscoring the impact of thermal energy on the cleavage of bonds within these complexes.

The Arrhenius analysis of activation energies highlights a correlation between slower dissociation rates and higher activation energies. Notably, complexes such as $[Asp(GSH+H)]^+$ and $[Glu(GSH+H)]^+$, have faster dissociation rates. Conversely, complexes with slower dissociation rates tend to exhibit more ordered transition states.

This study serves as the initial phase of a broader investigation into protonated amino acid-glutathione complexes. Further experimental and computational work is needed to deepen our understanding. Future research should aim to expand experimental techniques, such as

IRMPD and CID, to identify lower-energy structures, and include master equation modeling for comprehensive analysis.

4.6 References

(1) Alberts, B., Molecular biology of the cell. **2017**: Garland science.
(2) Blanco, A. and G. Blanco, Medical biochemistry. **2017**: Academic Press.
(3) Boza, J.J., et al., Plasma glutamine response to enteral administration of glutamine in human volunteers (free glutamine versus protein-bound glutamine). Nutrition, **2000**. 16(11-12): p. 1037-1042.
(4) Alban, F.T., et al., Reactive oxygen and nitrogen species and liver ischemia-reperfusion injury: role of lipoic acid, in The Liver. **2018**, Elsevier. p. 109-119.
(5) Hortin, G.L., Amino Acids, Peptides, and. Tietz Fundamentals of Clinical Chemistry and Molecular Diagnostics-E-Book, **2014**: p. 286.
(6) Forbes, J. and K. Krishnamurthy, Biochemistry, Peptide. **2020**.
(7) Meister, A. and S.S. Tate, Glutathione and related γ-glutamyl compounds: biosynthesis and utilization. Annual review of biochemistry, **1976**. 45(1): p. 559-604.
(8) Matsui, R., et al., Redox regulation via glutaredoxin-1 and protein S-glutathionylation. Antioxidants & Redox Signaling, **2020**. 32(10): p. 677-700.
(9) Price, W.D., P.D. Schnier, and E.R. Williams, Tandem mass spectrometry of large biomolecule ions by blackbody infrared radiative dissociation. Analytical Chemistry, **1996**. 68(5): p. 859-866.
(10) Thoelmann, D., D.S. Tonner, and T.B. McMahon, Spontaneous unimolecular dissociation of small cluster ions,(H_3O^+) Ln and Cl-(H_2O) n (n= 2-4), under Fourier transform ion cyclotron resonance conditions. The Journal of Physical Chemistry, **1994**. 98(8): p. 2002-2004.
(11) Schnier, P.D., et al., Blackbody infrared radiative dissociation of bradykinin and its analogues: Energetics, dynamics, and evidence for salt-bridge structures in the gas phase. Journal of the American Chemical Society, **1996**. 118(30): p. 7178-7189.
(12) Gross, D.S., Y. Zhao, and E.R. William, Dissociation of heme-globin complexes by blackbody infrared radiative dissociation: molecular specificity in the gas phase? Journal of the American Society for Mass Spectrometry, **1997**. 8(5): p. 519-524.
(13) Schnier, P.D., et al., Dissociation energetics and mechanisms of leucine enkephalin $(M+ H)^+$ and $(2M+ X)^+$ ions (X= H, Li, Na, K, and Rb) measured by blackbody infrared radiative dissociation. Journal of the American Society for Mass Spectrometry, **1997**. 8(8): p. 771-780.
(14) Azargun, M. and T.D. Fridgen, Guanine tetrads: an IRMPD spectroscopy, energy resolved SORI-CID, and computational study of M (9-ethylguanine) $^{4+}$(M= Li, Na, K, Rb, Cs) in the gas phase. Physical Chemistry Chemical Physics, **2015**. 17(39): p. 25778-25785.
(15) Gillis, E.A. and T.D. Fridgen, The hydrated Li^+–adenine–thymine complex by IRMPD spectroscopy in the N–H/O–H stretching region. International Journal of Mass Spectrometry, **2010**. 297(1-3): p. 2-8.
(16) Azargun, M., et al., The K 2 (9-ethylguanine) 12 2+ quadruplex is more stable to unimolecular dissociation than the K (9-ethylguanine) 8+ quadruplex in the gas phase: a

BIRD, energy resolved SORI-CID, IRMPD spectroscopic, and computational study. Physical Chemistry Chemical Physics, **2019**. 21(28): p. 15319-15326.
(17) Burt, M.B., S.G. Decker, and T.D. Fridgen, Water binding energies of [Pb (amino acid-H) H 2 O]$^{+}$ complexes determined by blackbody infrared radiative dissociation. Physical Chemistry Chemical Physics, **2012**. 14(43): p. 15118-15126.
(18) Deng, L., E.N. Kitova, and J.S. Klassen, Mapping protein–ligand interactions in the gas phase using a functional group replacement strategy. Comparison of CID and BIRD activation methods. Journal of The American Society for Mass Spectrometry, **2013**. 24(7): p. 988-996.
(19) Dunbar, R. and T. McMahon, Activation of unimolecular reactions by ambient blackbody radiation. Science, **1998**. 279(5348): p. 194-197.
(20) Bovet, C., et al., Estrogen receptor–ligand complexes measured by chip-based nanoelectrospray mass spectrometry: An approach for the screening of endocrine disruptors. Protein science, **2007**. 16(5): p. 938-946.
(21) Lin, Z.J., W. Li, and G. Dai, Application of LC–MS for quantitative analysis and metabolite identification of therapeutic oligonucleotides. Journal of pharmaceutical and biomedical analysis, **2007**. 44(2): p. 330-341.
(22) Yanes, O., et al., Exploring the "intensity fading" phenomenon in the study of noncovalent interactions by MALDI-TOF mass spectrometry. Journal of the American Society for Mass Spectrometry, **2007**. 18(2): p. 359-367.
(23) König, S., et al., Detection of ATP-binding to growth factors. Journal of the American Society for Mass Spectrometry, **2008**. 19(1): p. 91-95.
(24) Sheng, R., et al., EGCG inhibits cardiomyocyte apoptosis in pressure overload-induced cardiac hypertrophy and protects cardiomyocytes from oxidative stress in rats. Acta Pharmacologica Sinica, **2007**. 28(2): p. 191-201.
(25) CHIN, T.y., S.h. CHUEH, and P.l. TAO, S-Nitrosoglutathione and glutathione act as NMDA receptor agonists in cultured hippocampal neurons 1. Acta pharmacologica Sinica, **2006**. 27(7): p. 853-860.
(26) Dai, Z.-y., et al., Investigation of non-covalent complexes of glutathione with common amino acids by electrospray ionization mass spectrometry. Acta Pharmacologica Sinica, **2008**. 29(6): p. 759-771.
(27) Yao, X., Y. Wang, and G. Chen, Simultaneous determination of aminothiols, ascorbic acid and uric acid in biological samples by capillary electrophoresis with electrochemical detection. Biomedical Chromatography, **2007**. 21(5): p. 520-526.
(28) Schmidt, A.C., M. Neustadt, and M. Otto, Quantitative evaluation of the binding of phenylarsenic species to glutathione, isotocin, and thioredoxin by means of electrospray ionization time-of-flight mass spectrometry. Journal of mass spectrometry, **2007**. 42(6): p. 771-780.
(29) Fridgen, T.D., Infrared consequence spectroscopy of gaseous protonated and metal ion cationized complexes. Mass spectrometry reviews, **2009**. 28(4): p. 586-607.
(30) Gorman, G.S., et al., Proton affinities of the 20 common. alpha.-amino acids. Journal of the American Chemical Society, **1992**. 114(10): p. 3986-3988.
(31) K.M. Uddin, P.W. Warburton, R.A. Poirier J. Phys. Chem. B, **2012**, 116, 3220-3234.
(32) S. Gronert, D.C. Simpson, K.M. Conner *J. Am. Soc. Mass Spectrom.* **2009**, *20*, 2116.

(33) Hunter, E. and S. Lias, Proton Affinity Evaluation in NIST Chemistry WebBook, NIST Standard Reference Database Number 69. National Institute of Standards and Technology: Gaithersburg MD, **1998**. 20899.
(34) Gillis, E.A., et al., Structures and energetics of electrosprayed uracil n Ca 2+ clusters (n= 14–4) in the gas phase. Physical Chemistry Chemical Physics, **2012**. 14(10): p. 3304-3315.
(35) Grimme, S., et al., A consistent and accurate ab initio parametrization of density functional dispersion correction (DFT-D) for the 94 elements H-Pu. The Journal of chemical physics, **2010**. 132(15).

Chapter 5 - Summary and Outlook

Chapter 2 comprehensively examines the results and implications of SORI-CID and vibrational spectroscopy analyses of $[M(GSH)]^+$ complexes, where M represents various alkali metal (Li, Na, K, Rb, and Cs) cations. The study provides significant insights into the fragmentation behaviors and structural characteristics of these complexes, revealing key differences attributable to the size and charge density of the metal cations.

The SORI-CID results for the $[M(GSH)]^+$ complexes demonstrate a clear trend related to the nature of the metal cation. For all alkali metal complexes, common fragmentation pathways include the loss of water and pyroglutamic acid, with the latter also being prominent in other glutathione conjugates. Notably, $[Rb(GSH)]^+$ and $[Cs(GSH)]^+$ primarily fragment via the loss of neutral glutathione, indicating that these larger cations are less tightly bound compared to smaller cations like Li^+, Na^+, and K^+. This observation aligns with the expectation that smaller metal cations have a stronger binding affinity, leading to more extensive fragmentation and the appearance of secondary fragments, such as NH_3 and H_2S, especially in the $[Li(GSH)]^+$ and $[Na(GSH)]^+$ complexes. The absence of metal cation products in the CID spectra of $[K(GSH)]^+$ and the expected non-detection of smaller metal cations in complexes with Li^+ and Na^+ highlight the influence of metal size on fragmentation patterns. The data shows that smaller cations lead to more pronounced fragmentation of the glutathione molecule, while larger cations primarily result in the loss of glutathione itself.

The IRMPD spectra of $[M(GSH)]^+$ complexes, compared with computationally derived spectra, reveal detailed structural insights. The lowest energy structures consistently show that the metal cations are bound through ion-dipole interactions with amine and carbonyl groups,

with additional hydrogen bonding and S-H--O2 interactions observed. The elongation of the S-H--O2 distance and variations in the metal to N and O distances across different metal cations align with the expected increase in metal size, affecting the binding geometry. The vibrational spectra further emphasize these structural variations, with specific absorption features corresponding to different coordination environments and bond interactions. For instance, shifts in the C=O stretching frequencies and amide bending vibrations reflect changes in coordination and bonding with the metal cations. The observed spectral features, particularly in the higher energy region, confirm the presence of free carboxylic acid O-H groups and N-H stretching, indicating less diagnostic utility for structural determination in this region.

The exploration of higher energy structures for $[Li(GSH)]^+$, $[Na(GSH)]^+$, $[K(GSH)]^+$, and $[Rb(GSH)]^+$ provides further context on the stability and preferences of these complexes. For $[Li(GSH)]^+$ and $[Na(GSH)]^+$, the inclusion of additional interactions, such as SH—O2, stabilizes the lowest energy structures. This trend is consistent across all examined metal cations, where structures with stronger metal binding interactions and more favorable geometries align with the experimental IR spectra. Conversely, higher energy structures, including zwitterionic forms and pentacoordinated arrangements, generally do not match the experimental data well, reflecting their reduced stability or unfavorable bonding configurations.

The detailed analysis of these higher energy structures confirms the robustness of the lowest energy configurations predicted by the models and provides insight into the potential energy barriers associated with alternative binding modes. For $[Rb(GSH)]^+$, the study identifies both low-energy structures and higher energy forms with notable differences in vibrational spectra, suggesting a complex interplay between metal coordination and structural stability.

In conclusion, the combined SORI-CID and vibrational spectroscopy analyses presented in this chapter offer a thorough understanding of the fragmentation and structural characteristics of $[M(GSH)]^+$ complexes. The findings underscore the influence of metal cation size on fragmentation patterns, structural configurations, and vibrational properties. Smaller alkali metal cations induce more extensive fragmentation and tighter binding interactions, while larger cations primarily lead to the loss of glutathione. The study effectively demonstrates how computational modeling and experimental data can be integrated to elucidate the structural and dynamic properties of metal-glutathione complexes, contributing valuable insights to the field of metal-ligand interactions.

In Chapter 3, we have explored the fragmentation patterns and structural characteristics of doubly charged metal glutathione complexes using SORI-CID and IRMPD spectroscopy. The comprehensive analysis of SORI-CID results for complexes of doubly charged metals (Mg^{2+}, Ca^{2+}, Sr^{2+}, Ba^{2+}, Mn^{2+}, Fe^{2+}, Co^{2+}, Ni^{2+}, Cu^{2+}, Zn^{2+}, Cd^{2+}, Hg^{2+}, Pb^{2+}) reveals insightful trends and differences in fragmentation behaviors, driven by the metal's charge density and coordination environment. The primary fragmentation pathways observed in these complexes include the loss of water, ammonia, H_2S, glycine, pyroglutamic acid, and glutathione. Notably, the loss of water (18.0 Da) was predominant across most metal complexes, with exceptions in Ni^{2+}, Cu^{2+}, and Hg^{2+} complexes where the loss of ammonia (17.0 Da) was more common. Additionally, the fragmentation due to the loss of pyroglutamic acid (129.0 Da) was observed in all metals except Mn, Zn, and Hg. The significant loss of glycine (75.0 Da) was noted in Co^{2+}, Ni^{2+}, Zn^{2+}, and Cd^{2+} complexes, while Cu^{2+} and Pb^{2+} exhibited glycine loss as a minor pathway.

The results from SORI-CID are complemented by computed structures and vibrational spectra obtained through IRMPD experiments. The computed structures for alkaline earth metal complexes (Mg^{2+}, Ca^{2+}, Sr^{2+}, and Ba^{2+}) reveal that the metal cations coordinate with the amine group and carbonyl oxygens of glutathione, exhibiting significant structural variation based on metal size and coordination environment. The increasing size of metal cations from Mg to Ba leads to longer distances between the metal and ligand atoms, influencing the stability and fragmentation patterns of the complexes.

The computational and experimental data align well, particularly in the fingerprint region of the IRMPD spectra, validating the predicted lowest energy structures and providing insights into the coordination chemistry of these metal-glutathione complexes. The agreement between the experimental spectra and computed infrared spectra, with some deviations, emphasizes the importance of considering both theoretical and experimental approaches for a comprehensive understanding of these complex systems.

Overall, this chapter highlights the intricate relationship between metal cation properties, ligand interactions, and fragmentation pathways. The observed trends in fragmentation and structural configurations provide valuable insights into the stability and reactivity of metal glutathione complexes, with implications for their roles in biochemical processes and potential applications in analytical chemistry. The findings from this chapter set the stage for further investigations into the interactions of metal ions with biological ligands and contribute to a deeper understanding of metal-ligand chemistry.

In Chapter 4, we investigated the dissociation kinetics of protonated glutathione complexes with various amino acids through BIRD (beam-type ion mobility) experiments. The

analysis focused on the temperature-dependent dissociation behaviors of $[Arg(GSH+H)]^+$, $[Lys(GSH+H)]^+$, $[His(GSH+H)]^+$, $[Asn(GSH+H)]^+$, $[Gln(GSH+H)]^+$, $[Asp(GSH+H)]^+$, and $[Glu(GSH+H)]^+$. The findings highlight the influence of amino acid side chain properties on the dissociation kinetics and mechanisms of these complexes.

Arginine, with the highest proton affinity and gas basicity, shows a pronounced tendency for dissociation, reflecting its ability to stabilize the positive charge through resonance. This results in a significant amount of protonated Arginine being the primary product in dissociation. In contrast, other amino acids exhibit protonated GSH dissociation, with variations in proton affinity influencing their respective dissociation kinetics.

The temperature dependence of dissociation was analyzed across a range from 20°C to 74°C. As illustrated in this chapter, the dissociation rates for $[Arg(GSH+H)]^+$ increase with temperature, with a marked acceleration of the process observed at higher temperatures. The rate constant for $[Arg(GSH+H)]^+$ increases from 0.1911 s^{-1} at 74°C, indicating rapid dissociation as the temperature rises. This trend is corroborated by the data for $[Lys(GSH+H)]^+$, which, despite its slower dissociation rate and longer times to completion, exhibits a clear temperature dependence with lower rate constants compared to [Arg(GSH+H)]+.

Comparative analysis of the dissociation kinetics for different amino acid complexes reveals distinctive patterns. For example, $[Asp(GSH+H)]^+$ exhibits the highest dissociation rate constant (0.339 s^{-1} at 74°C), indicating its rapid dissociation relative to other complexes. On the other hand, $[Lys(GSH+H)]^+$ has the lowest rate constant at the same temperature, reflecting a more robust dissociation barrier. The observed variations in dissociation rates among the

amino acid complexes can be attributed to differences in their side chain structures and proton affinities, which impact the strength of the bonds within the complexes.

The Arrhenius plots provided insights into the activation energies for dissociation. The linear fits reveal that complexes with higher activation energies dissociate more slowly, consistent with the observed BIRD constants. The activation energies for the different complexes range from 0.94 to 0.99, reflecting the varying dissociation barriers associated with each amino acid's side chain characteristics.

Overall, the results from this chapter underscore the significant role of amino acid side chain properties in influencing the dissociation kinetics of protonated glutathione complexes. The temperature-dependent studies and Arrhenius analyses provide a comprehensive understanding of the factors driving dissociation rates, contributing to a broader knowledge of amino acid-glutathione interactions. These findings offer valuable insights into the chemical behavior of these complexes and enhance our understanding of their stability and reactivity under varying conditions.

Appendix A – Supplemental Information for Chapter 2

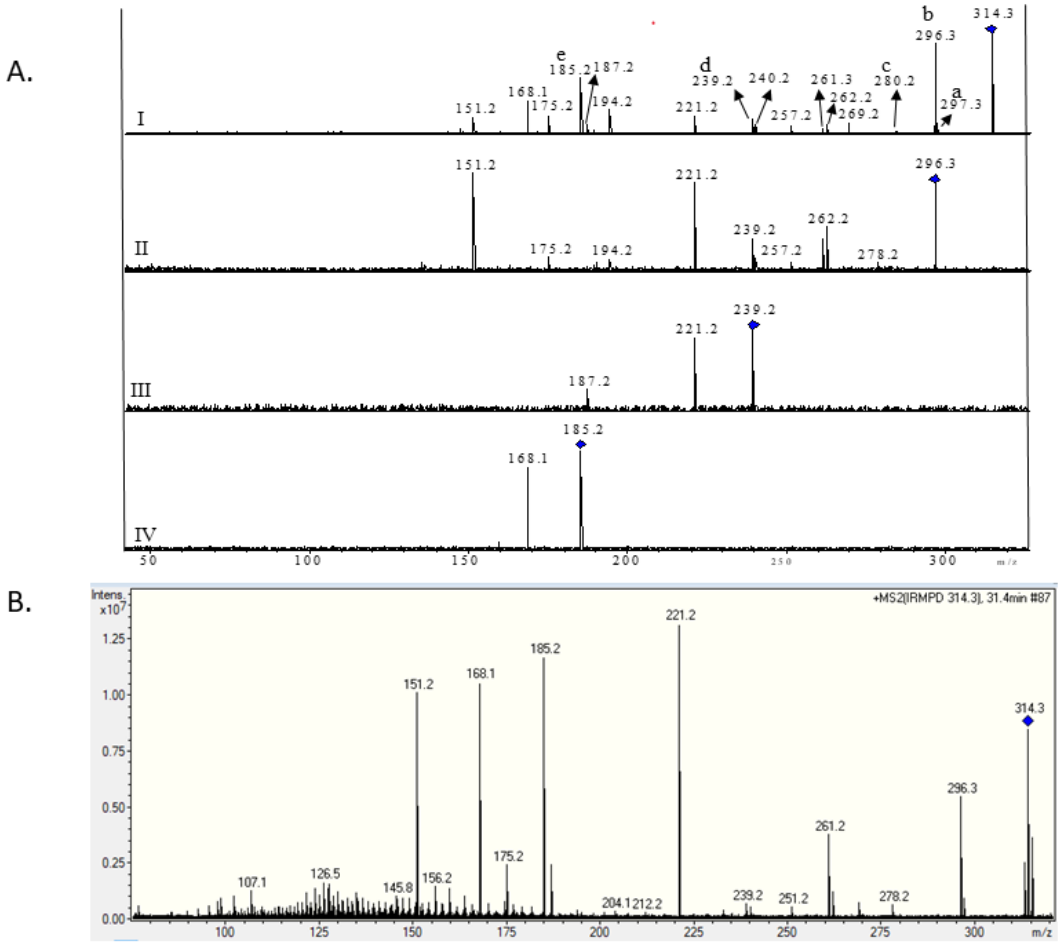

Figure S2. 1. SORI-CID (A) and IRMPD (B) mass spectra for $[Li(GSH)]^+$.

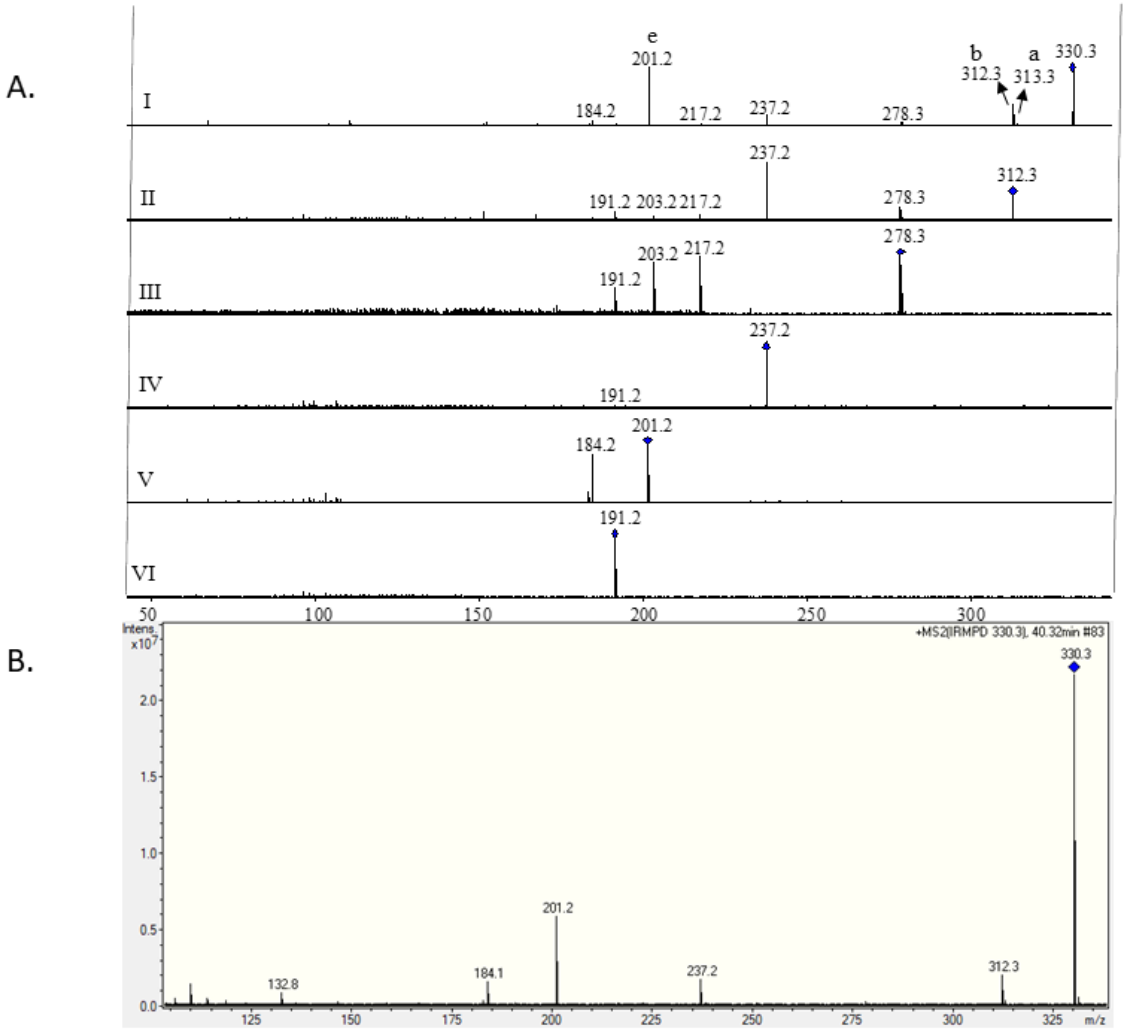

Figure S2. 2. SORI-CID (A) and IRMPD (B) mass spectra for $[Na(GSH)]^+$.

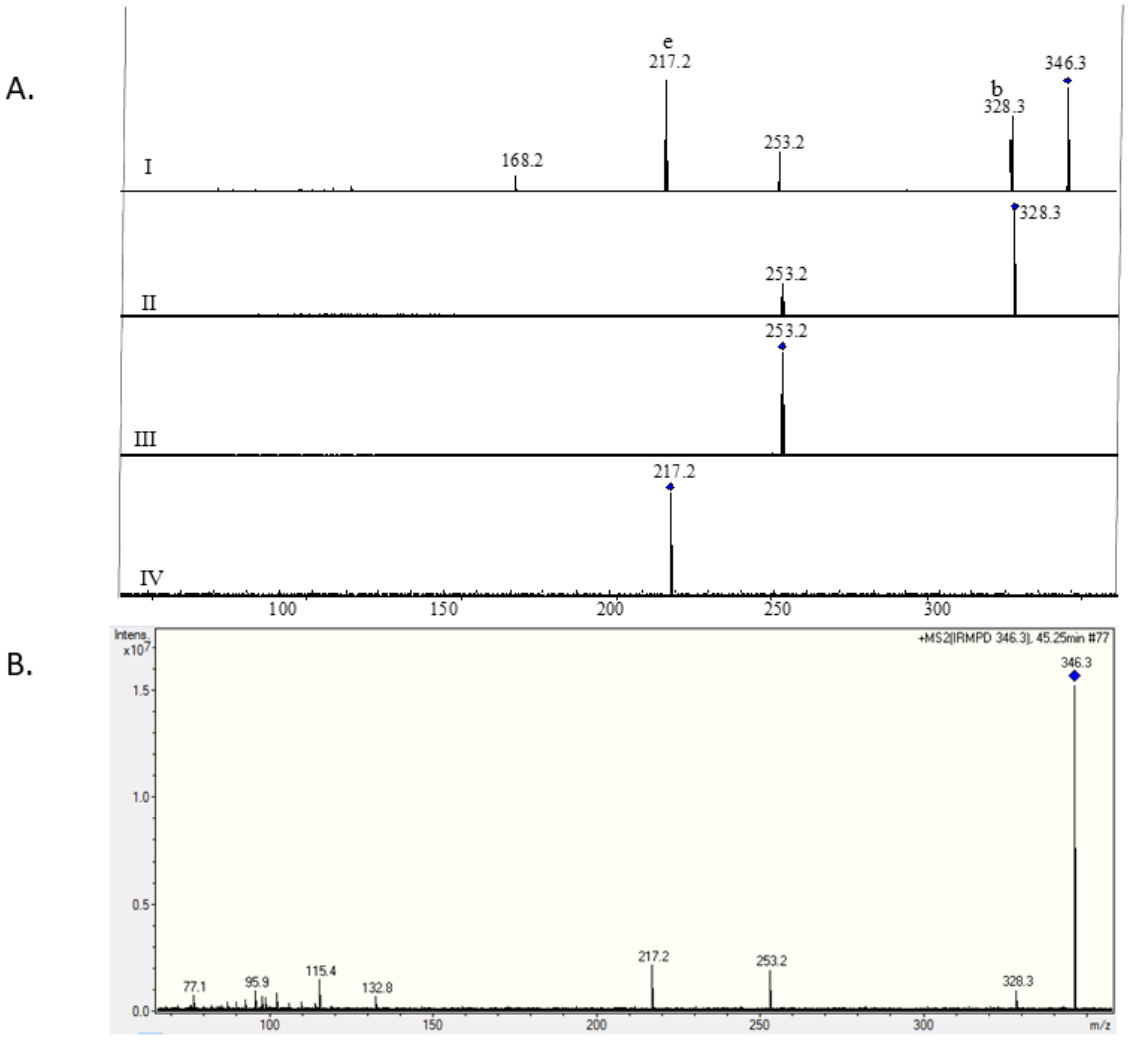

Figure S2. 3. SORI-CID (A) and IRMPD (B) mass spectra for $[K(GSH)]^+$.

A.

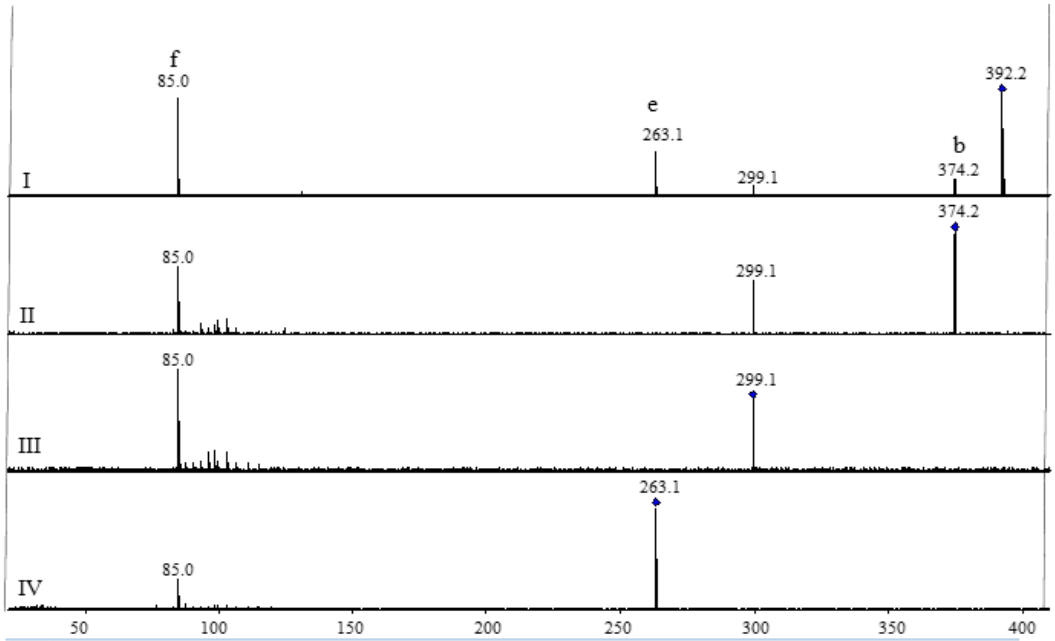

B.

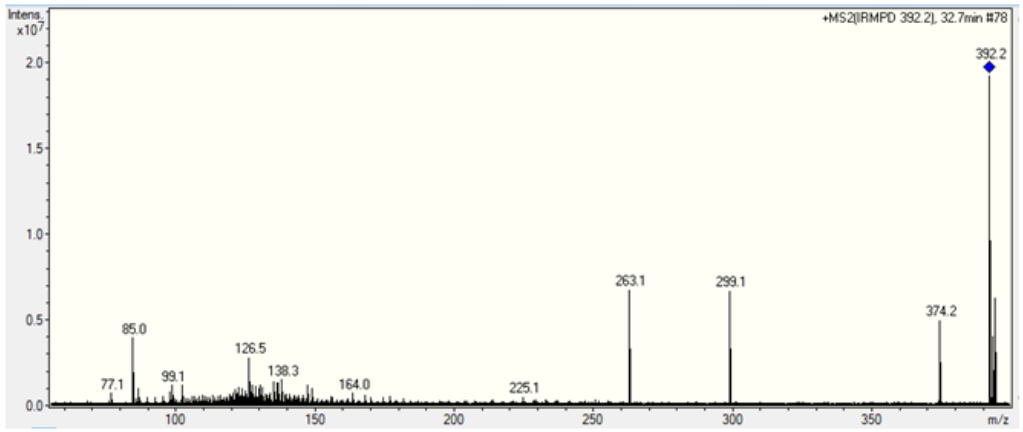

Figure S2. 4. SORI-CID (A) and IRMPD (B) mass spectra for $[Rb(GSH)]^+$.

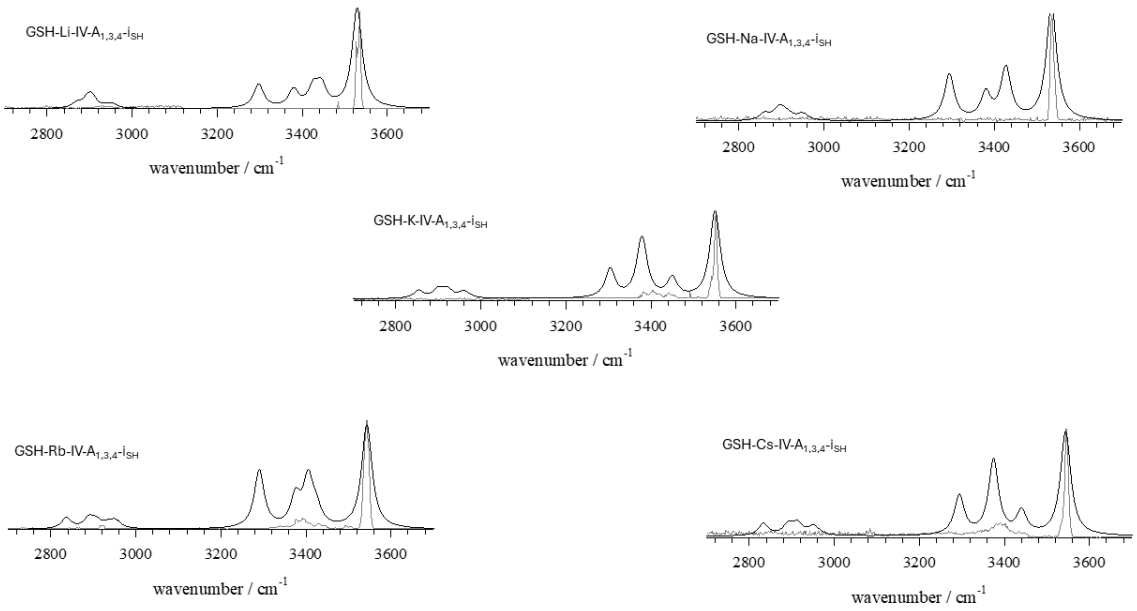

Figure S2. 5. Computed structures of $[M(GSH)]^+$ in the higher region.

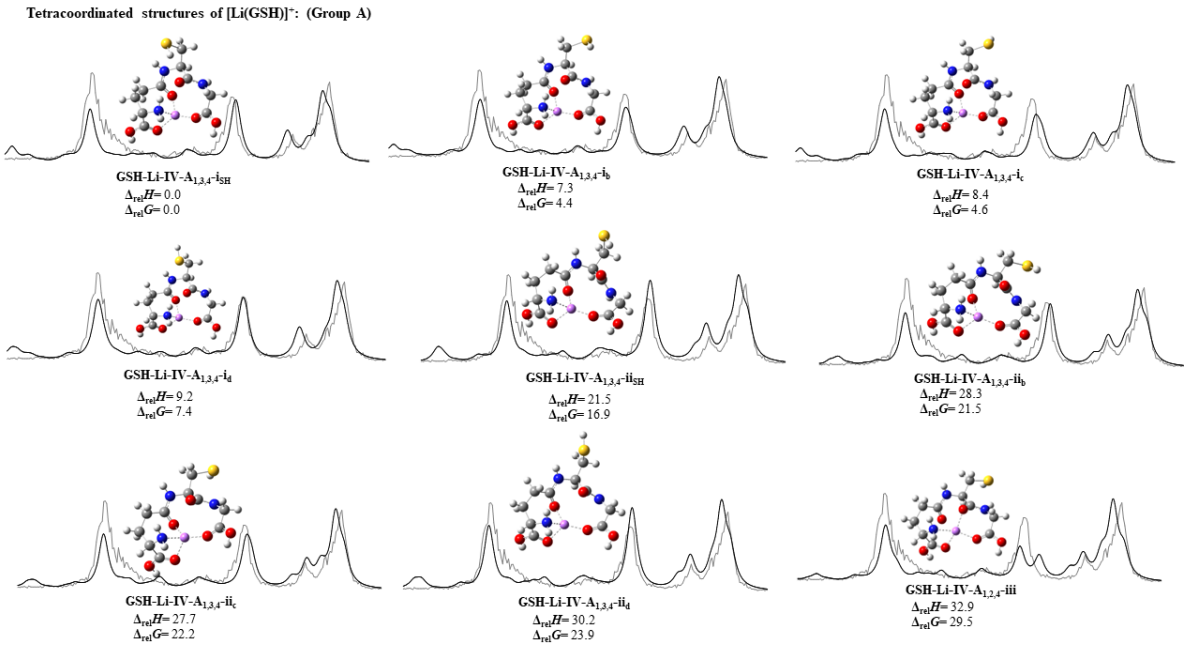

Figure S2. 6. Computed structures of $[Li(GSH)]^+$.

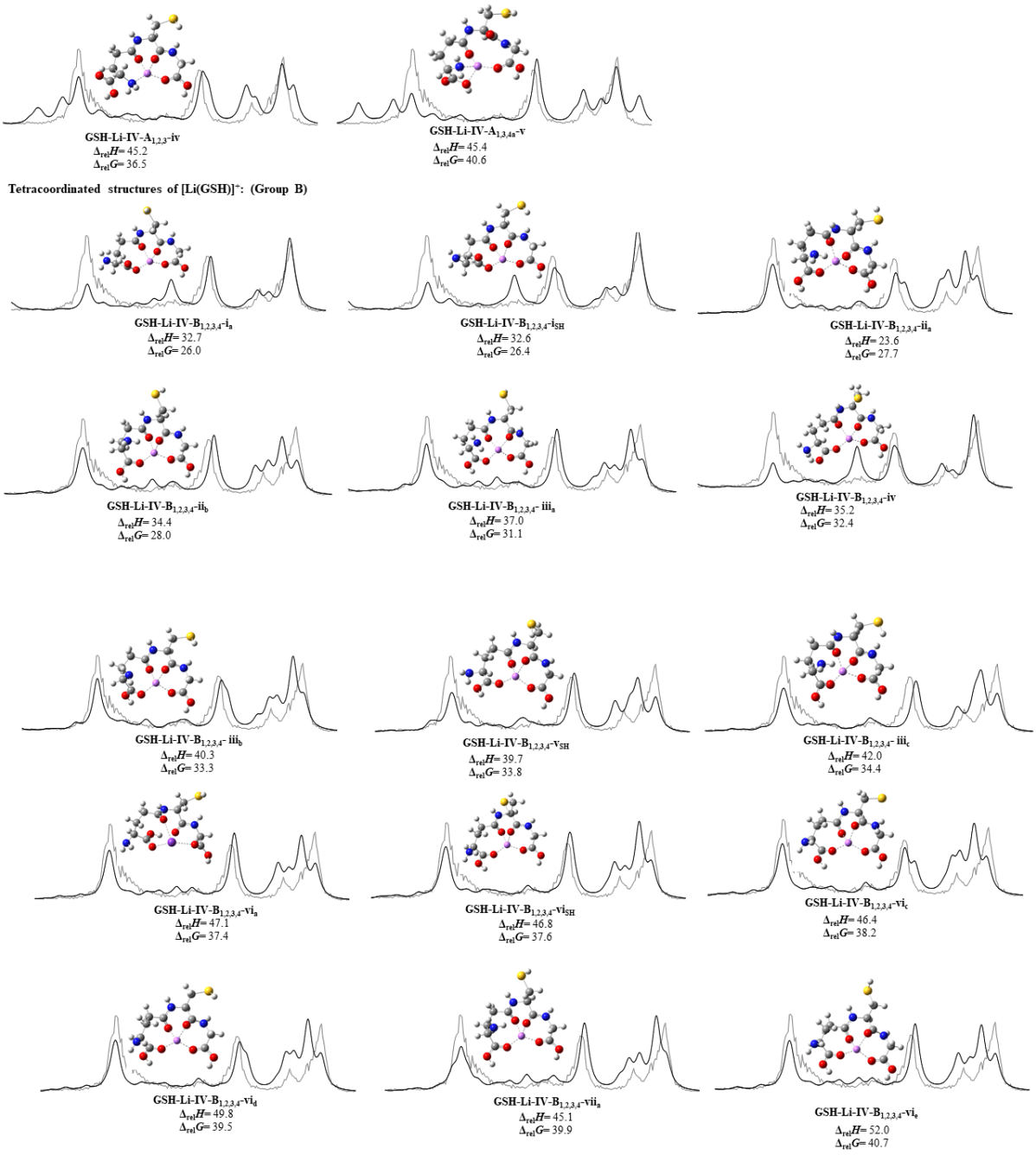

Figure S2.6: Computed structures of $[Li(GSH)]^{+}$.

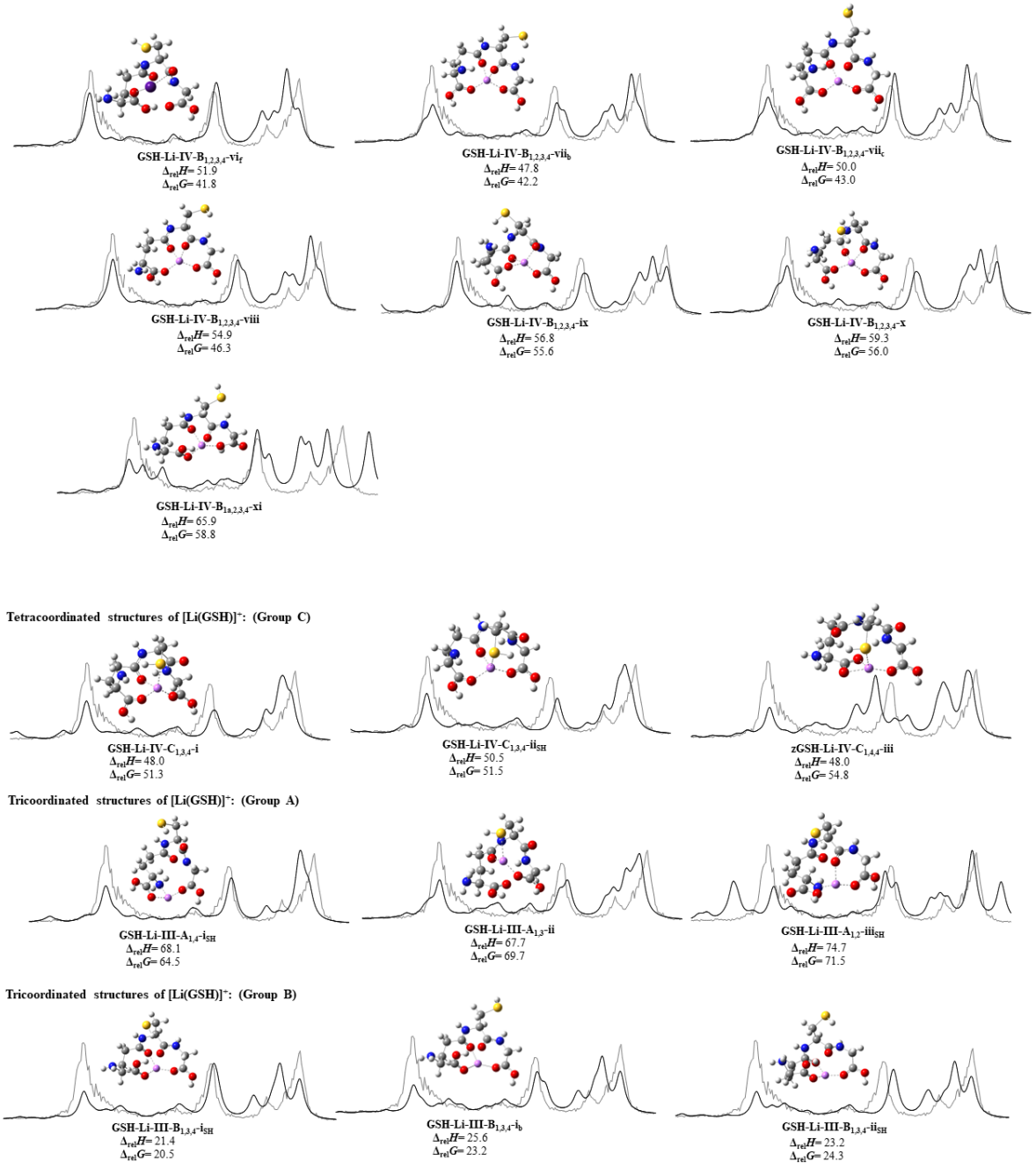

Figure S2.6: Computed structures of $[Li(GSH)]^+$.

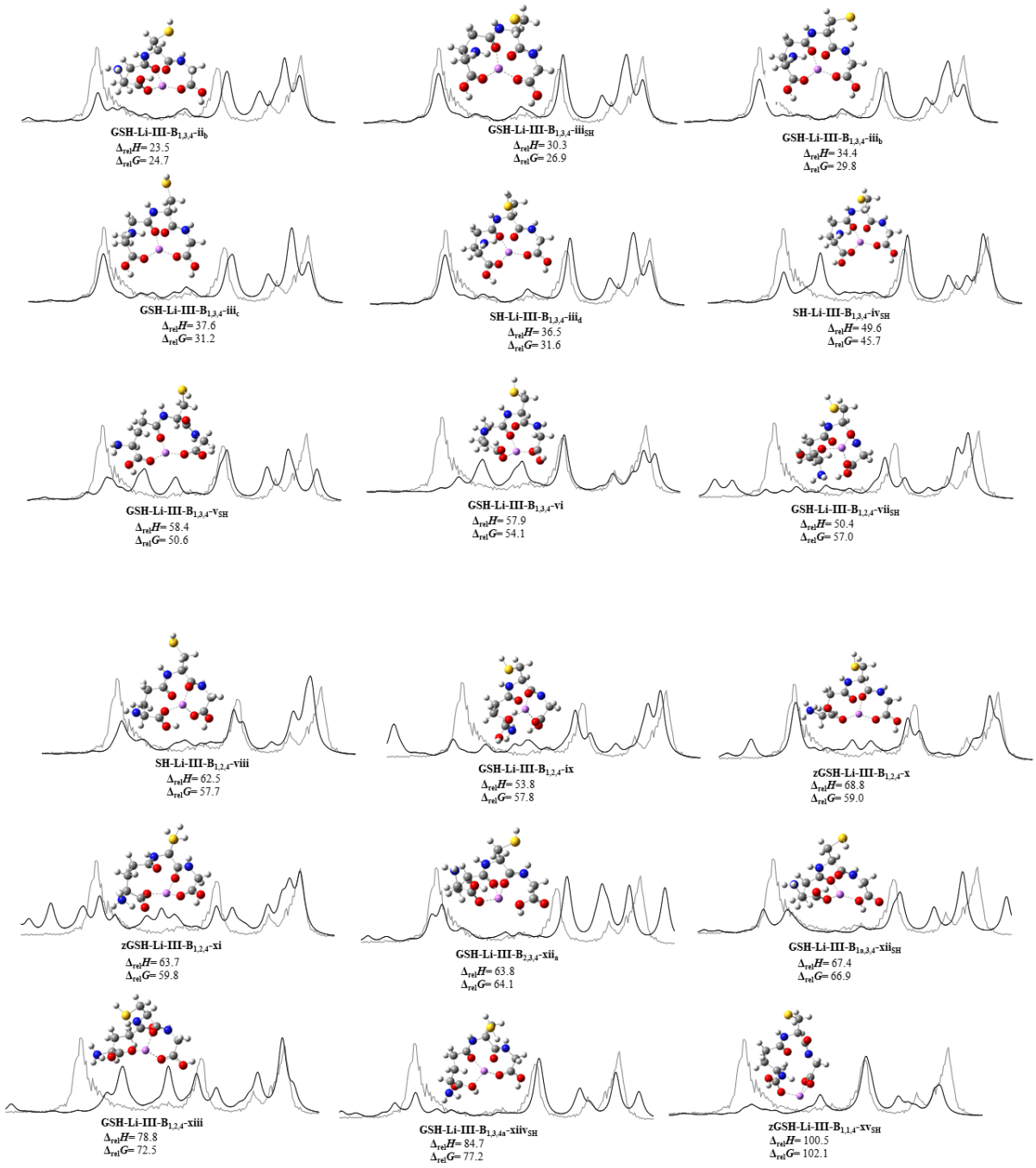

Figure S2.6: Computed structures of $[Li(GSH)]^{+}$.

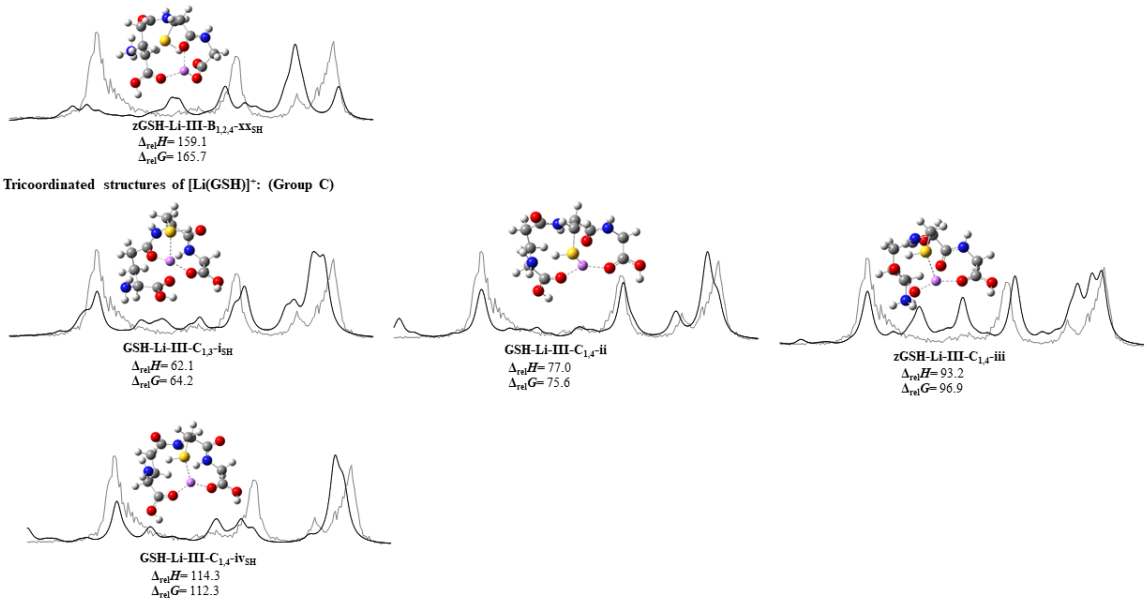

Figure S2.6: Computed structures of $[Li(GSH)]^{+}$.

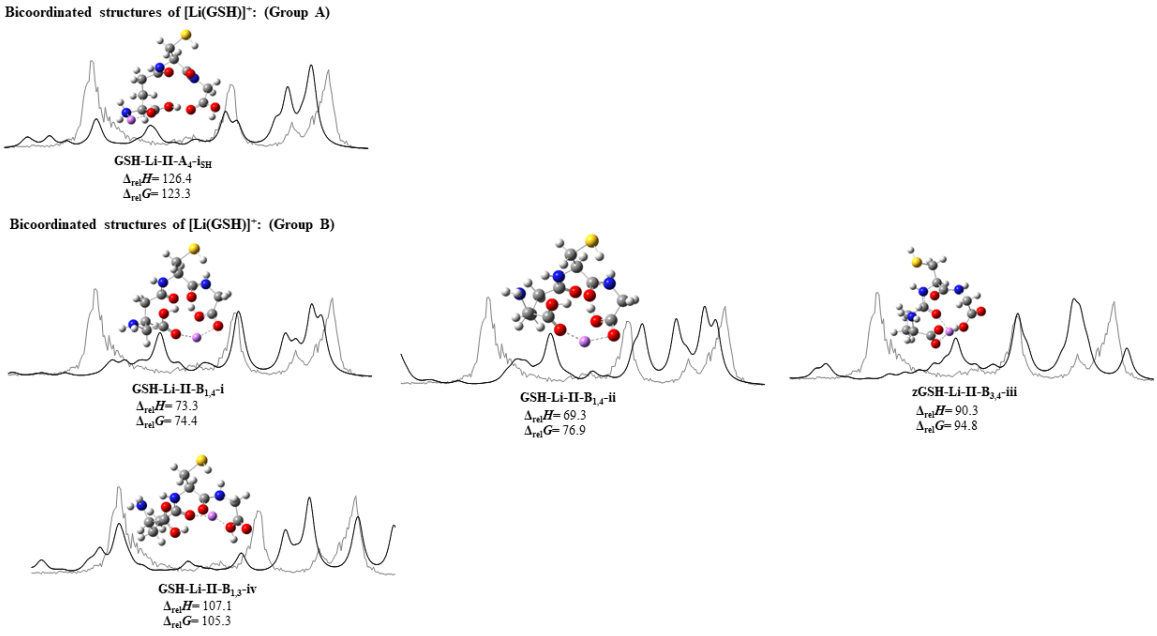

Figure S2. 7. Computed structures of $[Na(GSH)]^{+}$.

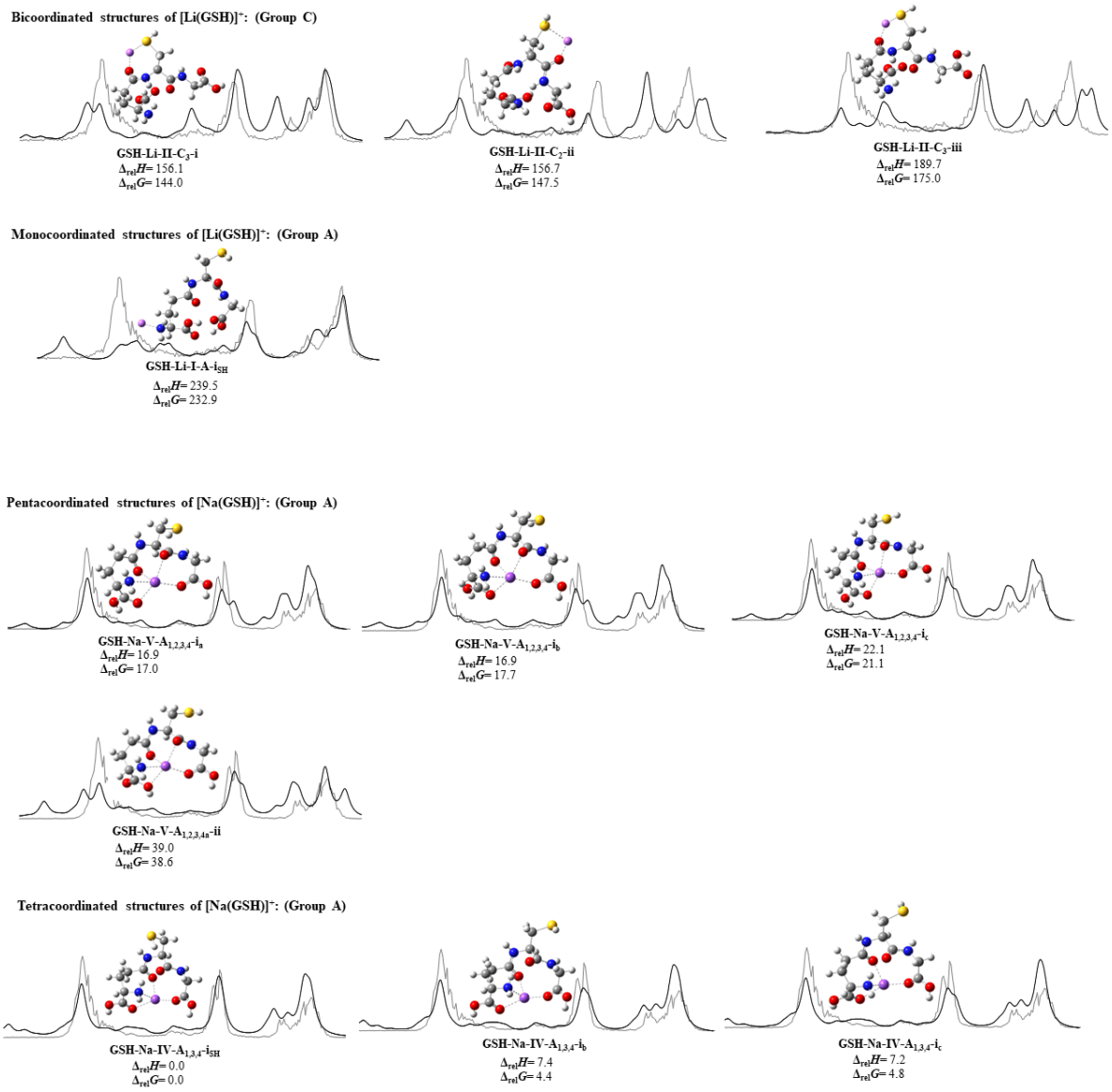

Figure S2.7: Computed structures of $[Na(GSH)]^{+}$.

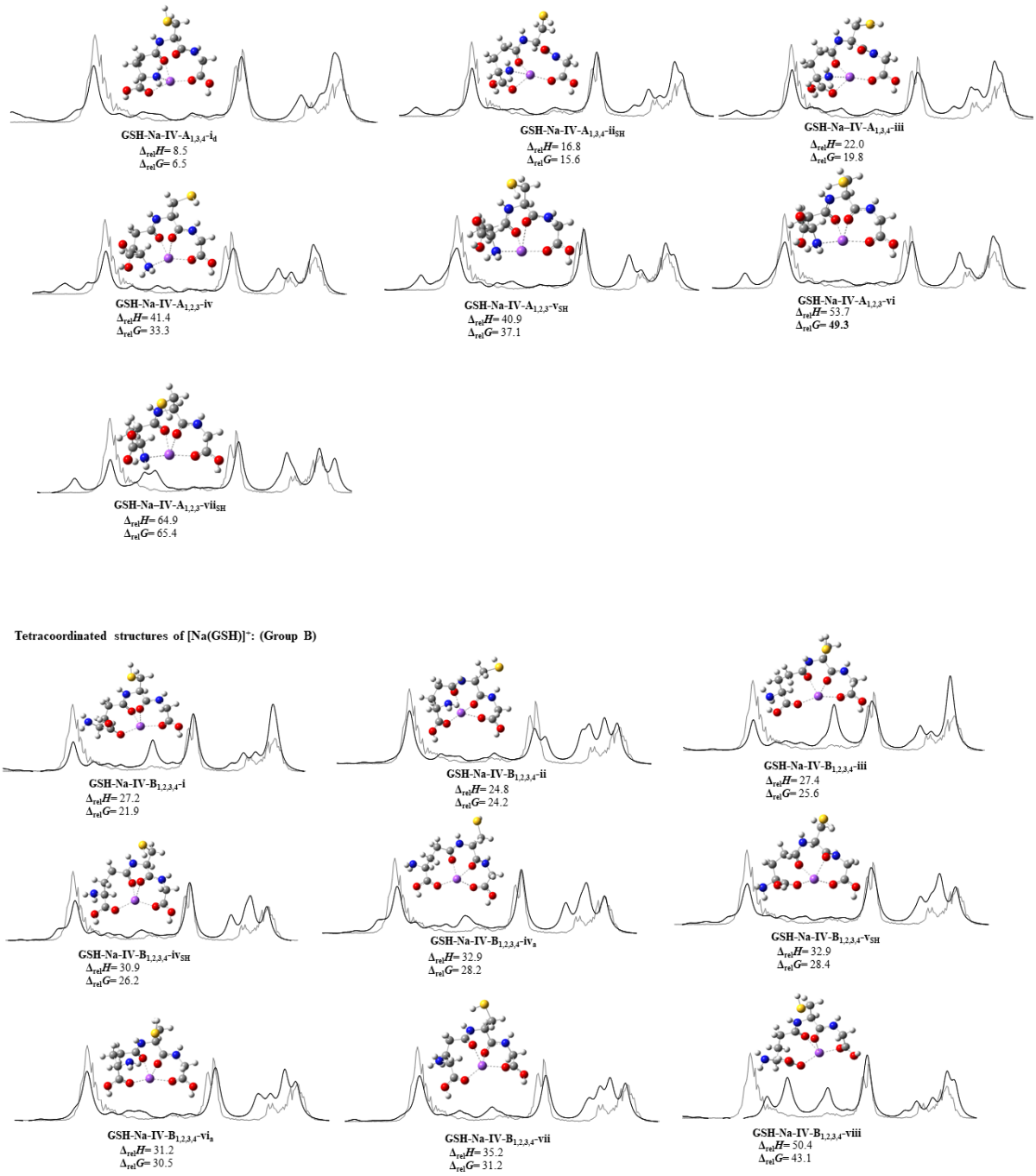

Figure S2.7: Computed structures of $[Na(GSH)]^+$.

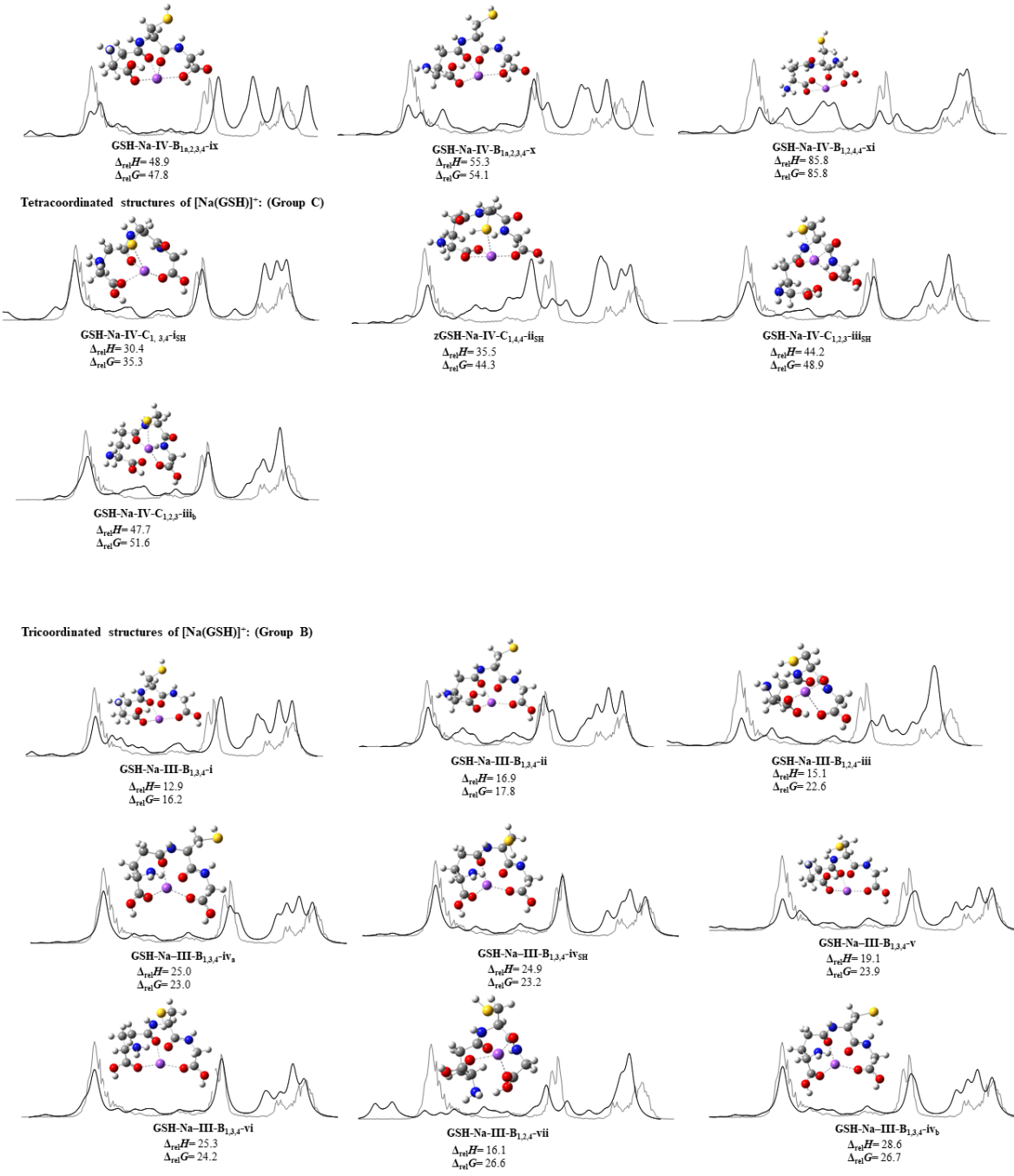

Figure S2.7: Computed structures of $[Na(GSH)]^+$.

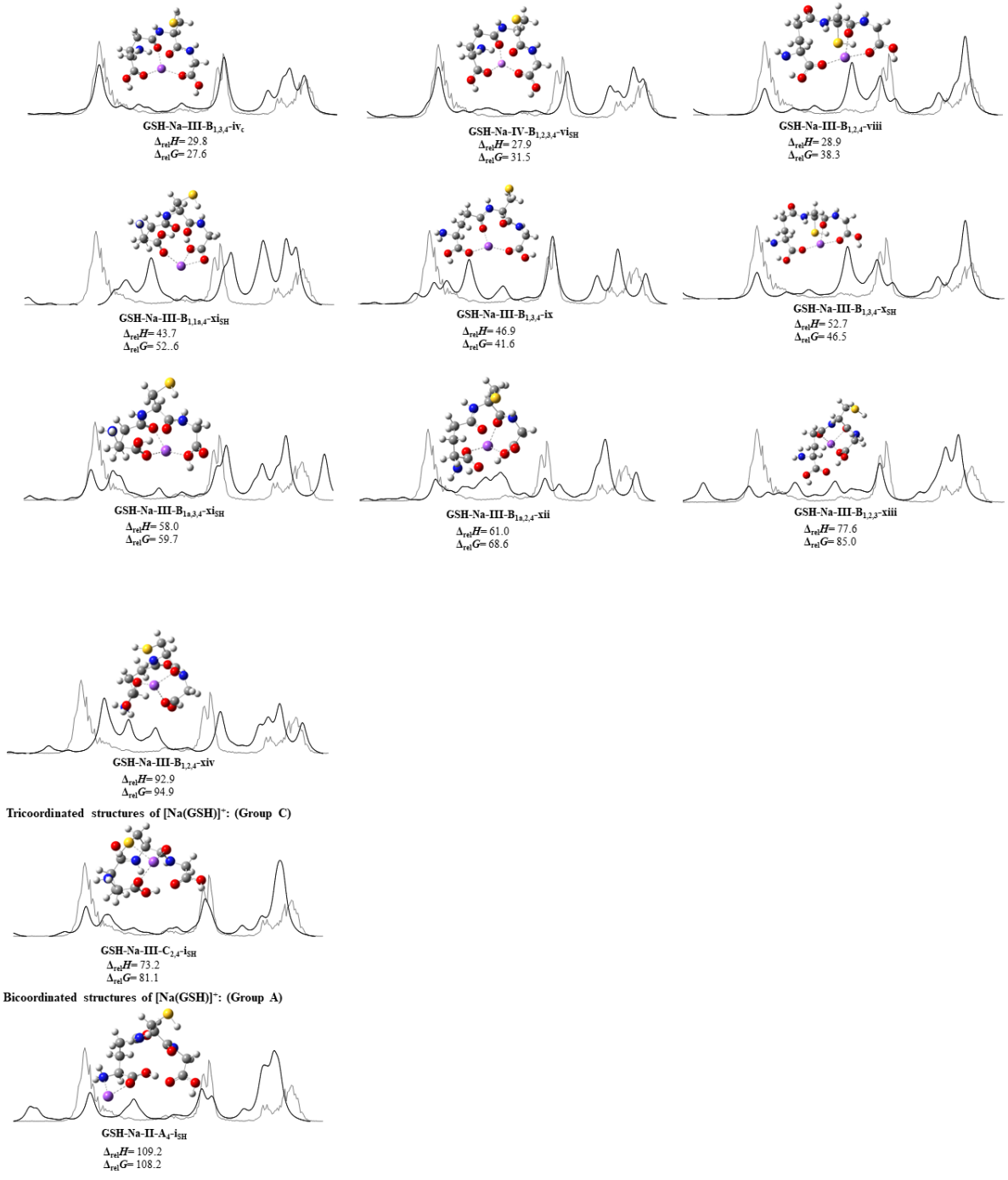

Figure S2.7: Computed structures of $[Na(GSH)]^{+}$.

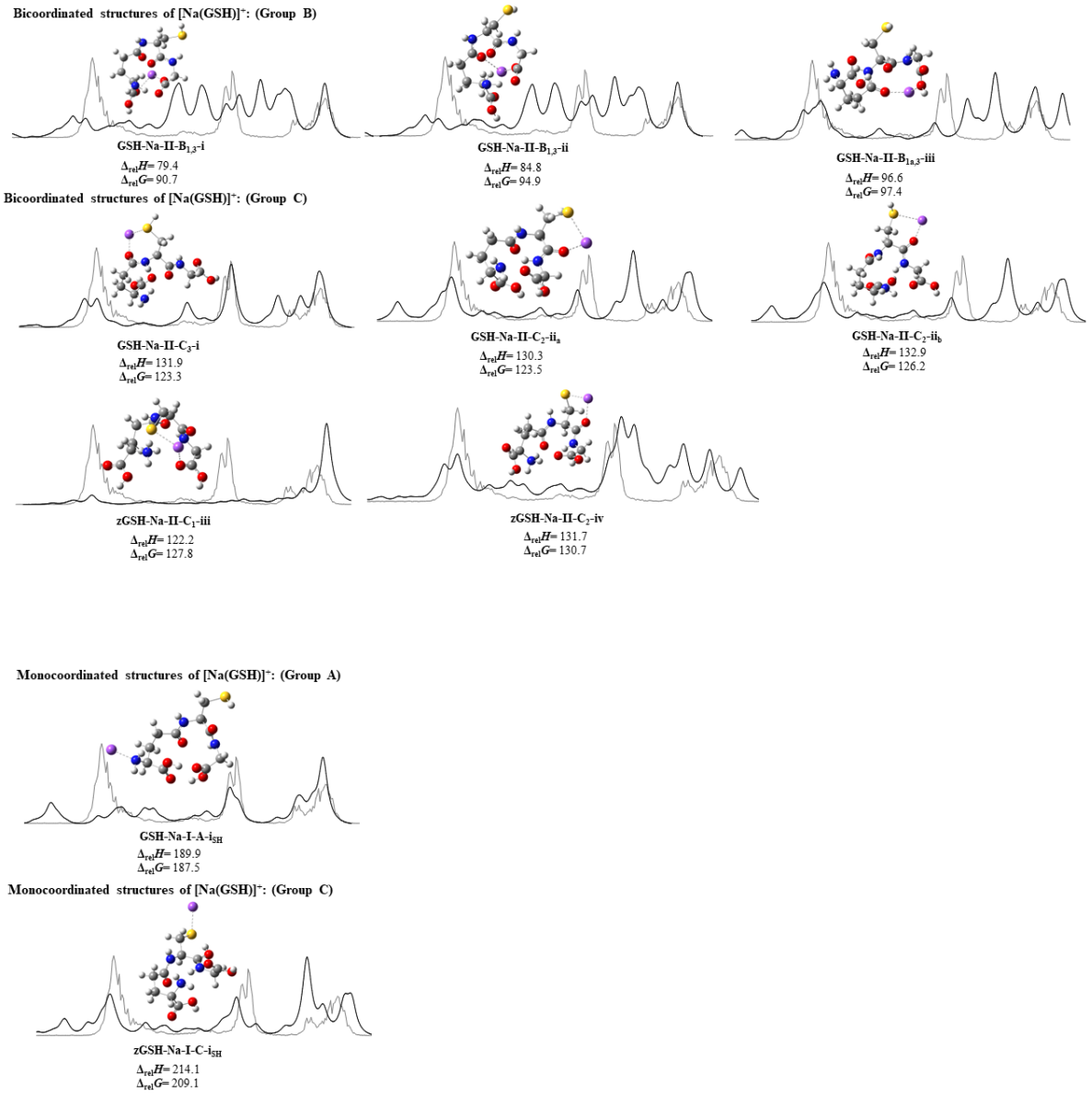

Figure S2. 8: Computed structures of $[K(GSH)]^+$.

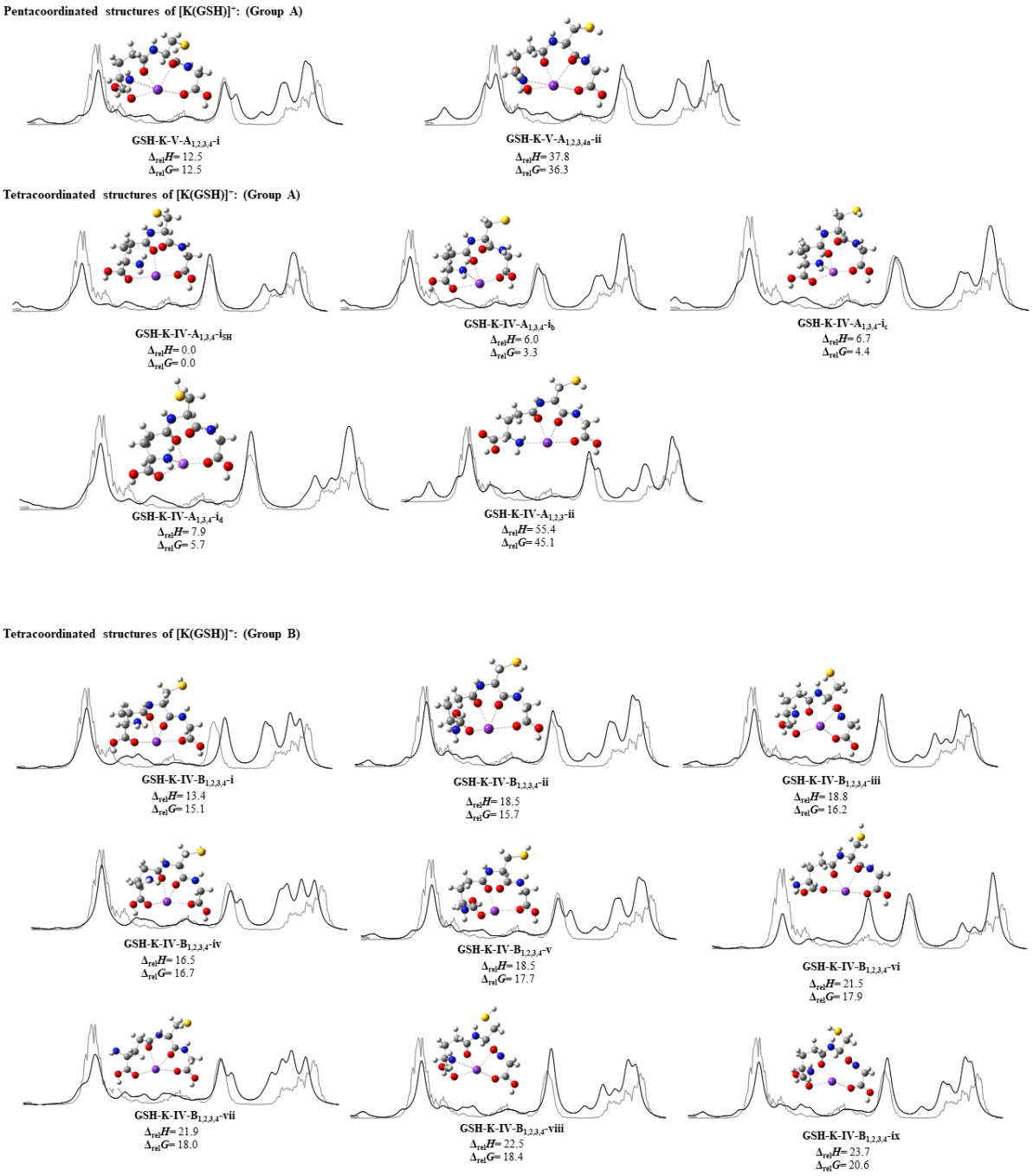

Figure S2.8: Computed structures of $[K(GSH)]^+$.

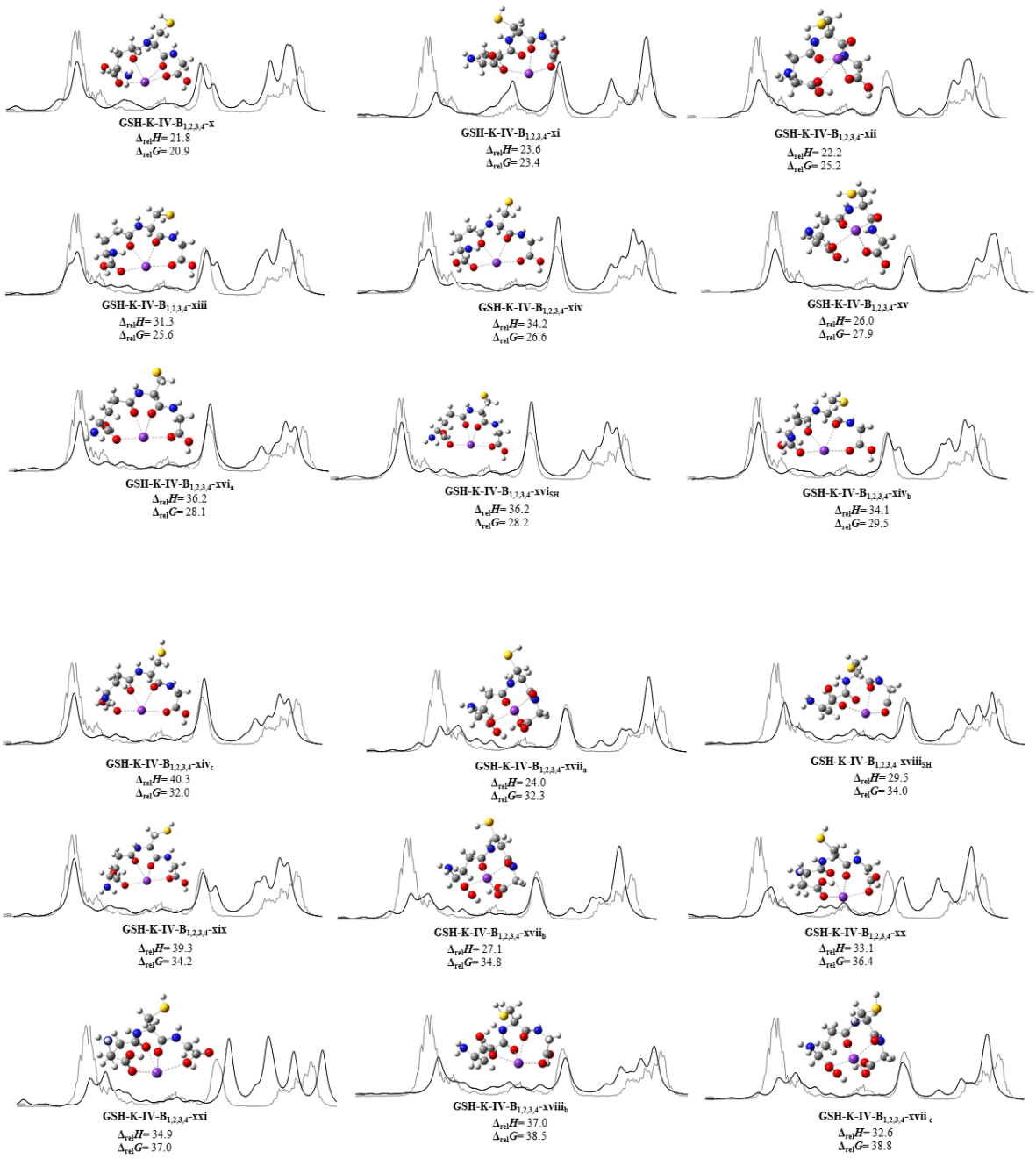

Figure S2.8: Computed structures of $[K(GSH)]^+$.

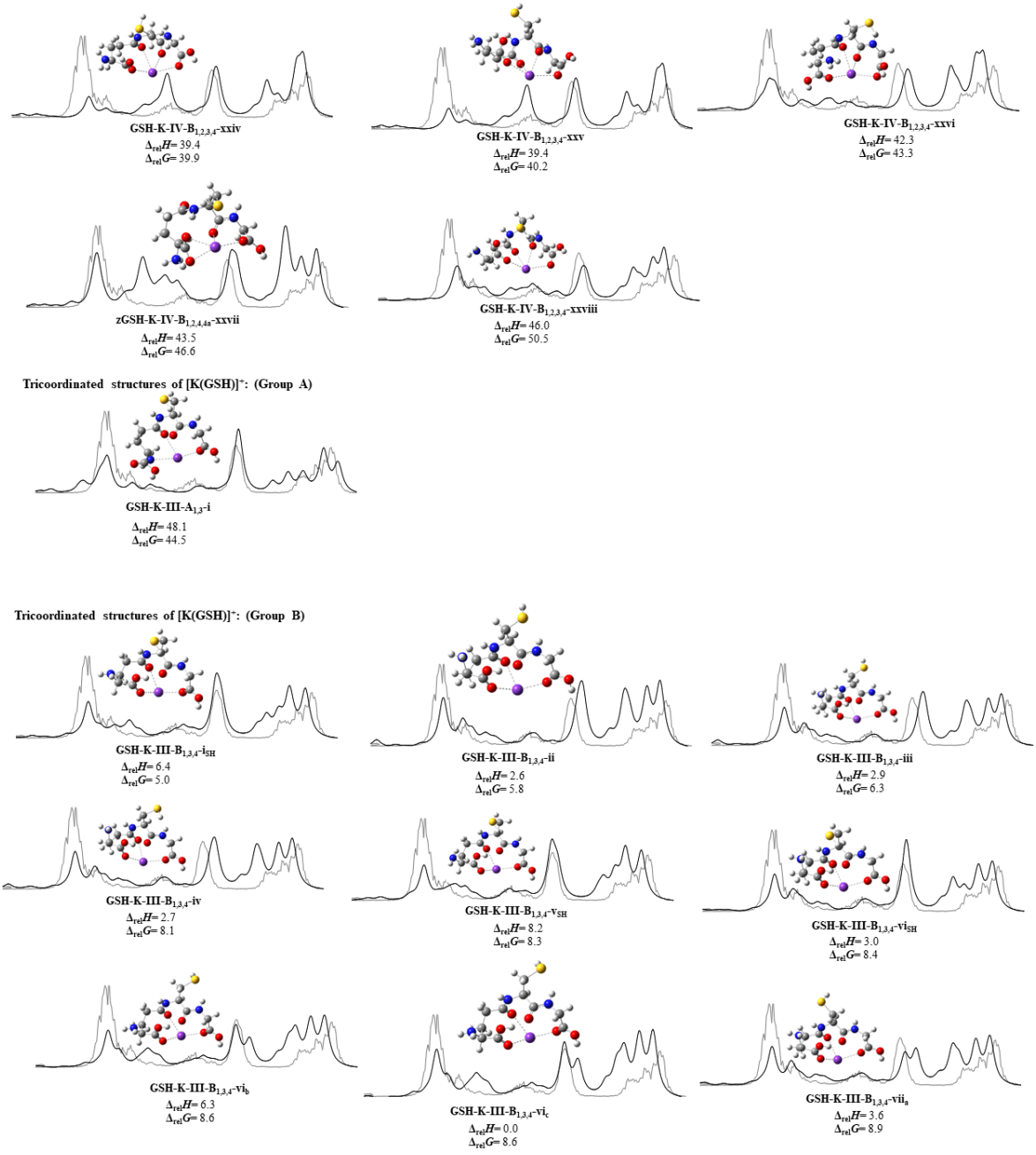

Figure S2.8: Computed structures of $[K(GSH)]^+$.

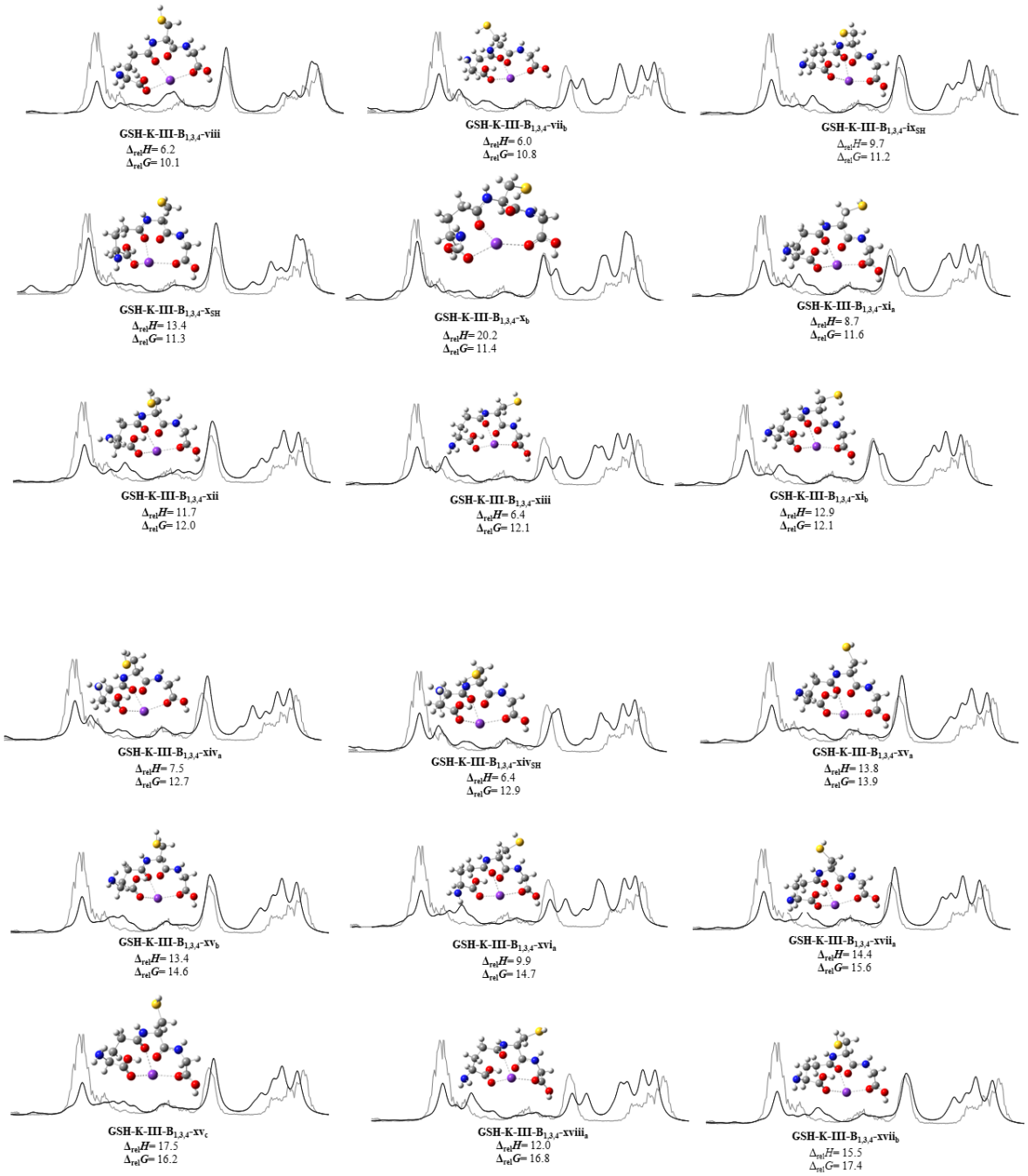

Figure S2.8: Computed structures of $[K(GSH)]^+$.

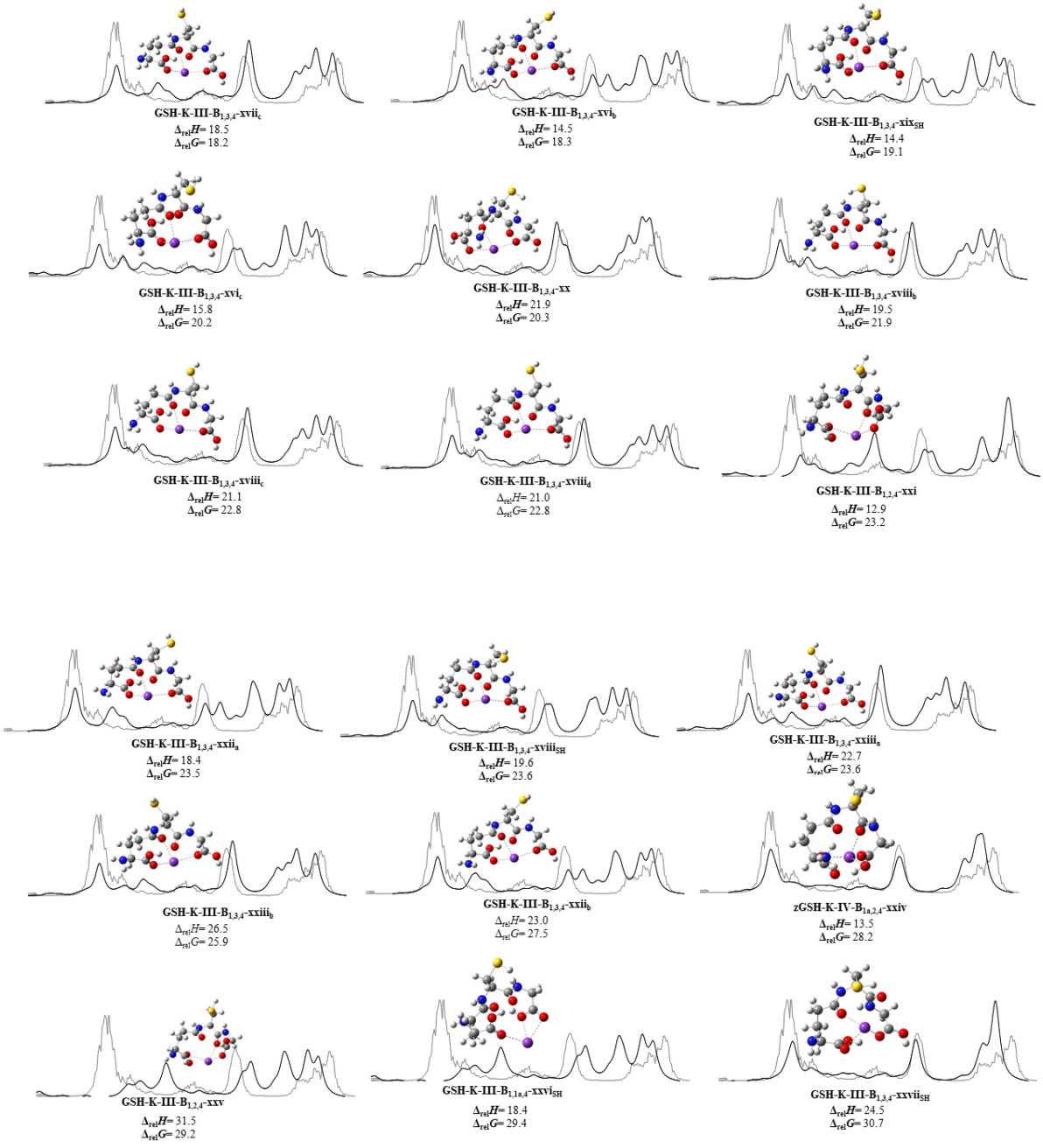

Figure S2.8: Computed structures of $[K(GSH)]^+$.

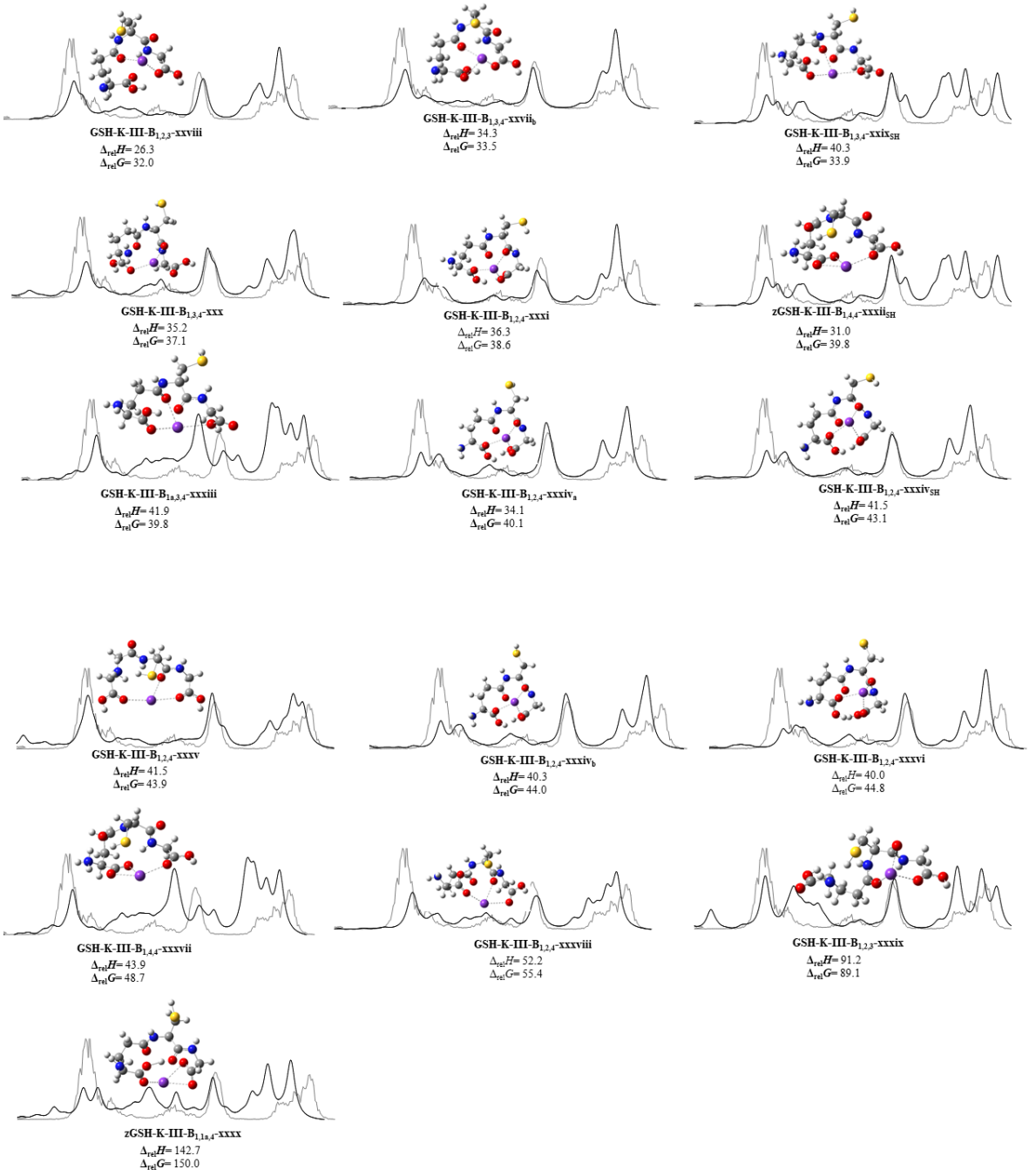

Figure S2.8: Computed structures of $[K(GSH)]^+$.

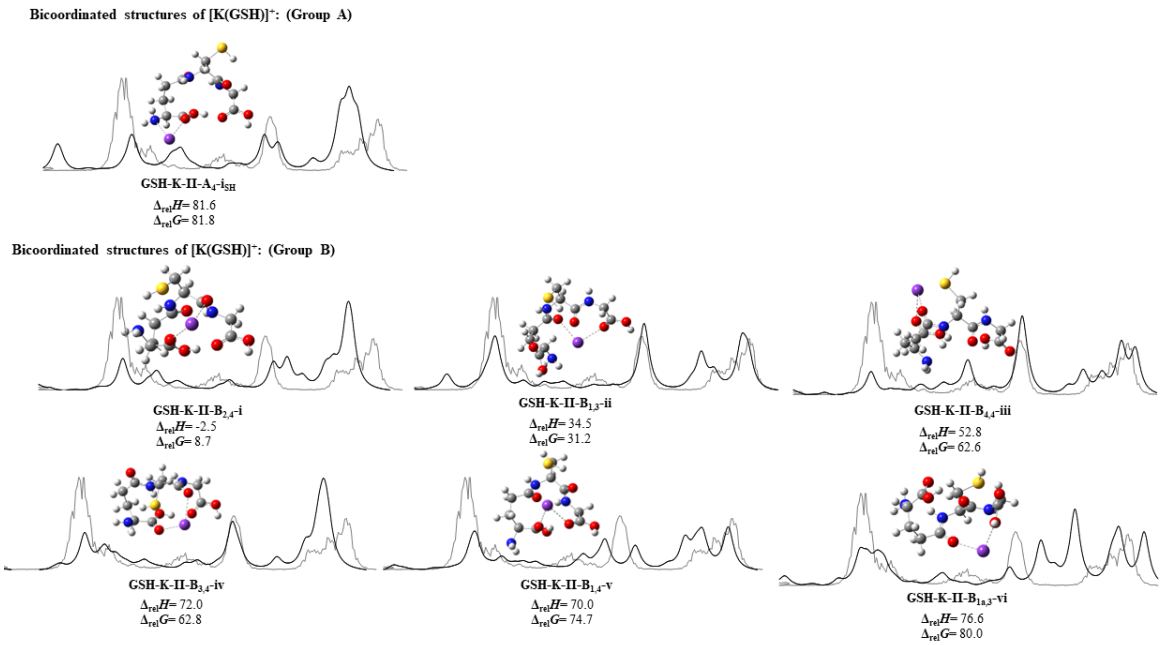

Figure S2.8: Computed structures of $[K(GSH)]^+$.

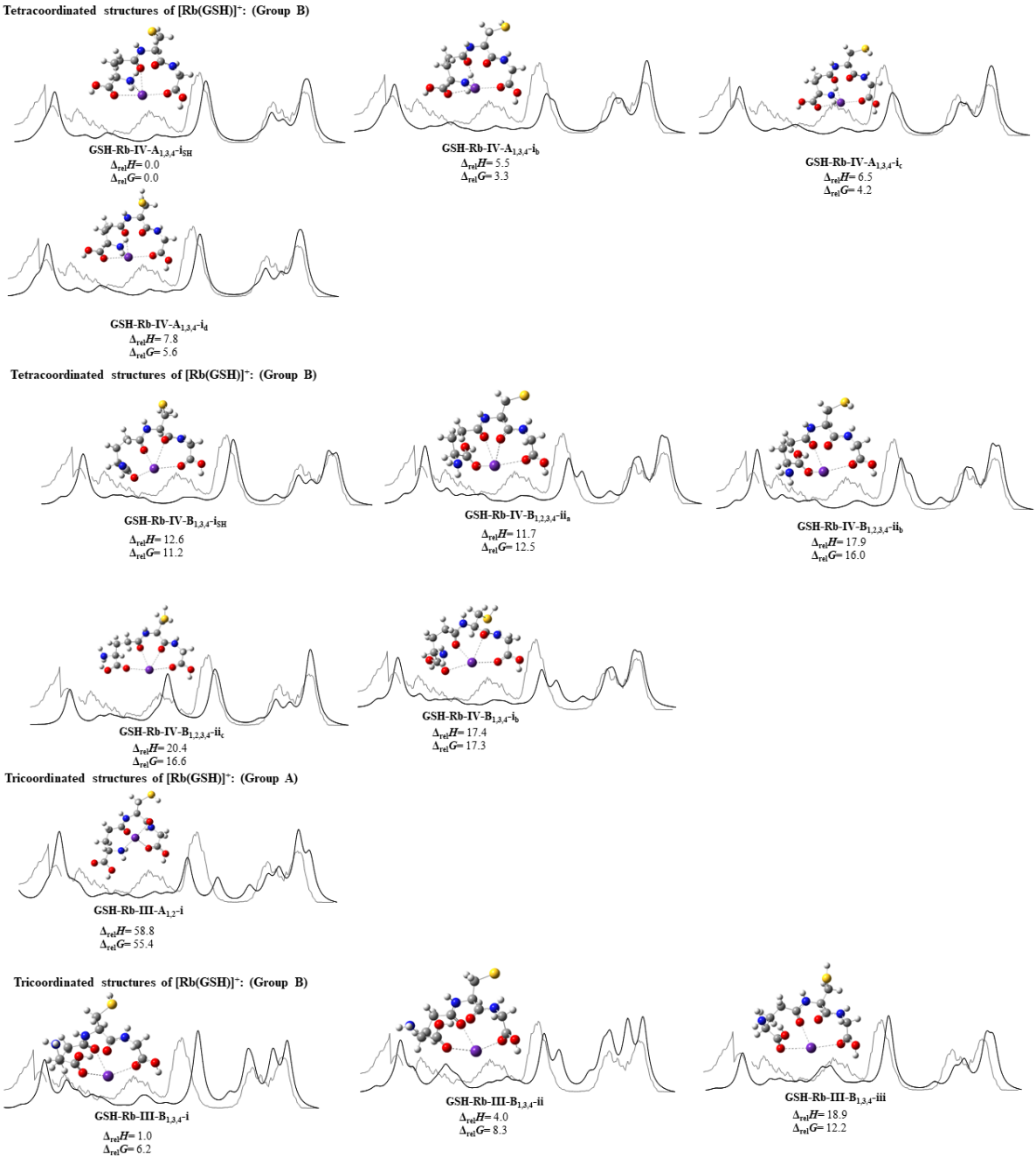

Figure S2. 9: Computed structures of $[Rb(GSH)]^+$.

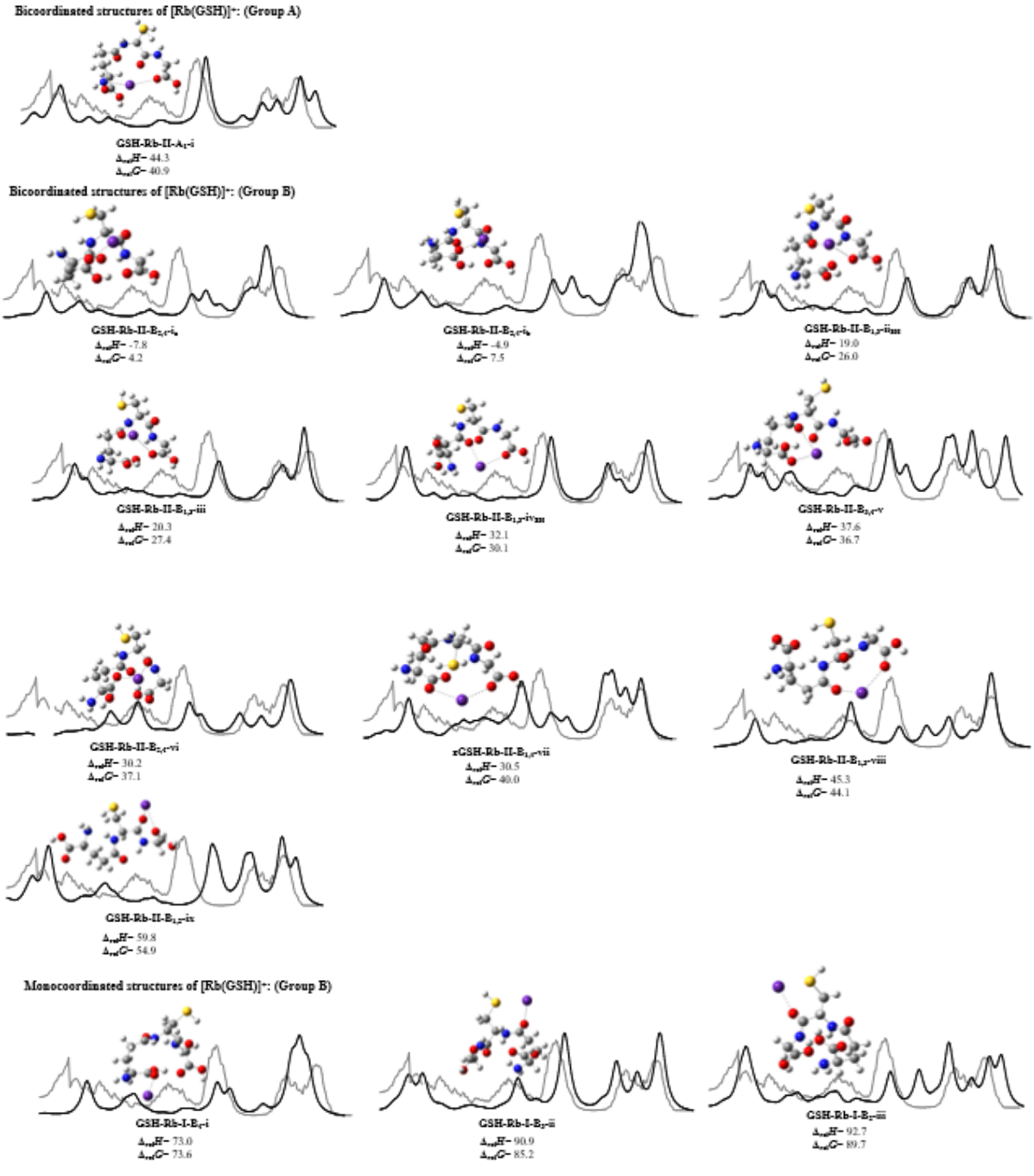

Figure S2.9: Computed structures of $[Rb(GSH)]^{+\cdot}$.

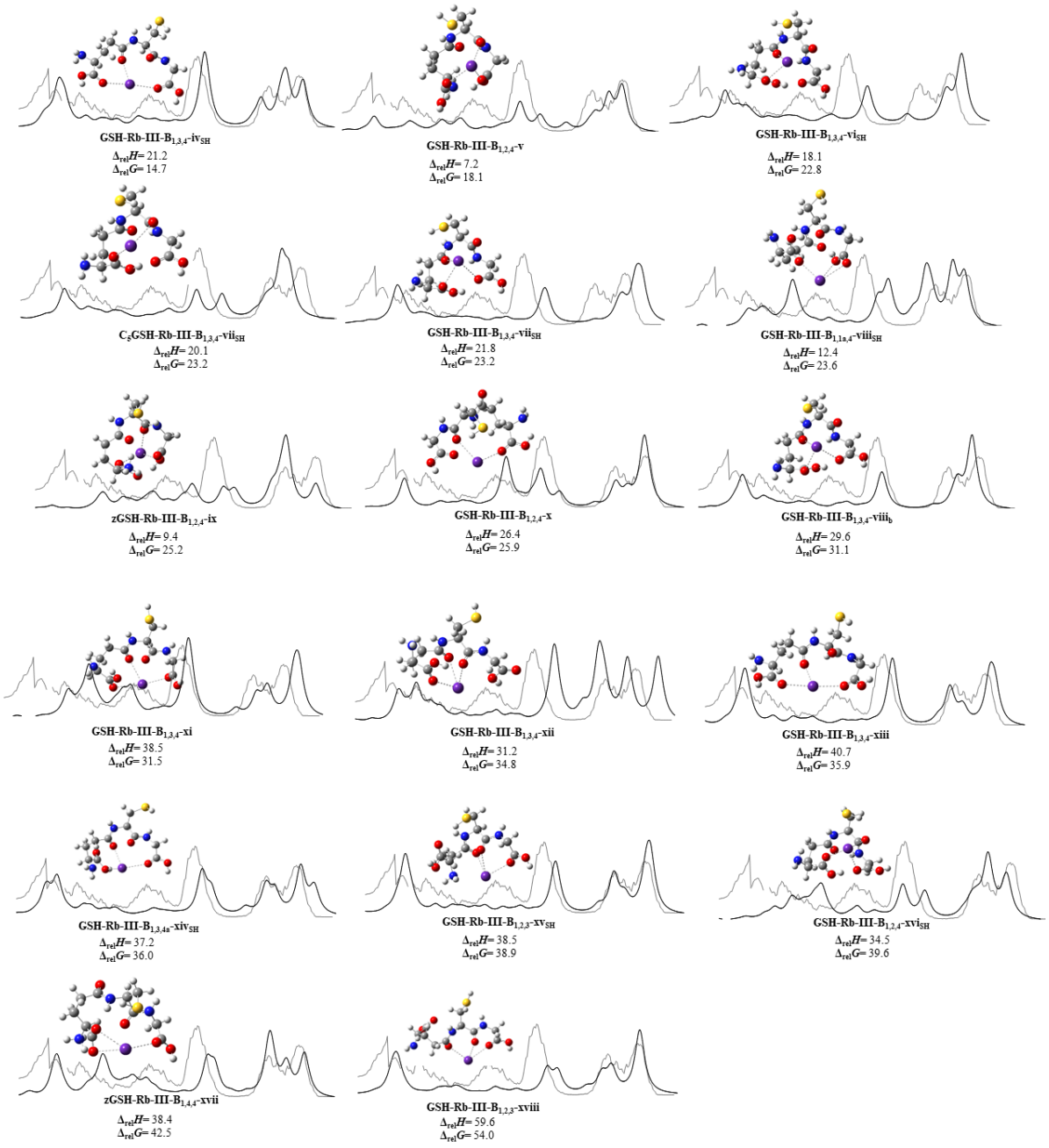

Figure S2.9: Computed structures of $[Rb(GSH)]^{+\cdot}$

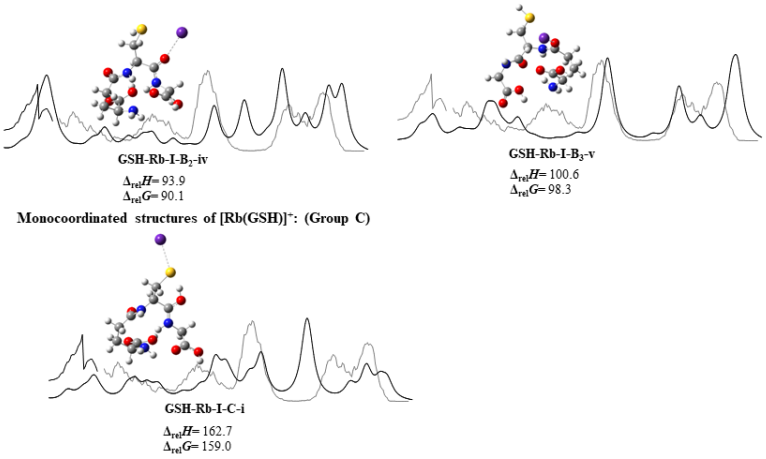

Figure S2.9: Computed structures of $[Rb(GSH)]^{+}$.

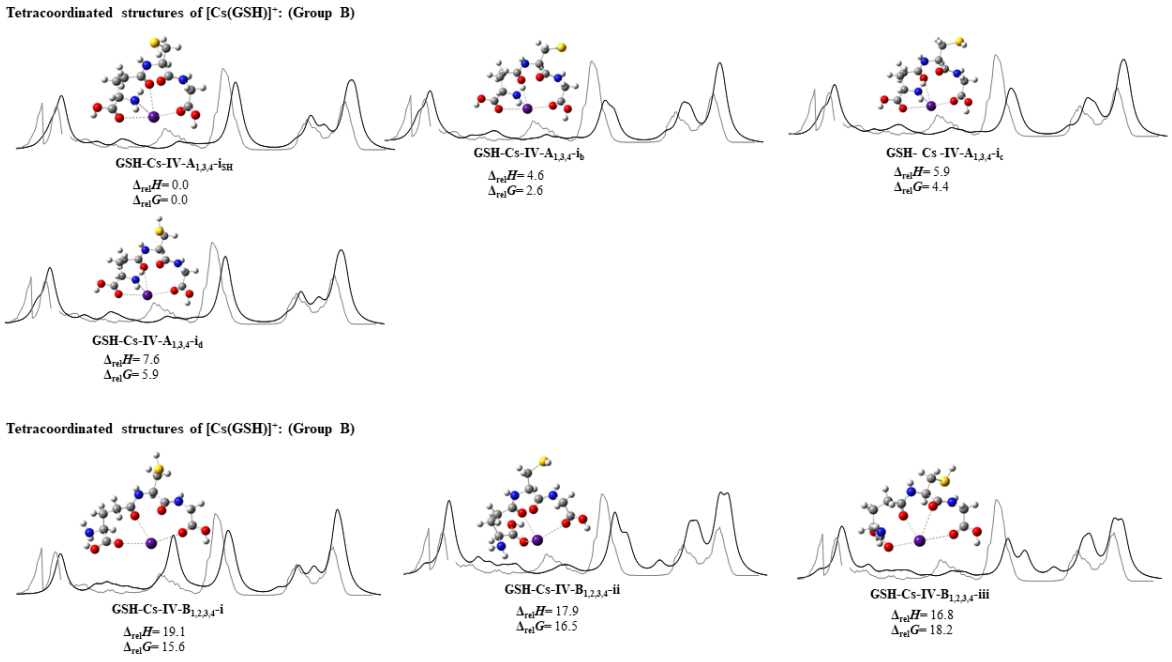

Figure S2. 10: Computed structures of $[Cs(GSH)]^{+}$.

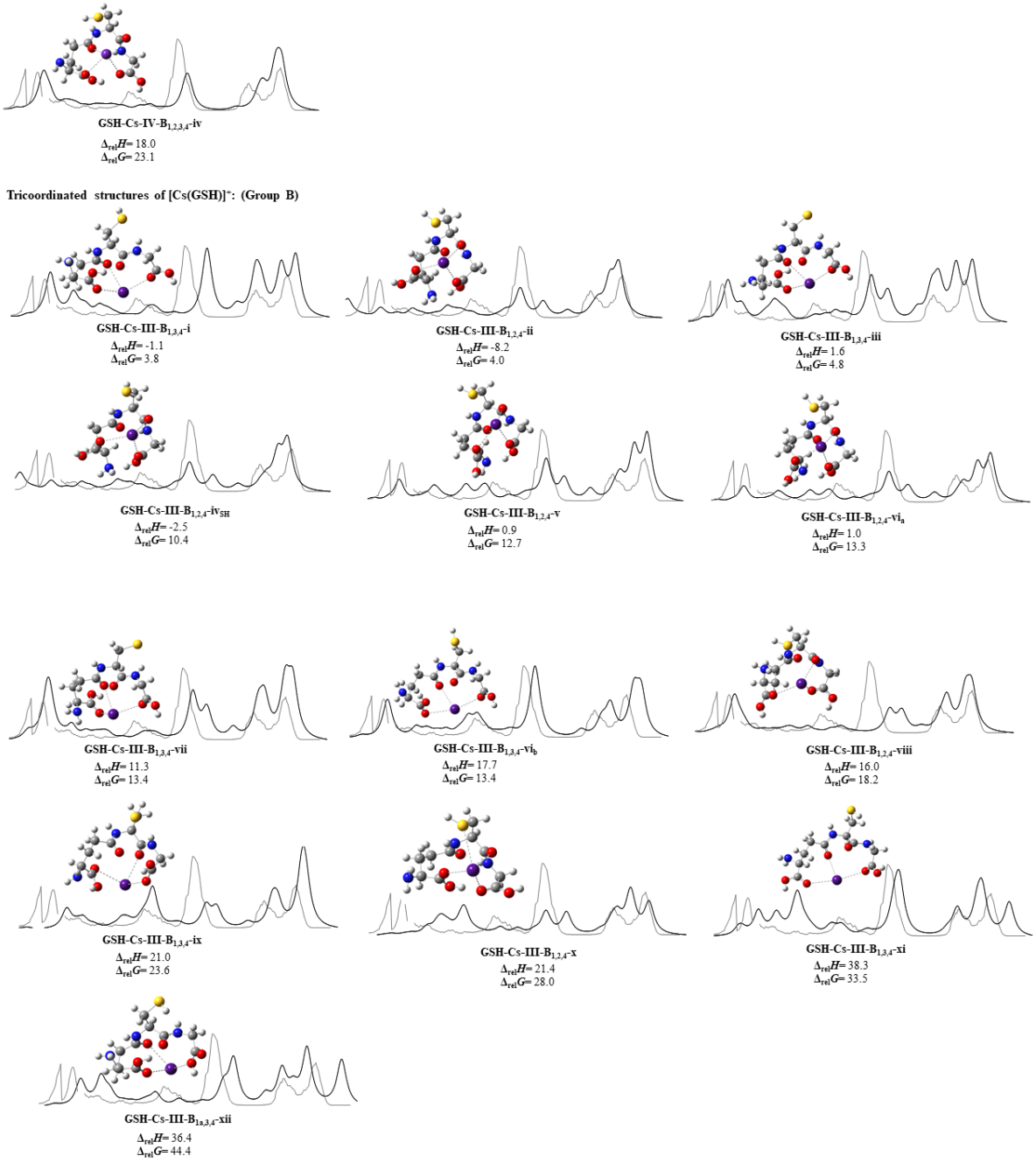

Figure S2.10: Computed structures of $[Cs(GSH)]^{+}$.

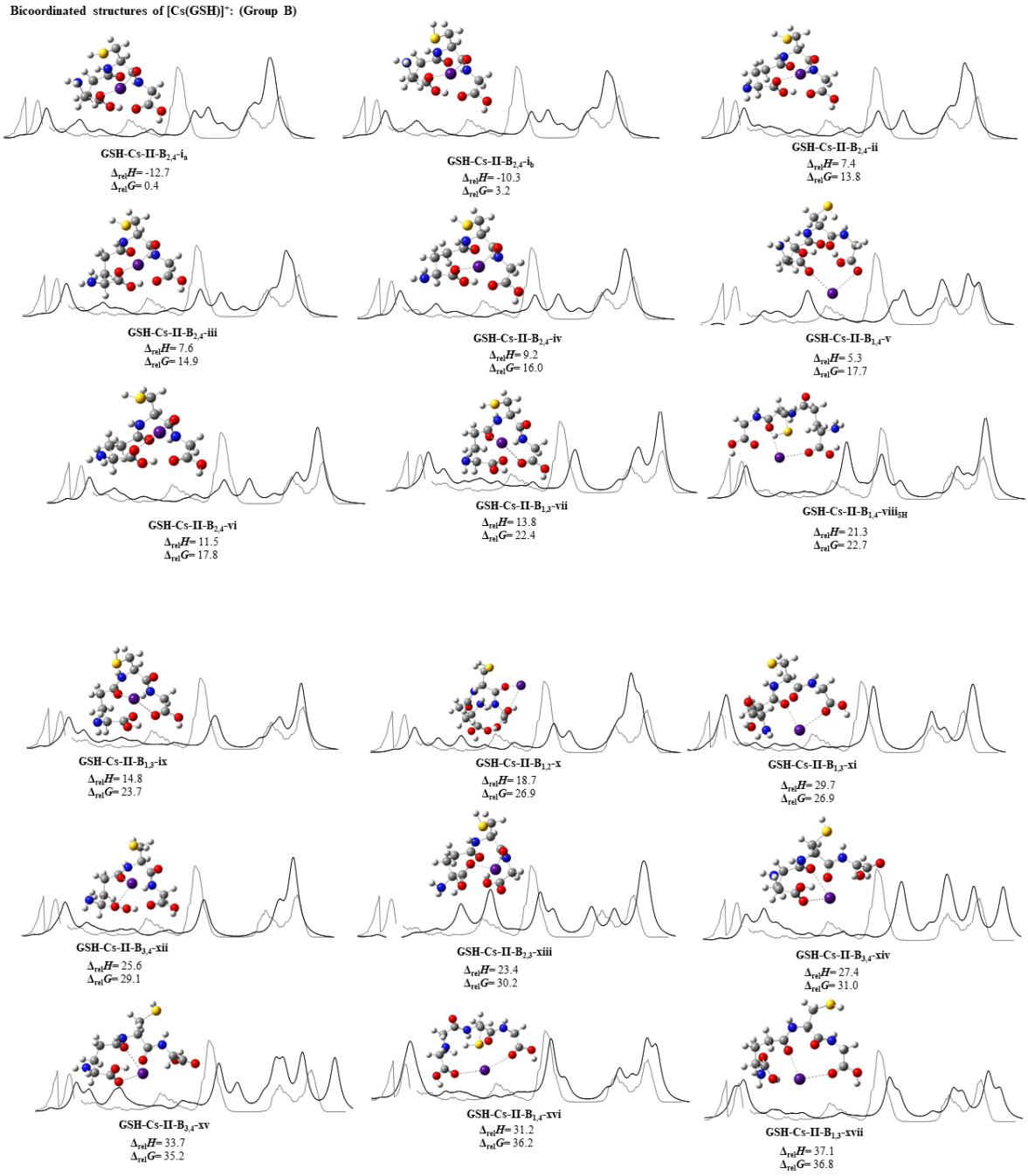

Figure S2.10: Computed structures of $[Cs(GSH)]^{+}$.

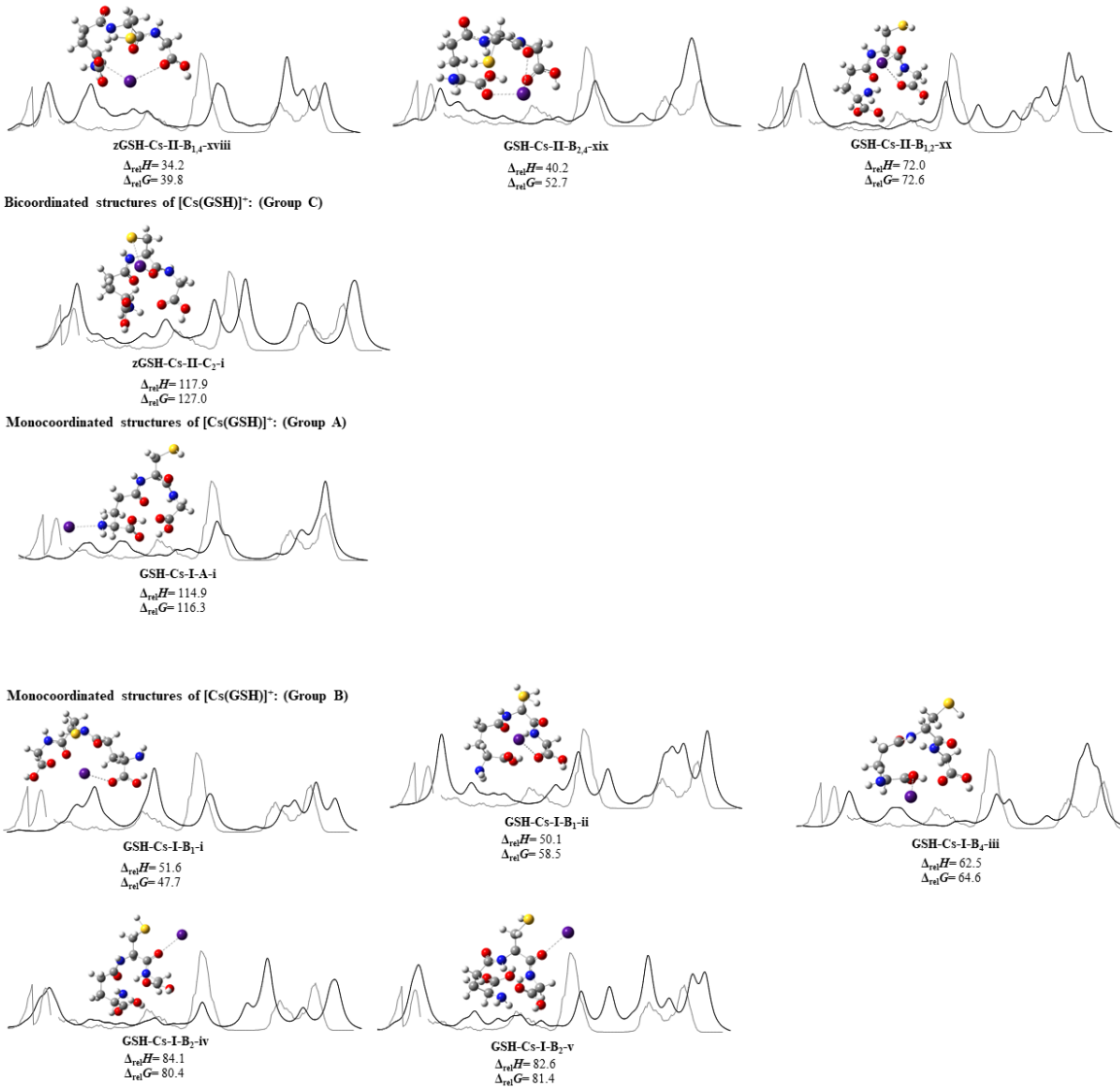

Figure S2.10: Computed structures of $[Cs(GSH)]^{+}$.

Table S2. 1: Relative standard 298 K enthalpies and Gibbs energies, in kJ mol-1, of $[Li(GSH)]^+$. Relative Gibbs energies are indicated in parentheses.

Structures of $[Li(GSH)]^+$	B3LYP/6-31+G(d,p) (For all atoms)	Single point: B3LYP/6-311+G(3df,3pd) (For all atoms)	CBS-QB3
GSH-Li-IV-$A_{1,3,4}$-i_{SH}	0.0 (0.0)	0.0 (0.0)	0.0 (0.0)
GSH-Li-IV-$A_{1,3,4}$-i_b	7.3 (4.4)	6.5 (3.6)	6.2 (3.6)
GSH-Li-IV-$A_{1,3,4}$-i_c	8.4 (4.6)	7.2 (3.5)	6.6 (3.7)
GSH-Li-IV-$A_{1,3,4}$-i_d	9.2 (7.4)	7.8 (5.9)	6.1 (4.8)
GSH-Li-IV-$A_{1,3,4}$-ii_{SH}	21.5 (16.9)	21.4 (17.6)	18.6 (14.6)
GSH-Li-III-$B_{1,3,4}$-i_{SH}	21.4 (20.5)	18.0 (17.1)	23.2 (21.3)
GSH-Li-IV-$A_{1,3,4}$-ii_b	28.3 (21.5)	27.6 (20.8)	25.1 (17.4)
GSH-Li-IV-$A_{1,3,4}$-ii_c	27.7 (22.2)	27.2 (21.7)	33.3 (24.9)
GSH-Li-III-$B_{1,3,4}$-i_b	25.6 (23.2)	22.0 (19.5)	26.1 (21.4)
GSH-Li-IV-$A_{1,3,4}$-ii_d	30.2 (23.9)	28.7 (22.5)	24.7 (19.2)
GSH-Li-III-$B_{1,3,4}$-ii_{SH}	23.2 (24.3)	22.8 (23.9)	24.3 (23.4)
GSH-Li-III-$B_{1,3,4}$-ii_b	23.5 (24.7)	22.8 (24.0)	23.8 (29.5)
GSH-Li-IV-$B_{1,2,3,4}$-i_a	32.7 (26.0)	29.7 (23.0)	
GSH-Li-IV-$B_{1,2,3,4}$-i_{SH}	32.6 (26.4)	29.5 (23.2)	
GSH-Li-III-$B_{1,3,4}$-iii_{SH}	30.3 (26.9)	26.9 (23.5)	
GSH-Li-IV-$B_{1,2,3,4}$-ii_a	32.6 (27.7)	30.6 (25.7)	
GSH-Li-IV-$B_{1,2,3,4}$-ii_b	34.4 (28.0)	30.9 (24.5)	
GSH-Li-IV-$A_{1,2,4}$-iii	32.9 (29.5)	33.7 (30.2)	
GSH-Li-III-$B_{1,3,4}$-iii_b	34.4 (29.8)	31.2 (26.6)	
GSH-Li-IV-$B_{1,2,3,4}$-iii_a	37.0 (31.1)	33.8 (27.9)	
GSH-Li-III-$B_{1,3,4}$-iii_c	37.6 (31.2)	33.9 (27.5)	
GSH-Li-III-$B_{1,3,4}$-iii_d	36.5 (31.6)	32.7 (27.8)	

Structures of $[Li(GSH)]^+$	B3LYP/6-31+G(d,p) (For all atoms)	Single point: B3LYP/6-311+G(3df,3pd) (For all atoms)
GSH-Li-IV-$B_{1,2,3,4}$-iv	35.2 (32.4)	31.8 (29.0)
GSH-Li-IV-$B_{1,2,3,4}$- iii_b	40.3 (33.3)	37.8 (30.8)
GSH-Li-IV-$B_{1,2,3,4}$-v_{SH}	39.7 (33.8)	37.6 (29.3)
GSH-Li-IV-$B_{1,2,3,4}$- iii_c	42.0 (34.4)	39.1 (31.6)
GSH-Li-IV-$A_{1,2,3}$-iv	45.2 (36.5)	46.0 (37.3)
GSH-Li-IV-$B_{1,2,3,4}$-vi_a	47.1 (37.4)	42.2 (32.5)
GSH-Li-IV-$B_{1,2,3,4}$-vi_{SH}	46.8 (37.6)	41.9 (32.7)
GSH-Li-IV-$B_{1,2,3,4}$-vi_c	46.4 (38.2)	43.0 (34.8)
GSH-Li-IV-$B_{1,2,3,4}$-vi_d	49.8 (39.5)	45.7 (35.4)
GSH-Li-IV-$B_{1,2,3,4}$-vii_a	45.1 (39.9)	40.8 (35.5)
GSH-Li-IV-$A_{1,3,4a}$-v	45.4 (40.6)	45.9 (41.1)
GSH-Li-IV-$B_{1,2,3,4}$-vi_e	52.0 (40.7)	47.4 (36.0)
GSH-Li-IV-$B_{1,2,3,4}$-vi_f	51.9 (41.8)	46.9 (36.8)
GSH-Li-IV-$B_{1,2,3,4}$-vii_b	47.8 (42.2)	44.1 (38.5)
GSH-Li-IV-$B_{1,2,3,4}$-vii_c	50.0 (43.0)	45.9 (38.9)
GSH-Li-III-$B_{1,3,4}$-iv_{SH}	49.6 (45.7)	43.0 (39.1)
GSH-Li-IV-$B_{1,2,3,4}$-viii	54.9 (46.3)	51.0 (42.4)
GSH-Li-III-$B_{1,3,4}$-v_{SH}	58.4 (50.6)	51.0 (43.1)
GSH-Li-IV-$C_{1,3,4}$-i	48.0 (51.3)	48.6 (51.8)
GSH-Li-IV-$C_{1,3,4}$-ii_{SH}	50.5 (51.5)	49.9 (50.9)
GSH-Li-III-$B_{1,3,4}$-vi	57.9 (54.1)	50.5 (46.7)
zGSH-Li-IV-$C_{1,4,4}$-iii	48.0 (54.8)	52.5 (59.3)
GSH-Li-IV-$B_{1,2,3,4}$-ix	56.8 (55.6)	55.8 (54.6)
GSH-Li-IV-$B_{1,2,3,4}$-x	59.3 (56.0)	57.4 (54.1)

Structures of $[Li(GSH)]^+$	B3LYP/6-31+G(d,p) (For all atoms)	Single point: B3LYP/6-311+G(3df,3pd) (For all atoms)
GSH-Li-III-$B_{1,2,4}$-vii_{SH}	50.4 (57.0)	49.7 (56.3)
GSH-Li-III-$B_{1,2,4}$-viii	62.5 (57.7)	58.2 (53.4)
GSH-Li-III-$B_{1,2,4}$-ix	53.8 (57.8)	53.6 (57.6)
GSH-Li-IV-$B_{1a,2,3,4}$-xi	65.9 (58.8)	65.6 (58.5)
zGSH-Li-III-$B_{1,2,4}$-x	68.6 (59.0)	67.3 (57.8)
GSH-Li-III-$B_{1,2,4}$-xi	63.7 (59.8)	63.3 (59.4)
GSH-Li-III-$B_{2,3,4}$-xii_a	63.8 (64.1)	65.8 (66.1)
GSH-Li-III-$C_{1,3}$-i_{SH}	62.1 (64.2)	60.5 (62.6)
GSH-Li-III-$A_{1,4}$-i_{SH}	68.1 (64.5)	68.1 (64.5)
GSH-Li-III-$B_{1a,3,4}$-xii_{SH}	67.4 (66.9)	70.3 (69.8)
GSH-Li-III-$A_{1,3}$-ii	67.7 (69.7)	65.5 (67.4)
GSH-Li-III-$A_{1,2}$-iii_{SH}	74.7 (71.5)	76.0 (72.8)
GSH-Li-III-$B_{1,2,4}$-xiii	78.8 (72.5)	73.9 (67.6)
GSH-Li-II-$B_{1,4}$-i	73.3 (74.4)	68.9 (70.1)
GSH-Li-III-$C_{1,4}$-ii	77.0 (75.6)	77.4 (76.0)
GSH-Li-II-$B_{1,4}$-ii	69.3 (76.9)	68.6 (76.2)
GSH-Li-III-$B_{1,3,4a}$-xiv_{SH}	84.7 (77.2)	81.5 (74.1)
zGSH-Li-II-$B_{3,4}$-iii	90.3 (94.8)	91.2 (95.7)
zGSH-Li-III-$C_{1,4}$-iii	93.2 (96.9)	97.0 (100.6)
zGSH-Li-III-$B_{1,1,4}$-xv_{SH}	100.5 (102.1)	103.4 (105.1)
GSH-Li-II-$B_{1,3}$-iv	107.1 (105.3)	109.6 (107.8)
GSH-Li-III-$C_{1,4}$-iv_{SH}	114.3 (112.3)	113.1 (111.1)
GSH-Li-II-A_4-i_{SH}	126.4 (123.3)	124.9 (121.8)
GSH-Li-II-C_3-i	156.1 (144.0)	148.6 (136.5)

Structures of $[Li(GSH)]^+$	B3LYP/6-31+G(d,p) (For all atoms)	Single point: B3LYP/6-311+G(3df,3pd) (For all atoms)
GSH-Li-II-C_2-ii	156.7 (147.5)	157.2 (148.6)
zGSH-Li-III-$B_{1,2,4}$-xx_{SH}	159.1 (165.7)	163.4 (169.9)
GSH-Li-II-C_3-iii	189.7 (175.0)	180.3 (165.7)
GSH-Li-I-A-i_{SH}	239.5 (232.9)	238.5 (231.9)

Table S2. 2: 298K relative enthalpies and Gibbs energies, in kJ mol-1, of $[Na(GSH)]^+$. Relative Gibbs energies are indicated in parentheses.

Structures of $[Na(GSH)]^+$	B3LYP/6-31+G(d,p) (For all atoms)	Single point: B3LYP/6-311+G(3df,3pd) (For all atoms)
GSH-Na-IV-$A_{1,3,4}$-i_{SH}	0.0 (0.0)	0.0 (0.0)
GSH-Na-IV-$A_{1,3,4}$-i_b	7.4 (4.4)	7.1 (4.1)
GSH-Na-IV-$A_{1,3,4}$-i_c	7.2 (4.8)	6.9 (4.5)
GSH-Na-IV-$A_{1,3,4}$-i_d	8.5 (6.5)	7.3 (5.4)
GSH-Na-IV-$A_{1,3,4}$-ii_{SH}	16.8 (15.6)	16.2 (14.9)
GSH-Na-III-$B_{1,3,4}$-i	12.9 (16.1)	13.5 (16.8)
GSH-Na-V-$A_{1,2,3,4}$-i_a	16.9 (17.0)	17.1 (17.1)
GSH-Na-V-$A_{1,2,3,4}$-i_b	16.9 (17.7)	14.3 (18.2)
GSH-Na-III-$B_{1,3,4}$-ii	16.9 (17.8)	15.9 (16.7)
GSH-Na–IV-$A_{1,3,4}$-iii	22.0 (19.8)	15.0 (15.8)
GSH-Na-V-$A_{1,2,3,4}$-i_c	22.1 (21.1)	21.3 (19.6)
GSH-Na-IV-$B_{1,2,3,4}$-i	27.2 (21.9)	21.6 (20.7)
GSH-Na–III-$B_{1,2,4}$-iii	15.1 (22.6)	23.9 (18.6)
GSH-Na–III-$B_{1,3,4}$-iv_a	25.0 (23.0)	23.7 (21.6)
GSH-Na–III-$B_{1,3,4}$-iv_{SH}	24.9 (23.2)	22.5 (20.9)
GSH-Na–III-$B_{1,3,4}$-v	19.1 (23.9)	20.2 (25.0)
GSH-Na-IV-$B_{1,2,3,4}$-ii	24.8 (24.2)	23.9 (23.3)
GSH-Na–III-$B_{1,3,4}$-vi	25.3 (24.2)	23.0 (22.0)
GSH-Na-IV-$B_{1,2,3,4}$-iii	27.4 (25.6)	18.5 (26.0)
GSH-Na-IV-$B_{1,2,3,4}$-iv_{SH}	30.9 (26.2)	24.6 (22.7)

Structures of $[Na(GSH)]^+$	-B3LYP/6-31+G(d,p) (For all atoms)	Single point: -B3LYP/6-311+G(3df,3pd) (For all atoms)
GSH-Na-III-$B_{1,2,4}$-vii	16.1 (26.6)	27.5 (22.8)
GSH-Na–III-$B_{1,3,4}$-iv_b	28.6 (26.7)	26.6 (24.7)
GSH-Na–III-$B_{1,3,4}$-iv_c	29.8 (27.6)	27.2 (25.1)
GSH-Na-IV-$B_{1,2,3,4}$-iv_a	32.9 (28.2)	29.1 (24.4)
GSH-Na-IV-$B_{1,2,3,4}$-v_{SH}	32.9 (28.4)	29.6 (25.1)
GSH-Na-IV-$B_{1,2,3,4}$-vi_a	31.2 (30.5)	29.1 (28.5)
GSH-Na-IV-$B_{1,2,3,4}$-vii	35.2 (31.2)	32.6 (28.5)
GSH-Na-IV-$B_{1,2,3,4}$-vi_{SH}	27.9 (31.5)	27.4 (31.0)
GSH-Na-IV-$A_{1,2,3}$-iv	41.4 (33.3)	18.3 (28.8)
GSH-Na-IV-$C_{1,3,4}$-i_{SH}	30.4 (35.3)	41.4 (33.3)
GSH-Na-IV-$A_{1,2,3}$-v_{SH}	40.9 (37.1)	31.7 (36.6)
GSH-Na-III-$B_{1,2,4}$-viii	28.9 (38.3)	41.8 (38.0)
GSH-Na-V-$A_{1,2,3,4a}$-ii	39.0 (38.6)	30.1 (39.5)
GSH-Na-III-$B_{1,2,4}$-ix	46.9 (41.6)	46.0 (45.6)
GSH-Na-IV-$B_{1,2,3,4}$-viii	50.4 (43.1)	44.6 (39.2)
zGSH-Na-IV-$C_{1,4,4}$-ii_{SH}	35.5 (44.3)	43.3 (36.0)
GSH-Na-III-$B_{1,3,4}$-x_{SH}	52.7 (46.5)	43.0 (40.2)
GSH-Na-IV-$B_{1a,2,3,4}$-ix	48.9 (47.8)	45.7 (39.5)
GSH-Na-IV-$C_{1,2,3}$-iii_{SH}	44.2 (48.9)	51.5 (50.5)
GSH-Na-IV-$A_{1,2,3}$-vi	53.7 (49.3)	44.2 (48.9)
GSH-Na-IV-$C_{1,2,3}$-iii	47.7 (51.6)	49.3 (53.5)
GSH-Na-III-$B_{1,1a,4}$-xi_{SH}	43.7 (52.6)	47.9 (51.7)

Structures of $[Na(GSH)]^+$	-B3LYP/6-31+G(d,p) (For all atoms)	Single point: -B3LYP/6-311+G(3df,3pd) (For all atoms)
GSH-Na-IV-$B_{1a,2,3,4}$-x	55.3 (54.1)	45.4 (54.2)
GSH-Na-III-$B_{1a,3,4}$-xi_{SH}	58.0 (59.7)	64.1 (60.5)
GSH-Na–IV-$A_{1,2,3}$-vii_{SH}	64.9 (65.4)	60.5 (62.2)
GSH-Na-III-$B_{1a,2,4}$-xii	61.0 (68.6)	61.7 (62.2)
GSH-Na-III-$C_{2,4}$-i_{SH}	73.2 (81.1)	70.8 (80.4)
GSH-Na-III-$B_{1,2,3}$-xiii	77.6 (85.0)	90.4 (88.6)
GSH-Na-IV-$B_{1,2,4,4}$-xi	85.8 (85.8)	76.3 (83.7)
GSH-Na-II-$B_{1,3}$-i	79.4 (90.7)	86.0 (85.9)
GSH-Na-III-$B_{1,2,4}$-xiv	92.9 (94.1)	82.3 (93.6)
GSH-Na-II-$B_{1,3}$-ii	84.8 (94.9)	93.5 (94.7)
GSH-Na-II-$B_{1a,3}$-iii	96.6 (97.4)	87.2 (97.2)
GSH-Na-II-A_4-i_{SH}	109.2 (108.2)	99.8 (100.6)
GSH-Na-II-C_3-i	131.9 (123.3)	109.6 (108.5)
GSH-Na-II-C_2-ii_a	130.3 (123.5)	127.7 (119.1)
GSH-Na-II-C_2-ii_b	132.9 (126.2)	131.7 (124.9)
zGSH-Na-II-C_1-iii	122.2 (127.8)	134.3 (127.6)
GSH-Na-II-C_2-iv	131.7 (130.7)	130.1 (135.7)
GSH-Na-I-A-i_{SH}	189.9 (187.5)	138.8 (137.9)
zGSH-Na-I-C-i_{SH}	214.1 (209.1)	190.7 (188.2)

Table S2. 3: 298K relative enthalpies and Gibbs energies, in kJ mol-1, of $K(GSH)]^+$. Relative Gibbs energies are indicated in parentheses.

Structures of $[K(GSH)]^+$	B3LYP/6-31+G(d,p) (For all atoms)	Single point: B3LYP/6-311+G(3df,3pd) (For all atoms)
GSH-K-IV-$A_{1,3,4}$-i_{SH}	0.0 (0.0)	0.0 (0.0)
GSH-K-IV-$A_{1,3,4}$-i_b	6.0 (3.3)	6.2 (3.5)
GSH-K-IV-$A_{1,3,4}$-i_c	6.7 (4.4)	6.8 (4.5)
GSH-K-III-$B_{1,3,4}$-i_{SH}	6.4 (5.0)	6.0 (4.6)
GSH-K-IV-$A_{1,3,4}$-i_d	7.9 (5.7)	7.0 (4.8)
GSH-K-III-$B_{1,3,4}$-ii	2.6 (5.8)	6.1 (9.3)
GSH-K-III-$B_{1,3,4}$-iii	2.9 (6.3)	6.2 (9.6)
GSH-K-III-$B_{1,3,4}$-iv	2.7 (8.1)	6.3 (11.7)
GSH-K-III-$B_{1,3,4}$-v_{SH}	8.2 (8.3)	7.1 (7.3)
GSH-K-III-$B_{1,3,4}$-vi_{SH}	3.0 (8.4)	5.7 (11.1)
GSH-K-III-$B_{1,3,4}$-vi_b	6.3 (8.6)	6.8 (9.1)
GSH-K-III-$B_{1,3,4}$-vi_c	0.0 (8.6)	5.2 (13.9)
GSH-K-II-$B_{2,4}$-i	-2.6 (8.7)	1.5 (12.8)
GSH-K-III-$B_{1,3,4}$-vii_a	3.6 (8.9)	6.3 (11.7)
GSH-K-III-$B_{1,3,4}$-viii	6.2 (10.1)	7.1 (11.0)
GSH-K-III-$B_{1,3,4}$-vii_b	6.0 (10.8)	8.9 (13.8)
GSH-K-III-$B_{1,3,4}$-ix_{SH}	9.7 (11.2)	9.1 (10.5)
GSH-K-III-$B_{1,3,4}$-x_{SH}	13.4 (11.3)	14.0 (11.9)
GSH-K-III-$B_{1,3,4}$-x_b	20.2 (11.4)	20.2 (11.4)
GSH-K-III-$B_{1,3,4}$-xi_a	8.7 (11.6)	8.8 (11.8)

Structures of $[K(GSH)]^+$	B3LYP/6-31+G(d,p) (For all atoms)	Single point: B3LYP/6-311+G(3df,3pd) (For all atoms)
GSH-K-III-$B_{1,3,4}$-xii	11.7 (12.0)	11.0 (11.3)
GSH-K-III-$B_{1,3,4}$-xiii	6.4 (12.1)	6.7 (12.3)
GSH-K-III-$B_{1,3,4}$-xi_b	12.9 (12.1)	12.3 (11.5)
GSH-K-V-$A_{1,2,3,4}$-i	12.5 (12.5)	14.2 (14.2)
GSH-K-III-$B_{1,3,4}$-xiv_a	7.5 (12.7)	10.0 (15.3)
GSH-K-III-$B_{1,3,4}$-xiv_{SH}	6.4 (12.9)	10.2 (16.7)
GSH-K-III-$B_{1,3,4}$-xv_a	13.8 (13.9)	12.4 (12.5)
GSH-K-III-$B_{1,3,4}$-xv_b	13.4 (14.6)	12.3 (13.5)
GSH-K-III-$B_{1,3,4}$-xvi_a	9.9 (14.7)	10.7 (15.5)
GSH-K-IV-$B_{1,2,3,4}$-i	13.4 (15.1)	15.8 (17.5)
GSH-K-III-$B_{1,3,4}$-$xvii_a$	14.4 (15.6)	13.4 (14.6)
GSH-K-IV-$B_{1,2,3,4}$-ii	18.5 (15.7)	19.4 (16.6)
GSH-K-IV-$B_{1,2,3,4}$-iii	18.8 (16.2)	18.7 (16.2)
GSH-K-III-$B_{1,3,4}$-xv_c	17.5 (16.2)	16.4 (15.1)
GSH-K-IV-$B_{1,2,3,4}$-iv	16.5 (16.7)	18.5 (18.7)
C_{17}GSH-K-III-$B_{1,3,4}$-$xviii_a$	12.0 (16.8)	12.0 (16.8)
GSH-K-III-$B_{1,3,4}$-$xvii_b$	15.5 (17.4)	14.6 (16.5)
GSH-K-IV-$B_{1,2,3,4}$-v	18.5 (17.7)	19.8 (19.0)
GSH-K-IV-$B_{1,2,3,4}$-vi	21.5 (17.9)	21.0 (17.4)
GSH-K-IV-$B_{1,2,3,4}$-vii	21.9 (18.0)	22.1 (18.3)
GSH-K-III-$B_{1,3,4}$-$xvii_c$	18.5 (18.2)	17.7 (17.4)

Structures of $[K(GSH)]^+$	B3LYP/6-31+G(d,p) (For all atoms)	Single point: B3LYP/6-311+G(3df,3pd) (For all atoms)
GSH-K-III-$B_{1,3,4}$-xvi$_b$	14.5 (18.3)	15.1 (18.9)
GSH-K-IV-$B_{1,2,3,4}$-viii	22.5 (18.4)	22.8 (18.7)
GSH-K-III-$B_{1,3,4}$-xix$_{SH}$	14.4 (19.1)	16.8 (21.5)
GSH-K-III-$B_{1,3,4}$-xvi$_c$	15.8 (20.2)	16.2 (20.6)
GSH-K-III-$B_{1,3,4}$-xx	21.9 (20.3)	23.5 (21.9)
GSH-K-IV-$B_{1,2,3,4}$-ix	23.7 (20.6)	24.4 (21.2)
GSH-K-IV-$B_{1,2,3,4}$-x	21.8 (20.9)	22.7 (21.8)
GSH-K-III-$B_{1,3,4}$-xviii$_b$	19.5 (21.9)	19.3 (21.7)
GSH-K-III-$B_{1,3,4}$-xviii$_c$	21.1 (22.8)	19.7 (21.4)
GSH-K-III-$B_{1,3,4}$-xviii$_d$	21.0 (22.8)	19.7 (21.4)
GSH-K-III-$B_{1,2,4}$-xxi	12.9 (23.2)	17.0 (27.3)
GSH-K-IV-$B_{1,2,3,4}$-xi	23.6 (23.4)	23.6 (23.4)
GSH-K-III-$B_{1,3,4}$-xxii$_a$	18.4 (23.5)	18.2 (23.3)
GSH-K-III-$B_{1,3,4}$-xviii$_{SH}$	19.6 (23.6)	20.7 (24.7)
GSH-K-III-$B_{1,3,4}$-xxiii$_a$	22.7 (23.6)	20.9 (21.8)
GSH-K-IV-$B_{1,2,3,4}$-xii	22.2 (25.2)	24.8 (27.8)
GSH-K-IV-$B_{1,2,3,4}$-xiii	31.3 (25.6)	30.5 (24.8)
GSH-K-III-$B_{1,3,4}$-xxiii$_b$	26.5 (25.9)	25.0 (24.5)
GSH-K-IV-$B_{1,2,3,4}$-xiv	34.2 (26.6)	32.3 (24.8)
GSH-K-III-$B_{1,3,4}$-xxii$_b$	23.0 (27.5)	22.6 (27.2)
GSH-K-IV-$B_{1,2,3,4}$-xv	26.0 (27.9)	28.5 (30.4)

Structures of $[K(GSH)]^+$	B3LYP/6-31+G(d,p) (For all atoms)	Single point: B3LYP/6-311+G(3df,3pd) (For all atoms)
GSH-K-IV-$B_{1,2,3,4}$-xvi$_a$	36.2 (28.1)	34.5 (26.4)
zGSH-K-III-$B_{1a,2,4}$-xxiv	13.5 (28.2)	19.9 (34.7)
GSH-K-IV-$B_{1,2,3,4}$-xvi$_{SH}$	36.2 (28.2)	34.5 (26.5)
GSH-K-III-$B_{1,2,4}$-xxv	31.5 (29.2)	32.0 (29.6)
GSH-K-III-$B_{1,1a,4}$-xxvi$_{SH}$	18.4 (29.4)	23.0 (34.0)
GSH-K-IV-$B_{1,2,3,4}$-xiv$_b$	34.1 (29.5)	33.6 (29.0)
GSH-K-III-$B_{1,2,3}$-xxvii$_{SH}$	24.5 (30.7)	27.2 (33.4)
GSH-K-II- $B_{1,3}$-ii	34.5 (31.2)	36.1 (32.8)
GSH-K-III-$B_{1,2,3}$-xxviii	26.3 (32.0)	29.2 (35.0)
GSH-K-IV-$B_{1,2,3,4}$-xiv$_c$	40.3 (32.0)	38.7 (30.4)
GSH-K-IV-$B_{1,2,3,4}$-xvii$_a$	24.0 (32.3)	27.5 (35.9)
GSH-K-III-$B_{1,3,4}$-xxvii$_b$	34.3 (33.5)	35.9 (35.2)
GSH-K-III-$B_{1,3,4}$-xxix$_{SH}$	40.3 (33.9)	36.7 (30.4)
GSH-K-IV-$B_{1,2,3,4}$-xviii$_{SH}$	29.5 (34.0)	32.0 (36.4)
GSH-K-IV-$B_{1,2,3,4}$-xix	39.3 (34.2)	38.5 (33.4)
GSH-K-IV-$B_{1,2,3,4}$-xvii$_b$	27.1 (34.8)	30.3 (38.0)
GSH-K-V-$A_{1,2,3,4a}$-ii	37.8 (36.3)	39.4 (37.9)
GSH-K-IV-$B_{1,2,3,4}$-xx	33.1 (36.4)	35.6 (38.9)
GSH-K-IV-$B_{1,2,3,4}$-xxi	34.9 (37.0)	40.1 (42.2)
GSH-K-III-$B_{1,2,4}$-xxx	35.2 (37.1)	35.0 (36.8)
GSH-K-IV-$B_{1,2,3,4}$-xxiii$_b$	37.0 (38.5)	37.1 (38.6)

Structures of $[K(GSH)]^+$	B3LYP/6-31+G(d,p) (For all atoms)	Single point: B3LYP/6-311+G(3df,3pd) (For all atoms)
GSH-K-III-$B_{1,2,4}$-xxxi	36.3 (38.6)	35.7 (38.0)
GSH-K-IV-$B_{1,2,3,4}$-xvii$_c$	32.6 (38.8)	34.9 (41.1)
GSH-K-III-$B_{1a,3,4}$-xxxiii	41.9 (39.8)	44.3 (42.3)
zGSH-K-III-$B_{1,4,4}$-xxxii$_{SH}$	31.0 (39.8)	38.3 (47.1)
GSH-K-IV-$B_{1,2,3,4}$-xxiv	39.4 (39.9)	39.0 (39.5)
GSH-K-III-$B_{1,2,4}$-xxxiv$_a$	34.1 (40.1)	34.9 (40.9)
GSH-K-IV-$B_{1,2,3,4}$-xxv	39.4 (40.2)	39.0 (39.7)
GSH-K-III-$B_{1,2,4}$-xxxiv$_{SH}$	41.5 (43.1)	41.9 (43.5)
GSH-K-IV-$B_{1,2,3,4}$-xxvi	42.3 (43.3)	43.9 (45.0)
GSH-K-III-$B_{1,2,4}$-xxxv	41.5 (43.9)	45.3 (47.7)
GSH-K-III-$B_{1,2,4}$-xxxiv$_b$	40.3 (44.0)	41.2 (44.9)
GSH-K-III-$A_{1,3}$-i	48.1 (44.5)	50.0 (46.4)
GSH-K-III-$B_{1,2,4}$-xxxvi	40.0 (44.8)	40.4 (45.2)
GSH-K-IV-$A_{1,2,3}$-ii	55.4 (45.1)	56.5 (46.3)
zGSH-K-IV-$B_{1,2,4,4a}$-xxvii	43.5 (46.6)	48.9 (52.1)
GSH-K-III-$B_{1,1a,4}$-xxxvii	43.9 (48.7)	48.5 (53.3)
GSH-K-IV-$B_{1,2,3,4}$-xxviii	46.0 (50.5)	47.9 (52.4)
GSH-K-III-$B_{1,2,4}$-xxxviii	52.2 (55.4)	51.8 (55.0)
GSH-K-II-$B_{4,4}$-iii	52.8 (62.6)	57.1 (67.0)
GSH-K-II- $B_{2,4}$-iv	72.0 (62.8)	73.0 (63.8)
GSH-K-II-$B_{1,4}$-iv	70.0 (74.7)	73.1 (77.7)

Structures of $[K(GSH)]^+$	B3LYP/6-31+G(d,p) (For all atoms)	Single point: B3LYP/6-311+G(3df,3pd) (For all atoms)
GSH-K-II-$B_{1a,3}$-v	76.6 (80.0)	81.5 (84.9)
GSH-K-II-A_4-i_{SH}	81.6 (81.8)	83.4 (83.7)
GSH-K-III-$B_{1,2,3}$-xxxix	91.2 (89.1)	90.6 (88.6)
GSH-K-I-B_2-i	101.2 (97.2)	105.0 (101.1)
zGSH-K-III-$B_{1,1a,4}$-xxxx	142.7 (150.0)	147.8 (155.1)

Table S2. 4: 298K relative enthalpies and Gibbs energies, in kJ mol-1, of $[Rb(GSH)]^+$. Relative Gibbs energies are indicated in parentheses.

Structures of $[Rb(GSH)]^+$	**-B3LYP/6-31+G(d,p)/ (For C, H,N,O,S atoms) -B3LYP/Def2SVP (Rb)**	**Single point: -B3LYP/6-311+G(3df,3pd) (For C, H,N,O,S atoms) -B3LYP/Def2TZVP (Rb)**
GSH-Rb-IV-$A_{1,3,4}$-i_{SH}	0.0 (0.0)	0.0 (0.0)
GSH-Rb-IV-$A_{1,3,4}$-i_b	5.5 (3.3)	5.8 (3.5)
GSH-Rb-IV-$A_{1,3,4}$-i_c	6.5 (4.2)	6.6 (4.3)
GSH-Rb-II-$B_{2,4}$-i_a	-7.8 (4.2)	-4.1 (7.9)
GSH-Rb-IV-$A_{1,3,4}$-i_d	7.8 (5.6)	7.0 (4.8)
GSH-Rb-III-$B_{1,3,4}$-i	1.0 (6.2)	3.9 (9.1)
GSH-Rb-II-$B_{2,4}$-i_b	-4.9 (7.5)	-0.9 (11.4)
GSH-Rb-III-$B_{1,3,4}$-ii	4.0 (8.3)	4.4 (8.6)
GSH-Rb-IV-$B_{1,3,4}$-i_{SH}	12.6 (11.2)	11.9 (10.5)
GSH-Rb-III-$B_{1,3,4}$-iii	18.9 (12.2)	17.9 (11.2)
GSH-Rb-IV-$B_{1,2,3,4}$-ii_a	11.7 (12.5)	12.1 (12.9)
GSH-Rb-III-$B_{1,3,4}$-iv_{SH}	21.2 (14.7)	19.7 (13.1)
GSH-Rb-IV-$B_{1,2,3,4}$-ii_b	17.9 (16.0)	17.5 (15.6)
GSH-Rb-IV-$B_{1,2,3,4}$-ii_c	20.4 (16.6)	19.0 (15.2)
GSH-Rb-IV-$B_{1,3,4}$-i_b	17.4 (17.3)	17.4 (17.3)
GSH-Rb-III-$B_{1,2,4}$-v	7.2 (18.1)	10.5 (21.4)
GSH-Rb-III-$B_{1,3,4}$-vi_{SH}	18.1 (22.8)	18.9 (22.1)
GSH-Rb-III-$B_{1,3,4}$-vii_{SH}	20.1 (23.2)	20.2 (23.2)
GSH-Rb-III-$B_{1,3,4}$-vii_{SH}	21.8 (23.2)	23.0 (24.2)
GSH-Rb-III-$B_{1,1a,4}$-$viii_{SH}$	12.4 (23.6)	16.0 (27.3)

Structures of $[Rb(GSH)]^+$	-B3LYP/6-31+G(d,p)/ (For C, H,N,O,S atoms) -B3LYP/Def2SVP (Rb)	Single point: -B3LYP/6-311+G(3df,3pd) (For C, H,N,O,S atoms) -B3LYP/Def2TZVP (Rb)
zGSH-Rb-III-$B_{1,2,4}$-ix	9.4 (25.2)	15.5 (31.4)
GSH-Rb-III-$B_{1,2,4}$-x	26.4 (25.9)	25.6 (25.0)
GSH-Rb-II-$B_{1,3}$-ii_{SH}	19.0 (26.0)	20.7 (27.7)
GSH-Rb-II-$B_{1,3}$-iii	20.3 (27.4)	22.0 (27.0)
GSH-Rb-II-$B_{1,3}$-iv_{SH}	32.1 (30.1)	33.0 (30.9)
GSH-Rb-III-$B_{1,3,4}$-$viii_b$	29.6 (31.3)	29.5 (29.0)
GSH-Rb-III-$B_{1,3,4}$-xi	38.5 (31.5)	34.1 (27.1)
GSH-Rb-III-$B_{1,3,4}$-xii	31.2 (34.8)	35.4 (39.0)
GSH-Rb-III-$B_{1,3,4}$-xiii	40.7 (35.9)	35.8 (31.1)
GSH-Rb-III-$B_{1,3,4}$-xiv_{SH}	37.2 (36.0)	37.6 (36.3)
GSH-Rb-II-$B_{3,4}$-v	37.6 (36.7)	39.2 (38.3)
GSH-Rb-II-$B_{2,4}$-vi	30.2 (37.1)	31.2 (38.1)
GSH-Rb-III-$B_{1,2,3}$-xv_{SH}	38.5 (38.9)	38.7 (39.1)
GSH-Rb-III-$B_{1,2,4}$-xvi_{SH}	34.5 (39.6)	32.1 (37.2)
zGSH-Rb-II-$B_{1,4}$-vii	30.5 (40.0)	37.5 (47.0)
GSH-Rb-II-A_1-i	44.3 (40.9)	44.6 (41.2)
zGSH-Rb-III-$B_{1,4,4}$-xvii	38.4 (42.5)	42.8 (46.8)
GSH-Rb-II-$B_{1,3}$-viii	45.3 (44.1)	45.4 (44.2)
GSH-Rb-III-$B_{1,2,3}$-xviii	59.6 (54.0)	57.8 (52.2)
GSH-Rb-II-$B_{1,2}$-ix	59.8 (54.9)	64.1 (59.2)
GSH-Rb-III-$A_{1,2}$-i	58.8 (55.4)	60.2 (56.8)

Structures of $[Rb(GSH)]^+$	-B3LYP/6-31+G(d,p)/ (For C, H,N,O,S atoms) -B3LYP/Def2SVP (Rb)	Single point: -B3LYP/6-311+G(3df,3pd) (For C, H,N,O,S atoms) -B3LYP/Def2TZVP (Rb)
GSH-Rb-I-B_4-i	73.0 (73.6)	74.5 (75.1)
GSH-Rb-I-B_3-ii	90.9 (85.2)	89.2 (83.5)
GSH-Rb-I-B_2-iii	92.7 (89.7)	95.9 (92.9)
GSH-Rb-I-B_2-iv	93.9 (90.1)	96.9 (93.2)
GSH-Rb-I-B_3-v	100.6 (98.3)	97.9 (95.6)
GSH-Rb-I-C-i	162.7 (159.0)	170.0 (166.3)

Table S2. 5: 298K relative enthalpies and Gibbs energies, in kJ mol-1, of $[Cs(GSH)]^+$. Relative Gibbs energies are indicated in parentheses.

Structures of $[Cs(GSH)]^+$	**-B3LYP/6-31+G(d,p)/ (For C, H,N,O,S atoms) -B3LYP/Def2SVP (Cs)**	**Single point: -B3LYP/6-311+G(3df,3pd) (For C, H,N,O,S atoms) -B3LYP/Def2TZVP (Cs)**
GSH-Cs-IV-$A_{1,3,4}$-i_{SH}	0.0 (0.0)	0.0 (0.0)
GSH-Cs-II-$B_{2,4}$-i_a	-12.7 (0.4)	-8.1 (5.0)
GSH-Cs-IV-$A_{1,3,4}$-i_b	4.6 (2.6)	5.1 (3.2)
GSH-Cs-II-$B_{2,4}$-i_b	-10.3 (3.2)	-5.5 (8.0)
GSH-Cs-III-$B_{1,3,4}$-i	-1.1 (3.8)	3.0 (7.8)
GSH-Cs-III-$B_{1,2,4}$-ii	-8.2 (4.0)	-3.4 (8.9)
GSH- Cs -IV-$A_{1,3,4}$-i_c	5.9 (4.4)	6.3 (4.7)
GSH-Cs-III-$B_{1,3,4}$-iii	1.6 (4.8)	2.9 (6.1)
GSH-Cs-IV-$A_{1,3,4}$-i_d	7.6 (5.9)	6.9 (5.2)
GSH-Cs-III-$B_{1,2,4}$-iv_{SH}	-2.5 (10.4)	2.7 (15.5)
GSH-Cs-III-$B_{1,3,4}$-v	0.9 (12.7)	5.4 (17.2)
GSH-Cs-III-$B_{1,2,4}$-vi_a	1.0 (13.3)	5.4 (17.8)
GSH-Cs-III-$B_{1,3,4}$-vii	11.3 (13.4)	12.7 (14.8)
GSH-Cs-III-$B_{1,2,4}$-vi_b	17.7 (13.4)	18.2 (13.9)
GSH-Cs-II-$B_{2,4}$-ii	7.4 (13.8)	8.3 (14.8)
GSH-Cs-II-$B_{2,4}$-iii	7.6 (14.9)	9.0 (16.2)
GSH-Cs-IV-$B_{1,2,3,4}$-i	19.1 (15.6)	19.1 (15.7)
GSH-Cs-II-$B_{2,4}$-iv	9.2 (16.0)	10.1 (16.8)
GSH-Cs-IV-$B_{1,2,3,4}$-ii	17.9 (16.5)	18.4 (17.0)
GSH-Cs-II-$B_{1,4}$-v	5.3 (17.7)	10.2 (22.7)

Structures of $[Cs(GSH)]^+$	-B3LYP/6-31+G(d,p)/ (For C, H,N,O,S atoms) -B3LYP/Def2SVP (Cs)	Single point: -B3LYP/6-311+G(3df,3pd) (For C, H,N,O,S atoms) -B3LYP/Def2TZVP (Cs)
GSH-Cs-II-$B_{2,4}$-vi	11.5 (17.8)	12.1 (18.4)
GSH-Cs-III-$B_{1,2,4}$-viii	16.0 (18.2)	19.1 (21.2)
GSH-Cs-IV-$B_{1,2,3,4}$-iii	16.8 (18.2)	17.8 (19.3)
GSH-Cs-II-$B_{1,3}$-vii	13.8 (22.4)	16.6 (25.3)
GSH-Cs-II-$B_{1,4}$-$viii_{SH}$	21.3 (22.7)	21.9 (23.3)
GSH-Cs-IV-$B_{1,2,3,4}$-iv	18.0 (23.1)	19.8 (25.3)
GSH-Cs-III-$B_{1,3,4}$-ix	21.0 (23.6)	22.7 (25.3)
GSH-Cs-II-$B_{1,3}$-ix	14.8 (23.7)	17.8 (28.9)
GSH-Cs-II-$B_{1,2}$-x	18.7 (26.9)	22.0 (30.1)
GSH-Cs-II-$B_{1,3}$-xi	29.7 (26.9)	30.9 (28.1)
GSH-Cs-III-$B_{1,2,4}$-x	21.4 (28.0)	20.2 (26.9)
GSH-Cs-II-$B_{3,4}$-xii	25.6 (29.1)	26.7 (32.4)
GSH-Cs-II-$B_{2,3}$-xiii	23.4 (30.2)	25.6 (32.4)
GSH-Cs-II-$B_{3,4}$-xiv	27.4 (31.0)	32.6 (36.2)
GSH-Cs-III-$B_{1,3,4}$-xi	38.3 (33.5)	35.2 (30.4)
GSH-Cs-II-$B_{3,4}$-xv	33.7 (35.2)	36.3 (37.9)
GSH-Cs-II-$B_{1,4}$-xvi	31.2 (36.2)	35.5 (40.5)
GSH-Cs-II-$B_{1,3}$-xvii	37.1 (36.8)	37.7 (37.5)
zGSH-Cs-II-$B_{1,4}$-xviii	34.2 (39.8)	39.3 (44.9)
GSH-Cs-III-$B_{1a,3,4}$-xii	36.4 (44.4)	40.9 (48.9)
GSH-Cs-I-B_1-i	51.6 (47.7)	48.0 (44.1)

Structures of $[Cs(GSH)]^+$	-B3LYP/6-31+G(d,p)/ (For C, H,N,O,S atoms) -B3LYP/Def2SVP (Cs)	Single point: -B3LYP/6-311+G(3df,3pd) (For C, H,N,O,S atoms) -B3LYP/Def2TZVP (Cs)
GSH-Cs-II-$B_{2,4}$-xix	40.2 (52.7)	45.6 (58.1)
GSH-Cs-I-B_1-ii	50.1 (58.5)	52.6 (61.0)
GSH-Cs-I-B_4-iii	62.5 (64.6)	64.7 (66.8)
GSH-Cs-II-$B_{1,2}$-xx	72.0 (72.6)	73.5 (74.1)
GSH-Cs-I-B_2-iv	84.1 (80.4)	89.3 (85.7)
GSH-Cs-I-B_2-v	82.6 (81.4)	87.2 (86.0)
GSH-Cs-I-A-i	114.9 (116.3)	117.4 (118.8)
zGSH-Cs-II-C_2-i	117.9 (127.0)	125.4 (134.6)

Appendix B – Supplemental Information for Chapter 3

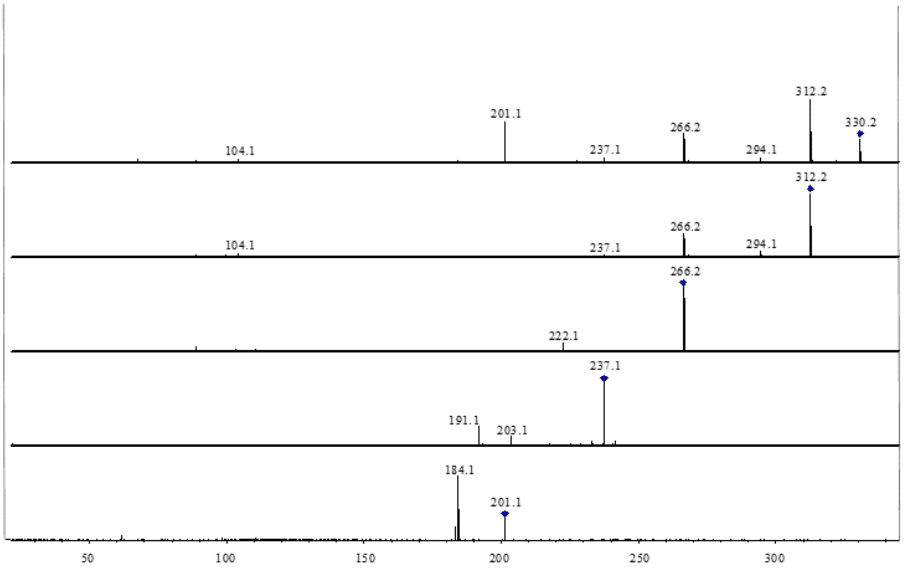

Figure S3. 1: SORI-CID mass spectra for $Mg(GSH-H)^+$.

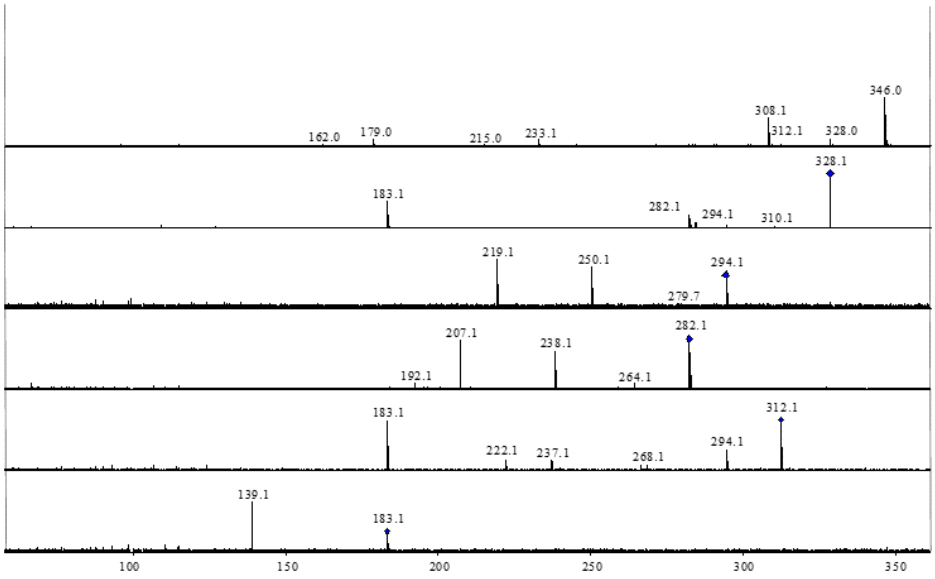

Figure S3. 2: SORI-CID mass spectra for $Ca(GSH-H)^+$.

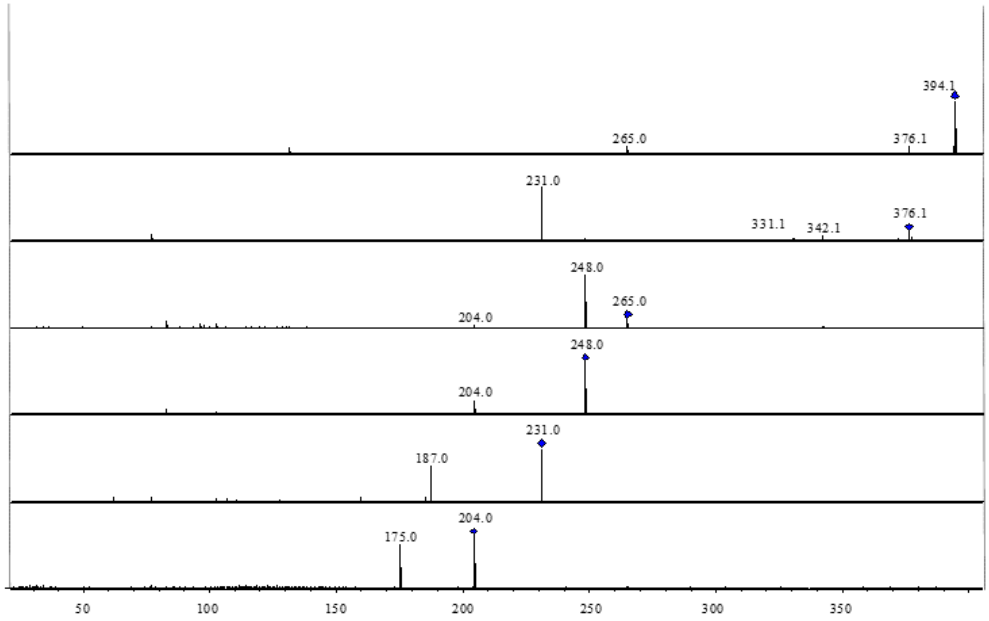

Figure S3. 3: SORI-CID mass spectra for $Sr(GSH-H)^{+}$.

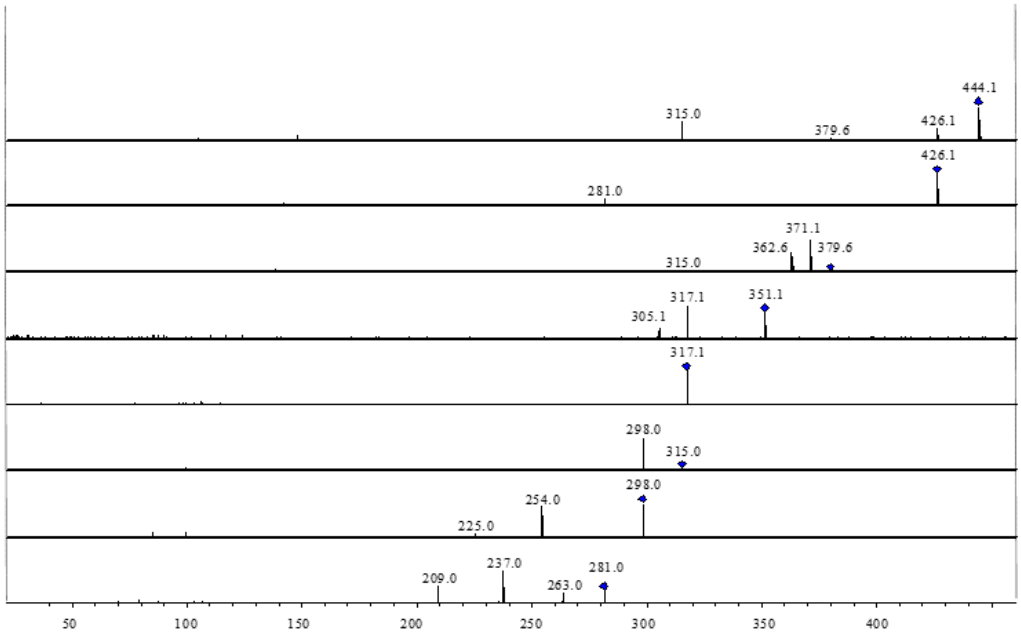

Figure S3. 4: SORI-CID mass spectra for $Ba(GSH-H)^{+}$.

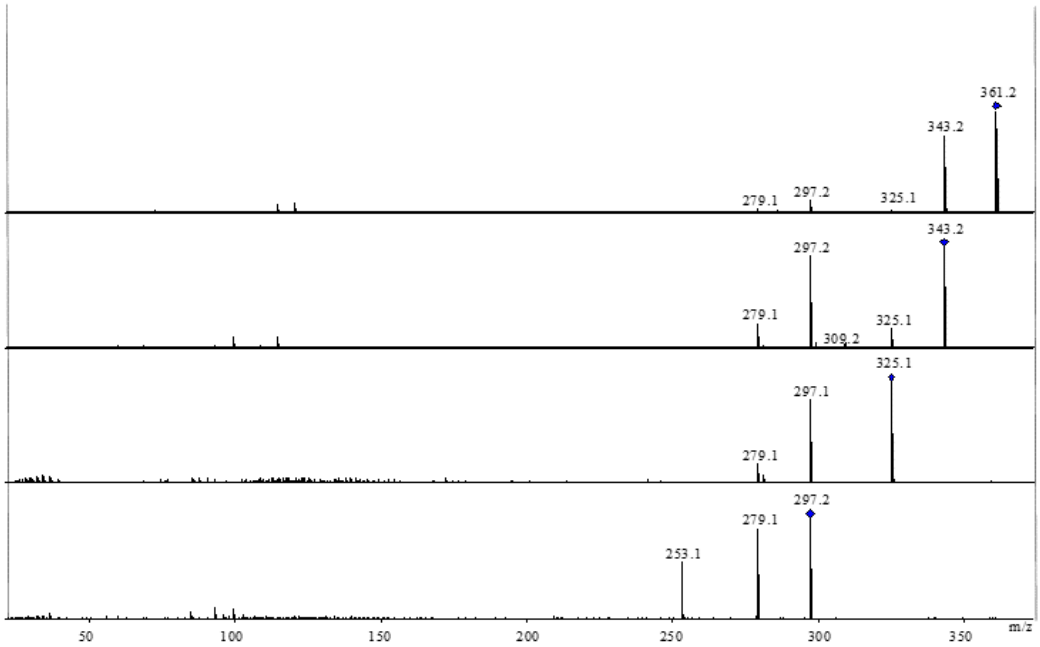

Figure S3. 5: SORI-CID mass spectra for $Mn(GSH-H)^{+}$.

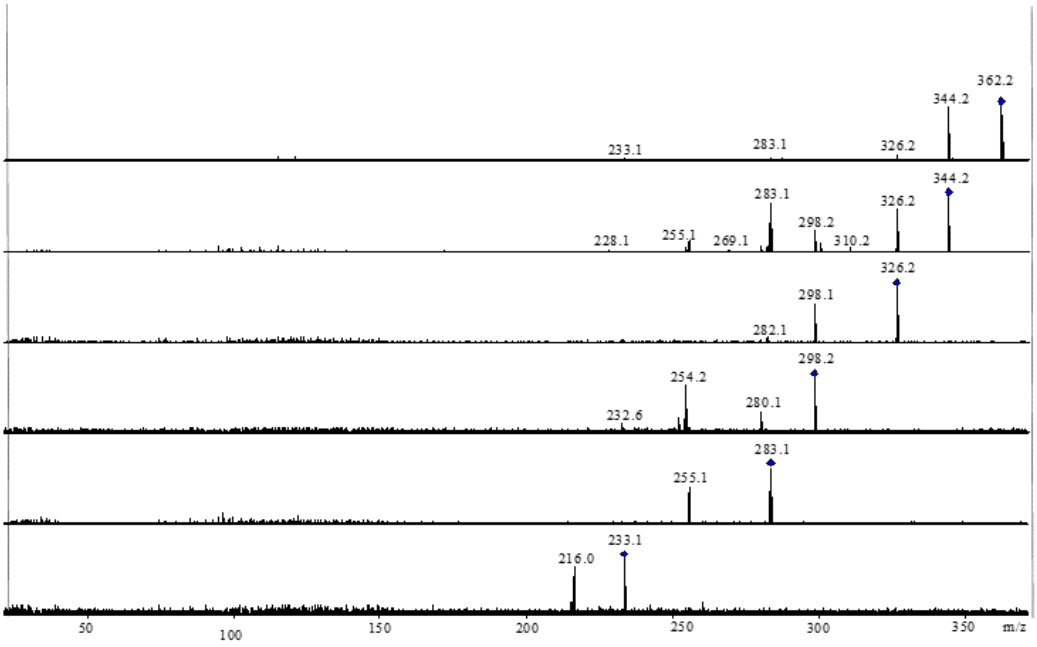

Figure S3. 6: SORI-CID mass spectra for $Fe(GSH-H)^{+}$.

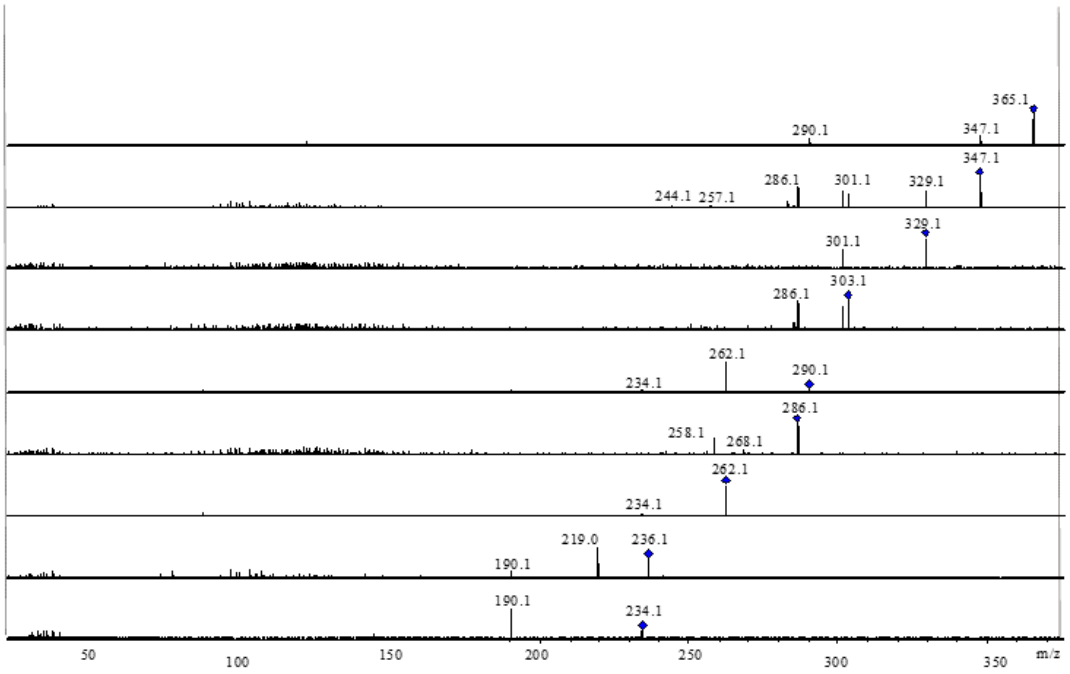

Figure S3. 7: SORI-CID mass spectra for $Co(GSH-H)^+$.

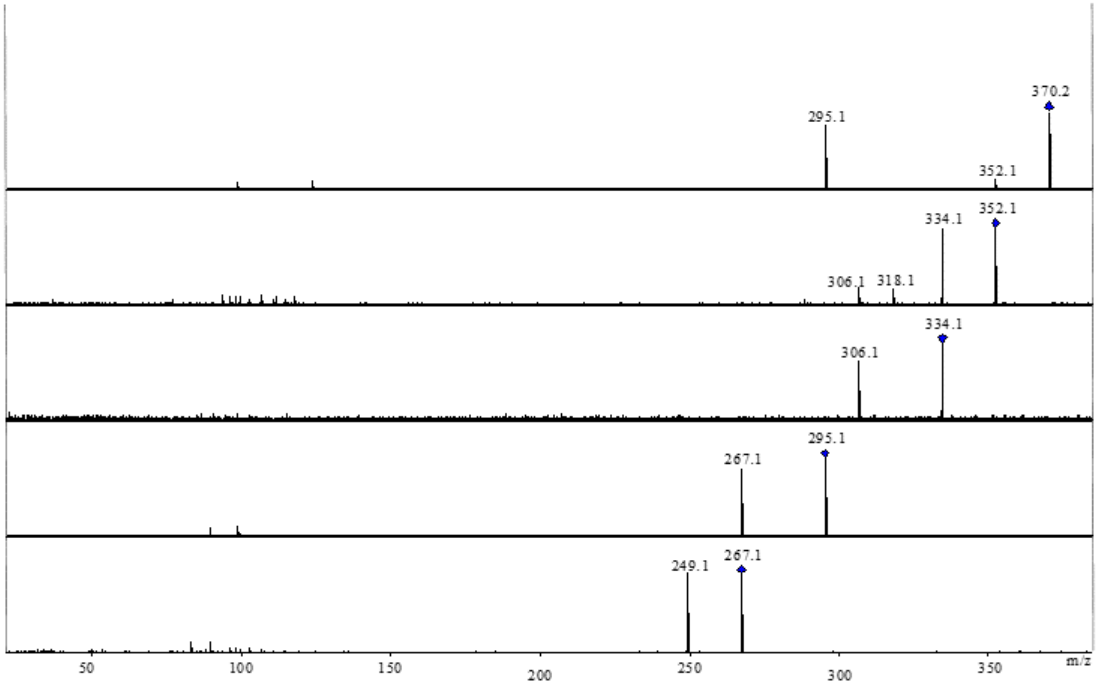

Figure S3. 8: SORI-CID mass spectra for $Zn(GSH-H)^+$.

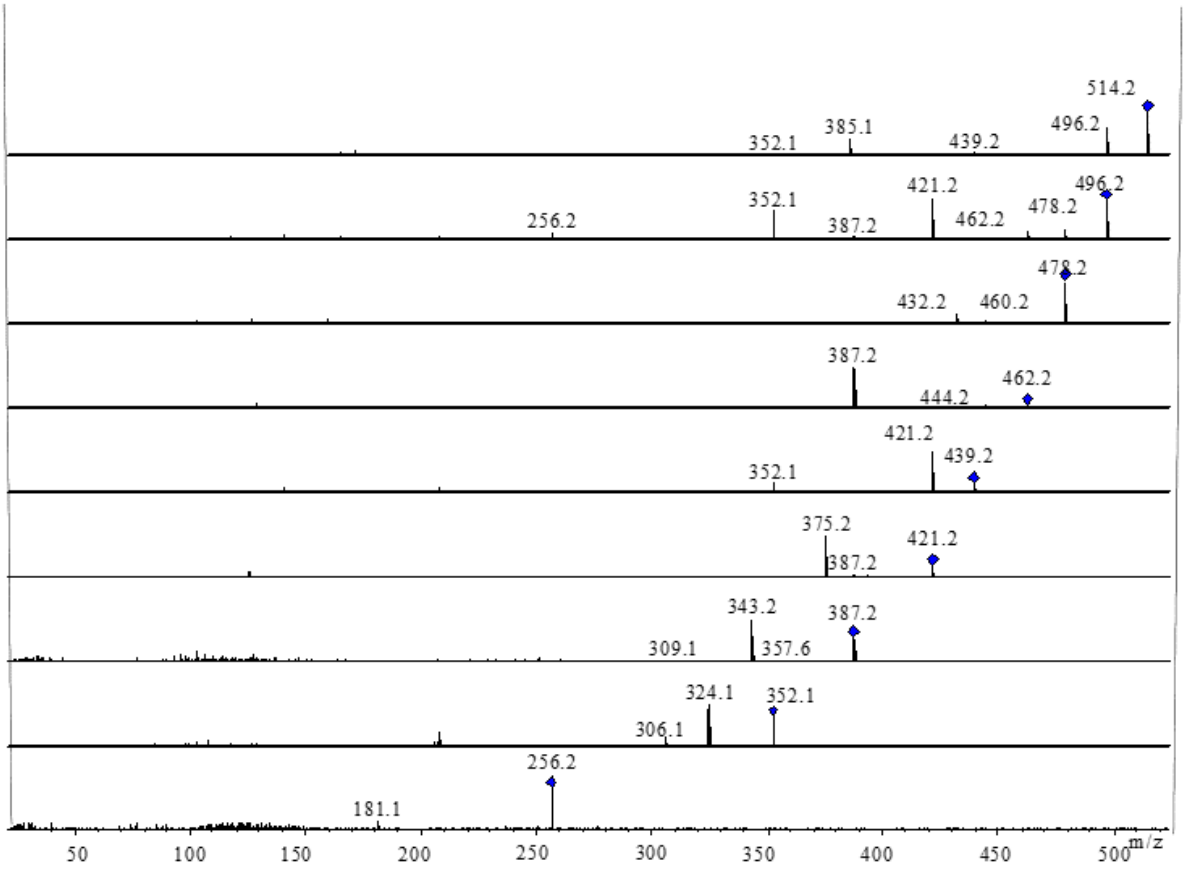

Figure S3. 9: SORI-CID mass spectra for $Pb(GSH-H)^{+}$.

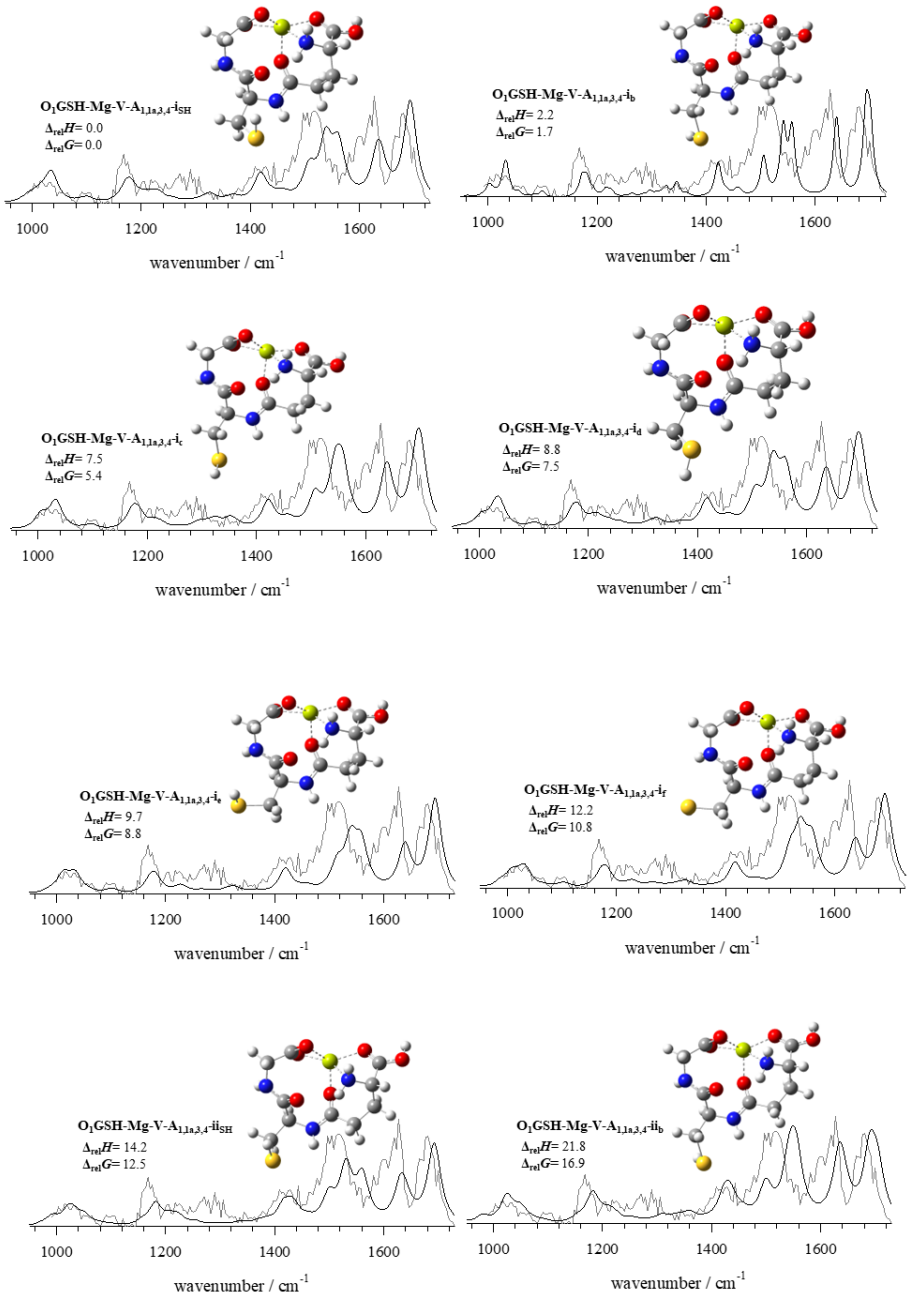

Figure S3. 10: Computed structures of $Mg(GSH-H)^{+}$.

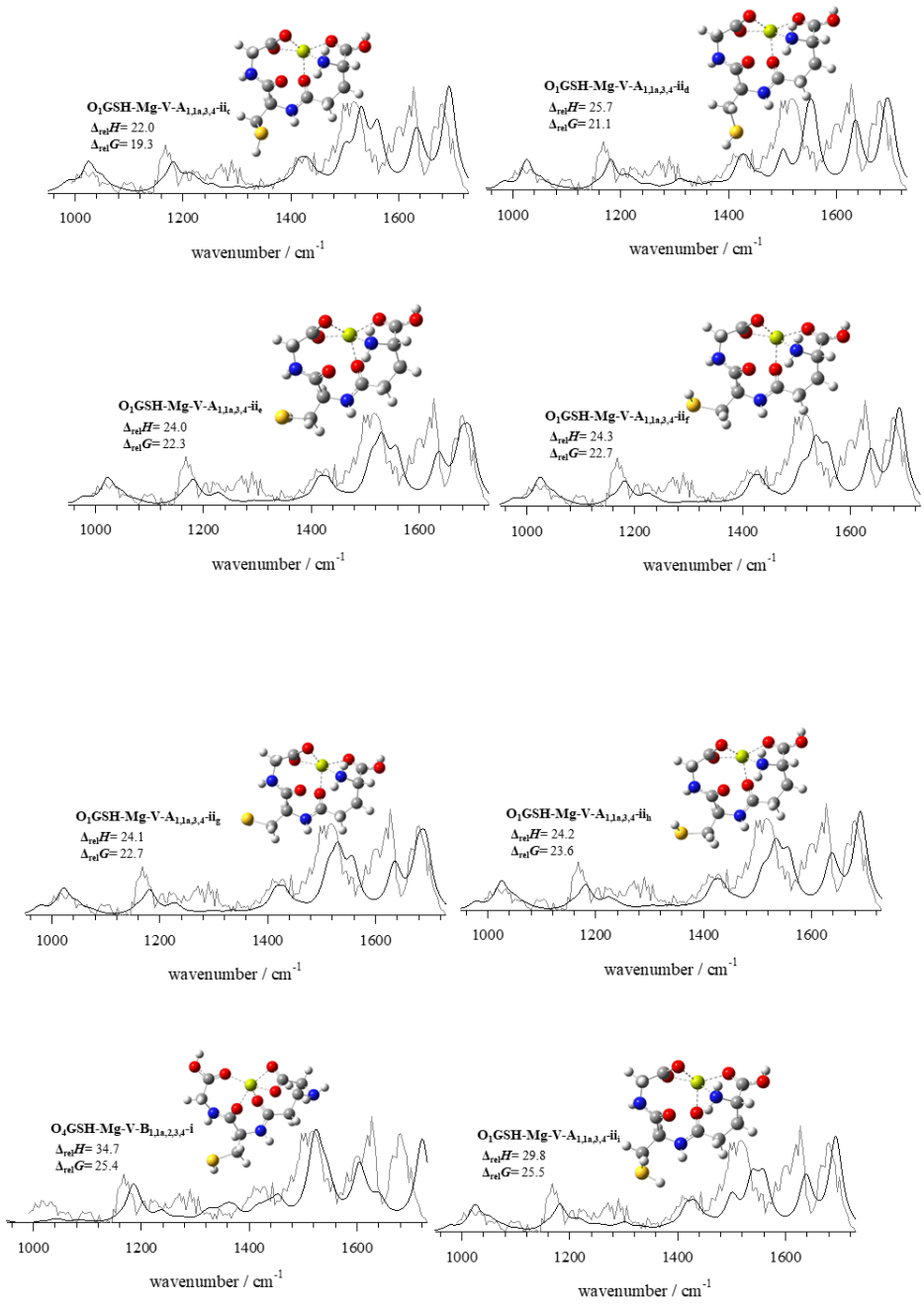

Figure S3. 10: Computed structures of $Mg(GSH-H)^{+}$.

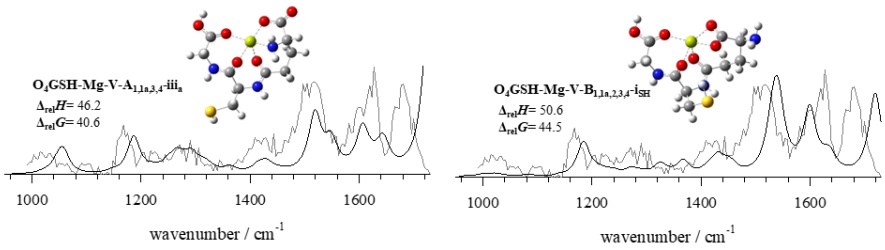

Figure S3. 10: Computed structures of $Mg(GSH-H)^+$.

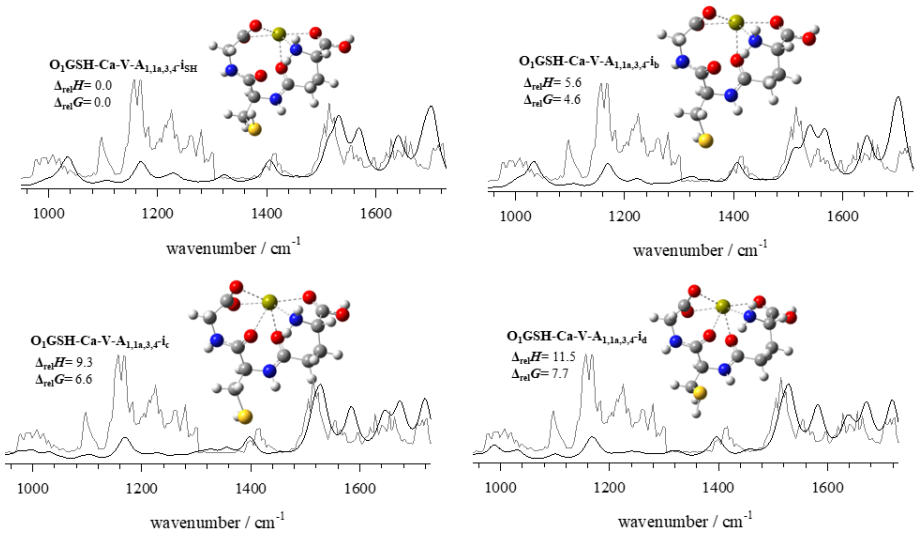

Figure S3. 11: Computed structures of $Ca(GSH-H)^+$.

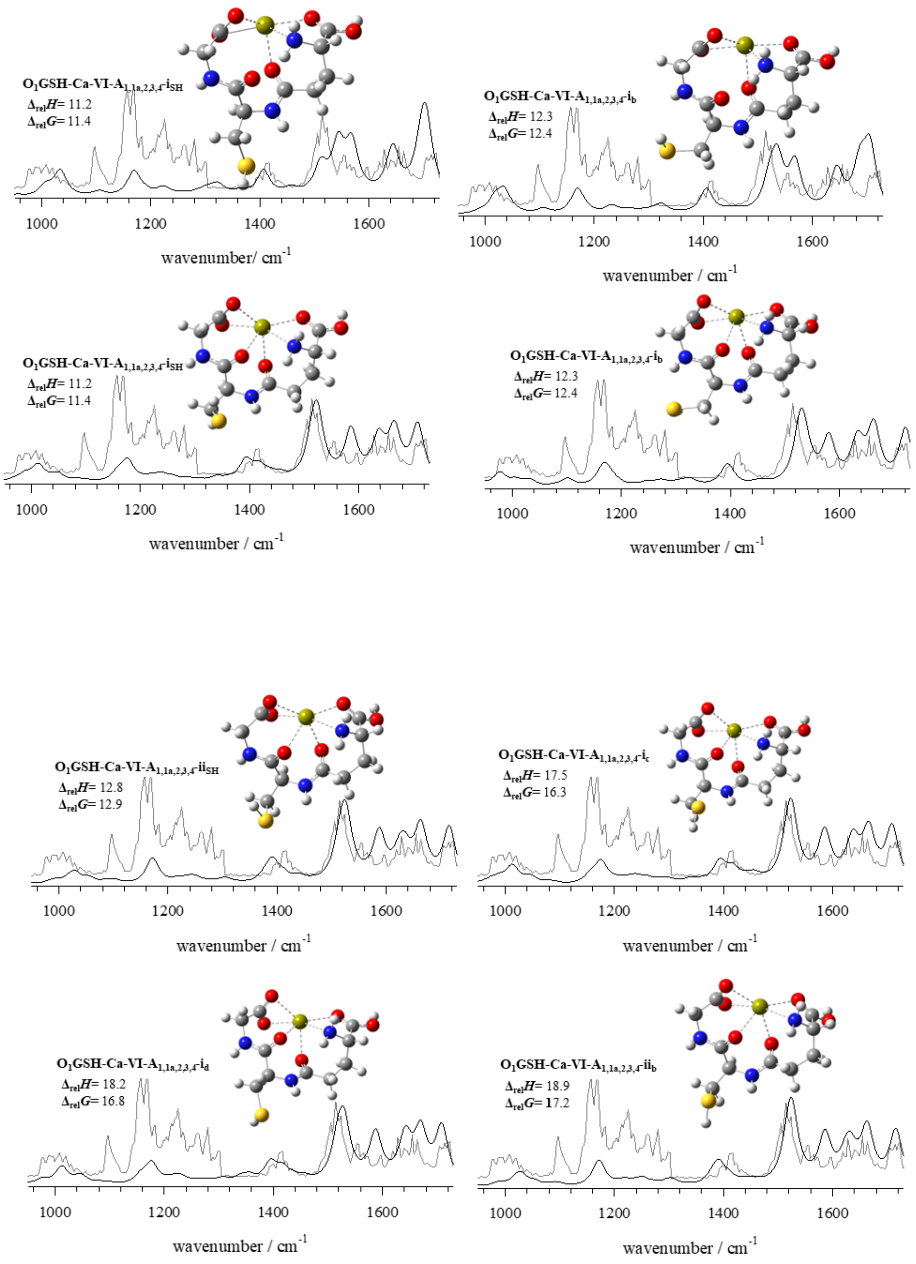

Figure S3.11: Computed structures of $Ca(GSH\text{-}H)^{+\cdot}$.

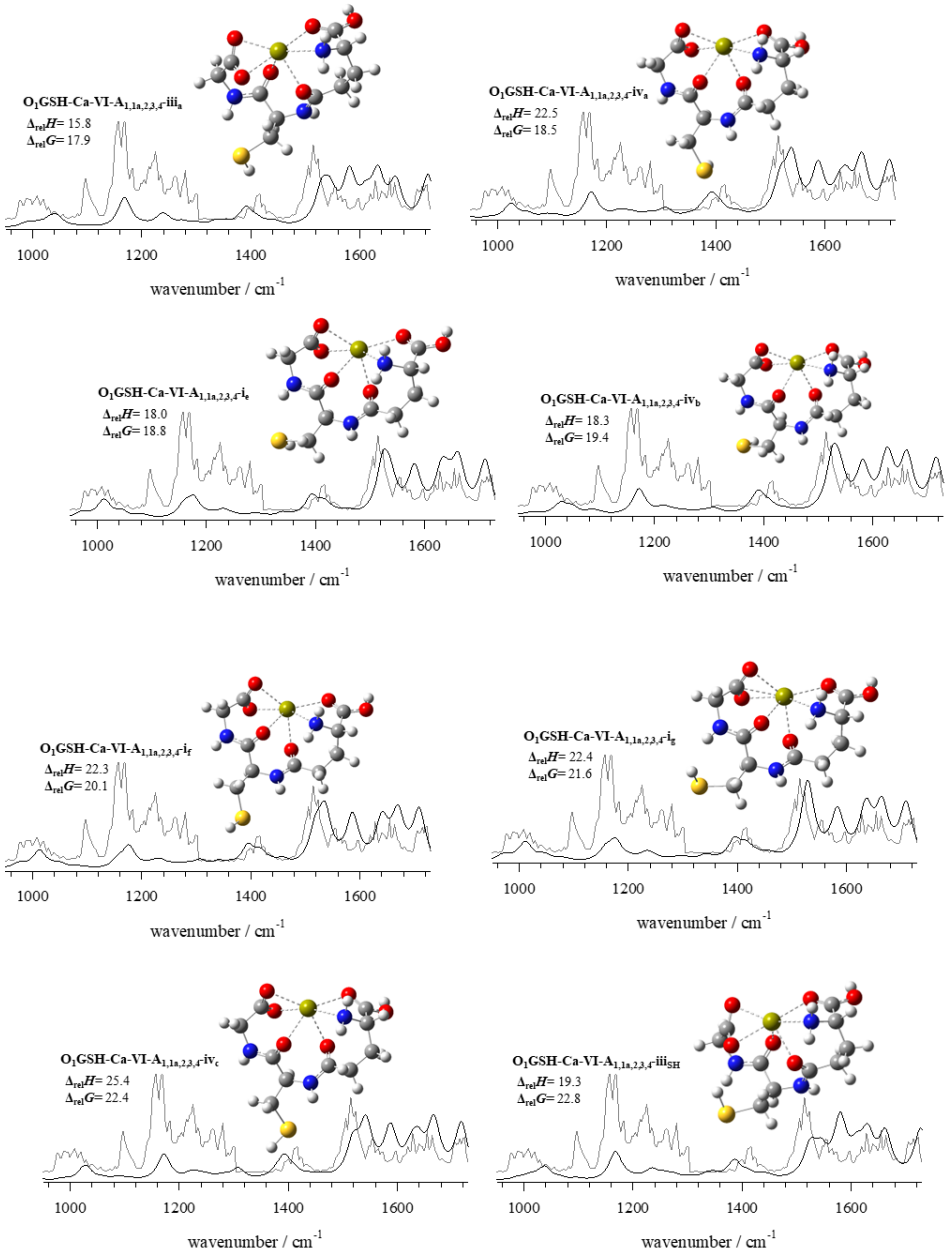

Figure S3.11: Computed structures of $Ca(GSH\text{-}H)^{+}$.

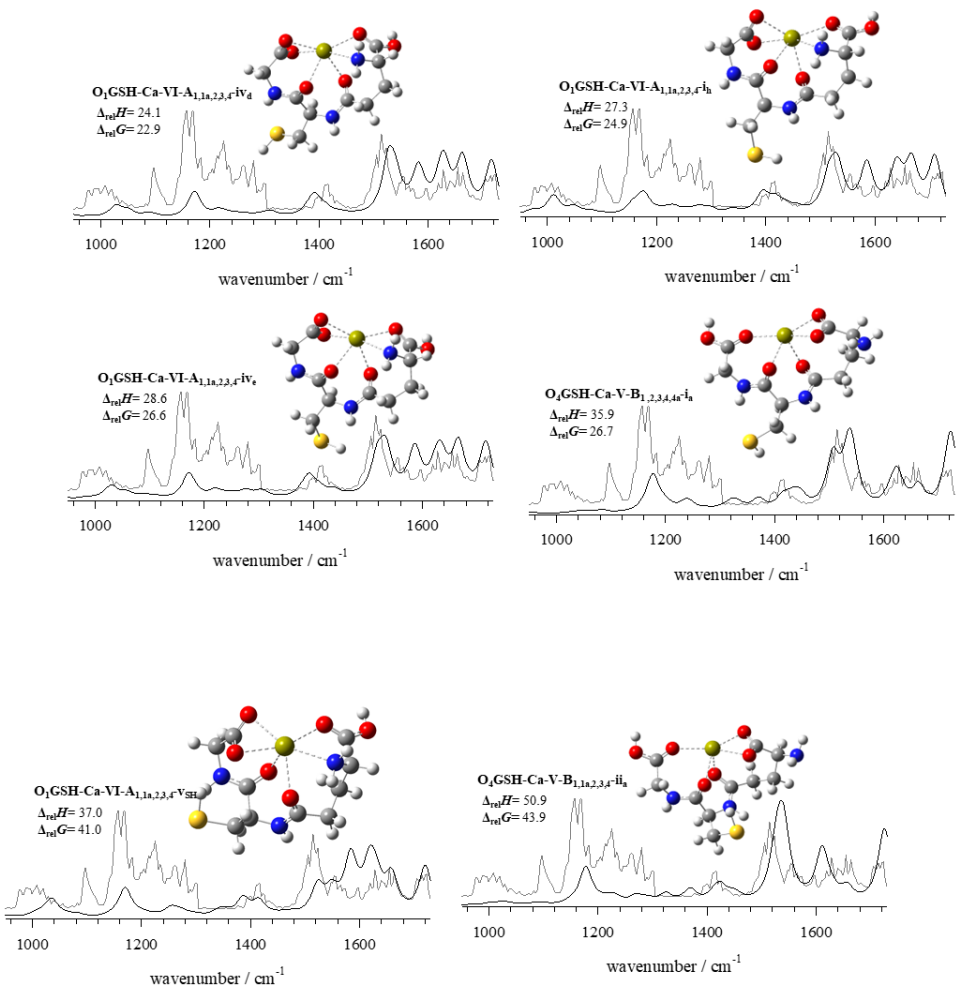

Figure S3.11: Computed structures of $Ca(GSH\text{-}H)^{+\cdot}$.

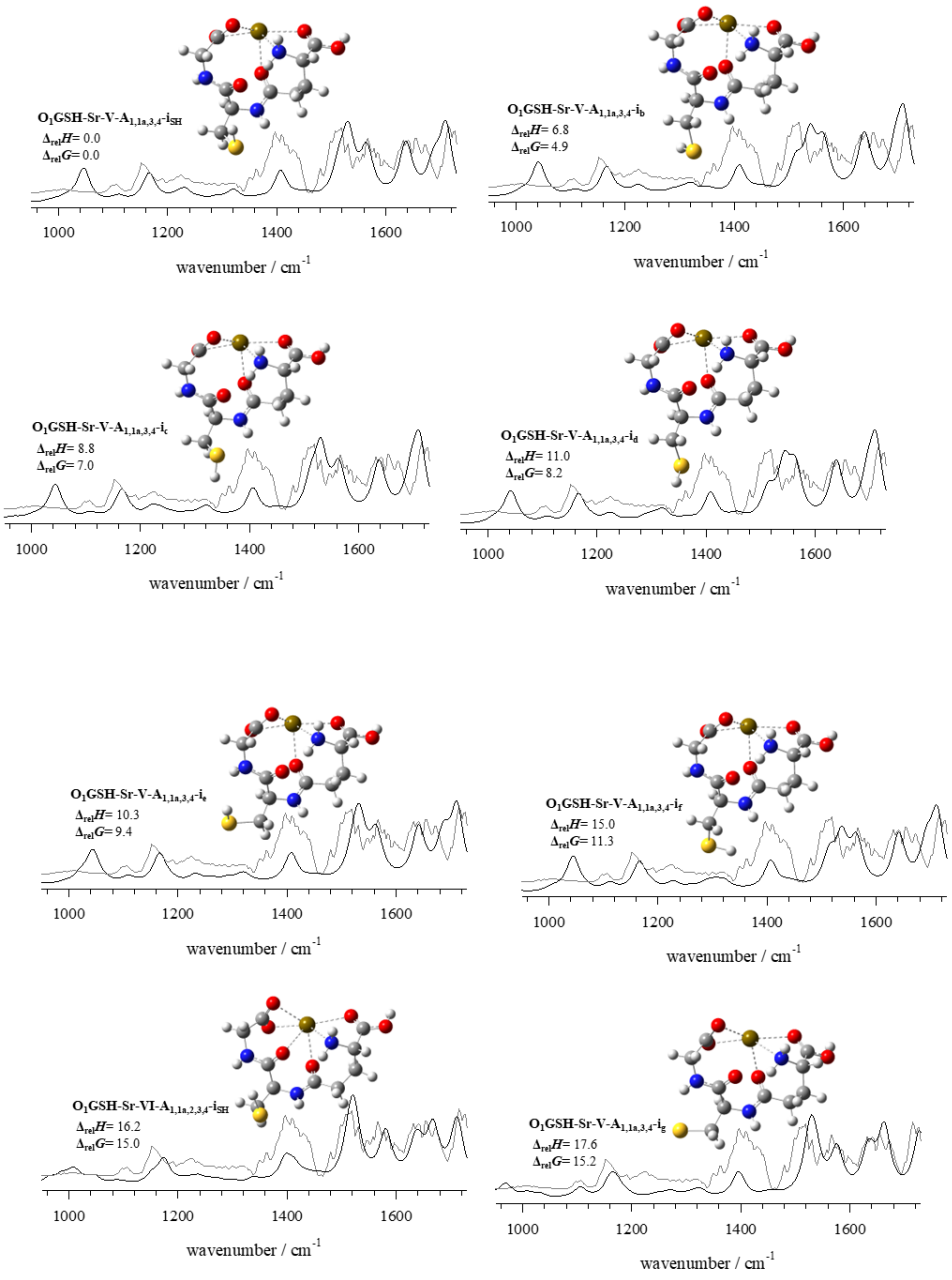

Figure S3. 12: Computed structures of $Sr(GSH-H)^{+}$.

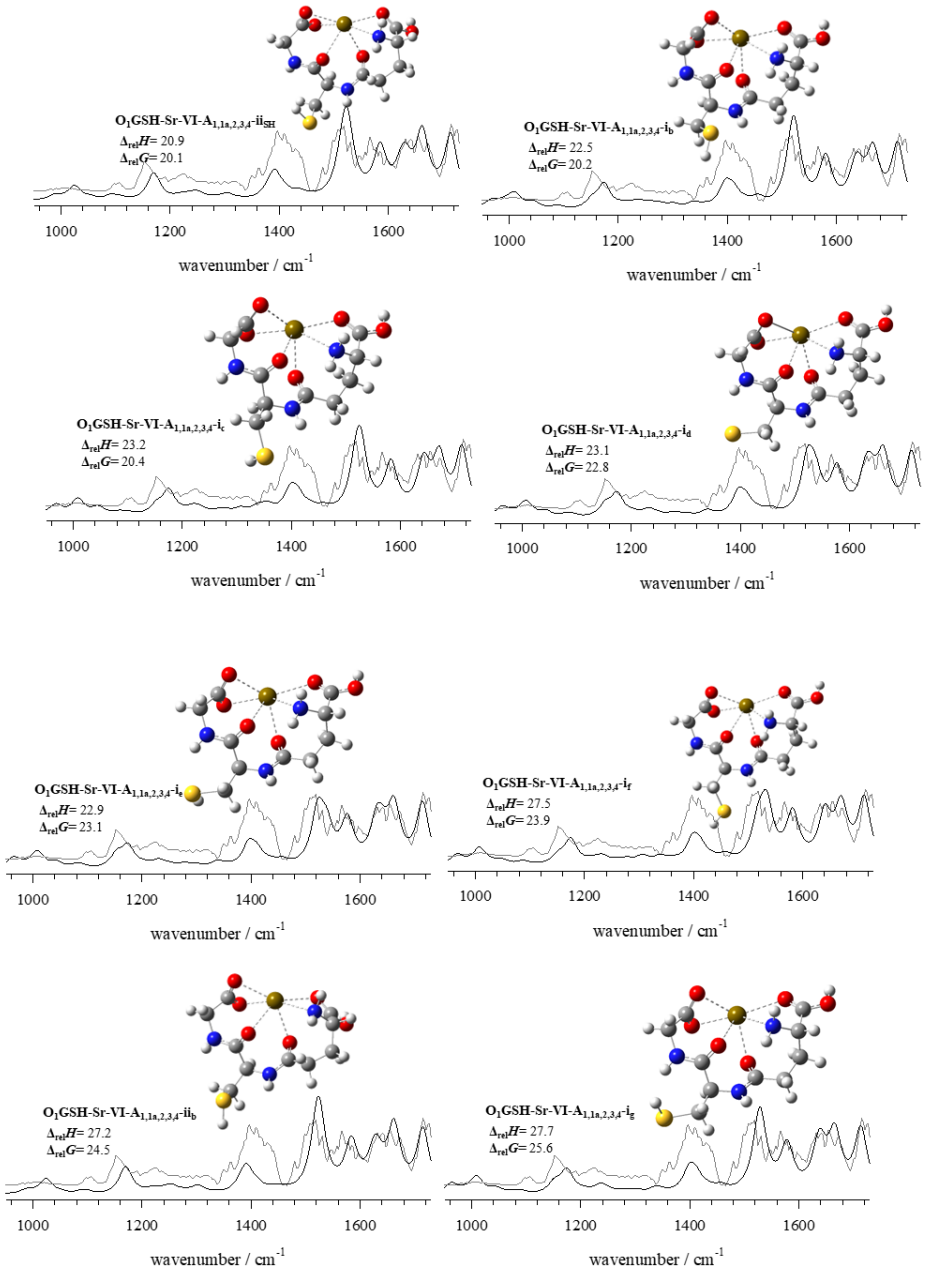

Figure S3.12: Computed structures of $Sr(GSH-H)^{+}$.

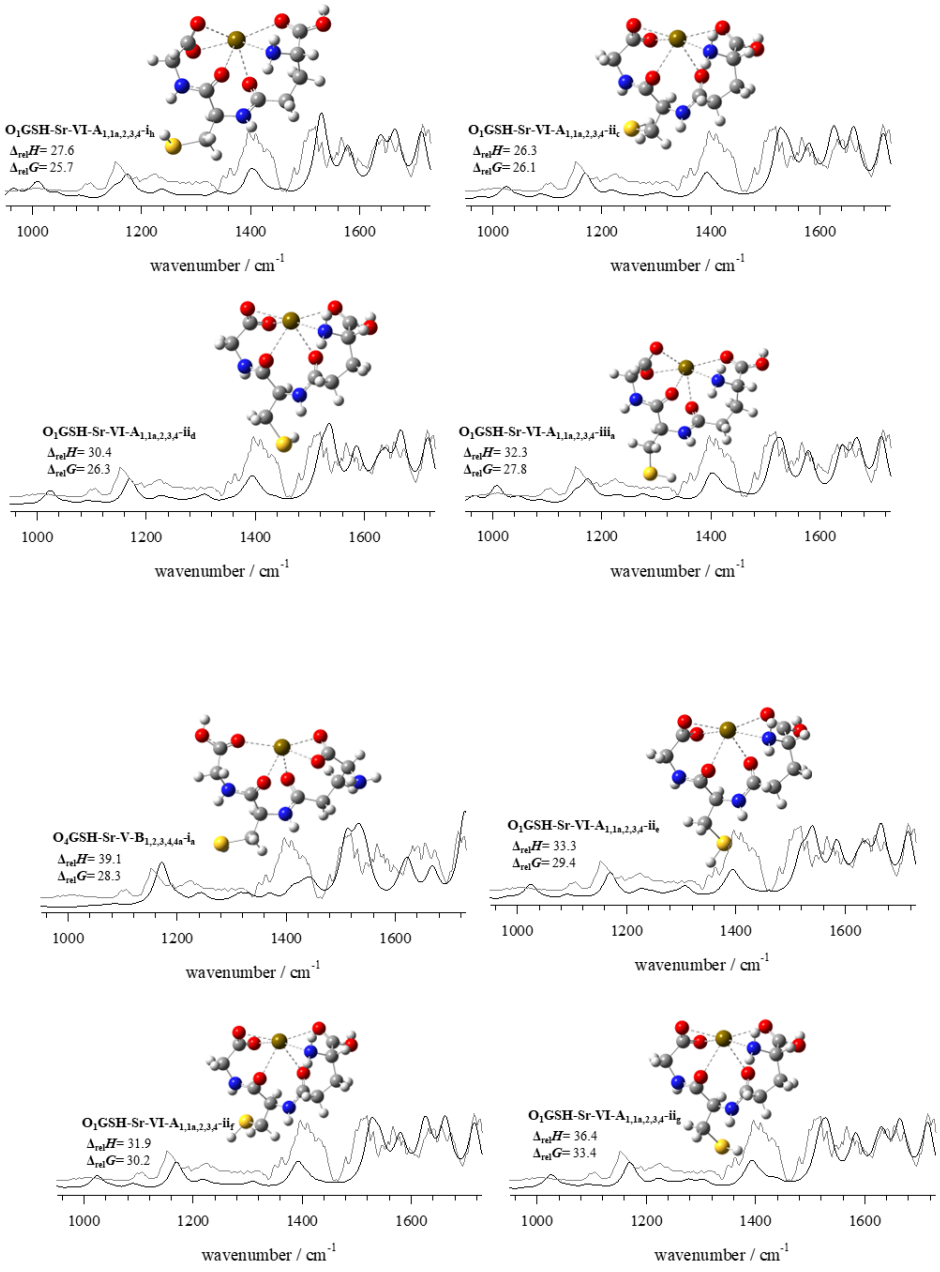

Figure S3.12: Computed structures of $Sr(GSH\text{-}H)^{+\cdot}$.

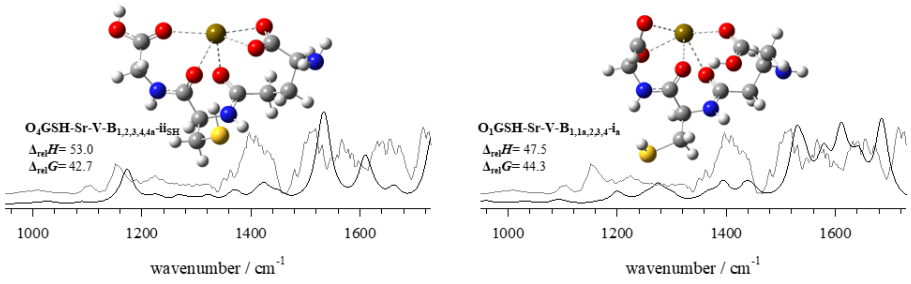

Figure S3.12: Computed structures of $Sr(GSH-H)^{+}$.

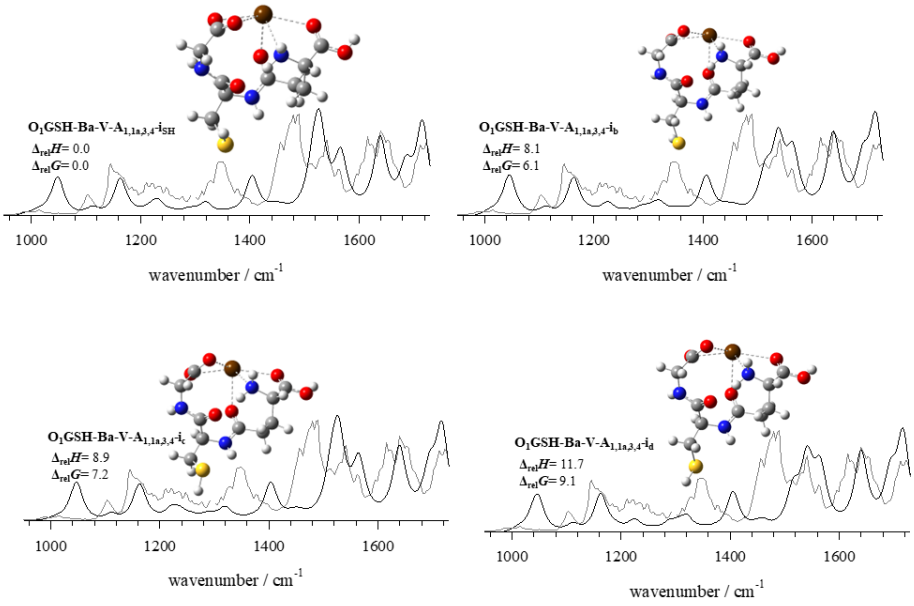

Figure S3. 13: Computed structures of $Ba(GSH-H)^{+}$.

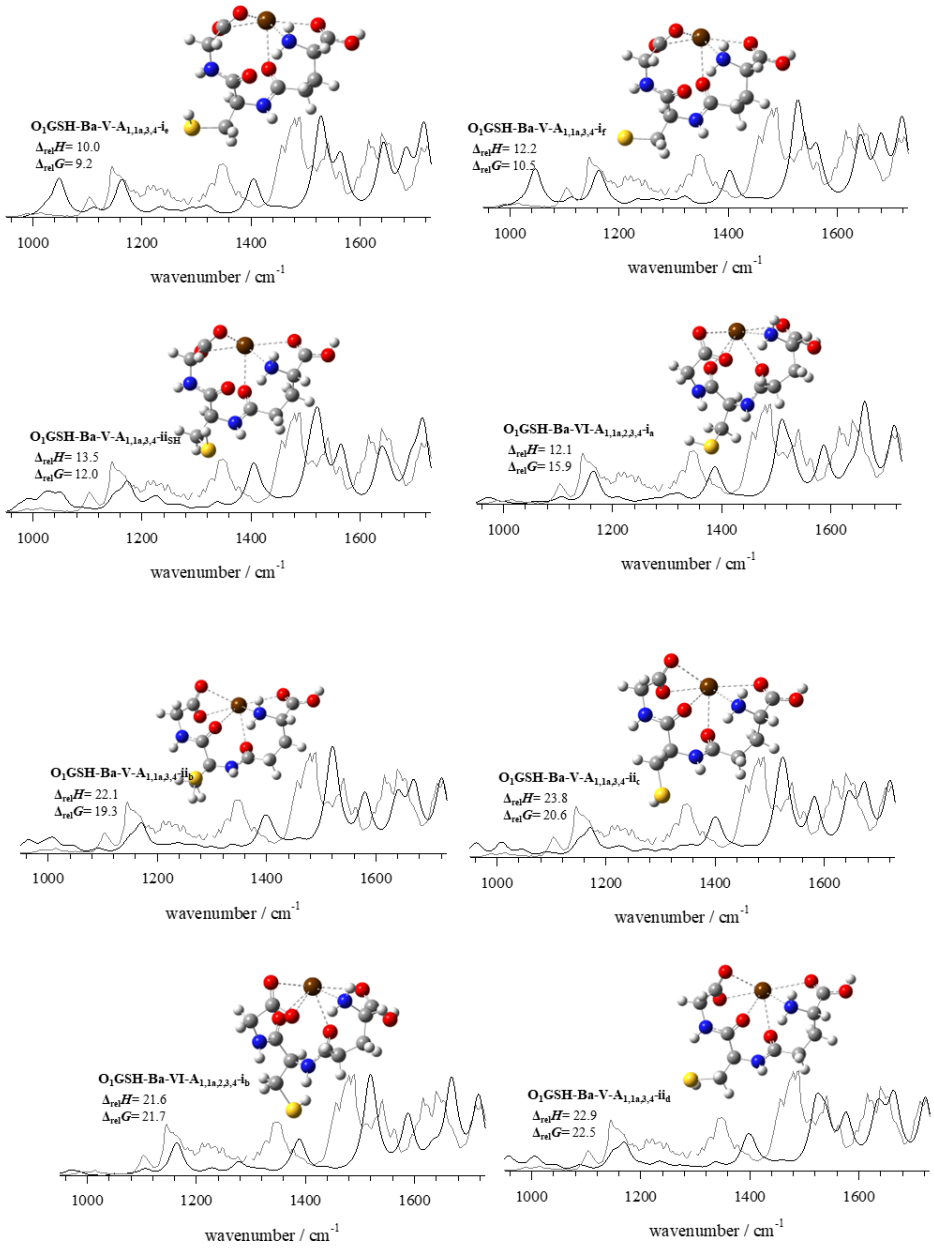

Figure S3.13. Computed structures of $Ba(GSH\text{-}H)^{+}\cdot$.

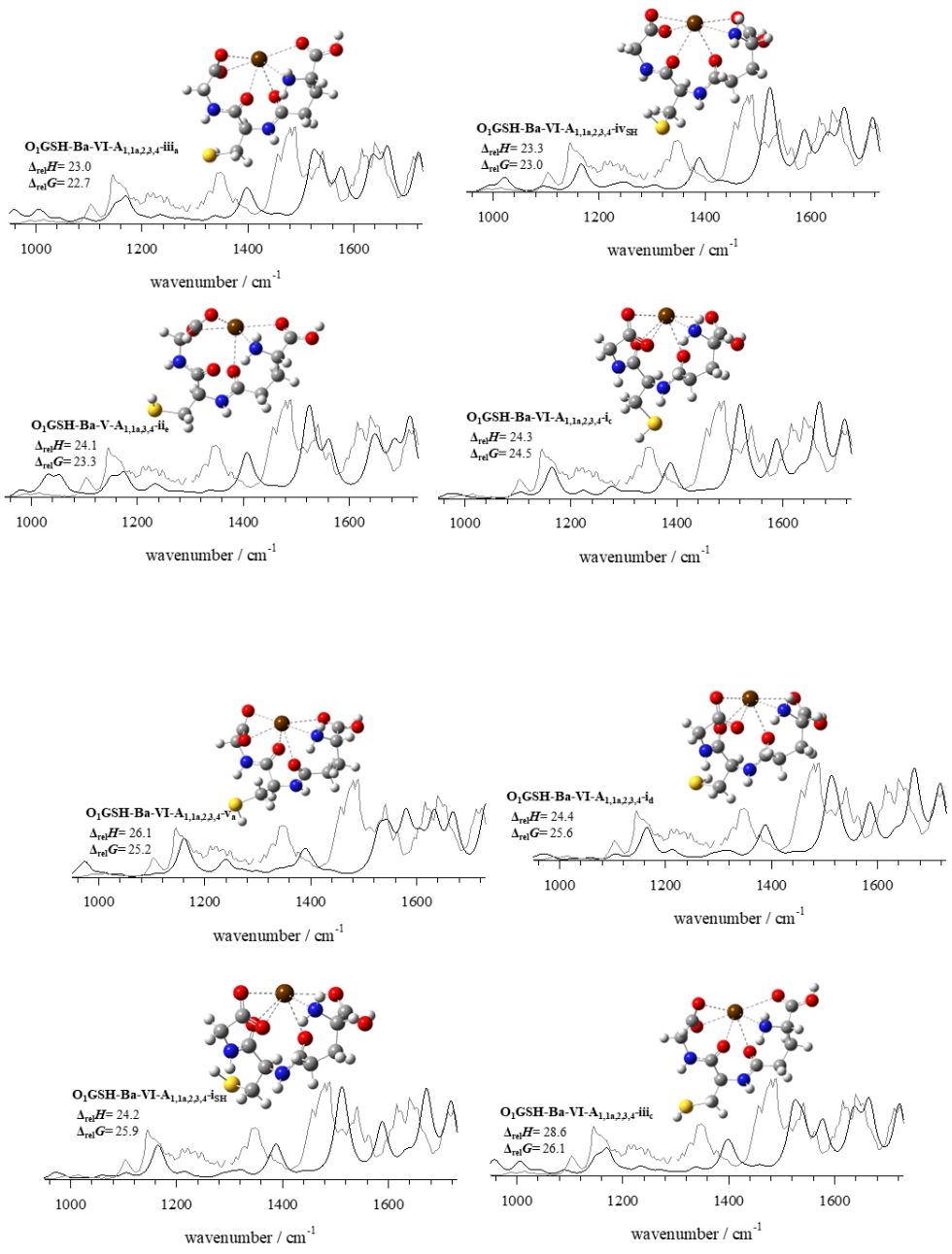

Figure S3.13. Computed structures of $Ba(GSH-H)^{+}$.

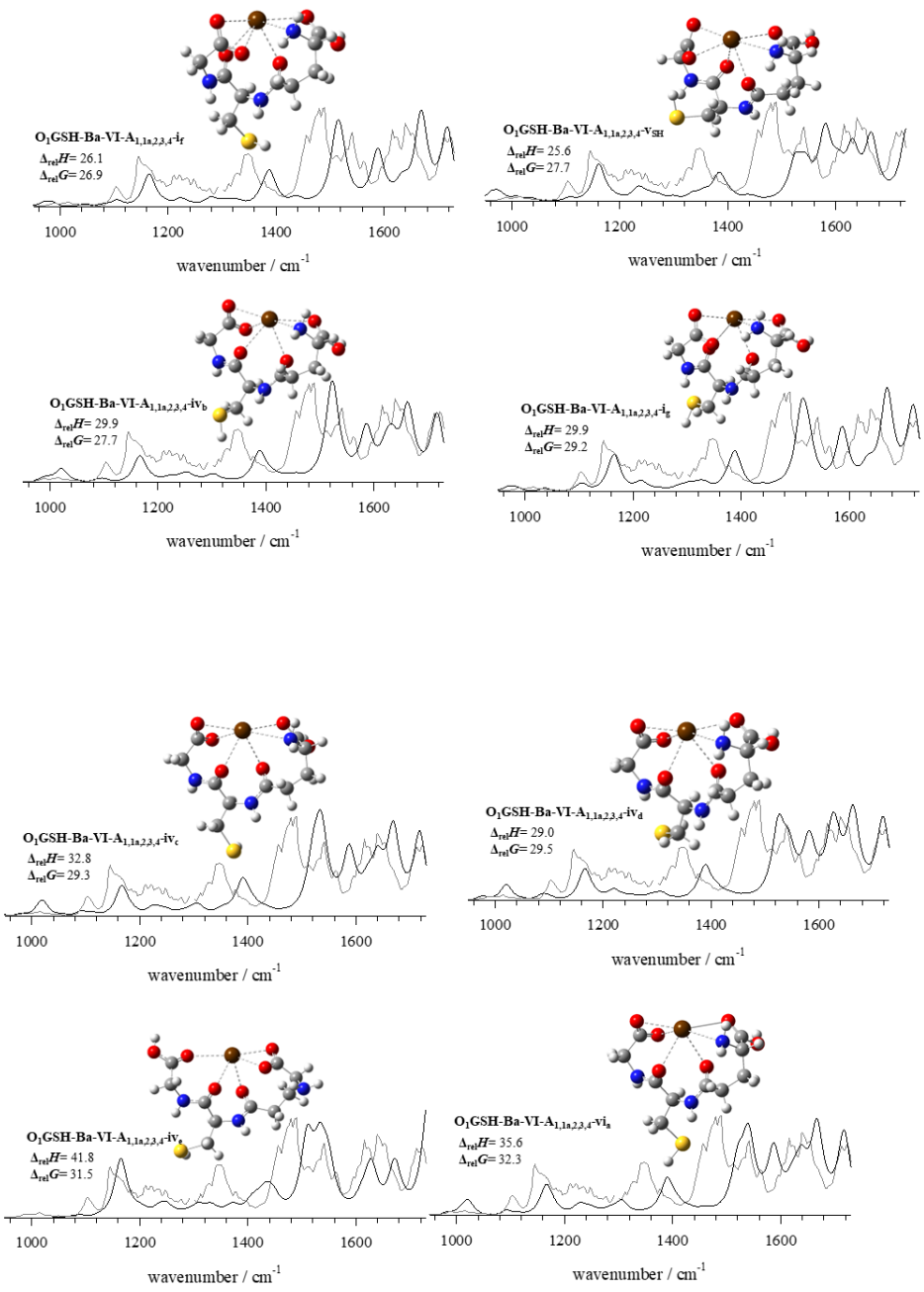

Figure S3.13. Computed structures of $Ba(GSH-H)^{+}$.

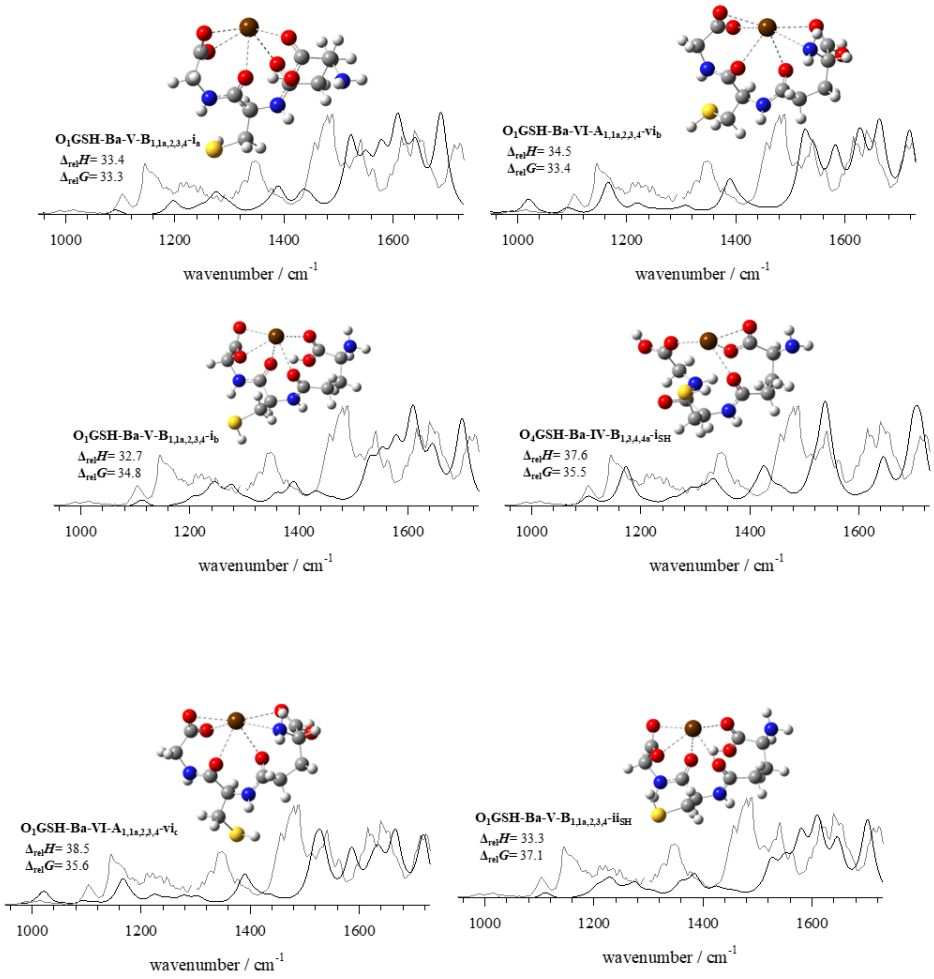

Figure S3.13. Computed structures of $Ba(GSH\text{-}H)^{+}\cdot$

Table S3. 1: 298K relative enthalpies and Gibbs energies, in kJ mol-1, of $Mg(GSH-H)^+$. Relative Gibbs energies are indicated in parentheses.

Structures of $Mg(GSH-H)^+$	**B3LYP/6-31+G(d,p) (For all atoms)**
O_1GSH-Mg-V-$A_{1,1a,3,4}$-i_{SH}	0.0 (0.0)
O_1GSH-Mg-V-$A_{1,1a,3,4}$-i_b	2.2 (1.7)
O_1GSH-Mg-V-$A_{1,1a,3,4}$-i_c	7.5 (5.4)
O_1GSH-Mg-V-$A_{1,1a,3,4}$-i_d	8.8 (7.5)
O_1GSH-Mg-V-$A_{1,1a,3,4}$-i_e	9.7 (8.8)
O_1GSH-Mg-V-$A_{1,1a,3,4}$-i_f	12.2 (10.8)
O_1GSH-Mg-V-$A_{1,1a,3,4}$-ii_{SH}	14.2 (12.5)
O_1GSH-Mg-V-$A_{1,1a,3,4}$-ii_b	21.8 (16.9)
O_1GSH-Mg-V-$A_{1,1a,3,4}$-ii_c	22.0 (19.3)
O_1GSH-Mg-V-$A_{1,1a,3,4}$-ii_d	25.7 (21.1)
O_1GSH-Mg-V-$A_{1,1a,3,4}$-ii_e	24.0 (22.3)
O_1GSH-Mg-V-$A_{1,1a,3,4}$-ii_f	24.3 (22.7)
O_1GSH-Mg-V-$A_{1,1a,3,4}$-ii_g	24.1 (22.7)
O_1GSH-Mg-V-$A_{1,1a,3,4}$-ii_h	24.2 (23.6)
O_4GSH-Mg-V-$B_{1,1a,2,3,4}$-i	34.7 (25.4)
O_1GSH-Mg-V-$A_{1,1a,3,4}$-ii_i	29.8 (25.5)
O_4GSH-Mg-V-$A_{1,1a,3,4}$-iii_a	46.2 (40.6)
O_4GSH-Mg-V-$B_{1,1a,2,3,4}$-i_{SH}	50.6 (44.5)

Table S3. 2: 298K relative enthalpies and Gibbs energies, in kJ mol-1, of $Ca(GSH-H)^+$. Relative Gibbs energies are indicated in parentheses.

Structures of $Ca(GSH-H)^+$	**B3LYP/6-31+G(d,p) (For all atoms)**
O_1GSH-Ca-V-$A_{1,1a,3,4}$-i_{SH}	0.0 (0.0)
O_1GSH-Ca-V-$A_{1,1a,3,4}$-i_b	5.6 (4.6)
O_1GSH-Ca-V-$A_{1,1a,3,4}$-i_c	9.3 (6.6)
O_1GSH-Ca-V-$A_{1,1a,3,4}$-i_d	11.5 (7.7)
O_1GSH-Ca-V-$A_{1,1a,3,4}$-i_e	10.1 (7.8)
O_1GSH-Ca-V-$A_{1,1a,3,4}$-i_f	10.3 (10.3)
O_1GSH-Ca-VI-$A_{1,1a,2,3,4}$-i_{SH}	11.2 (11.4)
O_1GSH-Ca-VI-$A_{1,1a,2,3,4}$-i_b	12.3 (12.4)
O_1GSH-Ca-VI-$A_{1,1a,2,3,4}$-ii_{SH}	12.8 (12.9)
O_1GSH-Ca-VI-$A_{1,1a,2,3,4}$-i_c	17.5 (16.3)
O_1GSH-Ca-VI-$A_{1,1a,2,3,4}$-i_d	18.2 (16.8)
O_1GSH-Ca-VI-$A_{1,1a,2,3,4}$-ii_b	18.9 (17.2)
O_1GSH-Ca-VI-$A_{1,1a,2,3,4}$-iii_a	15.8 (17.9)
O_1GSH-Ca-VI-$A_{1,1a,2,3,4}$-iv_a	22.5 (18.5)
O_1GSH-Ca-VI-$A_{1,1a,2,3,4}$-i_e	18.0 (18.8)
O_1GSH-Ca-VI-$A_{1,1a,2,3,4}$-iv_b	18.3 (19.4)
O_1GSH-Ca-VI-$A_{1,1a,2,3,4}$-i_f	22.3 (20.1)
O_1GSH-Ca-VI-$A_{1,1a,2,3,4}$-i_g	22.4 (21.6)
O_1GSH-Ca-VI-$A_{1,1a,2,3,4}$-iv_c	25.4 (22.4)
O_1GSH-Ca-VI-$A_{1,1a,2,3,4}$-iii_{SH}	19.3 (22.8)

Structures of $Ca(GSH-H)^+$	**B3LYP/6-31+G(d,p) (For all atoms)**
O_1GSH-Ca-VI-$A_{1,1a,2,3,4}$-iv_d	24.1 (22.9)
O_1GSH-Ca-VI-$A_{1,1a,2,3,4}$-i_h	27.3 (24.9)
O_1GSH-Ca-VI-$A_{1,1a,2,3,4}$-iv_e	28.6 (26.6)
O_4GSH-Ca-V-$B_{1,2,3,4,4a}$-i_a	35.9 (26.7)
O_1GSH-Ca-VI-$A_{1,1a,2,3,4}$-v_{SH}	37.0 (41.0)
O_4GSH-Ca-V-$B_{1,1a,2,3,4}$-ii_a	50.9 (43.9)

Table S3. 3: 298K relative enthalpies and Gibbs energies, in kJ mol-1, of $Sr(GSH-H)^+$. Relative Gibbs energies are indicated in parentheses.

Structures of $Sr(GSH-H)^+$	**-B3LYP/6-31+G(d,p)/ (For C, H,N,O,S atoms) -B3LYP/Def2SVP (Sr)**
$O_1GSH\text{-}Sr\text{-}V\text{-}A_{1,1a,3,4}\text{-}i_{SH}$	0.0 (0.0)
$O_1GSH\text{-}Sr\text{-}V\text{-}A_{1,1a,3,4}\text{-}i_b$	6.8 (4.9)
$O_1GSH\text{-}Sr\text{-}V\text{-}A_{1,1a,3,4}\text{-}i_c$	8.8 (7.0)
$O_1GSH\text{-}Sr\text{-}V\text{-}A_{1,1a,3,4}\text{-}i_d$	11.0 (8.2)
$O_1GSH\text{-}Sr\text{-}V\text{-}A_{1,1a,3,4}\text{-}i_e$	10.3 (9.4)
$O_1GSH\text{-}Sr\text{-}V\text{-}A_{1,1a,3,4}\text{-}i_f$	15.0 (11.3)
$O_1GSH\text{-}Sr\text{-}VI\text{-}A_{1,1a,2,3,4}\text{-}i_{SH}$	16.2 (15.0)
$O_1GSH\text{-}Sr\text{-}V\text{-}A_{1,1a,3,4}\text{-}i_g$	17.6 (15.2)
$O_1GSH\text{-}Sr\text{-}VI\text{-}A_{1,1a,2,3,4}\text{-}ii_{SH}$	20.9 (20.1)
$O_1GSH\text{-}Sr\text{-}VI\text{-}A_{1,1a,2,3,4}\text{-}i_b$	22.5 (20.2)
$O_1GSH\text{-}Sr\text{-}VI\text{-}A_{1,1a,2,3,4}\text{-}i_c$	23.2 (20.4)
$O_1GSH\text{-}Sr\text{-}VI\text{-}A_{1,1a,2,3,4}\text{-}i_d$	23.1 (22.8)
$O_1GSH\text{-}Sr\text{-}VI\text{-}A_{1,1a,2,3,4}\text{-}i_e$	22.9 (23.1)
$O_1GSH\text{-}Sr\text{-}VI\text{-}A_{1,1a,2,3,4}\text{-}i_f$	27.5 (23.9)
$O_1GSH\text{-}Sr\text{-}VI\text{-}A_{1,1a,2,3,4}\text{-}ii_b$	27.2 (24.5)
$O_1GSH\text{-}Sr\text{-}VI\text{-}A_{1,1a,2,3,4}\text{-}i_g$	27.7 (25.6)
$O_1GSH\text{-}Sr\text{-}VI\text{-}A_{1,1a,2,3,4}\text{-}i_h$	27.6 (25.7)
$O_1GSH\text{-}Sr\text{-}VI\text{-}A_{1,1a,2,3,4}\text{-}ii_c$	26.3 (26.1)
$O_1GSH\text{-}Sr\text{-}VI\text{-}A_{1,1a,2,3,4}\text{-}ii_d$	30.4 (26.3)
$O_1GSH\text{-}Sr\text{-}VI\text{-}A_{1,1a,2,3,4}\text{-}iii_a$	32.3 (27.8)

Structures of $Sr(GSH-H)^+$	**-B3LYP/6-31+G(d,p)/ (For C, H,N,O,S atoms) -B3LYP/Def2SVP (Sr)**
O_4GSH-Sr-V-$B_{1,2,3,4,4a}$-i_a	39.1 (28.3)
O_1GSH-Sr-VI-$A_{1,1a,2,3,4}$-ii_e	33.3 (29.4)
O_1GSH-Sr-VI-$A_{1,1a,2,3,4}$-ii_f	31.9 (30.2)
O_1GSH-Sr-VI-$A_{1,1a,2,3,4}$-ii_g	36.4 (33.4)
O_4GSH-Sr-V-$B_{1,2,3,4,4a}$-ii_{SH}	53.0 (42.7)
O_1GSH-Sr-V-$B_{1,1a,2,3,4}$-i_a	47.5 (44.3)

Table S3. 4: 298K relative enthalpies and Gibbs energies, in kJ mol-1, of $Ba(GSH-H)^+$. Relative Gibbs energies are indicated in parentheses.

Structures of $Ba(GSH-H)^+$	**-B3LYP/6-31+G(d,p)/ (For C, H,N,O,S atoms) -B3LYP/Def2SVP (Ba)**
O_1GSH-Ba-V-$A_{1,1a,3,4}$-i_{SH}	0.0 (0.0)
O_1GSH-Ba-V-$A_{1,1a,3,4}$-i_b	8.1 (6.1)
O_1GSH-Ba-V-$A_{1,1a,3,4}$-i_c	8.9 (7.2)
O_1GSH-Ba-V-$A_{1,1a,3,4}$-i_d	11.7 (9.1)
O_1GSH-Ba-V-$A_{1,1a,3,4}$-i_e	10.0 (9.2)
O_1GSH-Ba-V-$A_{1,1a,3,4}$-i_f	12.2 (10.5)
O_1GSH-Ba-V-$A_{1,1a,3,4}$-ii_{SH}	13.5 (12.0)
O_1GSH-Ba-VI-$A_{1,1a,2,3,4}$-i_a	12.1 (15.9)
O_1GSH-Ba-V-$A_{1,1a,3,4}$-ii_b	22.1 (19.3)
O_1GSH-Ba-V-$A_{1,1a,3,4}$-ii_c	23.8 (20.6)
O_1GSH-Ba-VI-$A_{1,1a,2,3,4}$-i_b	21.6 (21.7)
O_1GSH-Ba-V-$A_{1,1a,3,4}$-ii_d	22.9 (22.5)
O_1GSH-Ba-VI-$A_{1,1a,2,3,4}$-iii_a	23.0 (22.7)
O_1GSH-Ba-VI-$A_{1,1a,2,3,4}$-iv_{SH}	23.3 (23.0)
O_1GSH-Ba-V-$A_{1,1a,3,4}$-ii_e	24.1 (23.3)
O_1GSH-Ba-VI-$A_{1,1a,2,3,4}$-i_c	24.3 (24.5)
O_1GSH-Ba-VI-$A_{1,1a,2,3,4}$-v_a	26.1 (25.2)
O_1GSH-Ba-VI-$A_{1,1a,2,3,4}$-i_d	24.4 (25.6)
O_1GSH-Ba-VI-$A_{1,1a,2,3,4}$-i_{SH}	24.2 (25.9)
O_1GSH-Ba-VI-$A_{1,1a,2,3,4}$-iii_c	28.6 (26.1)

Structures of $Ba(GSH-H)^+$	-B3LYP/6-31+G(d,p)/ (For C, H,N,O,S atoms) -B3LYP/Def2SVP (Ba)
O_1GSH-Ba-VI-$A_{1,1a,2,3,4}$-i_f	26.1 (26.9)
O_1GSH-Ba-VI-$A_{1,1a,2,3,4}$-v_{SH}	25.6 (27.7)
O_1GSH-Ba-VI-$A_{1,1a,2,3,4}$-iv_b	29.9 (27.7)
O_1GSH-Ba-VI-$A_{1,1a,2,3,4}$-i_g	29.9 (29.2)
O_1GSH-Ba-VI-$A_{1,1a,2,3,4}$-iv_c	32.8 (29.3)
O_1GSH-Ba-VI-$A_{1,1a,2,3,4}$-iv_d	29.0 (29.5)
O_1GSH-Ba-VI-$A_{1,1a,2,3,4}$-iv_e	41.8 (31.5)
O_1GSH-Ba-VI-$A_{1,1a,2,3,4}$-vi_a	35.6 (32.3)
O_1GSH-Ba-V-$B_{1,1a,2,3,4}$-i_a	33.4 (33.3)
O_1GSH-Ba-VI-$A_{1,1a,2,3,4}$-vi_b	34.5 (33.4)
O_1GSH-Ba-V-$B_{1,1a,2,3,4}$-i_b	32.7 (34.8)
O_4GSH-Ba-IV-$B_{1,3,4,4a}$-i_{SH}	37.6 (35.5)
O_1GSH-Ba-VI-$A_{1,1a,2,3,4}$-vi_c	38.5 (35.6)
O_1GSH-Ba-V-$B_{1,1a,2,3,4}$-ii_{SH}	33.3 (37.1)

Appendix C – Supplemental Information for Chapter 4

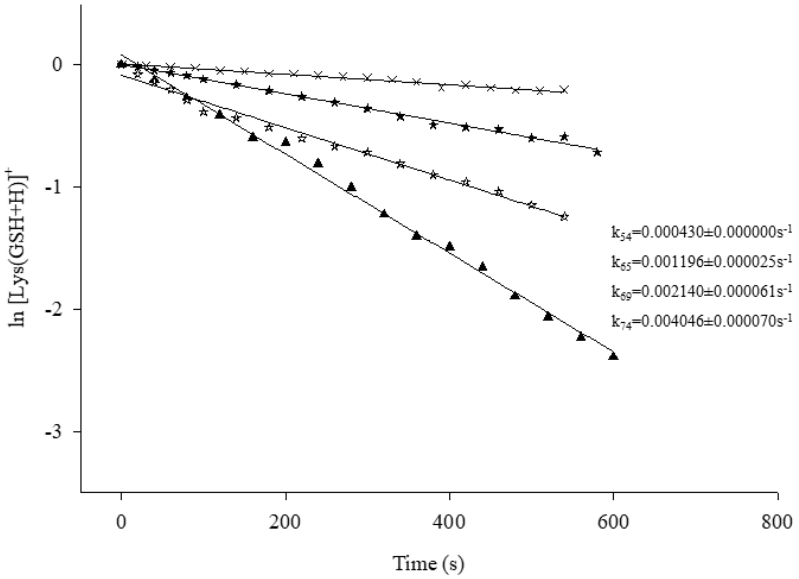

Figure S4. 1:Blackbody infrared radiative dissociation first-order kinetics plots at different temperatures. 54-74 °C for the $[Lys(GSH+H)]^+$.

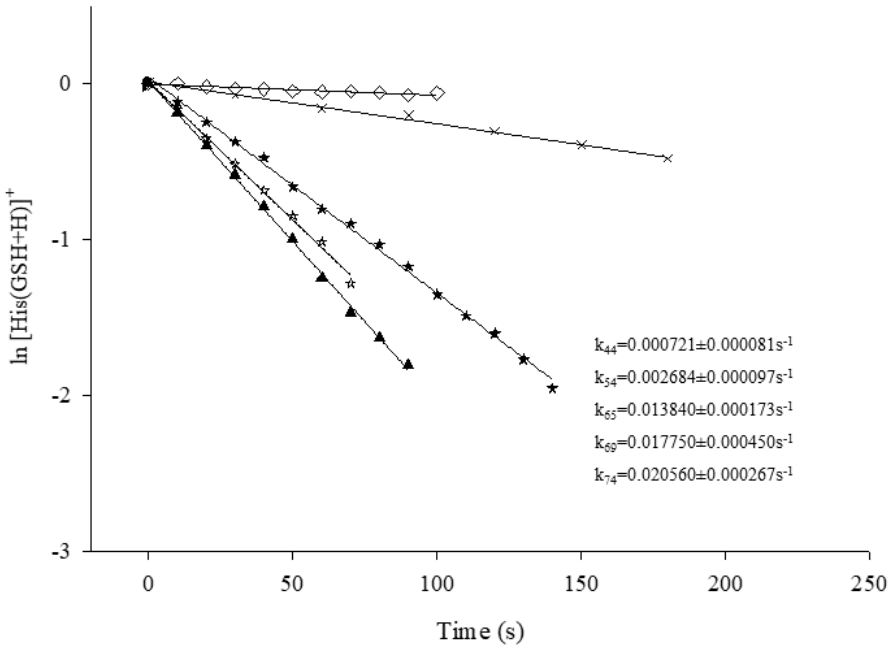

Figure S4. 2: Blackbody infrared radiative dissociation first-order kinetics plots at different temperatures. 44-74 °C for the $[His(GSH+H)]^+$.

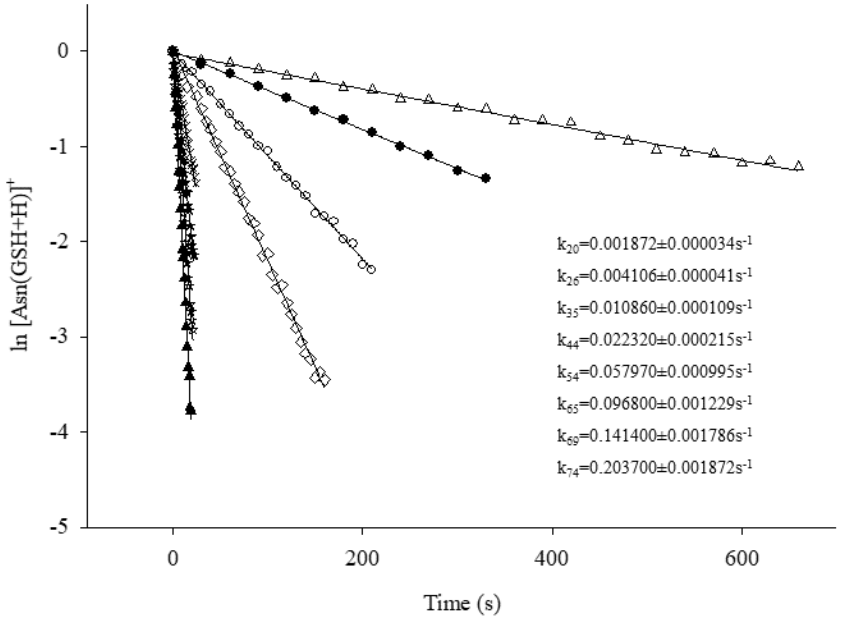

Figure S4. 3: Blackbody infrared radiative dissociation first-order kinetics plots at different temperatures. 20-74 °C for the $[Asn(GSH+H)]^+$.

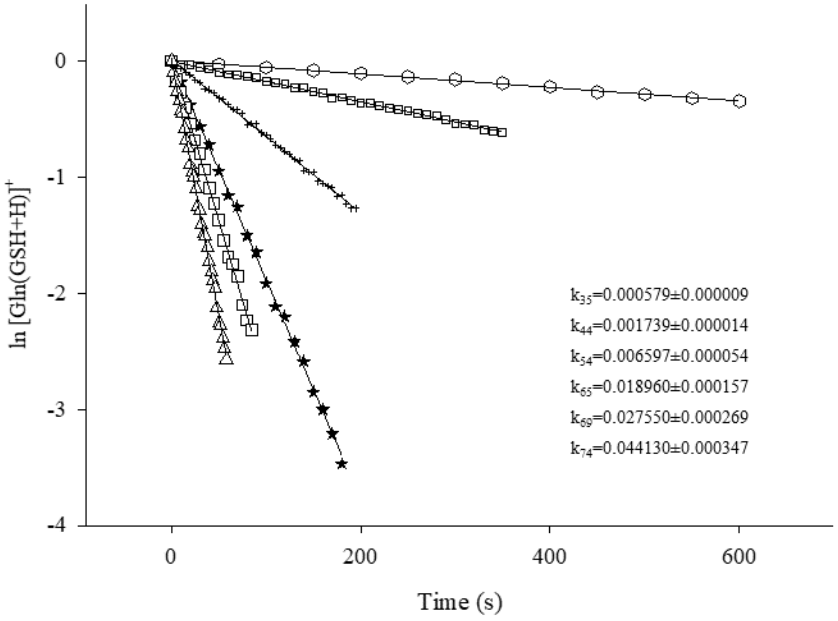

Figure S4. 4: Blackbody infrared radiative dissociation first-order kinetics plots at different temperatures. 54-74 °C for the $[Gln(GSH+H)]^+$.

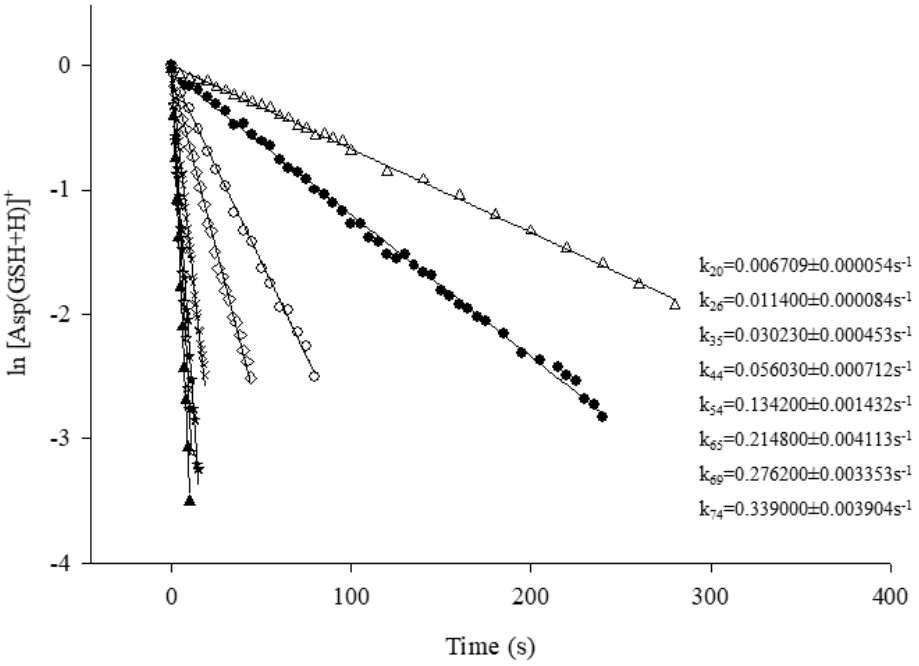

Figure S4. 5: Blackbody infrared radiative dissociation first-order kinetics plots at different temperatures. 20-74 °C for the $[Asp(GSH+H)]^+$.

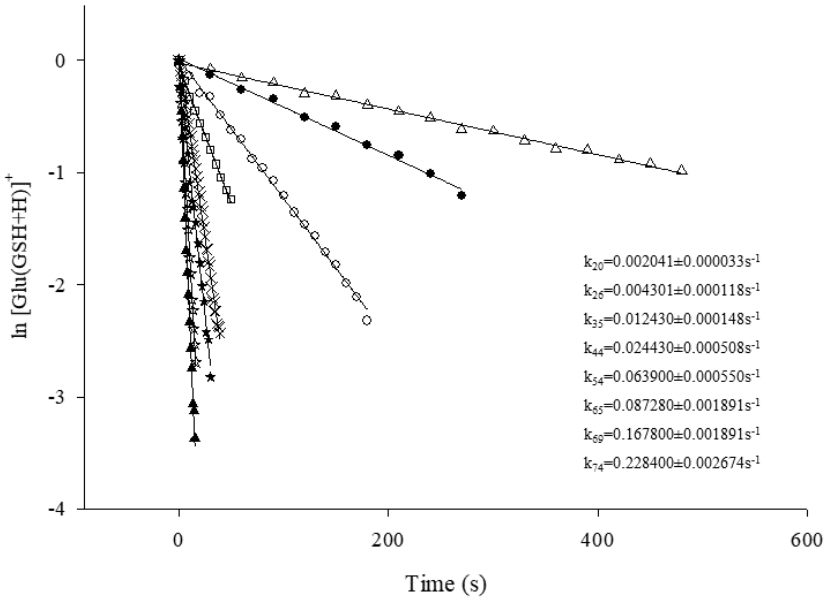

Figure S4. 6: Blackbody infrared radiative dissociation first-order kinetics plots at different temperatures. 20-74 °C for the $[Glu(GSH+H)]^+$.

Table S4. 1: Arrhenius activation energy E_0(KJ mol^{-1})), logarithm of pre-exponential factors (log A_{obs}), entropy of activation DS†.

Species	E_0(KJ mol^{-1})	Log A_{obs}	$\Delta S^{\dagger}$ (J mol^{-1} K^{-1})
[Asp(GSH+H)]$^+$	62.6±2.11	9.0±0.8	-80.6±3.1
[Glu(GSH+H)]$^+$	71.4±3.02	10.1±1.1	-59.8±2.9
[Gln(GSH+H)]$^+$	98.4±2.81	13.5±1.0	4.8±1.6
[Asn(GSH+H)]$^+$	72.2±2.04	10.2±0.8	-57.8±1.9
[Lys(GSH+H)]$^+$	114.3±6.10	14.8±2.2	30.1±1.9
[His(GSH+H)]$^+$	109.5±1.08	14.9±3.9	32.4±3.7
[Arg(GSH+H)]$^+$	94.4±5.49	12.5±1.9	-13.4±0.9